

ΠΑΝΕΠΙΣΤΗΜΙΟ ΚΡΗΤΗΣ
ΤΜΗΜΑ ΧΗΜΕΙΑΣ



ΔΙΔΑΚΤΟΡΙΚΗ ΔΙΑΤΡΙΒΗ

Μελέτη προσρόφησης αερίων σε νανοπορώδη υλικά με
προηγμένες πειραματικές μεθόδους για εφαρμογές αποθήκευσης
και διαχωρισμού αερίων

ΧΡΗΣΤΟΣ ΤΑΜΠΑΞΗΣ

Υπεύθυνος Καθηγητής: Παντελής Ν. Τρικαλίτης

ΗΡΑΚΛΕΙΟ, 2024

**UNIVERSITY OF CRETE
DEPARTMENT OF CHEMISTRY**



Doctoral Thesis

Advanced experimental studies of gas adsorption in nanoporous materials for gas storage and gas separations applications

CHRISTOS TAMPAXIS

Thesis Supervisor: Pantelis N. Trikalitis

HERAKLION, 2024

Στη μνήμη του Θεωρή.

Thesis Committee

Prof. Pantelis N. Trikalitis (Supervisor)

Department of Chemistry, University of Crete

Dr. Georgia Charalambopoulou (Advisory Board)

Research Director, Institute of Nuclear & Radiological Sciences and Technology, Energy & Safety, NCSR “Demokritos”

Dr. Theodoros A. Steriotis (Advisory Board)

Research Director, Institute of Nanoscience and Nanotechnology, NCSR “Demokritos”

Prof. Georgios E. Froudakis

Department of Chemistry, University of Crete

Prof. Dimitrios Gournis

Department of Materials Science & Engineering, University of Ioannina

Ass. Prof. Constantinos J. Milios

Department of Chemistry, University of Crete

Prof. Konstantinos S. Triantafyllidis

Department of Chemistry, Aristotle University of Thessaloniki

ΕΥΧΑΡΙΣΤΙΕΣ

Θα ήθελα να ευχαριστήσω τον καθηγητή Παντελή Τρικαλίτη που μου έδωσε τη δυνατότητα να πραγματοποιήσω αυτή τη διατριβή ως υποψήφιος διδάκτορας του Πανεπιστημίου Κρήτης καθώς και για την άρτια επιστημονική του καθοδήγηση. Ειδικότερα, θα ήθελα να ευχαριστήσω τα μέχρι πρότινος μέλη της ερευνητικής του ομάδας, Δρ. Ιωάννη Σπανόπουλο και Δρ. Σεμίνα Αγγέλη για την άψογη συνεργασία μας και τη στήριξη της διατριβής μου, προμηθεύοντάς με, πάντα με ενδιαφέρουσες νανοπορώδεις δομές, καρπούς της επίπονης συνθετικής εργασίας τους στο εργαστήριο Ανόργανης Χημείας του Πανεπιστημίου Κρήτης, υπό την επίβλεψη του καθηγητή Τρικαλίτη.

Θα ήθελα επίσης να ευχαριστήσω τους καθηγητές Γεώργιο Φρουδάκη (Πανεπιστήμιο Κρήτης), Δημήτριο Γουρνή (Πανεπιστήμιο Ιωαννίνων), Κωνσταντίνο Μηλιό (Πανεπιστήμιο Κρήτης) και Κωνσταντίνο Τριανταφυλλίδη (Αριστοτέλειο Πανεπιστήμιο Θεσσαλονίκης) για την τιμή που μου έκαναν συμμετέχοντας στην επταμελή εξεταστική επιτροπή.

Ευχαριστώ επίσης μέσα από την καρδιά μου όλα τα μέλη του εργαστηρίου Μεμβρανών/Υλικών για Περιβαλλοντικούς Διαχωρισμούς (MESL) του Ινστιτούτου Νανοεπιστήμης και Νανοτεχνολογίας, του ΕΚΕΦΕ «Δημόκριτος», για την καθημερινή τους υποστήριξη και για όλα όσα μοιραστήκαμε αυτά τα χρόνια. Εντελώς καταχρηστικά, θα αναφέρω ονομαστικά τους Δρ. Ευάγγελο Κούβελο και Δρ. Σέργιο Παπαγεωργίου για την πολύτιμη βοήθειά τους στις τεχνικές προκλήσεις που αντιμετώπισα καθώς και τον Δρ. Ιωάννη Μπράτσο, για την ακούραστη δουλειά του, συνθέτοντας σε μεγάλες ποσότητες τα υλικά που μελετώνται στην παρούσα διατριβή.

Τέλος, ευχαριστώ για όλους του λόγους του κόσμου, που δεν εξαντλούνται σε μια τυπική επίβλεψη διδακτορικής διατριβής και είναι αδύνατον να αποτυπωθούν σε χαρτί, τ@ ερευνητ@ (ΕΚΕΦΕ «Δημόκριτος») Δρ. Θεόδωρο Στεριώτη και Δρ. Γεωργία Χαραλαμποπούλου για την ανεκτίμητη στήριξή τους σχεδόν σε όλες τις εκφάνσεις της ζωής μου τα τελευταία χρόνια. Τους είμαι ευγνώμων για πάντα.

ΒΙΟΓΡΑΦΙΚΟ ΣΗΜΕΙΩΜΑ

Θησέως 2, Βόρωνας
16233, Αττική
ΕΛΛΑΔΑ

Κινητό: +306947846911
Γραφείο: +302106503636
E-mail: c.tampaxis@inn.demokritos.gr

ΧΡΗΣΤΟΣ ΤΑΜΠΑΞΗΣ

Προσωπικά Στοιχεία

- Οικογενειακή κατάσταση: Άγαμος
- Ημερομηνία γέννησης: 11 Οκτωβρίου, 1983
- Τόπος γέννησης: Χολαργός Αττικής, ΕΛΛΑΔΑ
- Γονείς: Θεόδωρος, Στυλιανή

Εκπαίδευση

- **Υποψήφιος Διδάκτωρ - Τμήμα Χημείας, Σχολή Θετικών Επιστημών Πανεπιστημίου Κρήτης (Μάρτιος 2014 – σήμερα)**
Τίτλος διδακτορικής διατριβής: “Μελέτη προσρόφησης αερίων σε νανοπορώδη υλικά με προηγμένες πειραματικές μεθόδους για εφαρμογές αποθήκευσης και διαχωρισμού αερίων”.
- **Μεταπτυχιακό Δίπλωμα Ειδίκευσης: M.Sc. Chemistry & Science Based Business, University of Leiden, The Netherlands (2008-2010)**
Master Thesis: “Synthesis of Iron and Copper Coordination Compounds as Catalysts for Oxidation Reactions and DNA-cleaving agents”.
Iron-Schiff base compounds were tested as biomimetic homogeneous catalysts in the oxidation reaction of cyclohexane to cyclohexanol and cyclohexanone. In addition copper-Schiff base compounds (after determining their single-crystal X-ray structures), were tested as potential DNA-cleaving agents (inducing double strand DNA-cleavages with respect to their geometry) using gel electrophoresis.
- **Πτυχίο: Τμήμα Χημείας, Σχολή Θετικών Επιστημών, Πανεπιστήμιο Ιωαννίνων (2001-2006)**
Πτυχιακή εργασία: “Μη-αιμικοί, βιομιμητικοί καταλύτες (ομογενείς και ετερογενείς) οξειδωσης”.
Σύνθεση συμπλόκων μαγνησίου, και χρήση τους ως καταλύτες σε εποξειδωση ολεφινών, και διερεύνηση της καταλυτικής τους ικανότητας ως ομογενή και ετερογενή (ακίνητοποιημένα σε πυριτικά υποστρώματα) μίγματα

Ξένες γλώσσες

- Certificate in Advanced English, University of Cambridge Grade B (2007)
- Diploma de Espanol como Lengua Extranjera Nivel Inicial (2005)

Αναλυτικές τεχνικές

- NMR, IR, XRD, Neutron Scattering, GC, GC-MS, Porosimetry, High pressure volumetric and gravimetric adsorption systems

Γνώση λογισμικού

- MS Windows, MS Office, OriginLab Origin, Chemoffice, Hg (Mercury), AS1 win, Labview

Εργασιακή εμπειρία

- Επιστημονικός συνεργάτης – Ινστιτούτο Νανοεπιστήμης και Νανοτεχνολογίας, ΕΚΕΦΕ «Δημόκριτος», Εργαστήριο HYSORB (01/02/2013 - σήμερα)

Αντικείμενο: Ανάπτυξη και χαρακτηρισμός νανοπορωδών και νανოსύνθετων υλικών

Επιστημονικές δημοσιεύσεις

- Επισκέπτης ερευνητής: **Steel Belt Systems**, Ιταλία (Φεβρουάριος - Ιούνιος 2016), **IBT Co. Ltd.**, Ισραήλ (Σεπτέμβριος - Δεκέμβριος 2016), **Βιομηχανία Ρητινών Μεγάρων Α. ΦΑΝΗΣ Α.Ε.**, Ελλάδα (Φεβρουάριος – Απρίλιος 2017)
- Πρακτική άσκηση στη **Janssen Pharmaceuticals** στο τμήμα στρατηγικού σχεδιασμού υπό την επίβλεψη του New Product Development Manager (Απρίλιος - Οκτώβριος 2010)
- Πρακτική άσκηση στα **Gorlaeus Laboratories**, Ολλανδία, υπό την επίβλεψη των Prof. dr. Jan Reedijk and Patrick Gamez. (Φεβρουάριος - Οκτώβριος 2008)
-
- 1. Stock S, Kostoglou N, Selinger J, Spirk S, Tampaxis C, Charalambopoulou G, Steriotis Th, et. al.. Coffee Waste-Derived Nanoporous Carbons for Hydrogen Storage. *ACS Appl Energy Mater.* 2022;5(9):10915–26.
- 2. Kostoglou N, Koczwarra C, Stock S, **Tampaxis Ch**, Charalambopoulou G, Steriotis T, et al. Nanoporous polymer-derived activated carbon for hydrogen adsorption and electrochemical energy storage. *Chemical Engineering Journal.* 2022;427(July 2021).
- 3. Kostoglou N, Liao CW, Wang CY, Kondo JN, **Tampaxis Ch**, Steriotis T, Giannakopoulos, K et. al. Effect of Pt nanoparticle decoration on the H₂ storage performance of plasma-derived nanoporous graphene. *Carbon N Y.* 2021;171:294–305.
- 4. Kostoglou N, **Tampaxis Ch**, Charalambopoulou G, Constantinides G, Ryzhkov V, Doumanidis C, Matovic B, Mitterer C, Rebholz C. Boron nitride nanotubes versus carbon nanotubes: A thermal stability and oxidation behavior study. *Nanomaterials.* 2020;10(12):1–9.
- 5. Nguyen, H. G. T. et al. A reference high-pressure CH₄ adsorption isotherm for zeolite Y: results of an interlaboratory study. *Adsorption* 26, 1253–1266 (2020)
- 6. Smyrnioti M, **Tampaxis Ch**, Steriotis T, Ioannides T. Study of CO₂ adsorption on a commercial CuO/ZnO/Al₂O₃ catalyst. *Catalysis Today.* (2020) 357 (November 2018):495–502.
- 7. Stefanopoulos KL, **Tampaxis Ch**, Sapalidis AA, Katsaros FK, Youngs TGA, Bowron DT, Steriotis T. Total neutron scattering study of supercooled CO₂ confined in an ordered mesoporous carbon. *Carbon N Y.* (2020);167:296–306
- 8. **Tampaxis Ch**, Steriotis T, Katsaros FK, Sapalidis AA, Youngs TGA, Bowron DT, Stefanopoulos K.. Enhanced Densification of CO₂ Confined in the Pores of a Carbon Material: an in Situ Total Neutron Scattering Study. *Journal of Surface Investigation.* (2020);14(Suppl. 1):S221–4
- 9. Holec, D., Kostoglou, N., **Tampaxis, Ch.**, Babic, B., Mitterer, C., Rebholz, C. “*Theory-guided metal-decoration of nanoporous carbon for hydrogen storage applications*”, *Surface and Coatings Technology*, 351, (2018), pp. 42-49.
- 10. Bratsos, I., **Tampaxis, Ch.**, Spanopoulos, I., Demitri, N., Charalambopoulou, G., Vourloumis, D., Steriotis, T.A., Trikalitis, P.N. “*Heterometallic In(III)-Pd(II) Porous Metal-Organic Framework with Square-Octahedron Topology Displaying High CO₂ Uptake and Selectivity toward CH₄ and N₂*”, *Inorganic Chemistry*, 57 (12), (2018), pp. 7244-7251.
- 11. Tsoufis, T., **Tampaxis, Ch.**, Spanopoulos, I., Steriotis, T., Katsaros, F., Charalambopoulou, G., Trikalitis, P.N. “*High-quality graphene sheets decorated with ZIF-8 nanocrystals*”, *Microporous and Mesoporous Materials*, 262, (2018), pp. 68-76.
- 12. Kostoglou, N., Koczwarra, C., Prehal, C., Terziyska, V., Babic, B., Matovic, B., Constantinides, G., **Tampaxis, Ch.**, Charalambopoulou, G., Steriotis, T., Hinder, S., Baker, M., Polychronopoulou, K., Doumanidis, C., Paris, O., Mitterer, C., Rebholz, C. “*Nanoporous activated carbon cloth as a versatile material for hydrogen*

- adsorption, selective gas separation and electrochemical energy storage*”, Nano Energy, 40, (2017), pp. 49-64.
13. V. Tzitzios, N. Kostoglou, M. Giannouri, G. Basina, **Ch. Tampaxis**, G. Charalambopoulou, Th. Steriotis, K. Polychronopoulou, Ch. Doumanidis, Ch. Mitterer, C. Rebholz, “*Solvothermal synthesis, nanostructural characterization and gas cryo-adsorption studies in a metal–organic framework (IRMOF-1) material*” International Journal of Hydrogen Energy, (2017), Article in Press
 14. Kostoglou, N., Tarat, A., Walters, I., Ryzhkov, V., **Tampaxis, Ch.**, Charalambopoulou, G., Steriotis, Th., Mitterer, C., Rebholz, C., “*Few-layer graphene-like flakes derived by plasma treatment: A potential material for hydrogen adsorption and storage*”, Microporous and Mesoporous Materials, 225 (2016) 482-487.
 15. Giasafaki, D., Charalambopoulou, G., **Tampaxis, Ch.**, Dimos, K., Gournis, D., Stubos, A., Steriotis, Th., “*Comparing hydrogen sorption in different Pd-doped pristine and surface-modified nanoporous carbons*”, Carbon 98 (2016) 1-14.
 16. Spanopoulos, I., Bratsos, I., **Tampaxis, Ch.**, Vourloumis, D., Klontzas, E., Froudakis, G., Charalambopoulou, G., Steriotis, Th., Trikalitis, P., “*Exceptional Gravimetric and Volumetric CO₂ Uptake in a Palladated NbO-type MOF Utilizing Cooperative Acidic and Basic, Metal-CO₂ Interactions*”, Chemical Communications, 52 (69), (2016), 10559-10562.
 17. Kourtellaris, A, Moushi, E, Spanopoulos, I, **Tampaxis, Ch**, Charalambopoulou, G, Steriotis, Th, Papaefstathiou, G, Trikalitis, P, Tasiopoulos, A, “*A microporous Cu₂⁺ MOF based on a pyridyl isophthalic acid Schiff base ligand with high CO₂ uptake*”, Inorganic Chemistry Frontiers3(12), (2016), pp. 1527-1535
 18. D. Giasafaki, G. Charalambopoulou, **Ch. Tampaxis**, D. Mirabile Gattia, A. Montone, G. Barucca, Th. Steriotis, “*Hydrogen storage properties of Pd-doped thermally oxidized single wall carbon nanohorns*”, Journal of Alloys and Compounds, 645, Issue S1, 11 (2015), S485-S489.
 19. Spanopoulos I., Bratsos, I., **Tampaxis, Ch.**, Kourtellaris, A., Tasiopoulos, A., Charalambopoulou, G., Steriotis, T. Trikalitis, P.N, “*Enhanced gas-sorption properties of a high surface area, ultramicroporous magnesium formate*”, CrystEngComm, 17 (3), (2015) 532-53
 20. Kostoglou, N, Tzitzios, V, Kontos A, Giannakopoulos K, **Tampaxis Ch**, Papavasiliou A, Charalambopoulou, G, Steriotis, T, Li, Y, Liao, K, Polychronopoulou, K, Mitterer, C, Rebholz, C, “*Synthesis of nanoporous graphene oxide adsorbents by freeze-drying or microwave radiation: Characterization and hydrogen storage properties*” International Journal of Hydrogen Energy 40 (2015) 6844-6852
 21. Giasafaki, D., Charalambopoulou, G., **Tampaxis, Ch.**, Stubos, A., Steriotis, T., “*Pd-doped molecular sieves for hydrogen storage*”, International Journal of Hydrogen Energy 39 (2014) 9830-9836

Συμμετοχή σε συνέδρια

- **Ch. Tampaxis**, S. Angeli, I. Bratsos, P. Trikalitis, G. Charalambopoulou, Th. Steriotis. “Air purification using hydrolytically stable fluorinated MOFs”, 13th Panhellenic Scientific Chemical Engineering Conference, June 2022, Patras, Greece
- N. Kostoglou, B. Babic, B. Matovic, **Ch. Tampaxis**, G. Charalambopoulou, Th. Steriotis, S. Hinder, M. Baker, G. Constantinides, Ch. Mitterer, C. Rebholz, Nanoporous graphene derived by plasma processing: properties towards hydrogen adsorption and selective carbon dioxide/methane gas separation, 1st Advanced Energy

Materials (AEM2016), combining the 8th International Conference on Advanced Nanomaterials and 2nd International Conference on Hydrogen Energy, 12-14 September 2016. Guildford/Surrey – UK.

- T. Tsoufis, **Ch. Tampaxis**, I. Spanopoulos, Th. Steriotis, F. Katsaros, G. Charalambopoulou, P.N. Trikalitis, High-quality Graphene/ZIF-8 & Carbon nanotube/ZIF-8 nanocomposites: Synthesis, Characterization and Gas Sorption Properties, Industrial Technologies 2016, 22 – 24 June 2016, Amsterdam – The Netherlands.
- Θ. Τσουφης, **X. Ταμπαξής**, I. Σπανόπουλος, Θ. Στεριώτης, Φ. Κατσαρός, Γ. Χαραλαμποπούλου, Π. Τρικαλίτης, Καινοτόμα Νανοσύνθετα Υλικά αποτελούμενα από Νανοδομές Άνθρακα και Πορώδη Υλικά τύπου ZIF, 7ο Πανελλήνιο Συμπόσιο Πορώδων Υλικών, Ιωάννινα, 2-4 Ιουνίου 2016.
- M-L Saboungi, D. Giasafaki, **Ch. Tampaxis**, G. Charalambopoulou, Th. Steriotis, Hydrogen storage properties of pristine and modified single wall carbon nanohorn structures, 7th Panhellenic Symposium on Porous Materials, Ioannina - Greece, 2-4 June 2016.
- I. Bratsos, **Ch. Tampaxis**, I. Spanopoulos, N. Demitri, D. Vourloumis, G. Charalambopoulou, P. Trikalitis, Th. Steriotis, 7th Panhellenic Symposium on Porous Materials, Ioannina - Greece, 2-4 June 2016.
- S. Garroni, F. Peru, **Ch. Tampaxis**, G. Charalambopoulou, Th. Steriotis, Hydrogen storage properties of imide-carbon composites, 7th Panhellenic Symposium on Porous Materials, Ioannina - Greece, 2-4 June 2016.
- P. Gamez, **Ch. Tampaxis**, G. Charalambopoulou, Th. Steriotis, Pore and gas sorption properties of a new series of pyridine containing metal organic frameworks, 7th Panhellenic Symposium on Porous Materials, Ioannina - Greece, 2-4 June 2016.
- C. Croitoru, **Ch. Tampaxis**, G. Charalambopoulou, Th. Steriotis, Hydrogen storage performance of ionic liquid-impregnated aerogels, 7th Panhellenic Symposium on Porous Materials, Ioannina - Greece, 2-4 June 2016.
- I. Bratsos, **Ch. Tampaxis**, I. Spanopoulos, N. Demitri, D. Vourloumis, G. Charalambopoulou, P. Trikalitis, Th. Steriotis, “*An unprecedented heterobimetallic In(III)-Pd(II) porous metal-organic framework with soc topology for hydrogen storage*”, E-MRS 2015 Fall Meeting, Warsaw-Poland, 15-18 September 2015.
- Ampoumogli, D. Giasafaki, **Ch. Tampaxis**, G. Charalambopoulou, A. Stubos, Th. Steriotis, “*Hydrogen storage in solids with the use of nanoporous carbon supports and scaffolds*”, Euro-Mediterranean Hydrogen Technologies Conference - EmHyTeC2014, 9-12 December 2014, Taormina, Italy
- N. Kostoglou, V. Tzitzios, **Ch. Tampaxis**, G. Charalambopoulou, Th. Steriotis, K. Giannakopoulos, A. Kontos, Y. Li, K. Liao, K. Polychronopoulou, C. Rebholz, “*Synthesis, characterization and hydrogen storage capacity of nanoporous graphene-based adsorbents*”, AVS 61st International Symposium & Exhibition, Baltimore-USA, 9-14 November 2014
- N.K. Kostoglou, C. Rebholz, V. Tzitzios, **C. Tampaxis**, T.A. Steriotis, K. Giannakopoulos, G.C. Charalambopoulou, K. Polychronopoulou, Y. Li, K. Liao, “Hydrogen storage capacity of different nanoporous carbon adsorbents”, 30th Panhellenic Conference on Solid-State Physics and Materials Science Heraklion, Crete, 21-24 September, 2014.
- D. Giasafaki, **Ch. Tampaxis**, G. Charalambopoulou, D. Mirabile Gattia, A. Montone, Th. Steriotis, “*Hydrogen storage properties of Pd-doped thermally oxidised Single Wall Carbon Nanohorns*”, 14th International Symposium on Metal-Hydrogen Systems (MH 2014), Salford, Manchester - UK, 20 - 25 July 2014

**Συμμετοχή σε
ερευνητικά
προγράμματα**

- D. Giasafaki, **Ch. Tampaxis**, A. Ampoumogli, G. Charalambopoulou, A. Bourlinos, A. Stubos, Th. Steriotis, “*Studying the effect of surface chemistry and metal-doping on the hydrogen storage capacity of carbon nanostructures*”, Symposium C: Nanostructured Materials for solid state hydrogen storage, E-MRS 2013 Fall Meeting, Warsaw-Poland, 16-20 September 2013.
- K. Dimos, M.A. Antoniou, **Ch. Tampaxis**, F.L. Kuo, R.F. Reidy, G. Charalambopoulou, Th.A. Steriotis, D. Gournis, “Synthesis and characterization of novel carbon based nanostructures for hydrogen storage”, 6th Panhellenic Symposium on Porous Materials, Kavala - Greece, 9-10 September 2013
- RESEARCH–CREATE–INNOVATE (Project nr: T1EΔK-00770, 2014-2020): “Application of Novel Porous Materials in Industrially Relevant Gas Separation/Purification Processes (PureGas)”.
- MC FP7-PEOPLE-2012-IAPP (Grant 324410), 06.2014-05.2016 New weather-stable low gloss powder coatings based on bifunctional acrylic solid resins and nano-additives (GLOW)
- FP7-INFRASTRUCTURES-2011-1 (Grant Agreement 284522, 2011-2015): “Integrating European Infrastructure to support Science and Development of Hydrogen- and Fuel Cell Technologies towards European Strategy for Sustainable, Competitive and Secure Energy (H2FC)”.

CURRICULUM VITAE

2, Thisseos str, Vironas
16233, Attica
GREECE

Mobile: +306947846911
Office: +302106503636
E-mail: c.tampaxis@inn.demokritos.gr

CHRISTOS TAMPAXIS

- Personal Information**
- Marital status: Single
 - Date of birth: October 11th, 1983
 - Place of birth: Athens, GREECE
 - Parents: Theodore, Styliani
- Current Position**
- Research Associate / PhD Candidate, *Porous Materials Group, National Center for Scientific Research “Demokritos”*, Athens-Greece (2012- today)
- Education**
- **M.Sc.** Chemistry & Science Based Business, **University of Leiden**, The Netherlands (2010)
Master Thesis: “Synthesis of Iron and Copper Coordination Compounds as Catalysts for Oxidation Reactions and DNA-cleaving agents”
Iron-Schiff base compounds tested as biomimetic homogeneous catalysts in the oxidation reaction of cyclohexane to cyclohexanol and cyclohexanone. Copper-Schiff base compounds after their single-crystal X-ray structures had been determined, were tested as potential DNA-cleaving agents (inducing double strand DNA-cleavages with respect to their geometry) using gel electrophoresis
 - **B.Sc. :** Chemistry, **University of Ioannina**, Greece (2007)
Thesis: “Non-heme biomimetic oxidation (homogeneous and heterogeneous) catalysts.”
Synthesis of Manganese compounds, use as catalysts in epoxidation of olephins, and research of their catalytic activity as homogeneous or heterogeneous (immobilized in silica gel) mixtures
- Foreign Languages**
- Certificate in Advanced English, University of Cambridge Grade B (2007)
 - Diploma de Espanol como Lengua Extranjera Nivel Inicial (2005)
- Analytical Techniques**
- NMR, IR, XRD, Neutron Scattering, GC, GC-MS, Porosimetry, High pressure volumetric and gravimetric adsorption systems
- Software Knowledge**
- MS Windows, MS Office, OriginLab Origin, Chemoffice, Hg (Mercury), AS1 win, Labview
- Working Experience**
- Visiting scientist, **IBT Co. Ltd.**, Israel (September - December 2016) (May - July 2017)
 - Visiting scientist **Megara Resins - Fanis Anastassios S.A.**, Greece (February - April 2017)
 - Visiting scientist, **Steel Belt Systems**, Italy (February - June 2016).

- Research Associate – Porous Materials Group, **National Center for Scientific Research “Demokritos”**, Athens-Greece (2012- today).
- Internship at **Janssen Pharmaceuticals** in Strategic Marketing Department under supervision of New Product Development Manager (April-October 2010)
- Internship at **Gorlaeus Laboratories**, The Netherlands, under the direct supervision of Prof. dr. Jan Reedijk and Patrick Gamez. (February-October 2008)
- Private teaching of Chemistry and Physics at second and third grade students (2001-2009), (2010-2012)

Publications

1. Stock S., Kostoglou N., Selinger J., Spirk S., **Tampaxis Ch.**, Charalambopoulou G., Steriotis Th., et. al. Coffee Waste-Derived Nanoporous Carbons for Hydrogen Storage. *ACS Appl Energy Mater.* 2022;5(9):10915–26.
2. Kostoglou N, Koczwara C, Stock S, **Tampaxis Ch.**, Charalambopoulou G, Steriotis T, et al. Nanoporous polymer-derived activated carbon for hydrogen adsorption and electrochemical energy storage. *Chemical Engineering Journal.* 2022;427(July 2021).
3. Kostoglou N, Liao CW, Wang CY, Kondo JN, **Tampaxis Ch.**, Steriotis T, Giannakopoulos, K et. al. Effect of Pt nanoparticle decoration on the H₂ storage performance of plasma-derived nanoporous graphene. *Carbon N Y.* 2021;171:294–305.
4. Kostoglou N, **Tampaxis Ch.**, Charalambopoulou G, Constantinides G, Ryzhkov V, Doumanidis C, Matovic B, Mitterer C, Rebholz C. Boron nitride nanotubes versus carbon nanotubes: A thermal stability and oxidation behavior study. *Nanomaterials.* 2020;10(12):1–9.
5. Nguyen, H. G. T. et al. A reference high-pressure CH₄ adsorption isotherm for zeolite Y: results of an interlaboratory study. *Adsorption* 26, 1253–1266 (2020)
6. Smyrnioti M, **Tampaxis Ch.**, Steriotis T, Ioannides T. Study of CO₂ adsorption on a commercial CuO/ZnO/Al₂O₃ catalyst. *Catalysis Today.* (2020) 357 (November 2018):495–502.
7. Stefanopoulos KL, **Tampaxis Ch.**, Sopalidis AA, Katsaros FK, Youngs TGA, Bowron DT, Steriotis T. Total neutron scattering study of supercooled CO₂ confined in an ordered mesoporous carbon. *Carbon N Y.* (2020);167:296–306
8. **Tampaxis Ch.**, Steriotis T, Katsaros FK, Sopalidis AA, Youngs TGA, Bowron DT, Stefanopoulos K.. Enhanced Densification of CO₂ Confined in the Pores of a Carbon Material: an in Situ Total Neutron Scattering Study. *Journal of Surface Investigation.* (2020);14(Suppl. 1):S221–4
9. Holec, D., Kostoglou, N., **Tampaxis, Ch.**, Babic, B., Mitterer, C., Rebholz, C. “*Theory-guided metal-decoration of nanoporous carbon for hydrogen storage applications*”, *Surface and Coatings Technology*, 351, (2018), pp. 42-49.
10. Bratsos, I., **Tampaxis, Ch.**, Spanopoulos, I., Demitri, N., Charalambopoulou, G., Vourloumis, D., Steriotis, T.A., Trikalitis, P.N. “*Heterometallic In(III)-Pd(II) Porous Metal-Organic Framework with Square-Octahedron Topology Displaying High CO₂ Uptake and Selectivity toward CH₄ and N₂*”, *Inorganic Chemistry*, 57 (12), (2018), pp. 7244-7251.
11. Tsoufis, T., **Tampaxis, Ch.**, Spanopoulos, I., Steriotis, T., Katsaros, F., Charalambopoulou, G., Trikalitis, P.N. “*High-quality graphene sheets decorated with ZIF-8 nanocrystals*”, *Microporous and Mesoporous Materials*, 262, (2018), pp. 68-76.
12. Kostoglou, N., Koczwara, C., Prehal, C., Terziyska, V., Babic, B., Matovic, B., Constantinides, G., **Tampaxis, Ch.**, Charalambopoulou, G., Steriotis, T., Hinder, S., Baker, M., Polychronopoulou, K., Doumanidis, C., Paris, O., Mitterer, C., Rebholz, C. “*Nanoporous activated carbon cloth as a versatile material for hydrogen adsorption, selective gas separation and electrochemical energy storage*”, *Nano Energy*, 40, (2017), pp. 49-64.

13. V. Tzitzios, N. Kostoglou, M. Giannouri, G. Basina, **Ch. Tampaxis**, G. Charalambopoulou, Th. Steriotis, K. Polychronopoulou, Ch. Doumanidis, Ch. Mitterer, C. Rebholz, “*Solvothermal synthesis, nanostructural characterization and gas cryo-adsorption studies in a metal–organic framework (IRMOF-1) material*” International Journal of Hydrogen Energy, (2017), Article in Press
14. Kostoglou, N., Tarat, A., Walters, I., Ryzhkov, V., **Tampaxis, Ch.**, Charalambopoulou, G., Steriotis, Th., Mitterer, C., Rebholz, C., “*Few-layer graphene-like flakes derived by plasma treatment: A potential material for hydrogen adsorption and storage*”, Microporous and Mesoporous Materials, 225 (2016) 482-487.
15. Giasafaki, D., Charalambopoulou, G., **Tampaxis, Ch.**, Dimos, K., Gournis, D., Stubos, A., Steriotis, Th., “*Comparing hydrogen sorption in different Pd-doped pristine and surface-modified nanoporous carbons*”, Carbon 98 (2016) 1-14.
16. Spanopoulos, I., Bratsos, I., **Tampaxis, Ch.**, Vourloumis, D., Klontzas, E., Froudakis, G., Charalambopoulou, G., Steriotis, Th., Trikalitis, P., “*Exceptional Gravimetric and Volumetric CO₂ Uptake in a Palladated NbO-type MOF Utilizing Cooperative Acidic and Basic, Metal-CO₂ Interactions*”, Chemical Communications, 52 (69), (2016), 10559-10562.
17. Kourtellaris, A, Moushi, E, Spanopoulos, I, **Tampaxis, Ch**, Charalambopoulou, G, Steriotis, Th, Papaefstathiou, G, Trikalitis, P, Tasiopoulos, A, “*A microporous Cu₂⁺ MOF based on a pyridyl isophthalic acid Schiff base ligand with high CO₂ uptake*”, Inorganic Chemistry Frontiers 3(12), (2016), pp. 1527-1535
18. D. Giasafaki, G. Charalambopoulou, **Ch. Tampaxis**, D. Mirabile Gattia, A. Montone, G. Barucca, Th. Steriotis, “*Hydrogen storage properties of Pd-doped thermally oxidized single wall carbon nanohorns*”, Journal of Alloys and Compounds, 645, Issue S1, 11 (2015), S485-S489.
19. Spanopoulos I., Bratsos, I., **Tampaxis, Ch.**, Kourtellaris, A., Tasiopoulos, A, Charalambopoulou, G., Steriotis, T. Trikalitis, P.N, “*Enhanced gas-sorption properties of a high surface area, ultramicroporous magnesium formate*”, CrystEngComm, 17 (3), (2015) 532-53
20. Kostoglou, N, Tzitzios, V, Kontos A, Giannakopoulos K, **Tampaxis Ch**, Papavasiliou A, Charalambopoulou, G, Steriotis, T, Li, Y, Liao, K, Polychronopoulou, K, Mitterer, C, Rebholz, C, “*Synthesis of nanoporous graphene oxide adsorbents by freeze-drying or microwave radiation: Characterization and hydrogen storage properties*” International Journal of Hydrogen Energy 40 (2015) 6844-6852
21. Giasafaki, D., Charalambopoulou, G., **Tampaxis, Ch.**, Stubos, A., Steriotis, T., “*Pd-doped molecular sieves for hydrogen storage*”, International Journal of Hydrogen Energy 39 (2014) 9830-9836

Conferences

- **Ch. Tampaxis**, S. Angeli, I. Bratsos, P. Trikalitis, G. Charalambopoulou, Th. Steriotis. “Air purification using hydrolytically stable fluorinated MOFs”, 13th Panhellenic Scientific Chemical Engineering Conference, June 2022, Patras, Greece
- N. Kostoglou, B. Babic, B. Matovic, **Ch. Tampaxis**, G. Charalambopoulou, Th. Steriotis, S. Hinder, M. Baker, G. Constantinides, Ch. Mitterer, C. Rebholz, Nanoporous graphene derived by plasma processing: properties towards hydrogen adsorption and selective carbon dioxide/methane gas separation, 1st Advanced Energy Materials (AEM2016), combining the 8th International Conference on Advanced

Nanomaterials and 2nd International Conference on Hydrogen Energy, 12-14 September 2016. Guildford/Surrey – UK.

- T. Tsoufis, **Ch. Tampaxis**, I. Spanopoulos, Th. Steriotis, F. Katsaros, G. Charalambopoulou, P.N. Trikalitis, High-quality Graphene/ZIF-8 & Carbon nanotube/ZIF-8 nanocomposites: Synthesis, Characterization and Gas Sorption Properties, Industrial Technologies 2016, 22 – 24 June 2016, Amsterdam – The Netherlands.
- Θ. Τσούφης, **X. Ταμπαξής**, I. Σπανόπουλος, Θ. Στεριώτης, Φ. Κατσαρός, Γ. Χαραλαμποπούλου, Π. Τρικαλίτης, Καινοτόμα Νανοσύνθετα Υλικά αποτελούμενα από Νανοδομές Άνθρακα και Πορώδη Υλικά τύπου ZIF, 7ο Πανελλήνιο Συμπόσιο Πορωδών Υλικών, Ιωάννινα, 2-4 Ιουνίου 2016.
- M-L Saboungi, D. Giasafaki, **Ch. Tampaxis**, G. Charalambopoulou, Th. Steriotis, Hydrogen storage properties of pristine and modified single wall carbon nanohorn structures, 7th Panhellenic Symposium on Porous Materials, Ioannina - Greece, 2-4 June 2016.
- I. Bratsos, **Ch. Tampaxis**, I. Spanopoulos, N. Demitri, D. Vourloumis, G. Charalambopoulou, P. Trikalitis, Th. Steriotis, 7th Panhellenic Symposium on Porous Materials, Ioannina - Greece, 2-4 June 2016.
- S. Garroni, F. Peru, **Ch. Tampaxis**, G. Charalambopoulou, Th. Steriotis, Hydrogen storage properties of imide-carbon composites, 7th Panhellenic Symposium on Porous Materials, Ioannina - Greece, 2-4 June 2016.
- P. Gamez, **Ch. Tampaxis**, G. Charalambopoulou, Th. Steriotis, Pore and gas sorption properties of a new series of pyridine containing metal organic frameworks, 7th Panhellenic Symposium on Porous Materials, Ioannina - Greece, 2-4 June 2016.
- C. Croitoru, **Ch. Tampaxis**, G. Charalambopoulou, Th. Steriotis, Hydrogen storage performance of ionic liquid-impregnated aerogels, 7th Panhellenic Symposium on Porous Materials, Ioannina - Greece, 2-4 June 2016.
- I. Bratsos, **Ch. Tampaxis**, I. Spanopoulos, N. Demitri, D. Vourloumis, G. Charalambopoulou, P. Trikalitis, Th. Steriotis, “*An unprecedented heterobimetallic In(III)-Pd(II) porous metal-organic framework with soc topology for hydrogen storage*”, E-MRS 2015 Fall Meeting, Warsaw-Poland, 15-18 September 2015.
- Ampoumogli, D. Giasafaki, **Ch. Tampaxis**, G. Charalambopoulou, A. Stubos, Th. Steriotis, “*Hydrogen storage in solids with the use of nanoporous carbon supports and scaffolds*”, Euro-Mediterranean Hydrogen Technologies Conference - EmHyTeC2014, 9-12 December 2014, Taormina, Italy
- N. Kostoglou, V. Tzitzios, **Ch. Tampaxis**, G. Charalambopoulou, Th. Steriotis, K. Giannakopoulos, A. Kontos, Y. Li, K. Liao, K. Polychronopoulou, C. Rebholz, “*Synthesis, characterization and hydrogen storage capacity of nanoporous graphene-based adsorbents*”, AVS 61st International Symposium & Exhibition, Baltimore-USA, 9-14 November 2014
- N.K. Kostoglou, C. Rebholz, V. Tzitzios, **C. Tampaxis**, T.A. Steriotis, K. Giannakopoulos, G.C. Charalambopoulou, K. Polychronopoulou, Y. Li, K. Liao, “*Hydrogen storage capacity of different nanoporous carbon adsorbents*”, 30th Panhellenic Conference on Solid-State Physics and Materials Science Heraklion, Crete, 21-24 September, 2014.
- D. Giasafaki, **Ch. Tampaxis**, G. Charalambopoulou, D. Mirabile Gattia, A. Montone, Th. Steriotis, “*Hydrogen storage properties of Pd-doped thermally oxidised Single Wall Carbon Nanohorns*”, 14th International Symposium on Metal-Hydrogen Systems (MH 2014), Salford, Manchester - UK, 20 - 25 July 2014

- D. Giasafaki, **Ch. Tampaxis**, A. Ampoumogli, G. Charalambopoulou, A. Bourlinos, A. Stubos, Th. Steriotis, “*Studying the effect of surface chemistry and metal-doping on the hydrogen storage capacity of carbon nanostructures*”, Symposium C: Nanostructured Materials for solid state hydrogen storage, E-MRS 2013 Fall Meeting, Warsaw-Poland, 16-20 September 2013.
- K. Dimos, M.A. Antoniou, **Ch. Tampaxis**, F.L. Kuo, R.F. Reidy, G. Charalambopoulou, Th.A. Steriotis, D. Gournis, “Synthesis and characterization of novel carbon based nanostructures for hydrogen storage”, 6th Panhellenic Symposium on Porous Materials, Kavala - Greece, 9-10 September 2013

Participation in research projects

- RESEARCH–CREATE–INNOVATE (Project nr: T1EΔK-00770, 2014-2020): “Application of Novel Porous Materials in Industrially Relevant Gas Separation/Purification Processes (PureGas)”.
- MC FP7-PEOPLE-2012-IAPP (Grant 324410), 06.2014-05.2016 New weather-stable low gloss powder coatings based on bifunctional acrylic solid resins and nano-additives (GLOW)
- FP7-INFRASTRUCTURES-2011-1 (Grant Agreement 284522, 2011-2015): “Integrating European Infrastructure to support Science and Development of Hydrogen- and Fuel Cell Technologies towards European Strategy for Sustainable, Competitive and Secure Energy (H2FC)”.

ΠΕΡΙΛΗΨΗ

Οι διεργασίες αποθήκευσης και διαχωρισμού αερίων σχετίζονται άμεσα με διάφορες εκφάνσεις της βιομηχανικής και κοινωνικής δραστηριότητας και εξέλιξης, όπως η προστασία του περιβάλλοντος, η ανάπτυξη αποδοτικών διεργασιών και προϊόντων και η παραγωγή/κατανάλωση ενέργειας. Η κλιματική αλλαγή που παρατηρείται αδιαμφισβήτητα τις τελευταίες δεκαετίες συνδέεται κυρίως με τις εκπομπές αέριων ρύπων στην ατμόσφαιρα, παραπροϊόντων της καύσης των ορυκτών καυσίμων, και περισσότερο με το CO₂.

Σε κάθε περίπτωση, αυτό που προβάλλει ως η πλέον πειστική και άμεση ανάγκη ανάληψη δράσης για την αντιμετώπιση της κλιματικής κρίσης, είναι η εκλεκτική δέσμευση του CO₂ από τα σημεία παραγωγής του πριν απελευθερωθεί στον αέρα και η ασφαλής αποθήκευσή του. Η τεχνολογία που χρησιμοποιείται ευρέως σήμερα στηρίζεται στη χημική δέσμευση του CO₂ με χρήση διαλυμάτων αμίνης. Η διεργασία παρουσιάζει 98% δέσμευση αλλά το βασικό μειονέκτημα της μεθόδου είναι το μεγάλο ενεργειακό κόστος που απαιτείται για τη διάσπαση του δεσμού μεταξύ του CO₂ και των αμινομάδων, έτσι ώστε το διάλυμα να αναγεννηθεί και να επαναχρησιμοποιηθεί.

Ταυτόχρονα, λόγω των πεπερασμένων και συνεχώς μειούμενων αποθεμάτων ορυκτών καυσίμων, η επιστημονική κοινότητα έχει στρέψει το βλέμμα της στη διερεύνηση εναλλακτικών πηγών ενέργειας που θα είναι το ίδιο αποδοτικές με τα συμβατικά καύσιμα και την ίδια στιγμή φιλικότερα προς το περιβάλλον.

Το υδρογόνο θεωρείται πλέον ευρέως ως το ιδανικό καύσιμο του μέλλοντος καθώς υπάρχει άφθονο στον πλανήτη και η καύση του έχει μηδενικό αποτύπωμα άνθρακα. Ωστόσο οι υπάρχουσες τεχνολογίες απέχουν ακόμη αρκετά από το σημείο γενικευμένης χρήσης του, λόγω μεγάλου εύρους τεχνικών δυσκολιών στον σχεδιασμό της εφοδιαστικής του αλυσίδας. Το φυσικό αέριο, που αποτελείται κυρίως από μεθάνιο (με συγκεντρώσεις CO₂ έως και 30%) εξετάζεται ως μια ενδιάμεση λύση, καθώς φέρει ικανοποιητικό ενεργειακό φορτίο ανά μονάδα μάζας και έχει τον υψηλότερο λόγο υδρογόνου προς άνθρακα από όλους τους υδρογονάνθρακες, καθιστώντας το περιβαλλοντικά φιλικότερο. Και σε αυτή την περίπτωση όμως υπάρχουν ακόμη σοβαρά τεχνολογικά εμπόδια με τα βασικότερα να είναι η ασφαλής και αποδοτική αποθήκευση καθώς και η αναβάθμισή ή ο καθαρισμός του (κυρίως απομάκρυνση CO₂) προς ένα αποδοτικότερο καύσιμο.

Τα τελευταία χρόνια η χρήση στερεών προσροφητικών υλικών, τα οποία μπορούν να συγκρατήσουν στην επιφάνειά τους σημαντικές ποσότητες αερίων μέσω φυσικής προσρόφησης έχει προσελκύσει έντονο ερευνητικό ενδιαφέρον. Η φυσική προσρόφηση οφείλεται στην ανάπτυξη ασθενών ηλεκτροστατικών δυνάμεων τύπου van der Waals μεταξύ της επιφάνειας του στερεού και του αερίου, γεγονός που οδηγεί σε ένα γρήγορο, αντιστρεπτό φαινόμενο που δεν απαιτεί μεγάλο ενεργειακό κόστος για αναγέννηση και επαναχρησιμοποίηση του προσροφητικού μέσου. Συνεπώς, το ζητούμενο που προκύπτει για μια αποδοτική διεργασία προσρόφησης (για διαχωρισμό ή αποθήκευση αερίων) είναι η μεγιστοποίηση της αλληλεπίδρασης αερίου-στερεού. Στο πλαίσιο αυτό έχει προταθεί η χρήση υλικών με εκτεταμένα νανοπορώδη δίκτυα τα οποία εμφανίζουν υψηλές τιμές ειδικής επιφάνειας (και άρα διεπιφάνειας στερεού-αερίου). Επιπλέον, έχει αποδειχθεί ότι σε πόρους με μεγέθη στην περιοχή της νανοκλίμακας, συγκρίσιμα δηλαδή με τη μοριακή διάμετρο των προς προσρόφηση αερίων, παρατηρείται αύξηση της προσρόφησης λόγω συνεργιστικών αλληλεπιδράσεων στερεού-ρευστού.

Διάφορα πορώδη υλικά έχουν διερευνηθεί εκτεταμένα με σκοπό τη χρήση τους σε διεργασίες αποθήκευσης και διαχωρισμού αερίων ως στερεοί προσροφητές, όπως ζεόλιθοι, ενεργοί άνθρακες κλπ. Τα μεταλλο-οργανικά πλέγματα (metal organic frameworks, MOFs), μια ομάδα κρυσταλλικών νανοπορωδών υλικών, έχουν προσελκύσει παγκοσμίως το ερευνητικό ενδιαφέρον λόγω των ιδιαίτερων ιδιοτήτων και δομικών χαρακτηριστικών τους. Παρασκευάζονται σχετικά εύκολα, συνήθως με αντιδράσεις ενός σταδίου, από τη συναρμογή οργανικών συνδετών με ιόντα μετάλλου ή μεταλλικές πλειάδες, με αποτέλεσμα τη δημιουργία τρισδιάστατων κρυσταλλικών νανοπορωδών πλεγμάτων που παρουσιάζουν πολύ υψηλές τιμές ειδικής επιφάνειας και συνολικού όγκου πόρων. Το ιδιαίτερο και πολύ ελκυστικό χαρακτηριστικό τους είναι όμως η δυνατότητα ελέγχου της δομής και των ιδιοτήτων τους καθώς είναι εύκολο να προσχεδιασθούν τα μεγέθη, το σχήμα και οι λειτουργικές ομάδες της επιφάνειας των πόρων τους, με την εφαρμογή «δικτυωτής χημείας» («reticular chemistry»), προσδίδοντας έτσι χαρακτηριστικά προσανατολισμένα στις απαιτήσεις της εκάστοτε διεργασίας.

Η παρούσα διατριβή εστίασε στην ενδελεχή μελέτη δύο υπαρχόντων, σχετικά νέων διμεταλλικών MOFs, με συνδυασμό αναλυτικών τεχνικών και ανάπτυξη νέων πειραματικών πρωτοκόλλων, για την αποθήκευση CH_4 και τον διαχωρισμό μιγμάτων CO_2 . Τα εν λόγω υλικά έχουν αναπτυχθεί μετά από συνεργασία του Τμήματος Χημείας του Παν. Κρήτης με το ΕΚΕΦΕ «Δημόκριτος» μέσω μιας καινοτόμας συνθετικής προσέγγισης και συγκεκριμένα

χρησιμοποιώντας έναν οργανικό συνδέτη ο οποίος είναι ουσιαστικά ένα σύμπλοκο του Pd. Με τον τρόπο αυτό, επιχειρήθηκε η αύξηση της ηλεκτρονιακής πυκνότητας του κρυσταλλικού πλέγματος των MOFs με σκοπό την αύξηση της αλληλεπίδρασης επιφάνειας-προσροφούμενου αερίου. Πιο συγκεκριμένα, ακολουθώντας ήδη δημοσιευμένες συνθετικές διαδικασίες παρασκευάστηκαν δύο αμιγώς μικροπορώδη υλικά: (α) ένα στο οποίο ο παλλαδιωμένος συνδέτης συναρμόζεται με μια διπυρηνική πλειάδα Cu και φέρει την τοπολογία pbo (Cu-Pd-pbo), και (β) ένα στο οποίο ο συνδέτης συνδέεται με μία τρι-πυρηνική πλειάδα In και τοπολογία soc (In-Pd-soc). Σημειώνεται ότι αυτό το υλικό είναι το πρώτο καταγεγραμμένο MOF με ίνδιο στο οποίο αποδόθηκε η τοπολογία soc. Ο συνδυασμός των ακόρεστων μεταλλικών κέντρων (στις πλειάδες) και των εκτεθειμένων τροχιακών του Pd (στον συνδέτη) καθιστούν τα δύο νέα αυτά MOFs ως υποσχόμενους προσροφητές σε διεργασίες αποθήκευσης CH₄ και διαχωρισμού CO₂ μέσω εκλεκτικής προσρόφησης τους από μίγματα που π.χ. περιέχουν CH₄ ή N₂.

Στο πρώτο μέρος της διατριβής, αρχικά μελετήθηκε η δυνατότητα ενεργοποίησης των νέων υλικών. Η ενεργοποίηση του Cu-Pd-pbo επετεύχθη χρησιμοποιώντας τη διαδομένη μέθοδο της θέρμανσης υπό κενό. Ωστόσο, για την περίπτωση του In-Pd-soc απαιτήθηκε η ανάπτυξη ιδιαίτερης μεθοδολογίας. Για το λόγο αυτό σχεδιάστηκε και κατασκευάστηκε πειραματική διάταξη ενεργοποίησης μέσω ροής υπερκρίσιμου διοξειδίου του άνθρακα, με σκοπό την απομάκρυνση από το πορώδες δίκτυο του δείγματος των παγιδευμένων (κατά τη σύνθεση) μορίων διαλύτη και άλλων προσμίξεων. Επιπλέον, διερευνήθηκε η χημική και θερμική σταθερότητα των υλικών καθώς και η μορφολογία των κρυστάλλων με συνδυασμό πειραματικών τεχνικών (XRD, IR, TGA, SEM). Στη συνέχεια, με μετρήσεις ισοθέμων προσρόφησης αζώτου/αργού στους 77/87 K αντίστοιχα, χαρακτηρίστηκε το πορώδες δίκτυο των υλικών και υπολογίστηκαν κρίσιμα μεγέθη όπως η ειδική επιφάνεια, ο συνολικός όγκος πόρων και η κατανομή μεγέθους των πόρων των δειγμάτων.

Στο δεύτερο μέρος της διατριβής, αποτιμήθηκαν οι προσροφητικές ιδιότητες των υλικών. Με τη χρήση εξειδικευμένων ογκομετρικών και σταθμικών πειραματικών μεθόδων πραγματοποιήθηκαν μετρήσεις ισοθέμων προσρόφησης CO₂, N₂ και CH₄ σε μεγάλο εύρος θερμοκρασιών (100 – 300 K) και πιέσεων (0 – 20 bar). Από την ανάλυση των πειραματικών αποτελεσμάτων υπολογίστηκαν κρίσιμα θερμοδυναμικά και κινητικά μεγέθη όπως, συνολική αποθηκευμένη ποσότητα προσροφούμενου αερίου, ισοστερική ενθαλπία προσρόφησης, συντελεστές διαχυτότητας ενώ προσαρμόζοντας στις ισόθεμες προσρόφησης κατάλληλες

θεωρητικές εξισώσεις εξήχθησαν κάποιες πρώτες εκτιμήσεις για τη διαχωριστική ικανότητα των υλικών σε μίγματα CO_2/N_2 και CO_2/CH_4 με υπολογισμό των αντίστοιχων εκλεκτικοτήτων. Το Cu-Pd-nbo, παρουσίασε αξιοσημείωτα δομικά χαρακτηριστικά και εντυπωσιακή προσροφητική ικανότητα ειδικά ως προς το CO_2 , για το οποίο καταγράφηκε τιμή 8.5 mmol/g στους 273 K και 1 bar. Αυτό το αποτέλεσμα το κατατάσσει το συγκεκριμένο υλικό μεταξύ των αποδοτικότερων ολόκληρης της οικογένειας των MOF, επί της ουσίας επιβεβαιώνοντας την επιλογή της συγκεκριμένης συνθετικής προσέγγισης. Για το λόγο αυτό, επελέγη για περαιτέρω διερεύνηση. Σε αυτό το πλαίσιο, διενεργήθηκαν ισόθερμες προσρόφησης CH_4 σε υψηλές πιέσεις έως 100 bar και διαφορετικές θερμοκρασίες (273, 288 και 298 K), με σκοπό την αποτίμηση της ικανότητας του για αποθήκευση CH_4 . Η ανάλυση των αποτελεσμάτων έδειξε πως παρόλο που το Cu-Pd-nbo δεν προσρόφησε σημαντική ποσότητα ανά μονάδα μάζας, παρουσίασε εντυπωσιακή τιμή στην συνολική προσροφημένη ποσότητα CH_4 ανά μονάδα όγκου, προσεγγίζοντας το 80% του στόχου που έχει θέσει το Υπουργείο Ενέργειας των ΗΠΑ (US DOE), λόγω της αυξημένης τιμής κρυσταλλογραφικής πυκνότητας του δείγματος, απόρροια της προσθήκης του παλλαδίου στον οργανικό συνδέτη.

Στο τελευταίο μέρος της διατριβής η διαχωριστική ικανότητα μίγματος αερίων του Cu-Pd-nbo διερευνήθηκε σε συνθήκες που προσομοιάζουν αυτές μιας πραγματικής διεργασίας. Πιο συγκεκριμένα, κατασκευάστηκε πειραματική συσκευή, στην οποία πραγματοποιήθηκαν πειράματα *in situ* διαχωρισμού μιγμάτων ($\text{CO}_2 / \text{CH}_4$, CO_2 / N_2) σε διαφορετικές συστάσεις, (10:90, 50:50), πιέσεις από 1 έως 5 bar και θερμοκρασία δωματίου. Οι μετρήσεις αυτές έδειξαν ότι με την χρήση του συγκεκριμένου υλικού επετεύχθη επιτυχής, πλήρης διαχωρισμός σε όλες τις περιπτώσεις. Από τις καμπύλες διάρρηξης που προέκυψαν υπολογίστηκαν μέσοι χρόνοι παραμονής των αερίων και πραγματικές εκλεκτικότητες ενώ τα πειραματικά δεδομένα θα χρησιμοποιηθούν μελλοντικά για την κατασκευή ενός θεωρητικού μοντέλου που θα περιγράφει πλήρως τη διεργασία διαχωρισμού μέσω εκλεκτικής προσρόφησης του CO_2 έναντι των άλλων συστατικών.

Λέξεις κλειδιά: Φυσική προσρόφηση, Μεταλλο-Οργανικά-Πλεγματα, Νανοπορώδη υλικά, Δέσμευση CO_2 , Αποθήκευση CH_4

ABSTRACT

Gas storage and separation processes are closely linked to various aspects of industrial and social activity and evolution, such as environmental protection, industrial processes and manufacturing as well as energy production/consumption. Climate change that has been unequivocally observed is considered to occur mainly due to the continuously increasing emission of harmful gas by-products of fossil fuels combustion into the atmosphere.

CO₂ represents almost 75 % of the of the so called green-house gases. Thus, controlling and subsequently reducing its atmospheric concentration level, constitutes a vital environmental priority globally. Therefore, selective capture of CO₂ from its emission points before it is released into the atmosphere, and its safe storage represent the most pressing and immediate course of action. The most common CO₂ capture technology is the use of amine solutions. CO₂ reacts with the amino group creating a chemical bond in a process showing 98% yield, nevertheless the process has a major drawback related to the high energy cost of regeneration.

Moreover, due to the finite, constantly decreasing reserves of fossil fuels, strong emphasis has been given to the use of alternative energy sources that can be as efficient as conventional fuels and at the same time more environmentally friendly. Hydrogen is considered to be the ideal fuel of the future as it is abundant on the planet and its combustion has zero carbon footprint. However, existing technologies are still far from widespread use, due to the significant technical difficulties related to its whole supply-use chain. Natural gas, consisting mainly of methane (CO₂ can be as high as 30%), is considered as an intermediate solution, since it carries sufficient energy density per unit mass and has the highest hydrogen-to-carbon ratio of all hydrocarbons, addressing some major environmental concerns. Nonetheless, similarly to hydrogen, there are still serious technological obstacles, the most important of which is its safe storage and efficient upgrade/purification.

During the last decades, the use of solid adsorbents, which can retain significant amounts of gases on their surface through physical adsorption, has attracted great interest. Physical adsorption occurs due to weak van der Waals-type electrostatic forces between

the surface of the solid and the gas, which leads to a fast, reversible phenomenon that is usually not connected with a significant energy penalty for regeneration and reuse of the adsorbent. Therefore, the main objective for an efficient adsorption-based process is to maximize the gas-solid interaction. Materials possessing extensive nanoporous networks exhibit high specific surface areas (and thus extended gas-solid interfaces) and total pore volume values. Furthermore, it has been shown that in nanosized pores, i.e., comparable to the molecular diameter of the adsorbate gases, increased interactions are observed due to the overlap of potential energies of the neighboring atoms.

Various materials have been extensively investigated as solid adsorbents for gas storage and separation processes, such as zeolites, activated carbons, etc. Metal-organic frameworks (MOFs), a particular group of crystalline nanoporous materials have attracted significant interest due to their remarkable properties and intrinsic structural features. They are usually produced through one-step reactions, from the assembly of organic ligands with metal ions or metal clusters, resulting to the creation of three-dimensional crystalline nanoporous networks presenting very high values of specific surface area and total pore volume. However, their most intriguing feature is the possibility to control their structure and properties through "reticular chemistry" syntheses, which allows to pre-design sizes, shapes and functional groups of their pore surface, thus incorporating characteristics tailored to the specific requirements of each process.

This thesis focused on the study of two existing, however relatively new bi-metallic MOF structures for CH₄ storage and CO₂ separations that have been prepared via an innovative synthetic concept, i.e. by using a palladated organic linker. By following this strategy, it was attempted to increase the electron density of the MOF crystal lattice in order to enhance the gas-surface interactions. In this context, two novel microporous structures have been successfully obtained: (a) Cu-Pd-nbo, utilizing the dinuclear Cu-paddlewheel cluster linked with the palladated linker, and (b) In-Pd-soc produced by the association of the In(III)-based trimeric oxo-centered cluster with the same ligand, constituting the first indium-based MOF with soc topology.

In the first part of the thesis, the possibility of activating the new materials was investigated. Cu-Pd-nbo was easily activated by means of mild heating under high vacuum. However, this was not the case for In-Pd-soc and a special activation methodology had to

be developed. For this reason, a supercritical carbon dioxide flow experimental device was designed and built, with the aim of removing the trapped (during synthesis) solvent molecules and other impurities from the material's porous network, while leaving the framework intact. In addition, the chemical and thermal stability as well as the morphology of the materials were investigated by means of a combination of experimental techniques (XRD, IR, TGA, SEM). Moreover, the structural features of the materials' porous network were fully characterized by measuring nitrogen/argon adsorption isotherms at 77 and 87 K respectively.

In a next step, the adsorption properties of the materials were systematically evaluated. Using specialized volumetric and gravimetric experimental methods, CO₂, N₂ and CH₄ adsorption isotherms were measured in a wide range of temperatures (100 – 300 K) and pressures (0 – 20 bar). From the analysis of the experimental results, critical thermodynamic and kinetic parameters such as, total capacities, isosteric heat of adsorption, diffusion time constants, etc., were determined. By fitting the adsorption isotherms with appropriate theoretical equations, it was possible to deduce some first estimates for the separation ability of the materials with respect to CO₂/N₂ and CO₂/CH₄ containing mixtures, by calculating the respective selectivities. Cu-Pd-nbo exhibited superior structural features and sorption capacities for all gases. More specifically, its excess CO₂ adsorption uptake was calculated to be 8.5 mmol/g at 273 K and 1 bar, a value which ranks it among the top performing CO₂ adsorbents within the whole family of MOFs, essentially verifying the novel synthetic approach. For this reason, Cu-Pd-nbo was selected to be further investigated for its CH₄ storage capacity. More specifically, high pressure CH₄ adsorption isotherms were performed up to 100 bar at 273, 288 and 298 K. Although Cu-Pd-nbo exhibited rather modest gravimetric storage capacities, it showed remarkable total volumetric uptake, approaching 80% of the DOE target. This is attributed to the relatively high crystallographic density of the material, as a result of the Pd presence in the organic linker. The latter constitutes an interesting choice for increasing the volumetric capacity, which is an important metric for CH₄ storage.

In the last part of the thesis the gas mixture separation properties of Cu-Pd-nbo were investigated under conditions simulating those of a real process. More specifically, an experimental rig was constructed for performing dynamic column breakthrough

experiments on the aforementioned mixtures (CO_2/CH_4 , CO_2/N_2) at different ratios, (10:90, 50:50), and pressures from 1 to 5 bar at room temperature. Complete separation was successfully achieved in every case. Mean retention times, and actual selectivities were calculated from the resulting breakthrough curves while the derived experimental data will be used to build a theoretical model that will fully describe the separation process through selective adsorption of CO_2 over the other components.

Keywords: Physical adsorption, Metal-Organic-Frameworks, Nanoporous materials, CO_2 capture, CH_4 storage

Table of Contents

1. Introduction.....	1
2. Theoretical Part.....	4
2.1 Adsorption	4
2.1.1 Adsorption isotherm.....	5
2.1.2. Adsorption forces.....	8
2.2 Diffusion	12
2.2.1 Diffusivity coefficients	12
2.2.2 Diffusion mechanisms.....	14
2.2.2.1. Molecular diffusion.....	14
2.2.2.2. Knudsen diffusion.....	15
2.2.2.3. Transition region	16
2.2.2.4. Surface diffusion.....	16
2.2.2.5. Micropore diffusion	17
2.3 Nanoporous materials	19
2.3.1 Physical adsorption on microporous adsorbents.....	20
2.3.2 Metal-organic-frameworks (MOFs).....	21
2.4 Gas storage and separation applications address energy and environmental concerns.....	23
2.4.1 Methane as an intermediate solution.....	23
2.4.1.1 Compressed, Liquified and Adsorbed Natural Gas (CNG, LNG and ANG).....	23
2.4.1.2 Nanoporous materials for ANG	24
2.4.1.3 Excess, absolute and total adsorption.....	27
2.4.1.4 Gravimetric and Volumetric capacity	29
2.4.1.5 Working/Deliverable Capacity.....	30
2.4.2 Carbon dioxide capture and separation from mixtures as an immediate solution.....	31
2.4.2.1. Post-combustion capture	33
2.4.2.2 Pre-combustion capture.....	34
2.4.2.3 Direct air-capture (DAC)	34
2.4.2.4 Natural gas / Biogas upgrading.....	34
2.5 Pressure swing adsorption processes (P.S.A.)	36
2.6 Scope of the dissertation	40
3. Experimental Part.....	42

3.1 Samples – Characterization.....	42
3.1.1. Cu-Pd-nbo	42
3.1.2. In-Pd-soc	43
3.1.3 Thermogravimetric analysis.....	44
3.1.4 Argon / Nitrogen porosimetry.....	45
3.1.4.1. Experimental procedure	46
3.1.4.2. Sample activation using super-critical CO ₂	47
3.1.4.3. BET surface area.....	49
3.1.4.4. Total pore volume (TPV).....	50
3.1.4.5. Pore size distribution (PSD).....	50
3.1.5. Other characterization techniques (SC-XRD, PXRD, IR, NMR, SEM).....	52
3.2 Gravimetric apparatus.....	54
3.2.1 Instrument description.....	54
3.2.2 Experimental procedure	57
3.2.3 Diffusion time constant calculation	59
3.2.4 Isotheric heat of adsorption calculation.....	60
3.3 High pressure volumetric apparatus.....	61
3.4 Breakthrough curves determination apparatus.....	62
3.4.1 Device description.....	62
3.4.2 Mass spectrometer.....	63
3.4.3 Experimental procedure	64
4. Results and Discussion	66
4.1. Synthesis and characterization of palladated ligand, <i>trans</i> -[dichlorido(3,5-dicarboxypyridyl) palladium(II)] (H₄L).....	66
4.2. Synthesis of Cu-Pd-nbo	69
4.3. Synthesis of In-Pd-soc	73
4.4. Thermogravimetric analysis of Cu-Pd-nbo.....	78
4.5. Thermogravimetric analysis of In-Pd-soc.....	80
4.6. Nitrogen/Argon adsorption isotherms for Cu-Pd-nbo.....	81
4.7. Low pressure single component isotherms for Cu-Pd-nbo	83
4.8 Thermal Desorption Spectroscopy (TDS) experiments for Cu-Pd-nbo.....	95
4.9. High pressure single component isotherms for Cu-Pd-nbo	99
4.10. Nitrogen/Argon porosimetry for In-Pd-soc.....	112

4.11. Low pressure single component isotherms for In-Pd-soc	115
4.12. High pressure single component isotherms for In-Pd-soc	124
4.13. Dynamic Column Breakthrough (DCB) experiments.....	133
5. Conclusions.....	141
6. References.....	146

1. Introduction

Gas storage and separation applications constitute physicochemical processes that are closely linked to various aspects of social evolution, such as protection of the environment, energy use and industrial production. Indicatively, carbon capture is considered to be crucial for tackling global warming, purification and storage of hydrogen and methane are necessary for the widespread implementation of "*clean*" energy technologies while the sequestration of toxic gases such as carbon monoxide and ammonia, are important for managing environmental pollution.¹

Climate change on the planet is believed to occur largely due to the emission of harmful, gas byproducts of fossil fuel combustion, the most prominent of which is considered to be CO₂.² Therefore, development of technological systems that will selectively capture CO₂ from its emission points and its subsequent sequestration has become a research subject of crucial importance.³ Meanwhile, due to the depletion of liquid fossil fuel deposits, alternative energy sources are being explored, which need to be as efficient as current fuels, but environmentally friendlier at the same time.^{4,5} Among the various clean energy sources investigated, the use of natural gas is preferred as an immediate solution⁶, while H₂ seems to be the ideal fuel of the future⁷. However, there are still significant technological obstacles that need to be overcome until their extensive application, the basic demands being safe storage systems with satisfactory performance characteristics (*capacity, kinetics*).⁸

Therefore, global scientific research interest has shifted in quest to discover new technologies for the capture/storage of these gases as well as their successful separation from impurities. One method that has emerged over the last decades as relatively efficient for the storage of H₂ and CH₄ as well as CO₂ capture from mixtures, is adsorption, i.e. storage and/or separation is based on the ability of solid materials to (selectively) retain substantial amounts of various gasses on their surface.^{9,10}

Nanoporous materials are being studied for their use on a broad range of sorption applications due to their fascinating structural characteristics. Activated carbons, zeolites and more recently metal-organic frameworks (MOFs), exhibit high surface areas and pore volumes per unit mass, resulting from their porous networks. In such materials, due to the extended gas-solid

interface but also the pore confinement, the physical adsorption phenomena are intensified leading to increased densities of adsorbed species inside their porous structures.

The aim of this dissertation is the in-depth understanding of the physical adsorption phenomenon on two newly synthesized nanoporous materials through systematic study of their pore properties and moreover the exploitation of their optimal interaction characteristics, for efficient CH₄ storage and successful CO₂ separation from its mixtures with CH₄ or N₂. More specifically, during this thesis, the following milestones were reached:

- Extensive structural characterization of two novel heterobimetallic MOFs using a variety of analytical techniques. In particular, by measuring nitrogen and argon adsorption isotherms at 77 or 87K, respectively, useful information was extracted about the porous networks of the materials, such as specific surface area, pore size distribution and total pore volume, among others. In combination with thermogravimetric analysis (*TGA*), which evaluates the thermal stability of the material and X-ray diffraction (*powder, PXRD and single crystal, SCXRD*) which provides information about their crystal structure, the overall picture of the adsorbents' structure was evaluated.
- Design and development of a device for the materials' "*activation*" using supercritical carbon dioxide (*sc-CO₂*). In order to accurately characterize and evaluate the storage / separation properties of the respective material, removal of the solvent molecules which remain attached in the pore structure after synthesis is required. For this purpose, a device was developed in which samples, sensitive to traditional activation methods (e.g. heating and/or evacuation), are treated initially with liquid and subsequently with super-critical CO₂ in order to gently "*activate*" them, without damaging their crystal framework.
- Systematic study and evaluation of the storage capacity of the materials at low and high pressures. Using volumetric and gravimetric methods, N₂, CH₄ and CO₂ adsorption isotherms were recorded over a wide range of pressures and temperatures. Important thermodynamic properties (*isosteric heats of adsorption, diffusion time constants etc*) were extracted providing useful information on the gas-surface interaction.
- Development of a novel experimental protocol for performing low-temperature CO₂ thermal desorption spectroscopy (TDS) by modifying a commercial volumetric instrument.

This new technique provides insight on the energetic landscape of the CO₂-adsorbent's interaction.

- Design and construction of an experimental device for performing gas mixture adsorption measurements mimicking the actual conditions of a gas separation application. Breakthrough curves were obtained for various predetermined ratios of CO₂/N₂ and CO₂/CH₄ mixtures providing valuable information such as in situ selectivity, competitive adsorption capacity etc.

2. Theoretical Part

2.1 Adsorption

Historically, the term adsorption emerges in the literature in 1881, when Kayser¹¹ described gas condensation on free surfaces, in an attempt to distinguish it from gaseous absorption, where gas molecules penetrate the crystal lattice of the absorbing material. Earlier in 1777, Fontana and Scheele, on separate occasions, had observed the phenomenon during their famous charcoal experiments in which they illustrated that a porous solid can adsorb on its surface substantial volumes of subcritical gases. Later, in experiments conducted by de Saussure in 1814 and Mitscherlich in 1843, it was realized that the amount of adsorbed gas varies depending on the nature of both the solid and the gas. The terms of surface area and porosity (*or pore volume*) were then recognized as crucial parameters for understanding the adsorption phenomena.¹²

Important milestones for the construction of adsorption theory were the works of Zsigmondy¹³ in 1911, who observed vapor condensation in micropores at pressure lower than vapor pressure (P^0), a phenomenon known as capillary condensation, of Polanyi¹² in 1914 who introduced the concept of the formation of an adsorbed layer on the gas-solid interface whose density decreases with increasing distance from the surface and Langmuir¹⁴ in 1916, who unified the existing data by proposing the concept of the adsorbed monolayer suggesting the Langmuir equation. In 1938 the Brunauer-Emmett-Teller¹⁵ (*BET*) theory was published introducing the adsorbed multilayer formation. Although BET theory uses some simplistic assumptions, it is still being used as the most prominent way for comparing calculated specific surface areas between different adsorbents. Finally, over 1950-1970, extensive studies from Dubinin and others illustrated that adsorption mechanism in pores with size of a few molecular diameters differs significantly than the one observed in larger mesopores or free surfaces, proposing the notion of micropore filling.¹²

Gas adsorption measurements have been widely recognized as a valuable technique for the characterization of the surface and textural properties of porous solids and powders. In general, adsorption is internationally defined as “the enrichment (*positive adsorption or simply adsorption*) or depletion (*negative adsorption or desorption*) of one or more components in the gas/solid interfacial layer”.¹⁶ Another important distinction that needs to be established is between physical

adsorption (*physisorption*) and chemical adsorption (*chemisorption*). Physical adsorption is a fast, reversible phenomenon which is accompanied by moderate release of heat. It occurs when an adsorbable gas, the adsorptive, interacts with the surface of a solid, the adsorbent. Gas molecules are “adsorbed” on the surface of the adsorbent through a combination of weak attractive dispersion forces, short range repulsive and occasionally electrostatic forces (depending on the adsorptive’s and adsorbent’s nature).¹⁷ On the other hand, chemisorption is characterized by large interaction potentials between the gas molecule and the surface resulting to an irreversible, activated, kinetically slow phenomenon which releases substantial amount of heat, approaching the value of chemical bonds.¹⁸ The present dissertation will focus on physical adsorption. For reasons of clarity, physical adsorption will be mentioned simply as adsorption from now on.

2.1.1 Adsorption isotherm

Considering an isolated space in which a solid material is exposed to a gas of specific pressure, the material will begin adsorbing gas molecules on its surface resulting to an increase on the solid’s weight and a decrease on the gas’ pressure. When the phenomenon reaches equilibrium, both the gas pressure and material’s weight will become constant. The quantity of adsorbed gas can be determined from the pressure drop or the weight increase, constituting the volumetric and gravimetric method of adsorption determination, respectively¹⁹.

The amount of adsorbed gas n , is proportional to the mass of the adsorbent and depends on the pressure of the gas P , the temperature of the system T as well as the nature of both the adsorbate and the adsorbent and is expressed as follows:

$$n = f(P, T, gas, solid) \quad (2.1)$$

For a particular adsorbate-adsorbent system under constant temperature T , equation 2.1 is modified to

$$n = f(P)_{T, gas, solid} \quad (2.2)$$

If the adsorbate is subcritical at the system’s constant temperature T and its saturation vapor pressure is P^0 , the equation takes the form

$$n = f(P/p_0)_{T,gas,solid} \quad (2.3)$$

Equations 2.2 and 2.3 are essentially definition of the adsorption isotherm and express the relationship between the adsorbed amount of gas and the pressure at which equilibrium has been achieved under isothermal conditions.

The adsorption properties of porous materials depend on the particular characteristics of their porous network, i.e., the shape, quantity and size of the solid adsorbent's pores, which reflect on their respective adsorption isotherm shape. In 1985, IUPAC published a manual on "Reporting Physisorption Data for Gas/Solid Systems"¹⁷, in which adsorption isotherms of subcritical gases were classified in six major types. However, over the years, advances in gas adsorption analysis have led to a revised manuscript, published in 2015²⁰, in which an updated adsorption isotherm categorization is proposed and illustrated below.

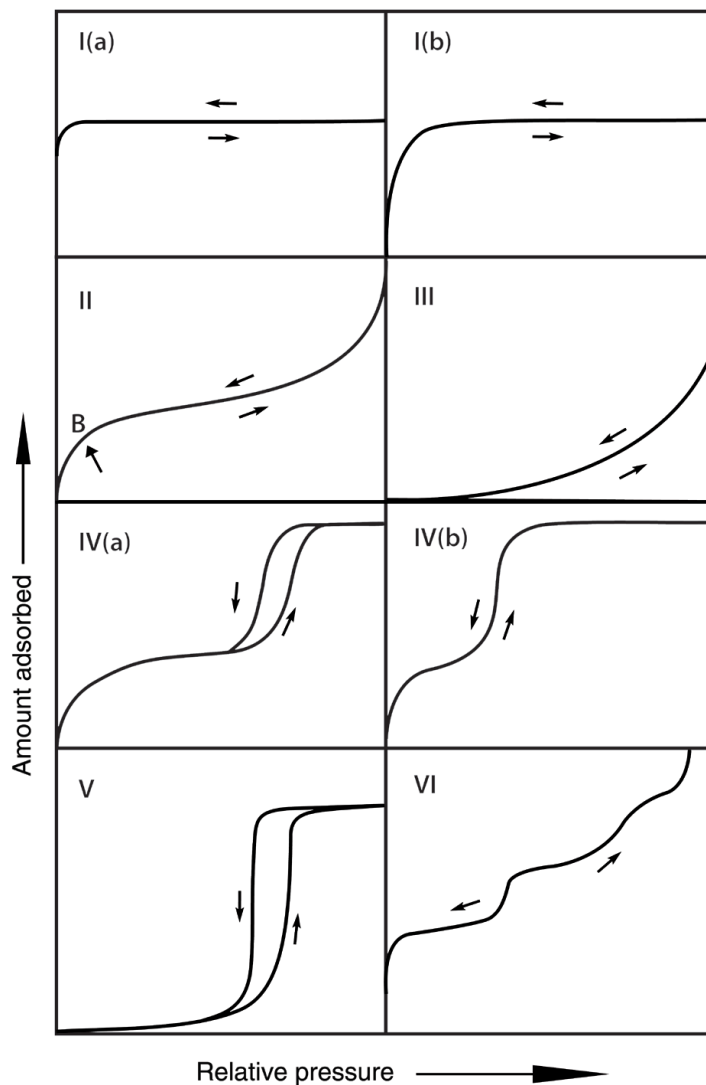


Figure 2.1: Classification of adsorption isotherms (subcritical gases).²⁰

The categorization of adsorption isotherms illustrated in figure 2.1 is briefly discussed below.

- Type I isotherms are given by exclusively microporous adsorbents (pore widths < 2 nm). Due to increased interaction potentials within the walls of very narrow pores, the reversible isotherm reaches a plateau at low pressure, indicative of micropore filling. At higher pressures, the adsorbed amount is not further increased, since all the micropores are already filled. For nitrogen/argon adsorption at 77/87K, type I(a) isotherms are given by materials having pores of width < 1 nm while type I(b) isotherms are given by materials exhibiting a

wider pore size distribution with larger micropores and even narrow mesopores of width < 2.5 nm, where the uptake step is not that steep.

- Type II reversible isotherms are given by adsorption of most gases on non-porous or macroporous adsorbents. The adsorbed gas covers the whole surface forming a monolayer and as the pressure rises multilayers are developed. Point B reflects the completion of the monolayer coverage.
- Type III isotherms are given by non-porous materials with relatively weak gas-surface interactions. As a result, there is no point B since gas molecules are adsorbed to distinct favorable adsorption sites rather than forming a monolayer.
- Type IV adsorption isotherms typically correspond to adsorbents possessing mesopores (pore widths $2 < w < 50$ nm). The main characteristic is the adsorption sharp step which is attributed to capillary condensation. The gas molecules initially form a film on the mesopore walls. At a particular pressure less than P^0 , associated with the pore diameter, the gas condenses inside the pore to a liquid like phase, due to interactions between the adsorbed molecules. In type IV(a), the phenomenon is accompanied by hysteresis, i.e., adsorption and desorption do not coincide. It has been observed that for nitrogen/argon at 77/87K hysteresis does not occur for pores smaller than 4 nm^2 , which is the case for the completely reversible isotherm of type IV(b).
- Type V isotherm, which is comparable to type III at low relative pressures, is given by micro and meso-porous adsorbents exhibiting weak adsorbate-adsorbent interactions. However, at higher pressures, capillary condensation occurs.
- Type VI isotherm is given by non-porous adsorbents exhibiting remarkably uniform surfaces. As a result, the well-defined adsorption steps correspond to the formation of individual adsorbed layers.

2.1.2. Adsorption forces

Physisorption phenomena are governed by van der Waals forces between the adsorptive and the adsorbent. Although the nature of these forces is well known for decades and has been theoretically studied extensively based on idealized models, it is still not possible to develop accurate calculations from inherent parameters of the gas and the solid. However, useful

understanding on the nature of the adsorption process can be gained by assessing different independent parameters, such as gas polarizability or solid polarity²².

Attractive dispersion forces and short-range repulsive forces are always present when physical adsorption occurs. Occasionally, coulombic forces are included, depending on the charges (or partial charges) of either the solid or the gas molecules²³.

Attractive dispersion forces occur due to transient fluctuations of electron density within each atom which leads to temporary charge separation, resulting to attraction between two neighboring atoms. London described the nature of these forces using quantum-mechanical theory and later studies developed the following simplified expression:

$$\varepsilon_D(r) = -Cr^{-6} \quad (2.4)$$

where $\varepsilon_D(r)$ is the potential energy between two distinct atoms separated by distance r , C is a dispersion constant related to spontaneous dipole-dipole interactions and the minus sign indicates the attraction between the two atoms, provided that they are not too distant from each other.

Short-range repulsive forces occur when two atoms approach each other to a degree where their electron clouds overlap. Their repulsive potential energy $\varepsilon_R(r)$, which is also derived by means of quantum-mechanical considerations, is described by the following approximated expression:

$$\varepsilon_R(r) = Br^{-m} \quad (2.5)$$

where B is an empirical constant while a value of 12 is usually assigned to m .²⁴ The sum of equations 2.4 and 2.5 (Figure 2.2) corresponds to the total potential energy, $\varepsilon(r)$ between the two atoms and is defined as the (6-12) Lennard-Jones potential²⁵:

$$\varepsilon(r) = -Cr^{-6} + Br^{-12} \quad (2.6)$$

If a Lennard-Jones particle (e.g., a gas molecule) positioned at distance z from an atomically described (e.g., flat) solid surface is considered, the total potential energy $\varphi(z)$ experienced by the particle would be the sum of all individual interactions of particle i , with each atom j of the solid (r_{ij} , is the i - j distance). Equation 2.6 then takes the form:

$$\varphi(z) = -C_{ij} \sum_j r_{ij}^{-6} + B_{ij} \sum_j r_{ij}^{-12} \quad (2.7)$$

The curve derived from equation 2.7 for the total potential energy $\varphi(z)$ of a gas molecule as a function of its distance from the surface of the solid is of identical shape to the Lennard-Jones potential which is illustrated in figure 2.2.

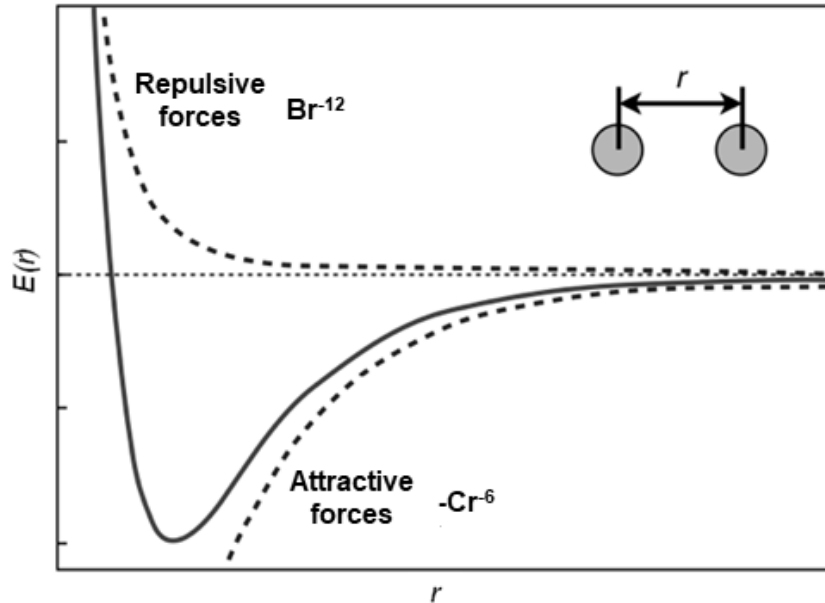


Figure 2.2: Schematic representation of the potential energy $\varepsilon(r)$ of a gas molecule as a function of its distance from another molecule.

Essentially, analyzing figure 2.2, as a free gas molecule approaches the surface of the solid, it begins to “feel” the interaction with the molecules of the adsorbent’s surface and the attraction forces are enhanced, until a critical distance where the potential energy reaches a minimum. Further decrease of the distance between them is less preferred since it would give rise to the short-range repulsive forces, leading to a sharp rise on the potential energy.

Furthermore, if the adsorbent is polar (bearing polar groups or π -electrons or ions), it will create an electric field which will subsequently induce a dipole in the adsorbate molecules resulting in an additional interaction φ_P . Moreover, in case the gas molecule maintains a permanent dipole, another interaction $\varphi_{F\mu}$ contributes to the total potential energy. Finally, gas molecules like CO_2 and N_2 possess quadrupole moments resulting to even more enhanced interaction φ_{FQ} with the adsorbent’s electrical field.

Consequently, taking into account all the parameters acknowledged above, the overall interaction energy $\varphi(z)$ between a gas molecule and the solid surface at distance z , can be expressed as follows¹⁸:

$$\varphi(z) = \varphi_D + \varphi_R + \varphi_P + \varphi_{F\mu} + \varphi_{FQ} \quad (2.8)$$

where φ_D and φ_R correspond to the attractive dispersion and short-range repulsion forces, respectively and, as already mentioned above, are always present when physical adsorption occurs. On the other hand, φ_P , $\varphi_{F\mu}$ and φ_{FQ} occur occasionally, depending on the nature of the gas and the solid.¹²

Besides the nature of the forces that transpire when a gas molecule interacts with a solid surface and actually determine the thermodynamic gas-solid equilibria, the kinetics of the adsorption process is another factor of crucial importance. For this reason, diffusion phenomena need to be considered in order to accurately describe the gas-solid dynamic behaviour and identify the optimal system characteristics.

2.2 Diffusion

The inherent property of matter to migrate in such a way as to eliminate local variations in composition, in order to bring the system into equilibrium, is called diffusion. This behavior of matter is observed at any temperature above absolute zero and is an expression of the tendency towards greater entropy or maximum randomness.²⁶ Diffusion phenomena may occur through two different ways:

- (a) as mass transfer (or transport diffusion), a result of a concentration gradient existence under isobaric and isothermal conditions and expressed by Fick's first law of diffusion, which essentially provides the definition of diffusivity, D :

$$J = -D \text{ grad } c \quad (2.9)$$

where J is the diffusive flux and c is the concentration of the diffused species. The minus sign indicates that the flow moves in the opposite direction from that of the concentration increase.

- (b) as self-diffusion, a consequence of the random Brownian motion of the molecules (or atoms) that constitute the system, under thermodynamic equilibrium conditions. The connection between Brownian motion and diffusion was first introduced by Einstein through equation 2.10, also known as Einstein's relation:

$$\langle r^2(t) \rangle = 6D_{sd}t \quad (2.10)$$

where $\langle r^2(t) \rangle$ is the mean square displacement of the diffusants present in the system, as a function of time t and D_{sd} is the diffusivity coefficient attributed to self-diffusion²⁷.

2.2.1 Diffusivity coefficients

This dissertation focuses on mass transfer in microporous media due to the existence of a concentration gradient. Therefore, the term diffusivity will be exclusively used as described in equation 2.9. However, considering the phenomenon of diffusion as a macroscopic manifestation of the tendency towards equilibrium, it becomes apparent that the real driving force is the degree of chemical potential (μ), a fact originally recognized by Einstein. If the diffusion mass transfer

phenomenon is treated as a flow due to the chemical potential gradient, the following equation is obtained:

$$u = -L_{\alpha} \frac{\partial \mu}{\partial x} \quad (2.11)$$

where u is the flow velocity of the diffusant and L_{α} is a proportion coefficient. The flux J , is given by $u * c$. The chemical potential is related with the (partial) pressure by the following expression:

$$\mu = \mu^0 + RT \ln(p) \quad (2.12)$$

In the center of a micropore where the potential energy reaches a minimum due to overlap of the pore wall interactions (see chapter 2.3.1), there is no clear distinction between adsorbed molecules on the surface and bulk gas. It is therefore convenient to consider the intracrystalline concentration (q). The flux then can be written as follows:

$$J = u * q = -RTL \frac{\partial \ln(p)}{\partial \ln(q)} \frac{\partial q}{\partial x} \quad (2.13)$$

Considering an ideal vapor phase (or low pressures) and comparing equation 2.13 with equation 2.9, the following expression is obtained:

$$D = D_0 \frac{\partial \ln(p)}{\partial \ln(q)} \quad (2.14)$$

where $D_0 = RTL$, is the “corrected diffusivity” and $d \ln(p)/d \ln(q)$ is the “thermodynamic correction factor”.²⁸ It is evident that the concentration dependence of the diffusion coefficient (D) is related to the term D_0 and/or the thermodynamic correction factor ($d \ln p/d \ln q$). However, for adsorption systems, taking into account that in the saturation region the isotherm becomes almost horizontal resulting in $d \ln(p)/d \ln(q) \rightarrow \infty$, or that in low pressures (Henry region) $d \ln(p)/d \ln(q) \rightarrow 1$, one realizes that the dependence of the thermodynamic correction factor on concentration is much higher than that of the term D_0 . In fact, in many cases it has been observed experimentally that the corrected diffusivity is practically independent of the concentration. Therefore, in order to gain meaningful insight on transport phenomena during gas adsorption at the molecular level, it is accustomed to use the “corrected” diffusivity instead of the Fickian.²⁹

2.2.2 Diffusion mechanisms

Diffusion in nanoporous adsorbents is governed by different mechanisms related to the respective regions of porosity. According to IUPAC classification, pore diameters less than 2 nm are classified as micropores, between 2 and 50 nm as mesopores and more than 50 nm as macropores. This classification is derived based on the different type of interactions that control the adsorption behavior of small molecules in the aforementioned pore size ranges.²³ Diffusion in micropores is an activated process dictated by interactions with the pore walls as well as steric effects. On the other hand, in the macropore range, mass transfer is dominated by collisions between the adsorbate molecules. Molecular diffusion and viscous flow occur, which mainly depend on the bulk pressure. In the mesopore region, capillary forces become important and consolidation between Knudsen and surface diffusion contribute to the mass transport.²⁷

Although this dissertation focuses on two novel materials which are purely microporous, implementation of a simple micropore diffusion resistance model does not always describe the system adequately. This is for instance the case when the synthetic procedure yields crystals with small particle size. The assemblage of primary particles can then appear as a macroporous structure due to the void between the crystals, affecting the diffusion rate significantly and requiring a complicated model to account for both the micropore and macropore resistances. Therefore, it is important to distinguish between the different mechanisms in order to identify which regime(s) may control the transport phenomena in an adsorption process. The main diffusion mechanisms are briefly discussed below.

2.2.2.1. *Molecular diffusion*

Macropores and large mesopores do not contribute significantly to the material's specific surface area. However, they are frequently incorporated in microporous adsorbents since they play an important role in enhancing the mass transfer characteristics. Therefore, it is of great importance to understand the diffusion process in this pore region. When the pore diameter is larger than the mean free path of the diffusing gas molecules, collisions between the diffusing molecules will be much more frequent than collisions with the pore walls. In this case the size of the pores does not

play a role and the regime is called molecular diffusion. The molecular diffusion coefficient (D_m) can be determined by the kinetic theory of gases³⁰:

$$D_m = \frac{3}{8\sigma^2} \frac{k_B T}{P} \left(\frac{k_B T}{m_g \pi} \right)^{1/2} \quad (2.15)$$

where σ is the molecular collision diameter, k_B the Boltzmann constant, T temperature, P pressure and m_g the adsorbate's molecular mass. However, in real solids the pore structure consists of a random network of interconnecting pores with various pore sizes, orientations and geometries. This results in substantial diversity in the adsorbate's diffusion path. In order to account for this deviation from ideality the effective molecular diffusivity (D_m)_{macro} in the macropores which is related to the molecular diffusivity coefficient according to the following equation is defined:

$$(D_m)_{macro} = \frac{D_m}{\tau} \quad (2.16)$$

where τ is the tortuosity factor which is assumed to account for all the structural variations of the adsorbent and a value of 3 is used in several occasions as a rough estimation.

2.2.2.2. Knudsen diffusion

As the pore size or the pressure decreases, the mean free path of the diffusant molecules can become comparable to or larger than the pore diameter. It then happens that the collisions of the molecules with the walls are more frequent than the intermolecular collisions. Each time a gas molecule collides with the pore walls, energy is exchanged with the surface atoms resulting in a totally random reflection of the diffusant. The above diffusion mechanism is known as the Knudsen mechanism. In the Knudsen region the rate of momentum transfer from one gas molecule to another is negligible, compared to the rate of momentum transfer from the diffusing molecules to the pore walls. Therefore, Knudsen diffusivity is independent of the pressure and is only affected by the pore size and the mean molecular velocity. Similarly to molecular diffusion, taking into account the kinetic theory of gases in order to calculate the velocity distribution of gas molecules, the following expression is obtained for the Knudsen diffusion coefficient (D_K)³¹:

$$D_K = 9700r_\mu\sqrt{\frac{T}{m_g}} \quad (2.17)$$

where r_μ is the pore diameter, T the temperature and m_g the molecular mass of the diffusant.

2.2.2.3. Transition region

In the transition region, the mean free path of the diffusant becomes comparable with the pore diameter, constituting the momentum transfer between colliding gas molecules equally significant to collisions of the diffusant with the pore walls. In this case, diffusion occurs as a combination of molecular diffusion and Knudsen mechanism. Therefore, the combined effective diffusivity (D_p) for the specific pore is expressed as follows²⁷:

$$\frac{1}{D_p} = \frac{1}{D_K} + \frac{1}{D_m} \quad (2.18)$$

Since D_K is proportional to the pore diameter and D_m inversely proportional to the pressure, the expression above essentially describes the transition from Knudsen mechanism in small pore sizes and low pressure, to molecular diffusion in larger pore sizes (meso and macropores) and higher pressure.

2.2.2.4. Surface diffusion

The mass transfer mechanisms discussed above, describe the diffusion of gas molecules in the pore structure of a solid material through the free gas phase. If the diffusive molecules exhibit high affinity for the material's surface, a film of physically adsorbed molecules occurs and an additional flux of the adsorbed phase, the "surface diffusion", has to be considered. Although the mobility of the diffusing adsorbate molecules is significantly lower than in the vapor phase in the center of the pore, the density of the adsorbed layer can be relatively high in thermodynamically favored adsorption systems and needs to be taken into account as an additive phenomenon. In this case the overall diffusivity for the specific pore (D_{ov}) is given by the following equation²⁷:

$$D_{ov} = D_p + K'D_s \quad (2.19)$$

where D_p is the diffusivity coefficient as described in equation 2.18, K' is a dimensionless adsorption equilibrium constant which expresses the ratio of the adsorbed molecules to the free gas molecules in vapor phase and D_s is the surface diffusion coefficient. However, considering a pore as part of an entire solid structure, it is accustomed to express the overall diffusivity coefficient as a function the particle's porosity (ε_p), which is the ratio of the structure's total pore volume to its bulk volume (solid+pores).²⁹

$$D_{ov} = D_p + K \left(\frac{1 - \varepsilon_p}{\varepsilon_p} \right) D_s \quad (2.20)$$

where K is the dimensionless Henry constant. The contribution of surface diffusion in the overall process depends on the term $K \cdot D_s / D_p$. Surface diffusion is an activated process described as a series of “jumps” between specific adsorption sites exhibiting low potential energies. However, the diffusional activation energy is significantly lower than the heat of adsorption so that the term $K \cdot D_s$ increases as the temperature is decreased. Therefore, the relative importance of surface diffusion becomes negligible at temperatures that are high with respect to the adsorbate's boiling point.

2.2.2.5. Micropore diffusion

Diffusion in micropores is dictated by the interaction between the adsorbate molecules and the material's surface since the gas molecules never escape the dynamic force field induced by the pore walls. Consequently, there is no clear distinction between adsorbed and free gas phase inside the micropores. Thus, it is considered that in a microporous material the diffusive flux under investigation is essentially the total intracrystalline adsorbed quantity denoted by q . Steric hindrance becomes particularly important while a dramatic diffusivity decrease is observed as the gas' molecular diameter is increased. Micropore diffusivity D_c can be experimentally determined by fitting the appropriate diffusion models on the adsorption kinetics as expressed by the material's uptake change in response to a pressure step change. Models developed to describe microporous diffusion usually result in relations similar to the form of equation 2.14, with the corrected diffusion coefficient $D_o(q)$ obeying an Arrhenius-type relation. Many characteristics of diffusion in microporous materials are similar to those of surface diffusion, both being activated processes.

Likewise, micropore diffusivity may depend on the adsorbed phase concentration in the non-linear region of the adsorption isotherm. For this reason, is accustomed to measure the so called limiting micropore (as well as the surface) diffusivity, i.e. the diffusivity in the Henry region of the isotherm.²⁹

2.3 Nanoporous materials

The use of solid adsorbents is considered comparatively advantageous over other methods for efficient gas storage and/or separation. It is a relatively safe, cost-effective method, in which increased densities of molecules in the adsorbed phase are achieved in a reversible way. In this respect, the aim is to maximize the gas-solid interfacial area in order to intensify the extent of physical adsorption. Specific surface area values vary considerably among different adsorbents and are affected by the porosity, ϵ , but also the number, size and shape of the pores.³²

Generally, porous materials are structures with voids within their matter, exhibiting thus extended gas-solid interfaces. The pores usually originate from the crystal structure (e.g., zeolites and MOFs) but also from the gaps that are created, either between the (primary) particles or between agglomerates of these particles, while some pores emerge due to defects in the crystal lattice of the solid. There are also pores, which are created when atoms are removed from the crystal lattice, during chemical reactions.³³

According to the 1985 IUPAC recommendations¹⁷, nanoporous materials are considered solid adsorbents that possess pores with widths in the nanometer scale (10^{-6} m), the upper limit being 100 nm. In the context of physical adsorption, nanopores are classified as follows (the classification is historically based on nitrogen adsorption/desorption isotherms analysis at 77 K):

- *Macropores*: pores with width >50 nm
- *Mesopores*: pores with width between 2 nm and 50 nm
- *Micropores*: pores with width <2 nm. Micropores can be further divided to *ultramicro pores* (width <0.7 nm) and *supermicro pores* (width between 0.7-2.0 nm).

As mentioned above, porous materials exhibiting high specific surface areas such as zeolites, activated carbons and more recently metal-organic frameworks (MOFs) are mainly used as solid adsorbents. These materials have the advantage of relatively low production cost and enhanced chemical stability. Furthermore, they show extremely fast kinetics when adsorbing gases on their surface, while the usually weak gas-solid interactions allow completely reversible processes that require minimal energy cost for their regeneration and reuse.

2.3.1 Physical adsorption on microporous adsorbents

The interaction between a specific gas molecule and the surface of a particular solid material is described by equation 2.8 and depends on the nature of both the adsorbent and the adsorbate. As already mentioned above, the attractive forces are maximized at a certain gas-solid distance, in which adsorption is thermodynamically most favored. In microporous materials, which have pores with width less than or equal to 2 nm, the potential fields of opposing walls (or neighboring atoms of the solid) overlap and the interaction of the solid with the gas molecules increases further within the pore³⁴, as can be seen in figure 2.3 below.

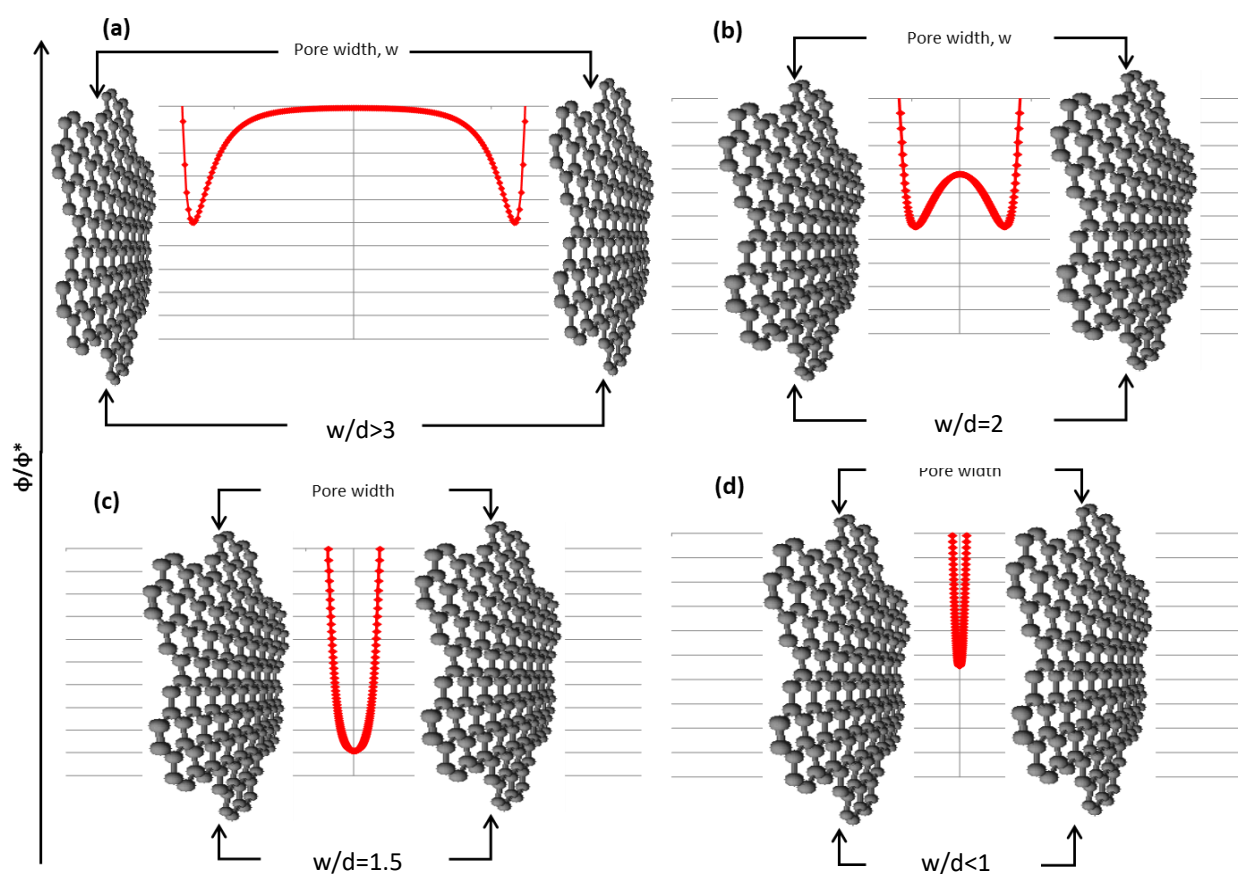


Figure 2.3: Interaction potential in a slit-shaped pore as a function of the ratio of the pore width w , to the gas molecular diameter, d .

The interaction enhancement is expressed by the dimensionless form ϕ/ϕ^* , which is the ratio of the adsorbate's potential energy ϕ between two opposing pore walls (the distance between them being w), to the potential energy of the adsorbate interacting with a free surface of the same

solid material, ϕ^* . For wide pores with respect to the adsorptive's molecular diameter (fig 2.3, a), the interaction exhibits two minima in the potential energy. Essentially this means that the gas molecule behaves like it is interacting with two separate free surfaces, the two minima corresponding to the minimum of figure 2.2 (in this case $\phi/\phi^*=1$), while in the center of the pore the gas molecule “feels” no interaction, behaving like bulk gas. As w/d is decreased, the interaction potentials of the two walls begin to overlap (b), leading to a critical pore width where the potential energy in its center reaches a single, even lower minimum. This results to increased adsorption, to such an extent that the pores are filled at fairly low relative pressures, a phenomenon known as micropore filling.³⁴

Therefore, design and development of materials that possess extended nanoporous networks, control of the surface chemistry, in depth understanding of the diffusion mechanisms and adsorbate – adsorbent interactions are the main research pillars for efficient gas storage and successful gas separation applications.

2.3.2 Metal-organic-frameworks (MOFs)

Metal – Organic – Frameworks (MOFs), represent a unique class of porous crystalline materials which have received extensive scientific interest owing to their outstanding intrinsic properties. MOFs are synthesized (usually solvothermally, in one step reaction) by the coordination of metal ions or clusters (termed as secondary building units, SBUs) with polytopic organic linkers resulting to three dimensional open structures exhibiting permanent porosity and exceptional structural characteristics such as high specific surface areas and total pore volumes compared to traditional porous solid materials.^{35,36} It needs to be noted that in literature MOF specific surface area values may extend beyond 6000 m²/g.³⁷

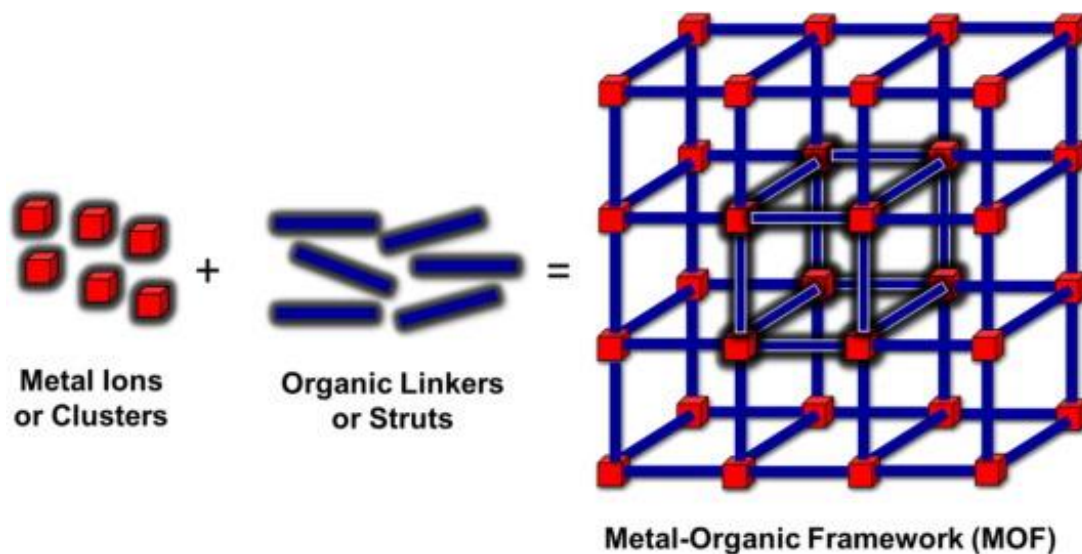


Figure 2.4: Simple schematic representation of the MOFs' molecular building blocks assembly

However, their most intriguing aspect lies within the core of what is called reticular synthesis, which is the process of assembling judiciously designed rigid molecular building blocks into predetermined ordered structures (networks), which are held together by strong bonding.³⁸ This process gives the ability to predesign the geometric characteristics of the MOF building blocks, in order to form a porous network with desired structural properties. This way, rational construction is achieved and has permitted the discovery of a vast variety of nanoporous MOF structures exhibiting an extensive range of different topologies, also offering the capability to tailor different pore sizes, shapes and surface functionalities towards specific applications.^{39,40}

MOFs, being crystalline, periodic structures are classified based on their network topology, which is essentially the way the metals (ions or clusters) are connected with the organic ligands. The underlying topology assigned is depicted by lower case three-letter codes according to the Reticular Chemistry Structure Resource (RCSR) Database developed by O'Keeffe and co-workers.⁴¹ The three letter codes listed in the database are derived due to their resemblance with known solid structures or based on the geometry of their building blocks. In this dissertation, two newly synthesized MOFs are studied; one assigned as **soc** (square octahedron) and one as **nbo** (niobium oxide type).

2.4 Gas storage and separation applications address energy and environmental concerns

2.4.1 Methane as an intermediate solution

The last decades, the exploding development of the economy, has led to a steady growth in demand for crude oil. The projected shortage of liquid fossil fuel reserves in the near future as well as raising environmental concerns, have shifted the scientific focus towards a quest for alternative, cost effective and cleaner fuel systems. Natural gas (NG), which essentially consists of methane, poses as the prime candidate to replace petroleum in the automotive sector (amongst others) due to its natural abundancy and low carbon footprint.⁴² Specifically, methane exhibits the highest H to C ratio amongst all hydrocarbons, therefore the greatest energy per unit mass. Compared to gasoline, combustion of methane has shown 86% less CO, 26% less CO₂, and 77% less NO_x emissions addressing a series of environmental issues related to the use of coal and petroleum products.⁴³

On the other hand, several technical drawbacks need to be overcome so that the widespread use of natural gas, especially in the automotive sector, can be implemented. At ambient temperature and pressure, methane is a supercritical gas which results to very low volumetric energy density (0.04 MJ L⁻¹) as opposed to gasoline (32.4 MJ L⁻¹).⁴⁴ Due to its low critical temperature (T_c : 190.6 K / -82.6 °C) methane cannot be liquefied solely by compression alone above T_c , rendering thus the increase of its volumetric energy density a challenging problem. Since it cannot be stored like the traditional liquid fossil fuels, three different natural gas storage technologies have been proposed, i.e., compressed natural gas (CNG), liquefied natural gas (LNG) and adsorbed natural gas (ANG).⁴⁵

2.4.1.1 Compressed, Liquefied and Adsorbed Natural Gas (CNG, LNG and ANG)

CNG is the most typical way to store natural gas and is used in mobile as well as stationary systems. Natural gas is compressed at ambient temperature up to 250 bar and is stored as a supercritical fluid. Although its volumetric energy density is increased and can reach up to 9 MJ L⁻¹, it still accounts for only 26% of that of gasoline.⁴⁶ Moreover, CNG demands expensive multi-

stage compressors in order to fill the thick and heavy stainless-steel tanks required, while major safety issues associated with the remarkably elevated pressures have halted its overall use, especially when it comes to light duty passenger vehicles.⁴⁷

In order to address these disadvantages, LNG is used to store methane as boiling liquid at 112K (−161 °C) and 5 bar in cryogenic tanks resulting to further increase of its volumetric energy to about 21 MJ L⁻¹, which still constitutes 64% of gasoline.⁴⁶ In this case the storage vessels required are much cheaper and lighter since they operate at moderate pressure. On the other hand, the use of complicated and expensive cryogenic systems in order to refuel and maintain the extremely low temperature generates a substantial energy penalty and raises the overall process costs significantly.⁴⁸

A promising alternative to the previously mentioned methods is the implementation of ANG in nanoporous materials. It has been observed that due to high confinement of the methane molecules within the material's porous structure, storing greater densities of natural gas can be achieved at comparatively moderate conditions with the use of relatively inexpensive gas cylinders and single stage compressors.⁴⁹ During the past three decades methane storage in porous materials has been a subject of intense research in order to establish the relationship between the amount of methane required for vehicle autonomy, the current technology in adsorbents development as well as the cost of on-board equipment.

2.4.1.2 Nanoporous materials for ANG

In 2012, the Advanced Research Projects Agency-Energy (ARPA-E) of the US DOE set the target for adsorbed natural gas to 350 cc (STP) /cc at 298 K and 65 bar (energy density of 12 MJ L⁻¹). A gravimetric ANG target was also set at 0.5 g (CH₄) /g or 700 cc (CH₄) /g (adsorbent), which accounts for the energy density of CNG at 250 bar considering a penalty of 25% of losses due to pelletization and packing inside the fuel tanks.⁵⁰ To date, the goals have not yet been met. Therefore, the quest for understanding the methane-adsorbent interactions in order to develop materials that can store ANG at relatively low pressure and near ambient temperature becomes of crucial importance.

Initially, zeolites, a purely inorganic microporous aluminosilicate class of materials attracted scientific attention. Zeolites exhibit relatively low surface areas ($<1000 \text{ m}^2 \text{ g}^{-1}$) and low micropore volumes which lead to insufficient amounts of sorbed methane as well as low packing densities.⁵¹ Moreover, their extreme hydrophilicity is a major disadvantage since vapors of water are favorably adsorbed over methane lowering even more their ANG storage capacity.⁴⁸

Subsequently, nanoporous carbons were systematically researched as efficient adsorbents for methane. Their cheap and facile synthesis from a wide range of precursors, extremely hydrophobic surface, high mechanical strength which can eliminate any packing related energy loss as well as their intriguing structural properties such as extended microporosity, high specific surface areas and pore volumes constitute them as prime candidates for ANG applications.⁵² Extensive studies in mainly carbon nanotubes and activated carbons have established a linear relationship between specific surface area and total gravimetric capacity.^{46,53} Moreover, theoretical studies suggested that an activated carbon that exhibits a predominantly microporous structure with slit-like pores of 7.6 \AA diameter, which can accommodate two layers of adsorbed CH_4 on the opposing surface walls, would be ideal for maximizing the volumetric capacity at 35 bar and 25 °C. Indeed, a highly porous activated carbon LMA738 (BET, $3290 \text{ m}^2/\text{g}$), which showed high volumetric working capacity of $174 \text{ cm}^3 \text{ (STP) cm}^{-3}$ at 298 K between 5-65 bar was reported, while high methane uptakes were also reported for ordered-mesoporous carbide-derived carbons (OM-CDC) with an excess adsorbed amount of 0.208 gg^{-1} at $\sim 100 \text{ bar}$ and 298 K.^{49,52}

Such values are promising; however, they are not high enough to meet the targets set by the DOE. Computational studies have predicted a maximum ANG volumetric capacity of 198 v/v at 34 bar and 25 °C.⁵⁴ This amount, even if the energy loss due to packing is neglected, is still much lower than anticipated. The adversity of fine tuning the structural properties of carbons such as pore size and shape and the difficulty of controlling surface functionality are the major drawbacks that prevented further optimization for this class of adsorbents.

In this respect, Metal-organic-frameworks (MOFs) have been considered as an alternative solution for CH_4 storage. Just like for activated carbons, a linear relation between specific surface area of MOFs and total methane gravimetric adsorption capacity has been established.^{43,48} Theoretical studies suggest that the gravimetric storage goal set by the DOE would be satisfied by a MOF which would hypothetically exhibit a surface area of around $7500 \text{ m}^2/\text{g}$, pore volume of

3.2 cm³/g and density of 0.28 g/ cm³ while at the same time this MOF would approach the volumetric target with an uptake estimated at around 200 cc(STP)/cc.⁴⁵ Indeed, Al-soc-MOF-17⁵⁵ and NU-111⁵⁶, presenting ultra-high porosities have been reported to reach the US DOE total gravimetric uptake at near ambient temperatures and relatively high pressures (288 K / 80 bar and 273 K / 65 bar, respectively). However, many MOFs possessing high specific surface areas have been found to perform poorly in terms of volumetric capacity.⁵⁷ Notably, Long and coworkers have illustrated that unlike gravimetric uptake, volumetric adsorption does not necessarily correlate with volumetric surface area.⁴³

Consequently, further understanding of the factors that influence the storage capacity of a material is required in order to achieve simultaneously the desired volumetric and gravimetric methane uptakes. Pore size (and shape to a certain degree) plays a crucial role in the efficiency of ANG systems by determining the methane molecules confinement within the material's pore structure. Simulation studies suggest that an ideal adsorbent should exhibit a pore size of 11.4 Å, which corresponds to accommodation of three methane molecular layers.⁴⁸ A strategy that has been proven efficient for CH₄ uptake enhancement is the incorporation of unsaturated metal sites (UMSs) in the framework.⁵⁸ In combination with confinement effects the CH₄-surface affinity is increased due to enhanced electrostatic interactions of the metal with the slightly polarized CH₄ molecule.⁵⁹ In fact, it has been postulated that although the CH₄ is a highly symmetric, nonpolar molecule, some binding enhancement may still be possible, since adsorption on a metal site could perturb the charge distribution of the CH₄ molecule, reduce the molecular symmetry, and induce multipole moments.⁶⁰ Moreover, modification of the organic linker by incorporating hydrophobic groups such as methyl or aromatic groups lead to enhanced framework electron density which in turn may increase the CH₄-adsorbent interactions.⁶¹

In order to accurately evaluate the performance of potential ANG adsorbents, high pressure adsorption isotherms are performed. It is of vital importance to distinguish between the different terminologies used in literature, avoiding unnecessary uncertainty, so that the reported storage and deliverable capacities of different materials can be compared in a consistent way, producing meaningful conclusions about the underlying methane-substrate interactions.⁴³

2.4.1.3 Excess, absolute and total adsorption

Excess, absolute and total amounts adsorbed are terms frequently used in literature to describe high pressure adsorption properties. Adsorption occurs when gas molecules interact with a solid surface through weak van der Waals forces, resulting to an adsorbed film of density greater than would normally be at the same temperature and pressure conditions in the absence of the material. The strength of the interaction, described by the Lennard- Jones potential, will decrease as the distance between the surface and the gas molecule is increased until the gas molecule is far enough from the surface where the attractive forces are negligible and only free gas molecules exist. The distance at which a gas molecule approaching the surface begins to “feel” the attractive interaction, constitutes an arbitrary border known as the Gibbs dividing surface.⁶² Gas molecules that are closer to the solid than the Gibbs dividing surface are considered to be adsorbed, while molecules beyond this surface are considered as bulk, free gas.

Absolute amount adsorbed refers to the number of molecules (statistically) that actually experience the potential field of the solid. By considering an ideal situation in a perfect uniform cylindrical pore, where the Gibbs dividing surface is clear and defines the “adsorption volume”, V_a , the absolute amount adsorbed (n_{abs}) is considered as the sum of the molecules that are found within V_a . including the molecules that interact with the pore walls, plus the free gas molecules that would be present in the absence of the attractive interaction.⁶³

Excess amount adsorbed (n_{ex}), is actually what is being directly measured using either volumetric or gravimetric experimental methods. This refers to the difference between the absolute amount adsorbed and the quantity of the bulk gas molecules that could be found in V_a (i.e. between the Gibbs dividing surface and the solid) in the absence of adsorption forces.⁶⁴ For the ideal case described above:

$$n_{ex} = n_{abs} - V_a d_{bulk}(P, T)$$

In fact, the Gibbs dividing surface and the pertinent adsorbed volume are imaginary concepts, and such a surface or volume cannot be geometrically defined. Therefore, the amount of molecules within the adsorption boundary layer (or the adsorbed volume) cannot be experimentally determined and the absolute amount adsorbed (n_{abs}), cannot ever be directly measured.⁶⁵ On the other hand, it should be mentioned that n_{abs} is the only thermodynamically

correct and relevant quantity that can describe adsorption. For this reason, in many cases some simplifying assumptions have been considered and are used (not always correctly though).

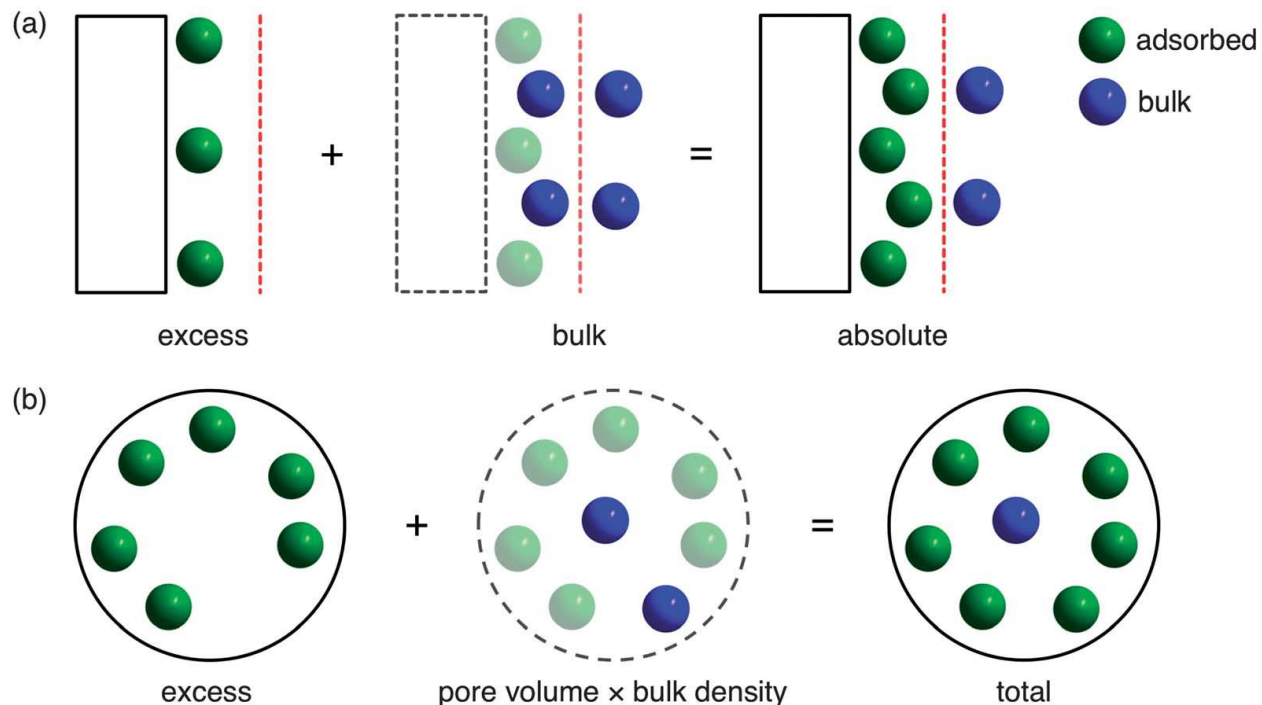


Figure 2.5: Schematic representation of the (a) Gibbs dividing surface for adsorption on a 2D surface and the corresponding absolute amount adsorbed. (b) total adsorption inside a cylindrical pore. (adopted from reference⁴³)

One assumption is that the adsorbed phase has the density of the liquid phase. Under this assumption the amount adsorbed is a fluid of constant density that occupies increasing volumes as pressure is increased. Then at each pressure a “virtual” adsorption volume can be estimated and n_{abs} can be consequently deduced. This introduces a common framework for comparing absolute isotherms but is of course an oversimplification as it has been many times proved by simulations that the density of the adsorbed phase has huge fluctuations (also depending strongly on the pore size). Another approach is to consider the total pore volume of the system as the adsorption volume and treat the amount adsorbed as a fluid that always occupy the same volume but has different density at different equilibrium pressures.⁶⁶ This concept is very logical (and quite accurate) for

microporous materials but loses its validity as the pore size increases. Moreover, at larger mesopores and beyond (e.g., >10 nm) it leads to huge overestimation of the amounts adsorbed.

As an alternative, the total amount adsorbed (n_{tot}) is sometimes used. Total adsorption accounts for all the molecules (bulk plus adsorbed) which are found within the pore volume of the adsorbent and can be derived from excess adsorption using the following equation.⁴³

$$n_{tot} = n_{ex} + TPVd_{bulk}(P, T)$$

where TPV is the total pore volume of the material and d_{bulk} is the bulk gas density at the experiment's temperature and pressure. For micro- and meso-porous materials the total pore volume can be experimentally determined by performing a nitrogen or argon adsorption isotherm (at 77 or 87 K respectively) and it accounts for the volume of condensed N₂ or Ar needed to completely fill the whole porous structure of the material at an adequately high pressure close to the gases vapor pressure.²⁰ Again when the material has very large pore sizes the calculation of n_{tot} leads to unreasonable results.

Nevertheless, since the materials used for gas storage are mainly micro- to meso- porous, for natural gas, reporting in total adsorption is the most common way for comparing capacities between different adsorbents as it is considered the most relevant property that represents the total amount of gas that is stored in the material's porous network. At elevated pressures, the gas density in the bulk phase raises significantly resulting to a substantial deviation between excess and total adsorption.⁶⁷ Thus, it becomes of vital importance to clearly distinguish between the two when reporting for high pressure isotherms.

2.4.1.4 Gravimetric and Volumetric capacity

Gravimetric capacity is expressed as the amount of gas adsorbed divided by unit mass of adsorbent and can be directly calculated simply by weighing the mass of the activated material. Volumetric capacity is defined as the amount of gas (usually volume of adsorbed gas under standard temperature and pressure conditions, STP) per unit volume of adsorbent.⁶⁸ In order to calculate the volumetric capacity, the value of material's apparent (or bulk) density needs to be determined. For highly crystalline materials, such as MOFs where crystallographic data can be

acquired by single crystal x-ray diffraction (SC-XRD) experiments, it is accustomed to use the crystallographic density. Although this method is considered to overestimate the material's uptake, it provides valuable information acting as a fingerprint at least for initial comparisons amongst different adsorbents. A more realistic approach, though more time consuming, is to perform helium pycnometry to the activated sample, prior to the high pressure adsorption isotherm.⁶⁹ This can provide a “skeletal density”, which can be used with the pore volume (obtained e.g. from adsorption experiments) to deduce the apparent density. A more “application related” approach is to use the so called “tap density” by measuring the volume that a certain mass of the adsorbent occupies (after “tapping” the container).

Both gravimetric and volumetric capacities contribute essential information for the adsorbent properties, especially the latter which is of decisive importance since it determines the amount of gas that can be stored in a fuel tank with specific size limitations.

2.4.1.5 Working/Deliverable Capacity

Working capacity is amongst the most crucial metrics for an adsorbent since it represents the actual amount of deliverable methane between specified working pressure conditions. It is derived through high pressure adsorption isotherms by subtracting the total adsorbed uptake at 5 bar (P_{des} , the typical working pressure for natural gas-powered internal combustion engines)⁷⁰ from the total adsorbed amount at 35 or 65 bar (P_{ads} , which are the upper working pressure limits for common single stage and dual stage compressors, respectively)⁷¹ for applications at moderate pressure or at 80 or 100 bar for high pressure ANG operations.⁷²

An ideal adsorbent should not only demonstrate high storage properties but mainly the ability to deliver the adsorbate in an efficient way, cost and energy wise. Considering a material designed for on board ANG storage in the automotive industry, the main objective is maximizing the working capacity between predetermined pressure limits, as mentioned above. An adsorbent exhibiting high total uptake via a steep adsorption isotherm at low pressure, indicates strong CH₄-substrate interactions and relatively high isosteric heats of adsorption Q_{st} . Such a material might look promising but in the particular application most of the methane cannot be desorbed at the delivery pressure, and only a small fraction of its capacity (figure 2.6 left) is released; the residual

amount would require the application of vacuum and/or heating in order to be released. Alternatively, a material designed to demonstrate reduced affinity between the adsorbate and the surface at low pressure but high overall uptake, results in a less steep isotherm (figure 2.6 center) thus increasing the fraction of the deliverable methane. Ideally, an adsorbent which would feature a flexible structure, undergoing a reversible phase transition from non-porous at low pressure to porous framework above a specific pressure, demonstrating an “S-shaped” adsorption isotherm (figure 2.6 right), maximizes the working capacity by releasing the adsorbed CH_4 in the most efficient way.⁷³ However, flexible MOFs are still way underdeveloped for gas storage applications, mostly because of their doubtful structural stability due to the continuous phase transitions in multiple charge-discharge cycles. Thus, the high-pressure isotherm shape bares critical information regarding the compatibility of a material with a specific application.

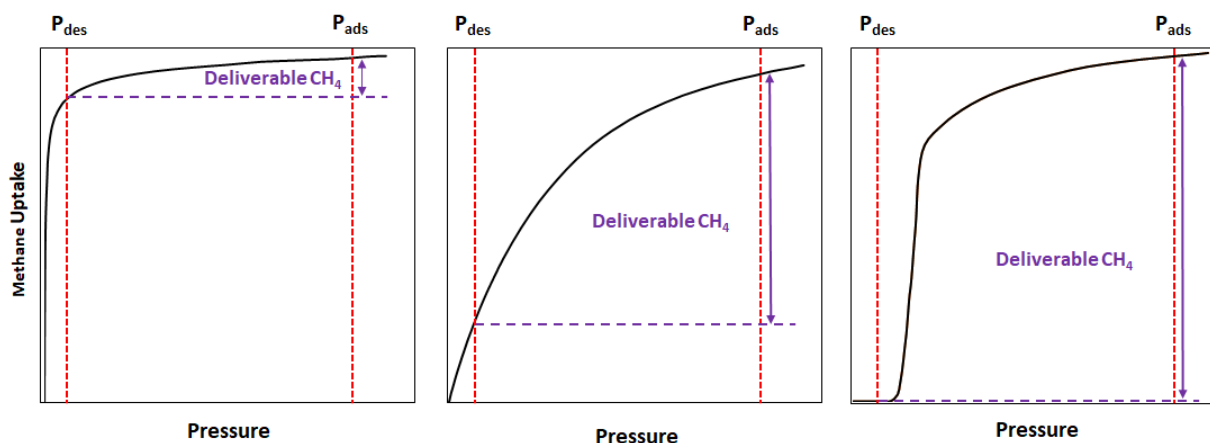


Figure 2.6: Schematic representation of the correlation between adsorption isotherm's shape and working capacity.

2.4.2 Carbon dioxide capture and separation from mixtures as an immediate solution

Modern human society has evolved to a point where its prosperity is heavily relied on the combustion of fossil fuels, which currently constitute the main source of energy. As a result, an unprecedented increase of carbon dioxide (CO_2) emissions into the atmosphere has been observed, which is considered to be the main cause of the projected global climate deterioration with disastrous consequences for all forms of life residing on earth.⁷⁴ Addressing these major

environmental concerns, the use of alternative, clean energy sources such as wind, solar, biomass, nuclear and hydrogen (*which is considered to be the ultimate fuel due to its natural abundance and zero carbon footprint*) have been investigated during the past decades. However, major technological challenges need to be addressed before widespread implementation of these systems. In this regard, fossil fuels are expected to be the primary source of energy in the near future for power generation as well as transportation.⁷⁵ The use of natural gas / biomethane (upgraded biogas) is being explored as a mid-term solution, since it produces significantly lower CO₂ emissions than the rest of the hydrocarbons. CO₂ coexists in substantial amounts in some natural gases and is around 50% of biogas, so it needs to be removed from the streams since it significantly lowers their heating value. Further carbon capture and sequestration (CCS) technologies must also be adopted as an immediate option. Essentially, four steps need to be employed in order to begin reducing the anthropogenic CO₂ emissions into the atmosphere, the first being the most urgent. CO₂ removal from emission sources, subsequent storage, transportation and finally permanent sequestration/reuse.⁷⁶

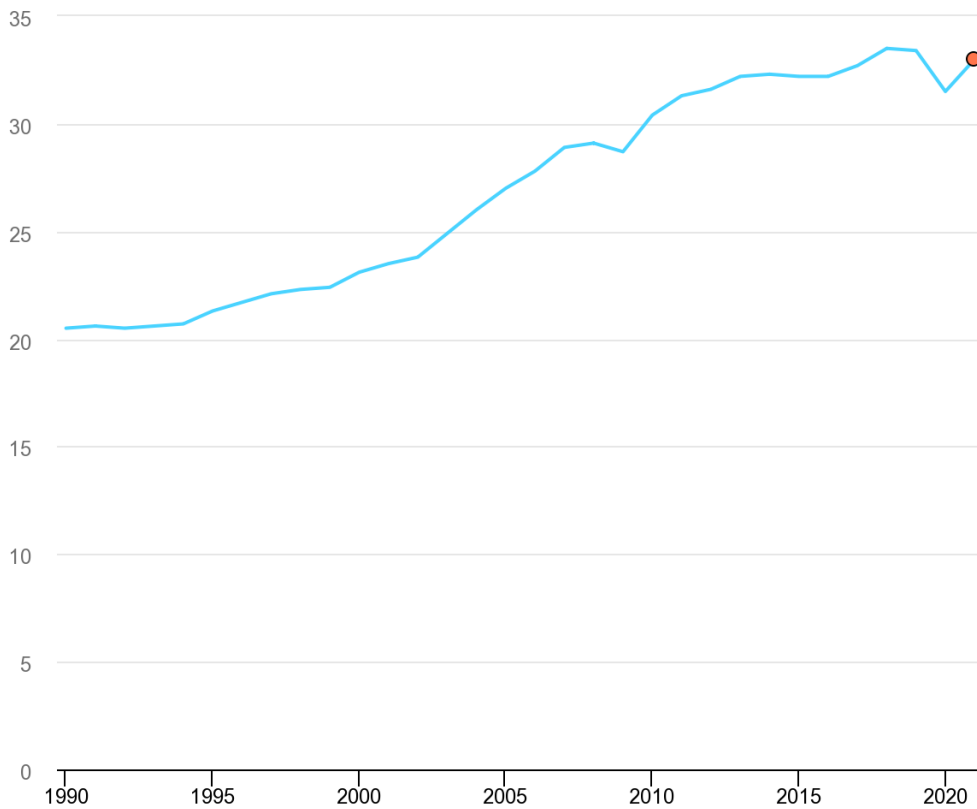


Figure 2.7: Global CO₂ emissions (Gt) since 1990.⁷⁷

The prevailing technology for CO₂ capture so far is mainly the use of amine solutions (amine scrubbing), which results from chemical reaction between the amine group and CO₂, yielding up to 98% capture.⁷⁸ However, the main disadvantage is the substantial energy penalty due to the high temperatures required for the regeneration and reuse of amine solutions, as well as the challenging handling of these highly corrosive and chemically unstable liquids. In this regard, the use of nanocomposite and nanoporous materials as adsorbents have attracted scientific attention during the last few decades since physisorption relies on relatively weak attractive dispersive forces, constituting a reversible process with considerably lower energy demands for regeneration. Zeolites were one of the first group of solid adsorbents that were systematically tested for CO₂ capture. They performed better than amine solutions in terms of energy required for regeneration while they exhibited superior adsorption kinetics. On the other hand, their instability in humid conditions as well as their limited CO₂ adsorption capacity, due to their relatively low surface areas halted their widespread use.⁷⁹ Activated carbons, display higher capacities than zeolites, especially at high pressures, but perform poorly in terms of CO₂/N₂ and CO₂/CH₄ selectivity.⁸⁰ MOFs, an emerging class of crystalline materials, are considered to be ideal candidates for the development of innovative CO₂ capture materials due to their outstanding intrinsic properties such as extended microporous networks, high surface areas, tunable pore sizes, facile introduction of surface functionalities etc.⁸¹

Below, the four most prominent CO₂ capture/separation applications and their respective thermodynamic characteristics are briefly discussed.

2.4.2.1. Post-combustion capture

The flue gas produced in power plants from combustion of coal in air consists mainly of N₂ (73-77%) and CO₂ (15-16%) and other minor components such as H₂O, O₂, CO, NO_x and SO_x with a total pressure of approximately 1 bar. The temperature of the mixture is estimated between 40 and 60 °C. In this case the process of interest essentially lies in the successful CO₂/N₂ separation while the partial pressure of CO₂ is equivalent to about 150 mbar.⁸² Therefore, a solid adsorbent that has an increased interaction with CO₂ and reduced interaction with N₂ at ambient pressures,

relatively high temperatures and probably in the presence of low moisture concentration should be sought.

2.4.2.2 Pre-combustion capture

Pre-combustion capture of CO₂ initially involves the conversion of the fuel into a mixture of mainly H₂ and CO₂ prior to combustion through processes such as "gasification" or "reforming". CO₂ needs to be separated from high pressure gas mixtures (5-40 bar) in order to produce pure hydrogen for the subsequent combustion stage.⁸³ Due to the obvious difference between the kinetic diameters of H₂ (2.89Å) and CO₂ (3.30Å), the separation of the two gases using solid sorbents (preferably in the form of membranes) with uniform pores of a certain size acting as "molecular sieves" is the most advantageous way.

2.4.2.3 Direct air-capture (DAC)

In both the cases mentioned above, the capture of CO₂ during its production is approached as a by-product of a reaction before its release in order to reduce its increasing concentration in the atmosphere. The concept of "negative carbon technology" has recently been proposed and examines the capture of CO₂ that has already been emitted into ambient air.⁸⁴ In addition, the DAC can also help maintain low CO₂ levels in confined spaces such as submarines or space crafts. Atmospheric CO₂ level is currently around 400 ppm, therefore its partial pressure during the DAC process is 0.4 mbar at 25 °C. This scenario requires a material that possesses a suitable microporous structure that will lead to increased (but at the same time reversible) interaction with the gas molecules at extremely low pressure and room temperature.

2.4.2.4 Natural gas / Biogas upgrading

Natural gas and its renewable analogue, biogas, consist mainly of CH₄, but CO₂, N₂ as well as traces of other impurities such as, H₂S, C₂₊ and H₂O vapor coexist in substantial amounts, depending on the stream's source. CO₂, which is not combustible, lowers their heat efficiency

and in the presence of humid conditions reacts with H₂O forming carbonic acid resulting to the corrosion of the pipes and the transportation equipment in general.⁸⁵ Therefore, CO₂ content needs to be reduced to below 2-3% before transportation and in order to obtain pure methane for combustion must be completely removed. Natural gas typically contains up to 8% CO₂ while biogas, depending on the production method, consists of much higher concentrations ranging from 25 to 50%.⁸⁶ Consequently, the design of an adsorbent that will selectively adsorb CO₂ resulting to pure methane needs to be tailored to the specific application. For natural gas purification with low CO₂ content, a microporous material which would exhibit high capacity at low pressure, hence increased substrate-adsorbate interaction is needed. For biogas upgrading, mixtures with CO₂:CH₄ compositions that can reach 50:50 are being studied, suggesting that the ideal candidate should possess high pore volume and a less steep isotherm reaching saturation at higher pressure.

2.5 Pressure swing adsorption processes (P.S.A.)

The use of solid nanoporous adsorbents on pressure swing adsorption processes has been industrially employed for gas separations since the late 1950s and nowadays is considered an established method used in several industrial applications such as production of N₂ and O₂ from atmospheric air, recovery of H₂ from synthesis gases from steam reforming processes etc^{87,88}. Therefore, application of P.S.A. processes for CO₂ capture from stationary emission points is feasible but needs to be optimized, both technically and economically, before widespread, large-scale implementation.

The P.S.A. principle of operation lies on the ability of a column packed with an adsorbent to selectively adsorb CO₂ on its surface, thus extracting it from the gas mixture. Selectivity can be achieved either due to thermodynamic (as expressed by the corresponding single component adsorption isotherms) or kinetic factors (difference on the components' diffusion coefficients). The process includes two main steps⁸⁹:

- a) the charging or adsorption cycle, during which the mixture components that exhibit the higher affinity for the material's surface are retained (e.g. those that are more strongly adsorbed or diffuse faster in the porous network) and
- b) the desorption or regeneration cycle, during which the retained components are released in order to "empty" the material's porous network so that it can be reused for the next adsorption cycle. Adsorbent regeneration can be achieved either by pressure reduction (PSA), temperature increase (TSA), application of vacuum (VSA) or a combination of the aforementioned methods (e.g. VTSA).

The extent of the process' technical practicability is governed by the adsorption step, while its economic sustainability is dictated by the desorption step. Careful screening for the use of the appropriate adsorbent is required. A successful material should exhibit superior sorption properties (capacity, kinetics) towards CO₂ based on its enhanced interaction with the adsorbent's surface compared to the other mixture components. However, a balanced interaction needs to be achieved, since the stronger the affinity with the surface, the harder the adsorbent regeneration, thus leading to increased cost for reuse in the next cycle.

A P.S.A. process includes one or more columns packed with an adsorbent, a simple schematic representation of which is illustrated in figure 2.8.

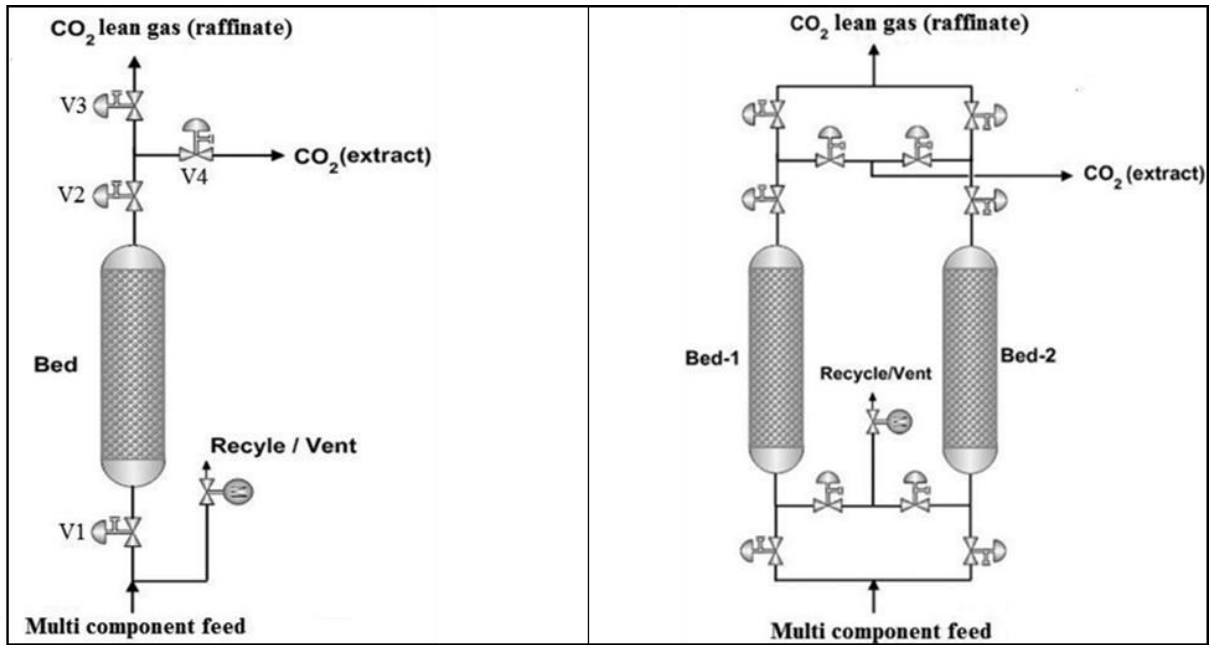


Figure 2.8: Schematic representation of single bed (left) and two packed-bed (right) PSA systems. (figure adopted from reference 89)

In industrial processes it is accustomed to use at least two columns which interchangeably operate so that continuous feed and product flow is achieved. The gas stream passing through the bed during adsorption is known as "raffinate", while the product obtained during regeneration is characterized by the term "extract". The desired components can be contained in either the raffinate or the extract⁸⁹.

Each bed undergoes a sequence of elementary steps⁹⁰, the most common of which are the following and are illustrated in figure 2.9:

- Compression to operating pressure.
- Adsorption with simultaneous raffinate production.
- Blowdown
- Pressure equalization (which is used in many variants of P.S.A. before blowdown, to save energy).

- Desorption or regeneration.

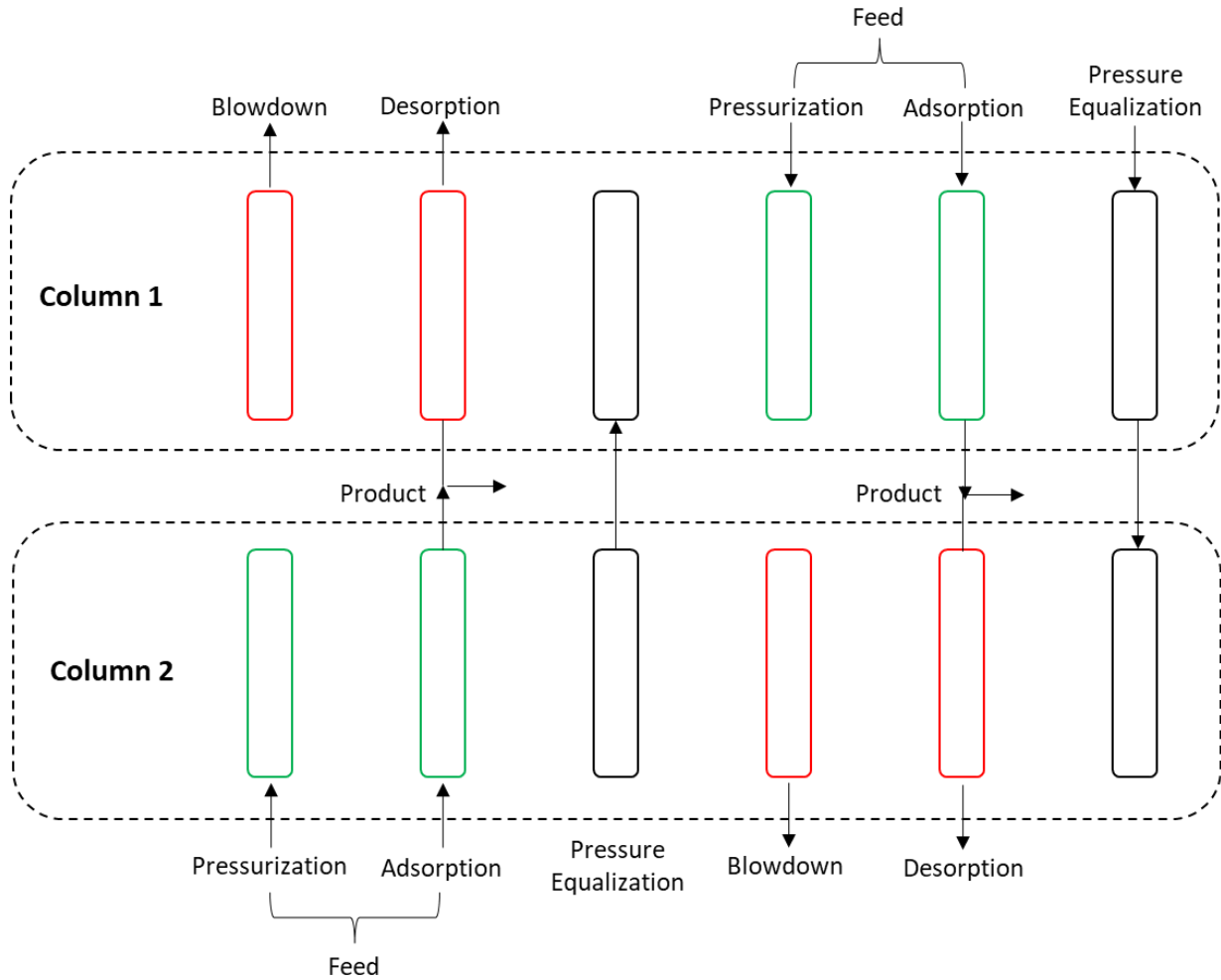


Figure 2.9: Schematic representation of the main steps sequence on a two-packed bed PSA process

Important information for designing the process is obtained by the breakthrough curves which are produced as the response of the initially “clean” column when introduced to a gas mixture. A typical single component breakthrough curve (normalized component concentration in the column’s outlet vs time) is depicted in figure 2.10.

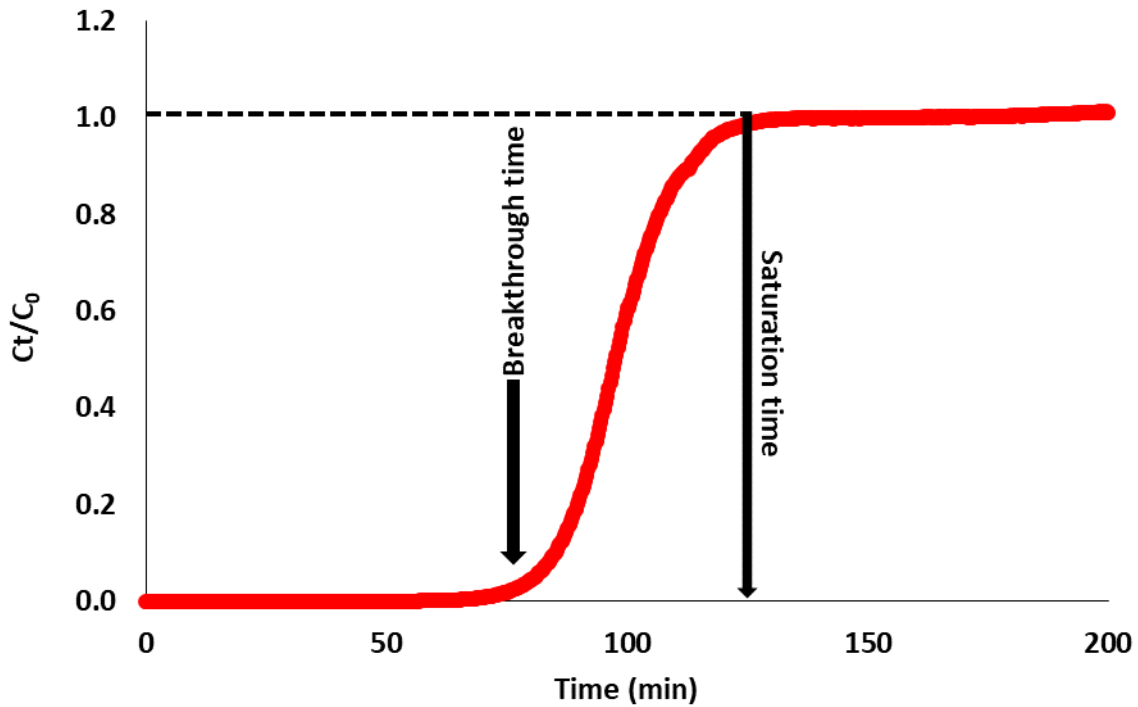


Figure 2.10: A typical single component breakthrough curve.

Breakthrough of a component is considered the time at which its normalized concentration (outlet/inlet) reaches 0.05 in the outlet stream. Saturation time is the time that is required for the component to reach adsorption equilibrium and is reached when the outlet concentration equals the one of the feed. Beyond this time, adsorption is considered not to occur in the column⁹¹. Moreover, by numerically integrating the breakthrough curves for each component, mean retention times (average time that each species are retained in the column) and competitive adsorption uptakes can be calculated and consequently values of real selectivities can be extracted. The adsorption cycle is usually terminated when the concentration, in the outlet stream, of the component which is retained from the bed exceeds a predetermined limit, based on economic and technical criteria related to the desired final product purity.⁹² Therefore, by studying the corresponding breakthrough curves in combination with the single component isotherms, the duration of each PSA cycle as well as critical parameters such bed volume, feed flow and feed pressure can be determined.

2.6 Scope of the dissertation

It has been well established that the use of solid nanoporous adsorbents in gas storage / separation processes have the potential to improve existing related technologies, addressing major environmental concerns. Metal-organic-frameworks, displaying outstanding structural properties and the ability to be synthetically tailored towards specific applications represent the most promising class of solid adsorbents to serve this purpose. However, several drawbacks need to be addressed before their widespread implementation in practical applications.

An ideal MOF should present high total uptake with fast adsorption kinetics and optimal thermodynamics, in order to simultaneously achieve good selectivity and mild requirements for regeneration and reuse. Although specific surface area and total pore volume are crucial parameters, special focus needs to be given on the strength of adsorbate-adsorbent interaction since it is considered to be a key factor associated with uptake, selectivity and regeneration ability.

Many synthetic strategies have been explored in order to enhance the gas-surface interaction including contraction of pore sizes by ligand shortening, incorporation of exposed metal cation sites in order to increase the number of strong adsorbing sites or functionalization of the organic linker with polar groups exhibiting either acidic or basic properties such as sulfonic acid⁹³, carboxylic acid⁹⁴, amine⁹⁵ and amide⁹⁶ groups.

The present dissertation attempts a complete experimental study on gas storage and separation processes through physical adsorption using nanoporous materials, coupling experimental techniques with theoretical tools. More specifically, the thesis focuses on the investigation of CO₂ selective adsorption from mixtures containing CH₄ or N₂ and the potential high pressure CH₄ storage ability by two newly synthesized MOFs, following a novel approach which is the use of a square planar metalated linker.^{97,98} This way, introduction of extra adsorption sites through the relatively low energy d_{z^2} orbital lying perpendicular to the square plane of the organic linker is attempted.

The two novel materials were successfully activated and extensively characterized using a variety of analytical techniques. In one case, where traditional activation methods proved to be unsuccessful, a custom-made, supercritical-CO₂ flow device had to be developed. Subsequently,

low- and high-pressure CO₂, CH₄ and N₂ isotherms were measured on various temperatures in order to comprehensively evaluate their adsorption properties; critical thermodynamic and kinetic properties were also extracted. By means of a new experimental protocol (low-temperature CO₂ TDS), CO₂-adsorbent interaction was thoroughly investigated in an attempt to verify previous theoretical calculations.

While CO₂/N₂ separation by MOFs has been the subject of intense research for the past decades, there is a lack of experimental studies reporting the competitive adsorption between them^{99,100}. Even more pronounced is the limited number of reports in literature presenting multi-component equilibrium adsorption data, while the corresponding process modeling studies are based on simple extensions of the single component isotherms^{101,102}. The reason for that is apparently the difficulty on performing breakthrough experiments with limited amount of material since MOFs are usually synthesized in the range of milligrams and are challenging to scale-up.¹⁰³

Consequently, an experimental rig designed to perform dynamic multicomponent breakthrough experiments for small amounts of sample was built. The two novel materials were extensively studied by performing dynamic column breakthrough experiments (DCB) for binary mixtures containing CO₂/CH₄ and CO₂/N₂ at different ratios, room temperature and pressure up to 5 bar.

3. Experimental Part

3.1 Samples – Characterization

3.1.1. Cu-Pd-nbo

As already mentioned, unsaturated metal sites (UMSs) in MOFs provide relatively strong metal-CO₂ interaction without chemical bonding thus leading to reversible adsorption. However, the number of UMSs in MOFs is limited by the nature and number of inorganic secondary building units (SBUs) per unit cell. The Cu(II)-based paddlewheel SBU with general chemical formula Cu₂(-COO)₄ provides two UMSs (figure 3.1), one per Cu(II) in the axial position as well as good framework stability³.

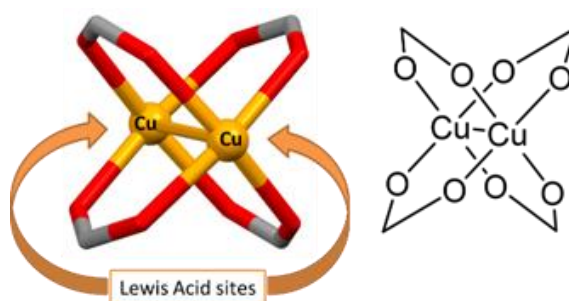


Figure 3.1: The Cu(II)-based paddlewheel SBU with general chemical formula Cu₂(-COO)₄ displaying the two UMS (Lewis acid sites).

An alternative general approach in MOFs, that is currently actively followed in order to increase the number of strong CO₂ binding sites while maintaining high porosities, is to functionalize the organic linker. In this Thesis, the two materials that are being studied were prepared following an already published novel approach, which is the use of d⁸ square planar metallated linkers suitable for the formation of Cu-based MOFs with nbo topology. The idea is to utilize the relatively low energy *d*_{z²} orbital lying perpendicular to the square plane of the d⁸ metal center in order to introduce Lewis base metal-CO₂ interactions on these sites and in combination with the Lewis acid Cu(II)-CO₂ interactions, to increase the overall CO₂ uptake and selectivity.

The idea was validated by utilizing the palladated ligand, *trans*-[dichlorido(3,5-dicarboxypyridyl)palladium(II)] (**H₄L**), which upon reaction with CuCl₂·2H₂O in DMF readily afforded the desired nbo-type MOF in single crystal form.

3.1.2. In-Pd-soc

Another important inorganic SBU that provides UMSs is the trimeric oxo-centered clusters with general chemical formula $M_3(\mu^3-O)(-COO)_6L_3$ (usually $L=H_2O$) known for s- (Mg^{2+}), d- (Cr^{3+} , Fe^{3+}), and p-block (Al^{3+} , In^{3+}) elements. This SBU possesses a trigonal prismatic linking geometry and is compatible with the augmented soc (square-octahedron), binodal edge-transitive net. Upon activation, the L ligands are removed resulting to unsaturated metal sites (Fig3.2). The designed synthesis of this important type of MOFs requires rectangular, 4-connected organic linkers and opens new pathways for the construction of a family of porous solids that will combine a particular topology with additional pore functionality, originating from the presence of Pd^{2+} sites. Using the same palladated metallolinker (**H₄L**), the first heterometallic MOF with soc topology based on the trimeric SBU $In_3(\mu^3-O)(-COO)_6Cl(H_2O)_2$ was synthesized, activated and extensively studied in order to evaluate its porous properties and gas storage and separation ability.

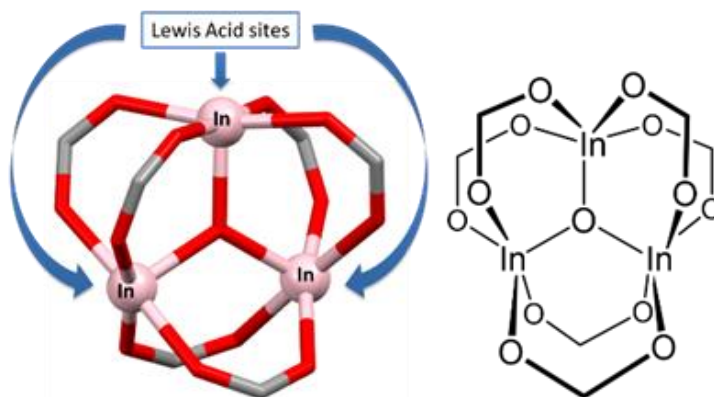


Figure 3.2: The In(III)-based trimeric oxo-centered cluster with general formula $M_3(\mu^3-O)(-COO)_6$ displaying the three UMS (Lewis acid sites).

3.1.3 Thermogravimetric analysis

The thermal analysis of a solid sample consists of monitoring (e.g. bond breakage, melting, etc.) as a function of temperature. Although this is a destructive method of materials' characterization, it is widely applied in both qualitative and quantitative analyzes since it demands only a small amount of sample while useful information is obtained. The term, thermal analysis, includes a variety of techniques, the main being thermogravimetric analysis (TGA), differential thermal analysis (DTA) and differential scanning calorimetry (DSC). In TGA experiments the sample's mass change is recorded as a function of temperature and time. Taking into account all the factors that contribute to the buoyancy effect, such as air buoyancy and heat driven gas flows inside the furnace, blank measurements become necessary. Thus, it is ensured that under identical experimental conditions these effects are compensated and the observed changes in the actual experiment can be attributed exclusively to the properties of the material under investigation. In DTA (temperature differences between sample and reference when the heat flow is constant) or DSC (changes in heat flow while the temperatures of both the sample and reference material are increased linearly over time) experiments the temperature difference ΔT between the sample and an inert reference substance (in this case an empty Al_2O_3 sample holder) is measured as a function of temperature and time. Therefore, changes in the thermal content of the test sample are detected due to physical or chemical change (phase change, degradation, etc.). Usually, the TG and DSC measurements are performed simultaneously during the analysis of the sample.

In the present work, TGA measurements were carried out in order to evaluate the thermal stability of the samples under air and/or inert atmosphere as well as to determine the concentration of the metal clusters in the framework of the prepared materials. More specifically, by studying the mass loss observed for the as made samples, safe outgassing temperatures can be determined; this is crucial for the successful activation of the sample. These measurements were performed on a SETARAM SETSYS Evolution 18 Analyzer, at a temperature range of 25 – 800 °C, with a heating rate of 5 °C/min and under argon flow (16 ml/min), using Al_2O_3 sample holders



3.1.4 Argon / Nitrogen porosimetry

In order to determine the specific surface areas as well as other attributes (e.g., total pore volume, pore size distribution etc.) correlated to the porous structure of the materials, nitrogen and argon porosimetry was employed at 77.35 and 88.45K, respectively. The measurements were performed on an automatic volumetric gas sorption analyzer (Quantachrome gas type Autosorb-1 MP) equipped with an oil-free high vacuum system (consists of a diaphragm pump, Pfeiffer MVP015-2 in combination with a turbo molecular pump, Pfeiffer TMH-071P) as well a series of pressure transducers that cover the 0-1 bar range. Using the above equipment, isotherms starting from very low relative pressures (P/P^0 : $10e^{-07}$), which are required for the detailed study of microporous materials, can be achieved. Moreover, the instrument is connected to a closed-cycle helium cryocooler, CTI-Cryogenics, which ensures accurate temperature control during the long measurements required to perform high-resolution low-pressure isotherms.

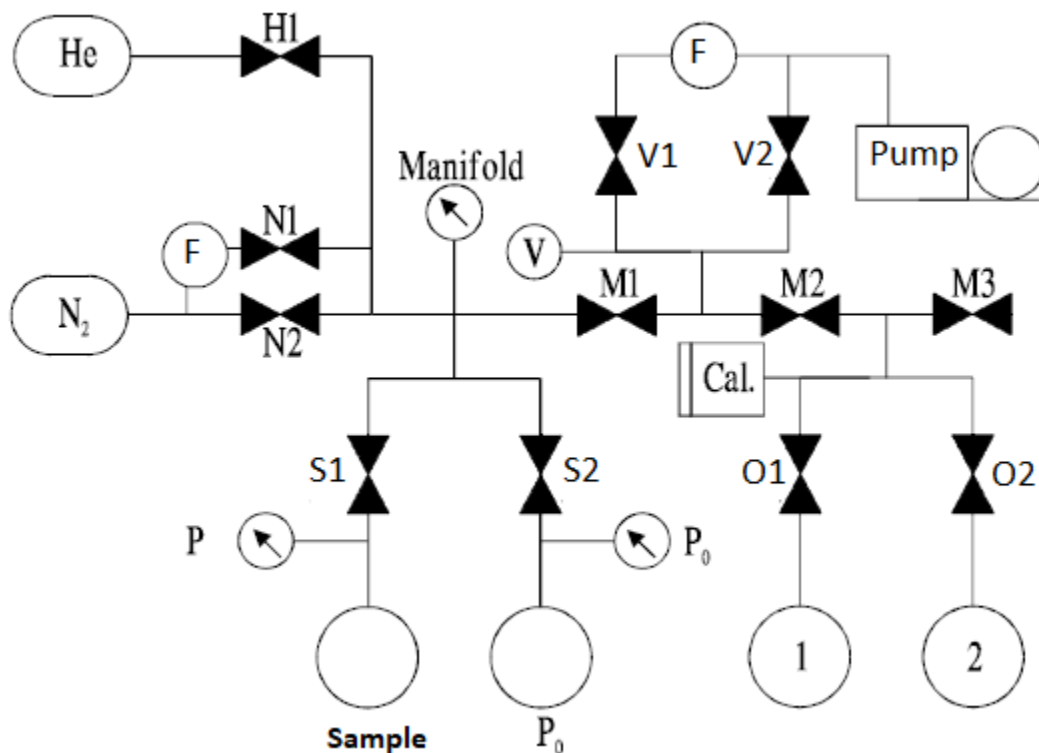


Figure 3.3: Schematic representation of volumetric Autosorb-1

Additionally, low pressure isotherms (up to 1 bar) were performed in the same instrument for CO₂, CH₄ and N₂ in a wide range of temperatures.

3.1.4.1. Experimental procedure

Prior to analysis the samples need to be activated; either by in-situ heating under high vacuum or by supercritical CO₂ drying (see chapter [3.1.4.2](#)). The experimental process is fully automated. Four main parameters need to be determined by the user before successful initiation of the measurement: the desired relative pressure points, the equilibrium time, the pressure deviation tolerance limits and the mass of the activated sample.

The measurement at a specific relative pressure point P/P^0 is performed through a series of steps. Initially, the sample pressure is measured and accordingly the pressure in the dosing space (manifold) is increased so that when valve S1 is opened, the relative pressure in the sample space will be equal to the desired P/P^0 value plus the upper pressure deviation tolerance set for that point, provided that no adsorption occurs. When the manifold pressure reaches the desired value, valve S1 opens for eight seconds allowing the sample to interact with the adsorbate through the combined (sample + manifold) volume. The sample space is then isolated and its pressure is measured after fifteen seconds. If the relative pressure has fallen below the specified tolerance value, a new pressure dose is built in the manifold based on the same process. Otherwise, after one minute, the device begins to measure the sample pressure every six seconds in order to determine if equilibrium has been achieved. The equilibrium criteria are on the one hand the relative pressure not to fall below the preset value minus the lower tolerance limit and on the other hand the pressure change to be less than 0.0008 atm for the equilibrium time the user has determined. In case both of the above conditions are met, the sample is considered in equilibrium. The specific relative pressure point has been achieved and the instrument proceeds to determine the next isotherm point. The amount adsorbed for each point is derived from the following equation:

$$n_x^a = \sum_{i=1}^N \Delta n_i^m + \Delta n_x^s \quad (3.1)$$

where n_x^a is the adsorbate amount adsorbed (mol) for the x isotherm point. Δn_i^m is the gas mole difference found in manifold before and after the gas relief (opening of S1 valve) in the sample space for the i dose of the x isotherm point. N is the total amount of doses required in order to reach equilibrium for the x point of the isotherm. $\Delta n_x^s = n_{x-1}^s - n_x^s$ are the gas moles in the sample space before the measurement for the x isotherm point and after equilibrium has been achieved, with $n_x^s = 0$ for x=0.

Ultra-high purity grade N₂ (99.999%), Ar (99.999%), CO₂ (99.9993%), and CH₄ (99.9995%) were used for all adsorption measurements. He (99.999%) was used for sample void volume determination.

3.1.4.2. Sample activation using super-critical CO₂

Solvent molecules or other residuals from the synthetic procedure occupying the sample's porous network need to be removed prior to analysis. Thus, its successful activation (i.e. removal of guest molecules from its porous framework) is required. Most commonly, this is achieved by exposing the sample to high vacuum and occasionally elevated temperature. However, outgassing sensitive materials may result to irreversible, partial or complete structural changes and in many cases total collapse of the framework upon solvent removal or pore blockage by the retained solvent molecules.¹⁰⁴

Super-critical CO₂ (sc-CO₂) drying has been successfully applied in polymer chemistry and for the preparation of aerogels¹⁰⁵ as well as activation of MOF structures that exhibited discrepancies between calculated and experimentally determined specific surface areas¹⁰⁶. It is believed that the structural collapse is prevented by initially exchanging the solvent molecules with liquid CO₂ of similar density and subsequently by the elimination of surface tension/capillary forces, taking advantage of the supercritical nature of CO₂ at elevated temperature and pressure.

For this purpose, a custom-made, super-critical CO₂ flow device was developed and is illustrated in figure 3.4. Accordingly, samples sensitive to high temperature are introduced to a stream of liquid CO₂ in order to exchange the solvent in the crystal structure. Subsequently, by increasing the temperature, CO₂ enters in the supercritical regime while flowing through the

sample and gaseous CO₂ can be vented in an extremely slow manner. The sample is thus “activated” in the most benign manner leaving its crystal lattice intact.

Prior to analysis, as-made samples were soaked in methanol, which is miscible with CO₂, at room temperature for three days during of which the supernatant solution was replaced six times. The methanol suspended samples were transferred inside the chamber of the supercritical CO₂ device and methanol was exchanged with liquid CO₂ over a period of 1.5 hours at room temperature and under constant flow of 1.5ml min⁻¹. The apparatus is equipped with a back pressure regulator set at 120 bar, so as to maintain full drying conditions inside the chamber. Subsequently, the temperature was raised to 50 °C (above the critical temperature of CO₂), kept there for 1.5 hours (under the same flow) and then slowly vented by a release valve in a controlled manner.

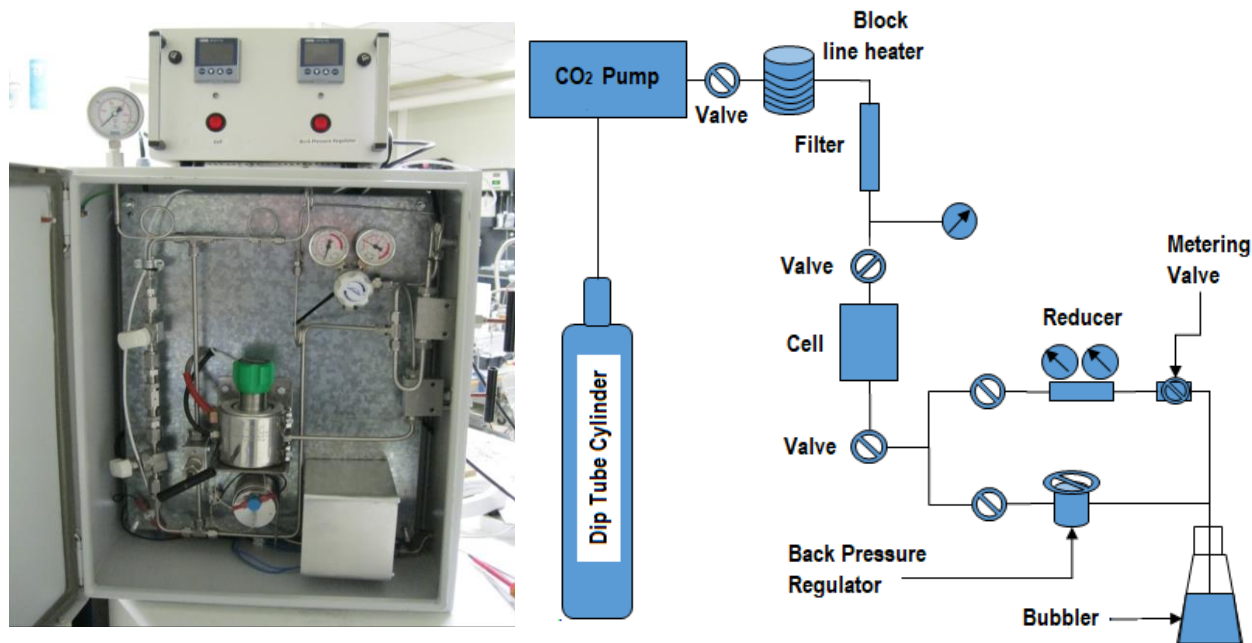


Figure 3.4: Simple schematic representation and actual photo of the super-critical CO₂ drying device

The chamber was sealed, de-attached and moved to an MBraun Argon glove box, where the dried sample was transferred immediately inside a pre-weighted, Argon filled sample cell while special “cell seals” (Quantachrome Instruments) were used to prevent intrusion of oxygen and atmospheric moisture during transfers and weighing. The cell was then transferred to the

outgassing station where the sample was outgassed under dynamic vacuum at room temperature until the outgas rate was less than 2 mTorr/min. The sample and cell were then reweighed to obtain the mass of the activated sample, and the cell was attached to the analysis port of the gas adsorption instrument.

3.1.4.3. BET surface area

The Brunauer-Emmett-Teller method, although based on assumptions that are not valid for microporous materials, is still considered as the most prominent way to evaluate and compare the surface area of porous materials. The theory's key element is the determination of the monolayer capacity, n_m . Considering the material's surface as an array of specific adsorption sites, n_m is defined as the amount of adsorbate (per unit mass of the solid) required to completely fill these sites, forming a single molecular layer. The monolayer capacity can be derived by transforming the model BET adsorption isotherm into the following linear relation:

$$\frac{P/P_0}{n(1 - P/P_0)} = \frac{1}{n_m C} + \frac{C - 1}{n_m C} \left(\frac{P}{P_0} \right) \quad (3.2)$$

where n is the adsorbed amount at relative pressure P/P_0 and C is a parameter associated to the monolayer's net heat of adsorption, which indicates the adsorbate's affinity for the adsorbent surface. n_m and C can be derived from fitting a straight line to the experimental points in a BET plot ($1/[n(P_0/P)-1]$ vs. P/P_0). Subsequently, the BET specific surface area, $a_s(\text{BET})$, can be calculated:

$$a_s(\text{BET}) = n_m L \sigma_m \quad (3.3)$$

where L is the Avogadro constant and σ_m is the cross-sectional area of the adsorbate molecule. The BET method can be directly applied to many type II and IV isotherms where the formation of the monolayer can be easily identified. However, the presence of micropores shifts the linear range of the BET plot and the monolayer formation cannot be easily distinguished from micropore filling and multilayer adsorption. In order to address this difficulty a procedure which consists of the three following main criteria has been proposed³²:

- (a) the value of the parameter C should always be positive
- (b) BET equation should be applied within the range where the term $n(1-P/P^0)$ continuously increases as P/P^0 increases
- (c) the P/P^0 value at which the monolayer is formed should be located within the aforementioned selected BET range.

As already mentioned, especially for type I isotherms of microporous adsorbents, the obtained BET surface area values only act as means for comparing “apparent” areas (BET areas) between different materials and do not necessarily correspond to realistic probe-accessible areas.

3.1.4.4. Total pore volume (TPV)

The total pore volume of a solid adsorbent can be approximated by measuring the adsorption isotherm of a gas or vapor at subcritical conditions. In the absence of macropores, beyond a certain pressure, all the pores are filled and the isotherm remains nearly horizontal at least at relative pressures close to unity. By applying the Gurvitch rule, which assumes that the pores are filled with adsorbate in the bulk liquid state, the amount adsorbed can be converted to the volume of liquid adsorbate. For instance, if the amount adsorbed is expressed in ideal gas volume at STP, the following equation can be used:

$$V_p = \frac{P_a V_{ads} V_m}{RT} \quad (3.4)$$

where P_a and T are ambient pressure and temperature, respectively, and V_m is the molar volume of the liquid adsorbate. However, even for microporous materials, most experimental isotherms exhibit a sudden increase of amounts adsorbed at relative pressures near $P/P^0 = 1$, indicating the presence of external surface or macropores formed by interparticle voids. In this case, the limiting adsorbed volume is assigned at a slightly lower relative pressure which needs to be clearly declared.

3.1.4.5. Pore size distribution (PSD)

The distribution of the material's pore volume with respect to its pore size is defined as pore size distribution. Kelvin equation, assuming mesopores of cylindrical geometry, correlates the pore size with a corresponding relative pressure:

$$r_K = \frac{-2\gamma V_m}{RT \ln(P/P^0)} \quad (3.5)$$

where γ is the surface tension of the adsorbate at its boiling point T , V_m is the molar volume of the liquid adsorbate and r_K is the kelvin radius of the pore in which condensation occurs at the respective relative pressure P/P^0 . However, prior to condensation, gas molecules have already been adsorbed on the pore walls forming an adsorbed layer with thickness, t . Therefore, the actual pore radius (r_p), is given by:

$$r_p = r_K + t \quad (3.6)$$

The statistical estimation of the adsorbed film's thickness can be based on "generic" model isotherms (e.g., de Boer (Harkins-Jura), Halsey) or experimental data on non-porous materials (e.g., carbon black method) while many macroscopic theories e.g., Dollimore and Hill (DH), or Barrett-Joyner-Halenda (BJH), considering pore condensation phenomena, have been proposed for the determination of pore size distributions. However, in the case of micropore filling and narrow mesopores these approaches do not produce a realistic description of the adsorption phenomena, thus resulting to underestimation of pore sizes. The main drawback is the assumption that the pore condensate has the same thermodynamic properties with the bulk fluid. On the contrary, numerous experimental and theoretical studies have shown that the confined adsorbate's thermodynamic properties can significantly deviate from the bulk properties.^{107,108,109,110}

Addressing this adversity, methods based on statistical mechanics such as the Density Functional Theory (DFT), Monte Carlo molecular (MC) or Molecular Dynamics (MD) simulations have been developed in order to provide a more accurate approach regarding the phase behavior of fluids confined in narrow pores. Considering intermolecular fluid-fluid as well as fluid-solid interactions, these microscopic methods allow for equilibrium density profiles to be determined for fluids adsorbed on various surfaces and for all locations inside pores of different geometries, bridging the macroscopic approaches with the molecular level. The past two decades, through optimization procedures, different DFT approaches have been proposed like the so called Non-

Local Density Functional Theory (NLDFT) which quantitatively predicts the range of capillary condensation and evaporation transitions of argon and nitrogen in ordered mesoporous materials with cylindrical and spherical pores or Quenched Solid Density Functional Theory (QSDFT) which accounts for the surface inhomogeneity with respect to the surface roughness.

Pore size distributions can be derived by relating individual “single pore” isotherms (local isotherms) determined by the aforementioned microscopic methods with the measured experimental adsorption isotherm of a material through the Generalized Adsorption Isotherm (GAI) equation:

$$N\left(\frac{P}{P_0}\right) = \int_{W_{min}}^{W_{max}} N\left(\frac{P}{P_0}, W\right) f(W) dW \quad (3.7)$$

where $N(P/P_0)$ is the experimental adsorption isotherm data, W is the pore width, $N(P/P_0, W)$ is the isotherm of a single pore of width W , also known as a kernel and $f(W)$ is a pore size distribution function. The GAI equation essentially describes the assumption that the total isotherm is the sum of a set of DFT-derived isotherms for individual single pores multiplied by a relative distribution $f(W)$, on the whole pore size range. The numerical solution of the GAI equation using a non-negative least square function corresponds to the pore size distribution.

3.1.5. Other characterization techniques (SC-XRD, PXRD, IR, NMR, SEM)

The crystalline structure, phase purity as well as chemical stability of the newly synthesized materials were investigated by powder x-ray diffraction. PXRD patterns of the samples were collected on a Rigaku R-AXIS IV Imaging Plate Detector mounted on a Rigaku RU-H3R Rotating Copper Anode X-ray Generator ($\lambda = 1.54 \text{ \AA}$). The patterns were recorded in the 2θ range from 5 to 50° .

During the synthetic procedure of both materials, crystals suitable for single-crystal XRD analysis were deposited. SC-XRD data for Cu-Pd-nbo were collected at beamline I19, 90 Diamond Light Source, Didcot, UK using a wavelength $\lambda = 1.0402 \text{ \AA}$ at 120 K. Solvated single-crystals were mounted on MiTeGen loops. Data collection, integration and reduction were performed using

CrystalClear software from Rigaku. The structure was solved by direct methods using SHELXS and refined by full-matrix least squares on F^2 using SHELXL software.

For In-Pd-soc, data were collected at the X-ray diffraction beamline (XRD1) of the Elettra Synchrotron, Trieste (Italy), with a Pilatus 2 M hybrid-pixel area detector. Complete data sets were collected at 250 K (nitrogen stream supplied through an Oxford Cryostream 700) with a monochromatic wavelength of 0.700 Å through the rotating crystal method. The crystals were dipped in N-paratone and mounted on the goniometer head with a nylon loop. The diffraction data were indexed, integrated, and scaled using XDS. The structure was solved by direct methods using SIR2014 Fourier analyzed and refined by the full-matrix least-squares based on F^2 implemented in SHELXL-2014.

Infrared spectra were performed using a Thermo Scientific Nicolet 6700 FTIR equipped with a N_2 purging system and a liquid N_2 -cooled wide range Mercuric Cadmium Telluride detector in the mid-infrared region of 4000–400 cm^{-1} .

1H NMR data which confirmed the successful synthesis of the new palladated linker were recorded on a 500 MHz Bruker Avance spectrometer. Samples were prepared by dissolving a small portion of the solid in a $DMSO-d^6$ solution. 1H NMR spectroscopy was also used to confirm the successful activation of the new MOFs. Samples were prepared by digesting a small portion of the degassed solid with a drop of HCl 37% in a $DMSO-d^6$ solution. The spectrum demonstrated the absence of residual peaks assigned to solvent or other guest molecules.

3.2 Gravimetric apparatus

3.2.1 Instrument description

All the gravimetric gas adsorption experiments were performed on an automated high-pressure instrument (up to 20 bar) (Intelligent Gravimetric Analyzer IGA-001 by HIDEN ISOHEMA). As shown in the figure below, the device comprises of a precision microbalance (resolution $\pm 0.1 \mu\text{g}$) with a dual suspension arm (for sample and counterweight respectively, as can be seen in Figure (3.5)). The same device also includes three 0.1, 1 and 20 bar manometers as well as two valves (one inlet and one outlet) fitted to stepper motors, thus ensuring excellent pressure control and stability even for very small pressure changes. The microbalance head, which contains the balance electronics, is always heated at a constant temperature ($50 \text{ }^\circ\text{C}$), in order to minimize electronic noise. The device is equipped with a vacuum system consisting of a diaphragm pump (Vacumbrand MZ-2D) in combination with a turbo molecular pump (PFEIFFER TMU 260) and a vacuum gauge (Edwards Penning CP25-K) as well as thermostatic units for degassing / heating samples and maintaining the desired temperature during the experiment.

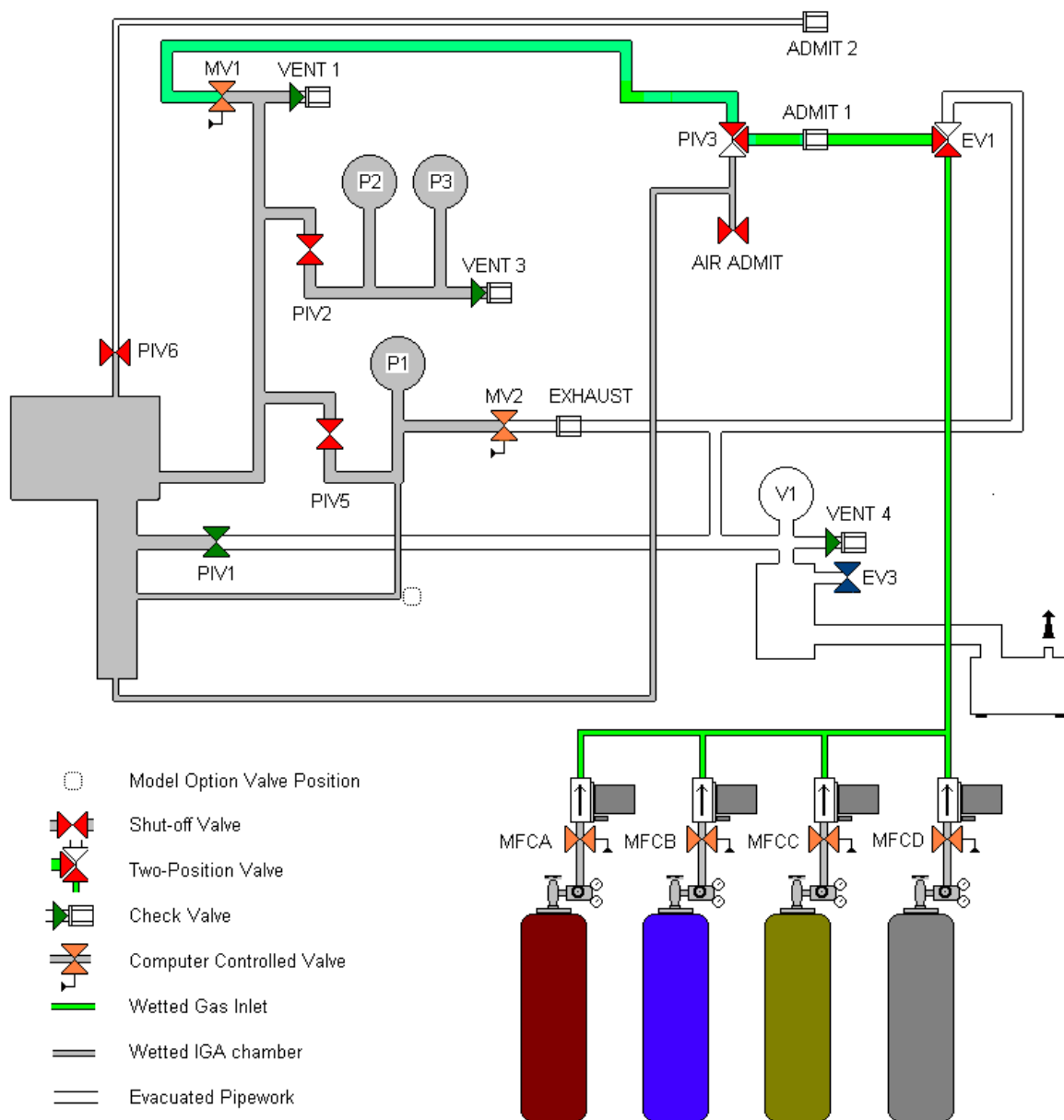


Figure 3.5: Schematic representation of the IGA-001 gravimetric device

The microbalance's principle of operation is based on the induction phenomenon. Specifically, the arm of the microbalance (which is almost perfectly weighed with respect to its center) is the rotor, which rotates inside an electromagnet (stator). An electric current of such intensity passes through the electromagnet so that the arm is kept in a horizontal position, which is detected by a sensor. If there is a change in weight either in the sample area or in the counterweight the arm tends to rotate. This movement is detected by the sensor, which instructs a

PID controller to change the electrical current flow through the electromagnet in such a way that the arm returns to the horizontal position. This change in current, through the inductive effect, translates into a change in weight from the electronic circuits of the balance.

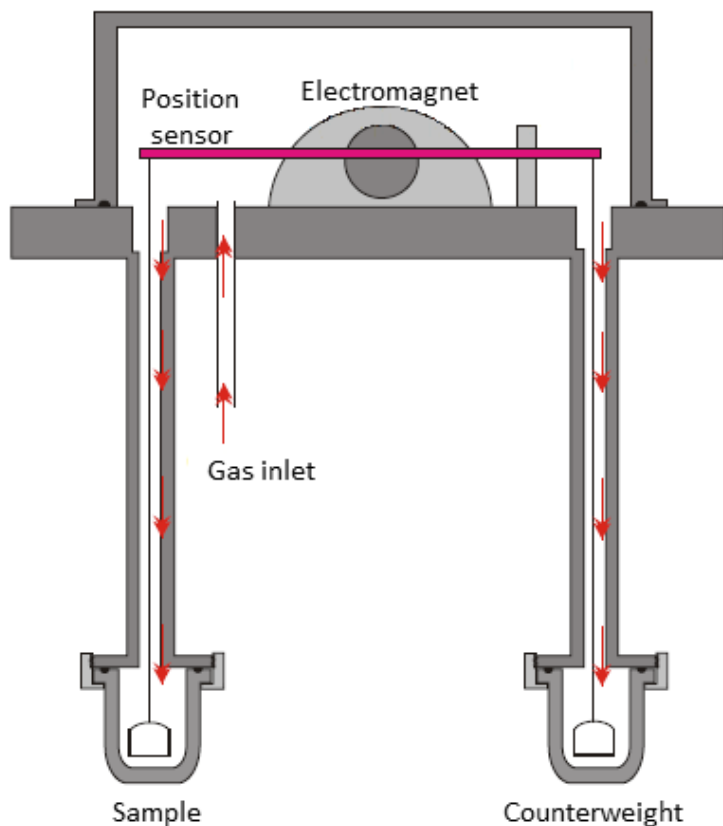


Figure 3.6: Schematic representation of the microbalance

The force caused by the mass of the adsorbed molecules (m_a) is equal to $F_a = m_a * g$, where g is the gravitational acceleration. The magnitude of the buoyancy (C_b) is derived from Archimedes' Principle: "Every body of mass m_s and density ρ_s immersed in a fluid of density ρ_g , experiences an upward buoyant force equal to the weight of the fluid that the body displaces" and can be written as

$$C_b = m_s g \rho_g / \rho_s \quad (3.8)$$

The total force F_t is defined as

$$F_t = F_a - C_b = m_s g \left\{ 1 - \rho_g / \rho_s \right\} \quad (3.9)$$

The density, ρ_g , is related to the molecular weight MW, pressure P , temperature T , and the compressibility factor Z , through the expression:

$$\rho_g = (MW P) / (Z_{(P,T)} RT) \quad (3.10)$$

Taking into account the correction of buoyancy for weighing in air, a sample of mass m_s and density ρ_s , while in the counterweight area there is a reference body of mass m_l and density ρ_l , in a balanced system the following equation applies:

$$m_l (1 - \rho_{air} / \rho_l) g = m_s (1 - \rho_{air} / \rho_s) g \quad (3.11)$$

Assuming that due to the small distance between the sample and the counterweight space the acceleration of gravity is practically unchanged, the sample mass can be calculated:

$$m_s = m_l \frac{1 - \rho_{air} / \rho_l}{1 - \rho_{air} / \rho_s} \quad (3.12)$$

3.2.2 Experimental procedure

The experimental procedure consists of a series of steps through a semi-automatic process with the help of the instrument software.

Initially, all the accessories (counterweights, sample holder, etc. but not the sample), are attached to the balance and their respective masses, densities and temperatures (depending on which part of the balance they are located) are entered in the buoyancy calculation table so that the initial indication of the balance, L_{in} is correctly calculated.

The sample holder is then filled with the sample and after equilibration for a short amount of time, the indication L_{fin} is recorded. The initial, non-outgassed mass of the material m_0 is derived from the equation $m_0 = L_{fin} - L_{in}$.

The material is then activated in situ by heating it to a predetermined temperature under high vacuum ($<1.0e^{-6}$). The outgassing process is considered concluded when no further weight loss is recorded and the mass reading becomes stable.

The determination of the sample's initial outgassed mass m_s is calculated by the instrument software. In particular, the mass m_0 initially introduced into the sample holder of the balance is equal to the activated mass of material (m_s , density ρ_s) and the impurities adsorbed in its pores and surface, (mass m_2 and density ρ_2), as weighed in air, according to the equation:

$$m_0 = m_s(1 - \rho_{air}/\rho_s) + m_2(1 - \rho_{air}/\rho_2) \quad (3.13)$$

Upon completion of the degassing, mass loss dm_0 is determined, by taking into account not only the removal of unwanted impurities, but also the buoyancy of all the parts of the balance that are suspended either in the sample area or in the counterweight (chain, sampler hook, etc.). If we denote by m_i and ρ_i the masses and densities respectively of all the elements in the sample space and m_j , ρ_j those of the elements in the counterweight space, the following relation is obtained:

$$dm_0 = m_s(\rho_{air}/\rho_s) + m_2(1 - \rho_{air}/\rho_2) + \sum_{i=1}^i m_i (\rho_{air}/\rho_i) - \sum_{j=1}^j m_j (\rho_{air}/\rho_j) \quad (3.14)$$

Solving equation 3.13 with respect to m_s and substituting it in the above equation (3.14) an expression for m_2 is obtained, which is used to calculate the outgassed mass of the material. Due to the fact that the activation of the material takes place under vacuum, the relation is simplified to $dm_0 = m_2$. However, equation 3.14 is used to calculate the adsorbed amount in the pores of the material at various step pressure changes which essentially constitute the gas isotherm (by replacing ρ_{air} with ρ_g which is given by eq. 3.10). Given that the temperature varies between the different parts of the balance (hence the different gas densities surrounding the various components of the balance), buoyancy corrections become of critical importance for accurate calculations.

The IGA cryofurnace that accompanies the instrument and can control the reactor/sample temperature in the range -150°C (by means of a liquid nitrogen flow) to 500°C , was used to adjust the appropriate degassing temperature. During the measurements, a GRANT refrigerated circulating bath was used to control the reactor temperature ($0-35^\circ\text{C}$) during adsorption measurements.

The experimental procedure starts after the sample's temperature has been stabilized at the analysis setpoint and the input of the basic experimental parameters such as the gas to be used, the isothermal pressure points for which the amount of adsorbed gas will be calculated, the minimum and maximum equilibrium time of each point, etc, have been determined. During the measurement, the kinetic experimental data (weight change versus time) are also recorded while a kinetic model function can be constantly fitted to the measured points in order to predict the equilibrium time as well as the amount of adsorbed gas at each isotherm point. For the measurements described in this Thesis, the Linear Driving Force (LDF) model for gas adsorption kinetics¹¹¹ was used in the following form:

$$m_t = m_{init} + \Delta m \left(1 - e^{-\left(\frac{t-t_0}{k}\right)} \right) \quad (3.15),$$

where m_t is the mass of the material at random time t , m_{init} is the initial mass of the sample, Δm is the change in mass of the sample after a step change in pressure, t_0 is the moment at which the equilibrium measurement is considered to begin and k is a time constant. The values of Δm and k are determined by the method of least squares for each point of the isotherm. The material is considered to be in equilibrium when the change in mass approaches 99% of the theoretical value or if an arbitrary maximum equilibrium time has been set by the user. When the equilibrium condition is satisfied, the instrument proceeds to the next predetermined point of the isotherm.

3.2.3 Diffusion time constant calculation

Adsorption kinetics can be additionally analyzed by a more elaborate approach. In more detail, by assuming micropore diffusion, the apparent diffusion coefficient D , can be calculated by fitting the proper solution of Fick's second equation to the experimental adsorption kinetic data. The solution for isobaric, isothermal uptake and micropore diffusion in spherical particles is given below:

$$\frac{m_t}{m_\infty} = 1 - \frac{6}{\pi^2} \sum_{N=1}^{\infty} \frac{1}{N^2} \exp \left[\frac{-N^2 D \pi^2 (t - t_0)}{r^2} \right] \quad (3.16)$$

where m_t is the uptake at any random time t , m_∞ is the equilibrium uptake of the material, N is the equation's number of terms, t_0 is the time at which data recording begins and r is the radius of the

particle. Although the above equation applies to spheres, it can also be used for particles of various shapes provided that the radius is replaced by an equivalent size, defined as the sphere radius having the same ratio of outer surface area to volume as the particle to be studied. In the case where the radius of the particle is not known, as in the present case, the diffusion time constant D/r^2 is calculated.

3.2.4 Isotheric heat of adsorption calculation

The value of the isotheric heat of adsorption (Q_{st}) is an indication for the intensity of the interaction between adsorbed gas molecules and the surface of the adsorbent. More specifically, it describes the amount of heat released during the adsorption of gas molecules on the surface of the material as a function of the surface coverage. As the pressure increases, the interaction between the adsorbed molecules within the porosity of the material becomes of critical importance as well.

The Q_{st} values were calculated by using the virial coefficients method. In particular, adsorption isotherms of the gas to be studied are required at different temperatures (as Q_{st} may change with temperature, usually three neighboring temperatures are used with e.g., a difference of 10 °C). The data of the three isotherms are fitted to an equation having the form:

$$\ln P = \ln N + \left(\frac{1}{T}\right) \sum_{i=0}^m a_i N^i + \sum_{i=0}^n b_i N^i \quad (3.17)$$

where P is the equilibrium pressure, N is the adsorbed amount, T is the temperature, a_i and b_i are the virial coefficients and m, n are the numbers of coefficients required to adequately describe the isotherms. Finally, the adsorption enthalpy for zero coverage (Q_{st0}), which is practically the interaction energy of the first molecule that comes in contact with the surface of the material, and the adsorption enthalpy as a function of the amount of adsorbed phase are given respectively by the following two equations, where R is the universal gas constant:

$$Q_{st0} = -R a_0 \quad (3.18)$$

$$Q_{st}(N) = -R \sum_{i=0}^m a_i N^i \quad (3.19)$$

3.3 High pressure volumetric apparatus

The materials' methane storage properties were evaluated by measuring gas excess adsorption isotherms at pressures up to 100 bar and near ambient temperatures. More specifically, the experiments were performed on a high pressure volumetric apparatus (Hy Energy PCTPro 2000, SETARAM), simple schematic representation of which is illustrated in figure 3.7.

Appropriate sample quantities (approximately 100 mg) were loaded on a stainless steel sample holder and were activated (when needed) in situ with heating under high vacuum ($< 10^{-6}$ mbar) for approximately 12 h. Isothermal conditions during the measurements were ensured by means of a water bath in which the sample holder was immersed while the main part of the device remained at 30 °C with the aid of an integrated air bath.

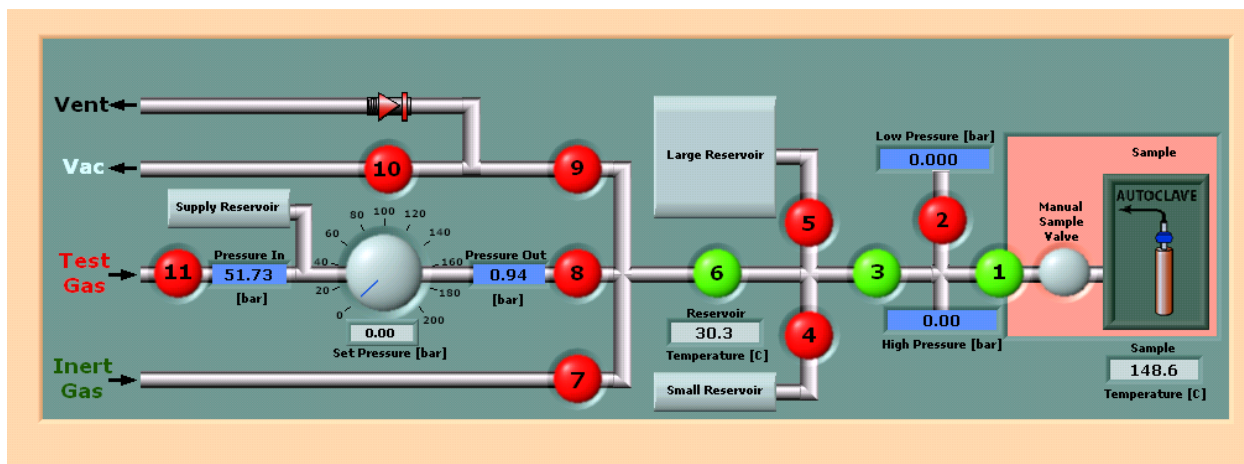


Figure 3.7: Schematic representation of the high pressure volumetric apparatus

The principle of the volumetric method is described in chapter 3.1.4.1 and is identical to Autosorb-1 which as already mentioned is a low pressure volumetric analyzer. Ultra pure He (5.0) was used for void volume determination at instrument and sample temperature prior to each measurement. For the isotherms, ultra pure CH₄ (5.0) was used.

3.4 Breakthrough curves determination apparatus

3.4.1 Device description

The experimental device for the study of breakthrough curves, simple schematic representation of which is given in figure 3.8, has been constructed entirely in the HySorb laboratory of NCSR "Demokritos" and has the ability to perform gas mixture experiments under flow at high pressures (up to 20 bar) and temperatures (up to 350 °C), by means of a custom made heating mantle. It consists of stainless-steel pipes (size 1/4 "and 1/8" type 103 SS 316), connected through stainless steel valves and either Swagelok® or VCR® connectors. The device is essentially divided into the following three main parts:

- 1) Gas mixing chamber connected to the mass flow controllers
- 2) Fixed bed (adsorption column) and bypass manifold
- 3) Gas analyzer.

Specifically, the gas mixing area includes three digital mass flow controllers (Bronkhorst EL-FLOW F-201CV), factory calibrated for various gases (N₂, CH₄, He, H₂, CO₂, etc.). The first, connected to an Ar cylinder (5.0) has a flow-rate of 4 - 200 ml NTP / min and the other two, optionally connected to CH₄ (5.0), He (5.0), N₂ (5.0) and CO₂ have a flow rate of 0.1 - 5 ml NTP / min. The outlets of the above regulators are connected to isolation valves that are in turn connected to a cross-type connector (Swagelok®), which is essentially the mixing space.

The column section consists of a) the packed bed itself, which contains the sample to be analyzed. It is made of a 77.50 mm long stainless-steel cylinder with internal diameter of 3.0 mm. At the ends of the cylinder VCR connectors are welded for easy connection and disconnection from the set-up. By using nickel gaskets equipped with a 2 µm diameter filter, an airtight connection is achieved and the elution of material particles in the remaining piping of the device is avoided, b) the sample bypass tube using two three-way valves located in the column's inlet and outlet, c) a pressure transducer (Wika Tronic Line) mounted at the column inlet, d) an electronic flow regulator (Bronkhorst EL-FLOW F-201CV, digital mass flow controller), which essentially acts as a flowmeter at the column's outlet and e) an electronic pressure regulator (back pressure regulator ELPRESS, 0-20 bar, 400 ml / min, by Bronkhorst).

Finally, the analyzer is a residual gas analyzer (RGA) mass spectrometer (PFEIFFER OMNISTARTM GSD 301 O2), which is connected to the system after the back pressure regulator via a cross-type connector (Swagelok®), to which venting valve and a vacuum metering valve are also connected. The vacuum valve is connected to a high vacuum turbomolecular pumping station.

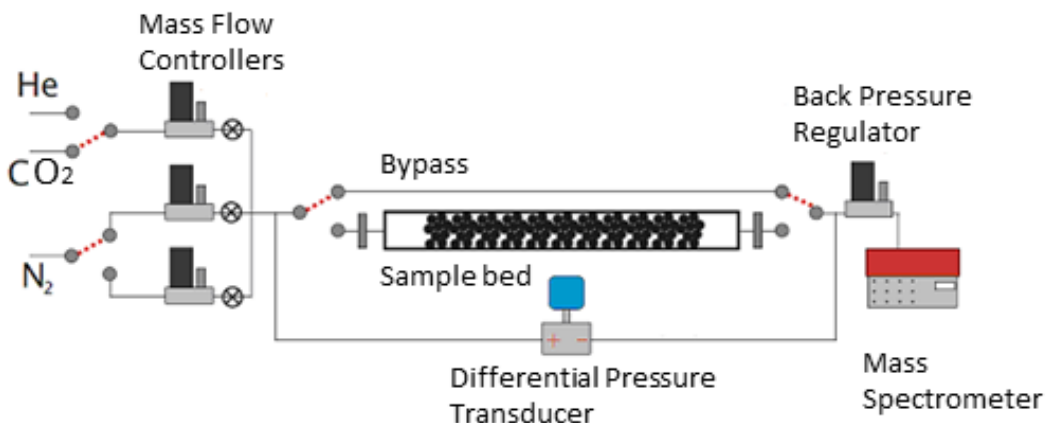


Figure 3.8: Experimental device for gas mixture break through experiments containing: i) Gas mixing chamber connected to the mass flow controllers, ii) Fixed bed and bypass manifold, iii) Gas analyzer

3.4.2 Mass spectrometer

The analyzer is a quadrupole mass gas spectrometer OMNISTAR™ GSD 301 O2 constructed by PFEIFFER. It consists of three main parts: a) the inlet system, b) the vacuum part and c) the mass analyzer and the appropriate electronic components. The inlet includes a thermostated 1/16" diameter, 1m long stainless steel capillary tube, with a solenoid valve and a 0.02 μm diameter constrictor. The gas mixture to be analyzed is pumped in the system through the capillary tube, which is heated to 120 °C to avoid vapor condensation, under a flow of 1-2 ml/min (when the mixture is at atmospheric pressure). The vacuum compartment includes a diaphragm pump in combination with a turbo molecular pump as well as a full-scale combined pirani/penning gauge of range from 1e⁻⁹ to 1000 mbar. The analyzer's simple schematic representation is depicted in figure 3.9. It consists of the ionization source, a quadrupole mass filter and of two detectors: a) a Faraday type (Faraday Cup) and b) a Channeltron with Secondary Electron Multiplier. The latter exhibits at least 100 times more sensitivity than the first.

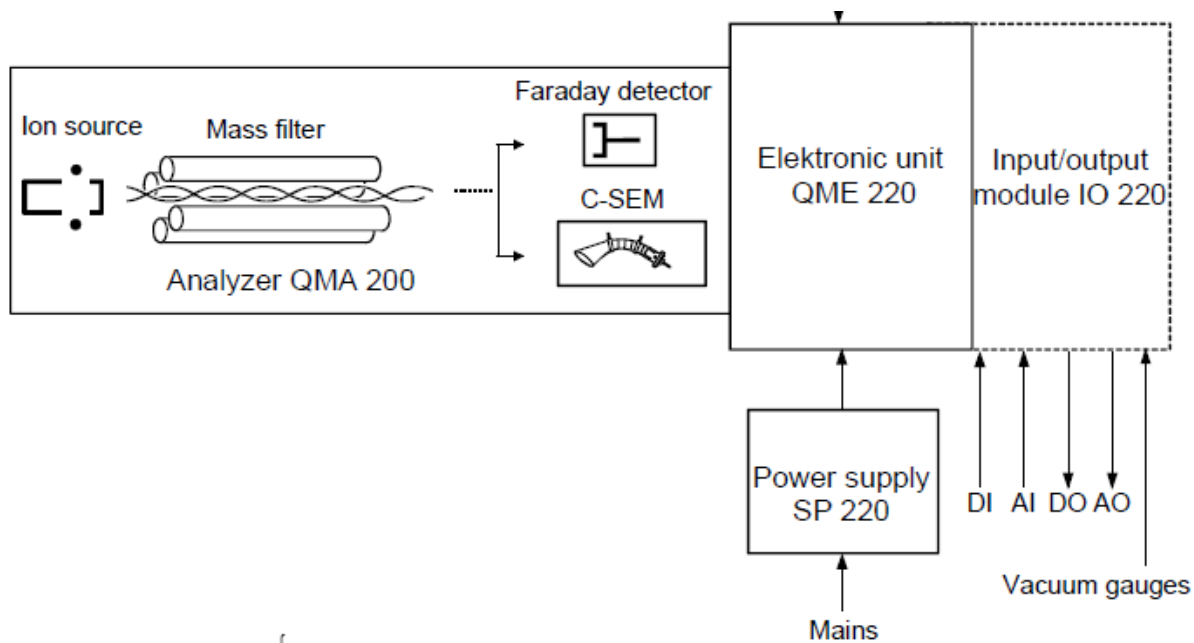


Figure 3.9: Schematic representation of the mass spectrometer

The RGA instrument can work under different modes, the most common being a m/z (mass over charge) scan (0-200 amu for the specific instrument). However, the most convenient for breakthrough experiments is the temporal measurement of intensities at predetermined m/z values. In order to carry out such a measurement, an appropriate method needs to be established. The main parameters to be resolved are: a) the definition of individual m/z values to be monitored, (b) the measurement time period per m/z and c) the type of detector to be used.

3.4.3 Experimental procedure

CO_2/N_2 and CO_2/CH_4 separation experiments were performed at pressures ranging from 1 to 5 bar at room temperature. Due to the small amount of material available to be studied, the aim was to achieve low flow-rates in order to increase the analysis time and observe the separation phenomenon in detail with well-defined breakthrough curves. Thus, CO_2 , CH_4 and N_2 were introduced with the 0.1-5 ml NTP / min mass flow controllers (MFCs) and the Ar with the 4-200 ml NTP/min MFC. Double stage pressure reducers set to 8 bar were connected to all gas cylinders.

The adsorption column, containing the material, is then weighed and after calculating the tare weight, is reattached to the device. Subsequently, the sample is degassed on the device (in situ) under argon flow (10 ml/min) or vacuum while heating at the desired temperature. During the activation, the exhaust gases are analyzed by the mass spectrometer, in order to monitor the progress of the process. After the activation process is completed successfully, the system is cooled to room temperature. Then, using the Argon MFC, a pressure equal to the separation process is applied to the sample (it is assumed that Argon adsorption at room temperature is negligible). Then, by using the vacuum pump the rest of the system (i.e., 3-way valves to bypass) is cleaned. In the next step, the proper flow rate values for nitrogen or methane and carbon dioxide are adjusted in the MFCs while the pressure of the process (in which the sample is already under argon) is adjusted using the back pressure regulator. When the signals recorded by the mass spectrometer are stabilized, the three-way valves are used to guide the flow of the mixture through the column. This moment is considered as the start time of the experiment. The experiment is completed when the gas mixture composition at the outlet of the bed is the same as that of the feed.

The breakthrough curves obtained during the experiment require a correction corresponding to the time it takes for the "dead" volume of the device to be filled by the gas mixture. The correction is done by following the same procedure described above, with the only difference that instead of the mixture, helium is used, (helium adsorption is considered negligible at room temperature).

4. Results and Discussion

In this chapter, the synthetic procedure of the palladated ligand and the corresponding two heterobimetallic MOFs is briefly described. Subsequently, structural characterization using a combination of the analytical methods described in the previous chapter was achieved. Low- and high-pressure CO₂, CH₄ and N₂ isotherms at a broad range of temperatures were measured in order to extensively evaluate the material's adsorption properties. Finally, dynamic column breakthrough (DCB) experiments were performed in order to assess the separating ability of the best performing adsorbent by selective CO₂ adsorption from mixtures containing CH₄ or N₂.

4.1. Synthesis and characterization of palladated ligand, *trans*-[dichlorido(3,5-dicarboxypyridyl) palladium(II)] (**H₄L**)

An amount of 3 5-pyridinedicarboxylic acid (PDC 334.2 mg, 2.0 mmol) was suspended in tetrahydrofuran (THF) (150 mL) and the mixture was degassed by three vacuum/Ar cycles. After the addition of [Pd(PhCN)₂Cl₂] (383.6 mg, 1.0 mmol) the mixture was degassed again, and then was stirred for 5 h under Ar atmosphere at room temperature to yield a yellow solution. Rotary concentration under reduced pressure to ca. 1/3 of the initial volume and addition of hexane (250 mL) induced the formation of the product as a pale-yellow solid. It was collected by filtration, washed with THF/hexane (1:2) and hexane, and vacuum dried. 501.1 mg of the final product was recovered, which corresponds to a yield of 98%.⁹⁸

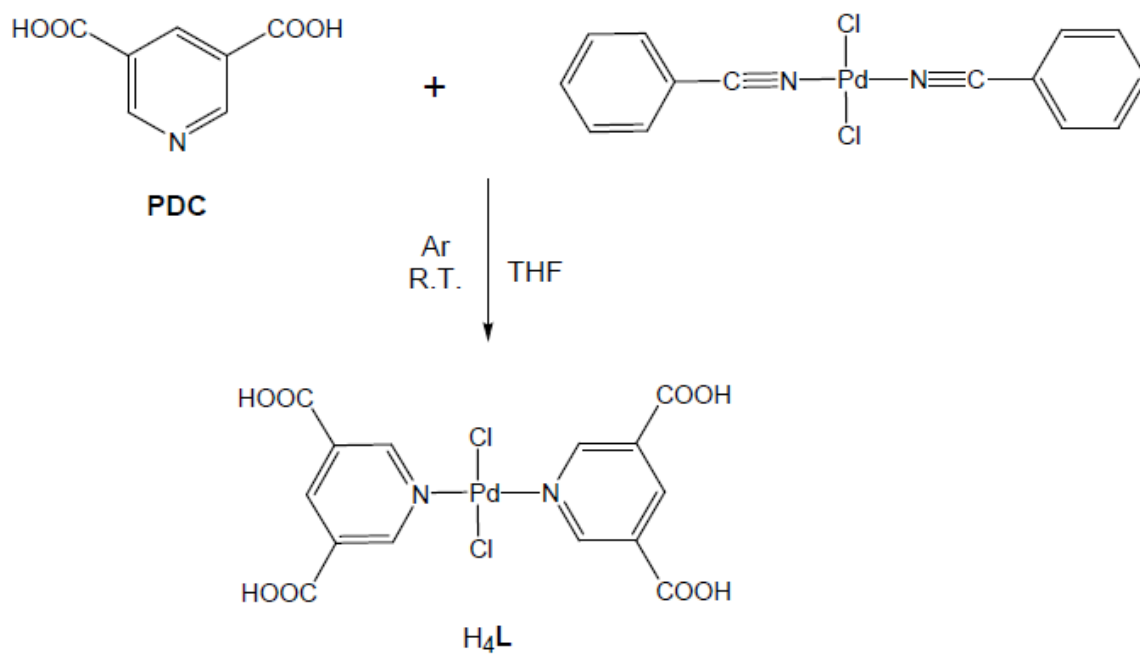


Figure 4.1: Synthetic route for the synthesis of palladated ligand, *trans*-[dichlorido(3,5-dicarboxypyridyl)palladium(II)] (H_4L)

1H NMR of the sample was collected (figure 4.2) and confirms the successful synthesis and purity of the palladated ligand (H_4L).

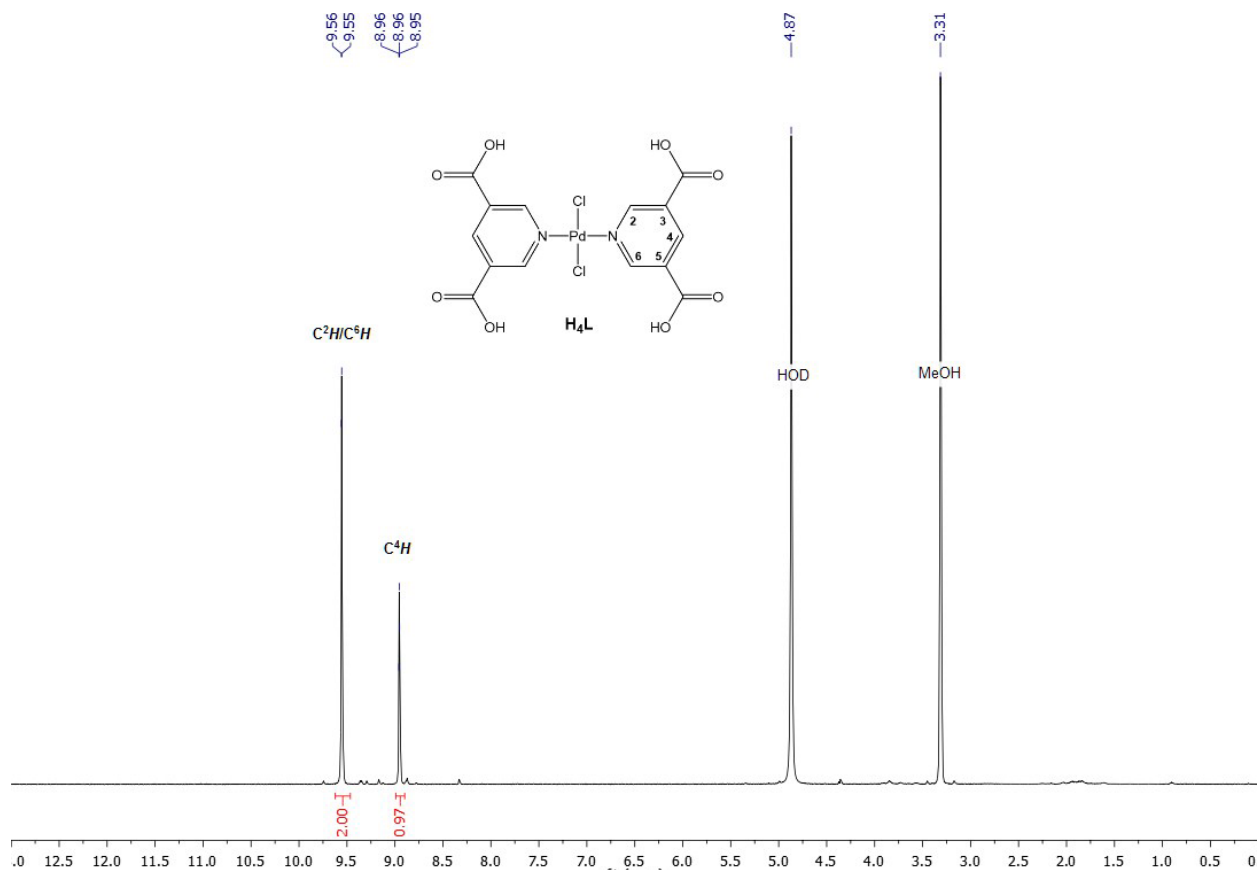


Figure 4.2: ^1H NMR spectrum of H_4L in CD_3OD (500 MHz).

Subsequently, H_4L was used for the synthesis of two new heterobimetallic metal-organic-frameworks according to the experimental procedure briefly described in chapters 4.2 and 4.3.

4.2. Synthesis of Cu-Pd-nbo

A solution of 10 mL dimethylformamide (DMF), 0.025 g (0.049 mmol) of H₄L and 0.025 g (3 equiv., 0.147 mmol) of CuCl₂·2H₂O were placed in a 20 mL glass scintillation vial. The vial was sealed and placed in an isothermal oven at 85 °C for 72 hours. During this period, small light green cubic crystals of [Cu₂L], suitable for single crystal X-ray diffraction analysis (SC-XRD), were deposited. The crystals were washed in fresh DMF (3 × 8 mL) for 1 day and MeOH (4 × 8 mL per day) for 4 days, and vacuum dried (40% yield based on H₄L). SEM images were collected for the newly synthesized material, revealing a broad distribution of crystal sizes as can be seen in figure 4.3.

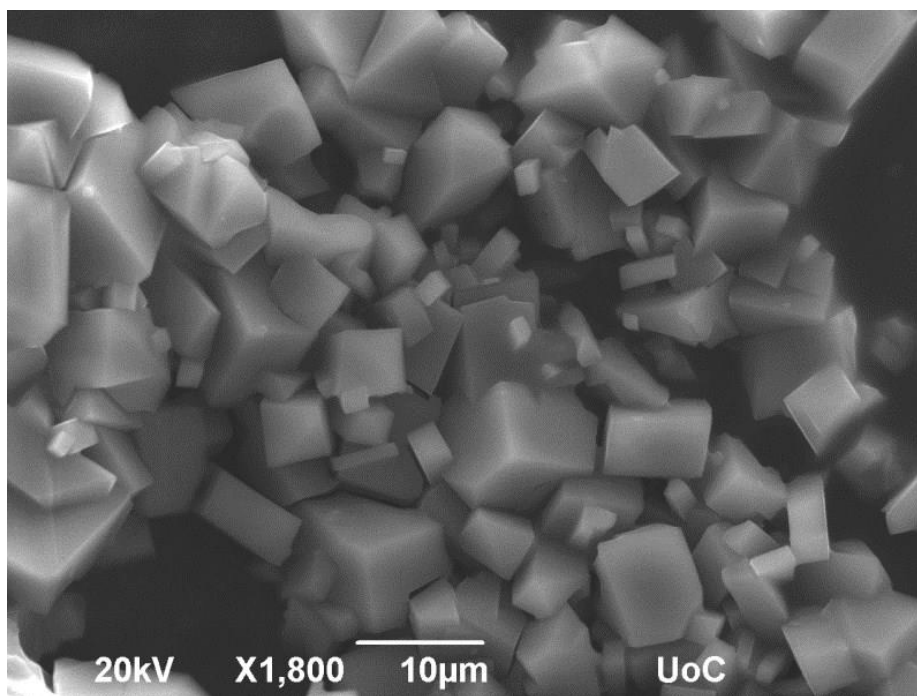


Figure 4.3: A representative SEM image of Cu-Pd-nbo crystals

The InfraRed spectrum of the as made Cu-Pd-nbo is depicted in figure along with the spectrum of the ligand. As can be seen, the peaks in the region above 3000 cm⁻¹ that are assigned to the hydroxyls in the carboxylic acid groups of the ligand have disappeared indicating the formation of the complex via de-protonation of the ligand. Moreover, the strong sharp peak at 1715 cm⁻¹ characteristic of the C=O stretch has been split and shifted to lower wavenumbers (i.e. asymmetric $\nu_{as}(\text{COO}) = 1616$ and 1568 cm⁻¹ and symmetric $\nu_s(\text{COO}) = 1375$ cm⁻¹ carboxylate

stretching vibrations characteristic of coordinated L) suggesting the formation of C-O-Cu bonds that constitute the creation of the Cu²⁺ based paddlewheel SBU.

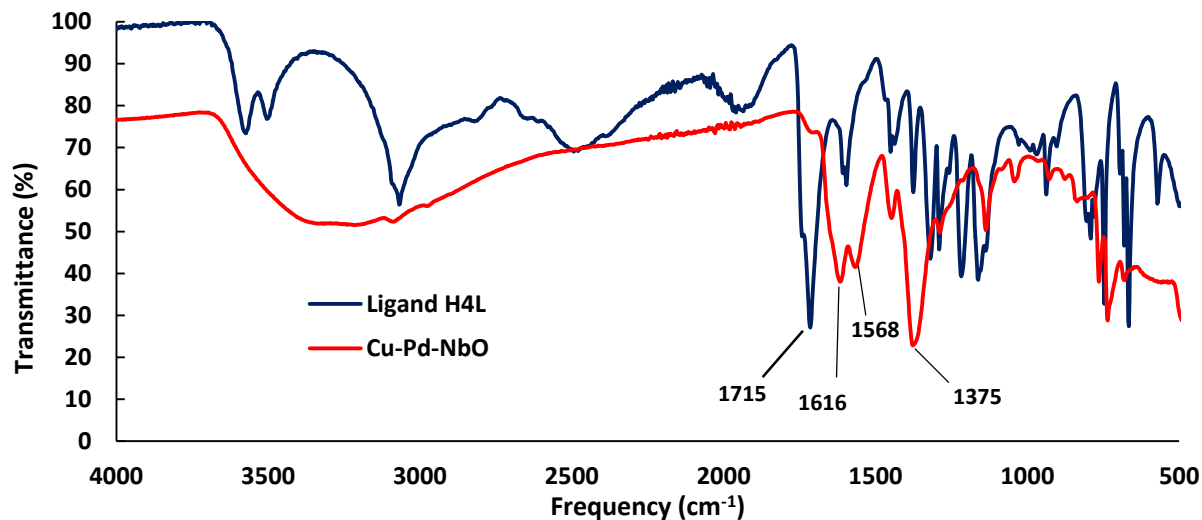


Figure 4.4: ATR-IR spectrum of as-made Cu-Pd-nbo. For comparison, the corresponding spectrum of palladated ligand H₄L is also shown.

Single-crystal X-ray diffraction studies revealed that the framework consists of dimeric paddlewheel units [Cu₂(O₂C-)₄] and L₄- linkers forming a 4,4-connected, non-interpenetrated 3D network with the nbo topology. The structure features two types of cavities, alternating along the c-axis, one made of 12 ligands and 6 paddlewheel units which is illustrated as a yellow sphere in figure 4.5 and the other, made of 6 ligands and 12 paddlewheel units corresponding to the light blue sphere. These cavities are decorated with -PdCl₂- units in which the Cl⁻ anions are found disordered over two positions. Taking into account the van der Waals radii of the atoms, the diameter of these cavities is about 10 Å. The total solvent accessible volume was found to be 64 %, using the PLATON software.⁹⁸

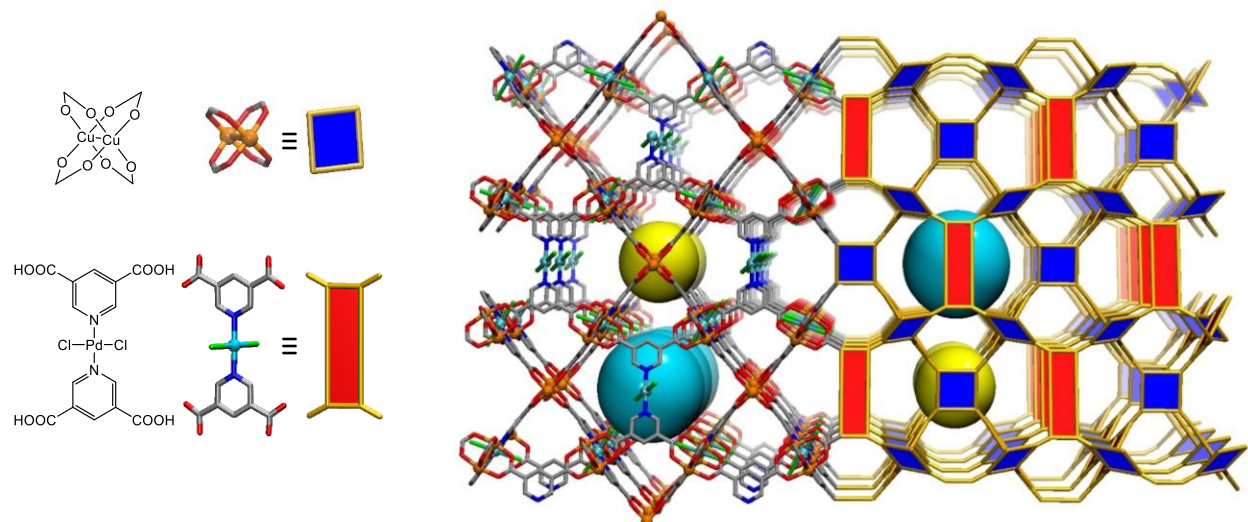


Figure 4.5: Visual representation of the Cu₂-paddlewheel cluster and the palladated organic linker H₄L (left) and X-ray structure of Cu-Pd-nbo (right). [C = gray, N = blue, O = red, Pd = pale blue, Cl = green, Cu = orange; H's have been omitted for clarity].

Phase purity was confirmed by powder X-ray diffraction (PXRD) analysis, and the experimental patterns compared to the calculated from SCXRD data, are illustrated in figure 4.6. Moreover, it was found that even after the activation procedure in which guest molecules are removed from the porous network, the material's structure remains intact, as can be seen in figure 4.6.

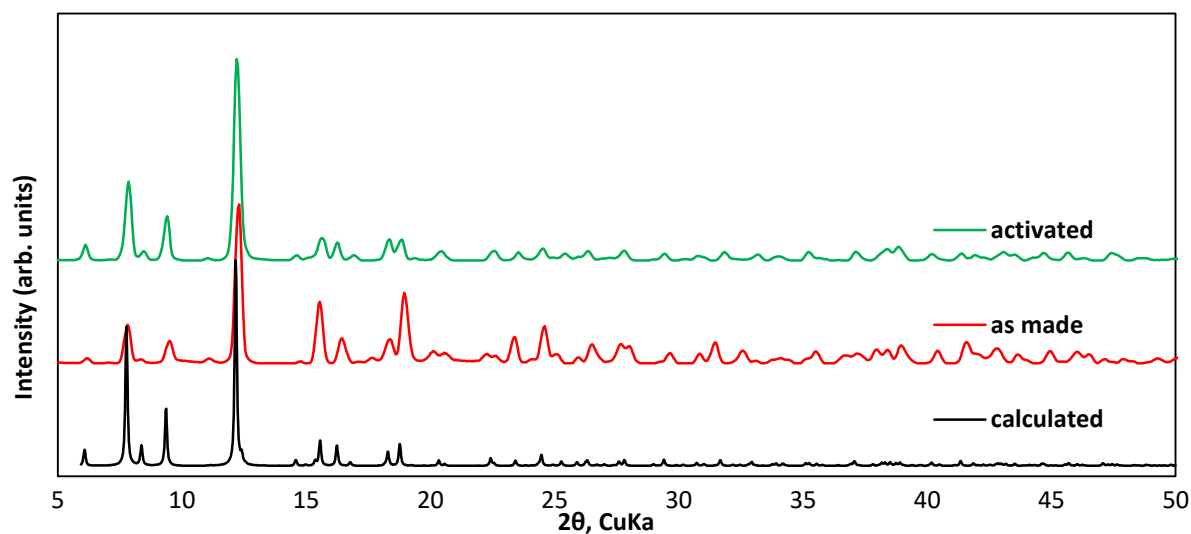


Figure 4.6: Experimental PXRD patterns of the as-made (red) and activated (green) Cu-Pd-nbo. For comparison, the PXRD pattern calculated from the single crystal structure (black) is also shown.

Studying the XRD pattern of the activated sample, an estimation of the average crystallite size (L) was attempted using the Scherrer equation¹¹²:

$$L = \frac{K_{Sch}\lambda}{FWHM \cos\theta} \quad (4.1)$$

where K_{Sch} is a constant related to crystallite shape usually taking the value of 0.94, λ is the X-ray wavelength (1.54178 Å) and FWHM is the width at half maximum height of the diffraction peak centered in 2θ degrees. Analyzing the three high intensity peaks that can be seen from 7 to 14 degrees in figure 4.6, an average crystallite size of 29.8 nm was calculated for Cu-Pd-nbo.

Subsequently, small amounts of crystals were introduced to various solvents and their corresponding XRD patterns were collected in order to evaluate the sample's chemical stability. The results are depicted in figure 4.7 suggesting that the Cu-Pd-nbo is stable in most of the common organic solvents but partially collapses in water and is completely destroyed in chloroform.

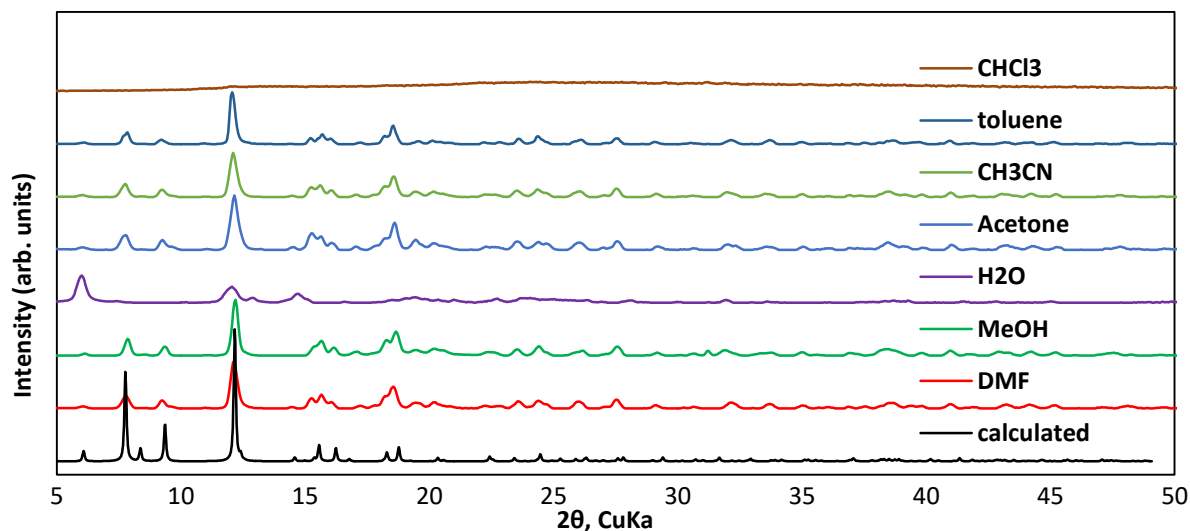


Figure 4.7: Experimental PXRD patterns of Cu-Pd-nbo in various solvents. For comparison, the PXRD pattern calculated from the single crystal structure (black) is also shown.

4.3. Synthesis of In-Pd-soc

A solid mixture of H₄L (112.5 mg, 0.22 mmol) and InCl₃ (116.8 mg, 0.53 mmol) was dissolved in 56 mL of THF/DMF/H₂O (4:3:1) in a round-bottomed flask after vigorous magnetic stirring at room temperature for several minutes. The resulting yellow solution was dispensed evenly into 10 scintillation vials (8 ml size), which were sealed and placed in an isothermal oven at 65 °C for 3 days. During this period, high-quality yellow cubic crystals of the sample, suitable for single-crystal X-ray analysis, were deposited. After cooling the vials to room temperature, the crystals were removed by decanting with mother liquor, samples merged into one batch and washed in fresh DMF (3 × 8 mL per day) for 3 days, MeOH (3 × 8 mL per day) for 1 day, and activated under SC CO₂ resulting to 121 mg of sample and a corresponding yield of 30% based on H₄L. SEM images were collected for the newly synthesized material, revealing a broad distribution of crystal sizes as can be seen in figure 4.8.

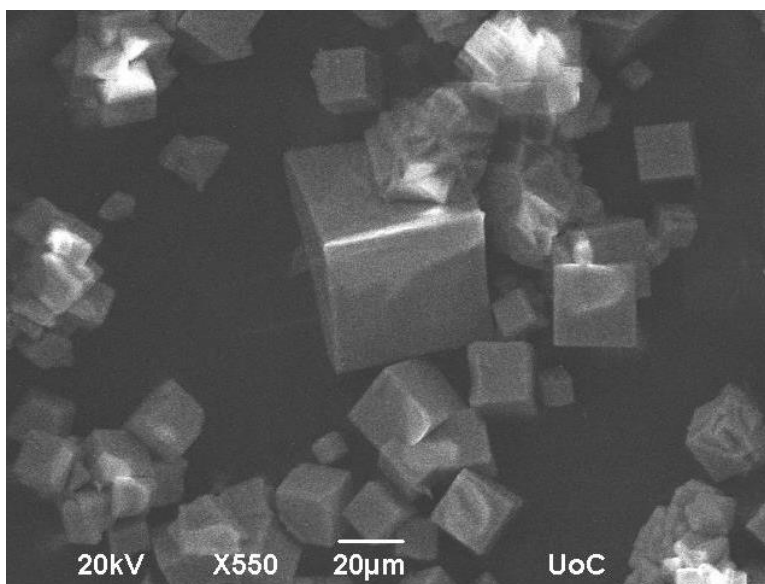


Figure 4.8: Representative SEM image of the crystals of activated In-Pd-soc

The InfraRed spectrum of the as made In-Pd-soc along with the spectrum of the ligand is presented in figure 4.9. As discussed above for the Cu based MOF, the pattern is similar. The peaks in the region above 3000 cm⁻¹ that are assigned to the hydroxyls in the carboxylic acid groups of the ligand have disappeared indicating the formation of the complex via deprotonation of the ligand. Moreover, the strong sharp peak at 1715 cm⁻¹ characteristic of the C=O stretch has been

split and shifted to lower wavenumbers (i.e. asymmetric $\nu_{as}(\text{COO}) = 1618$ and 1570 cm^{-1} and symmetric $\nu_s(\text{COO}) = 1355 \text{ cm}^{-1}$ carboxylate stretching vibrations characteristic of coordinated L) suggesting the formation of C-O-In bonds that represent the creation of the oxo-centered indium carboxylate cluster.

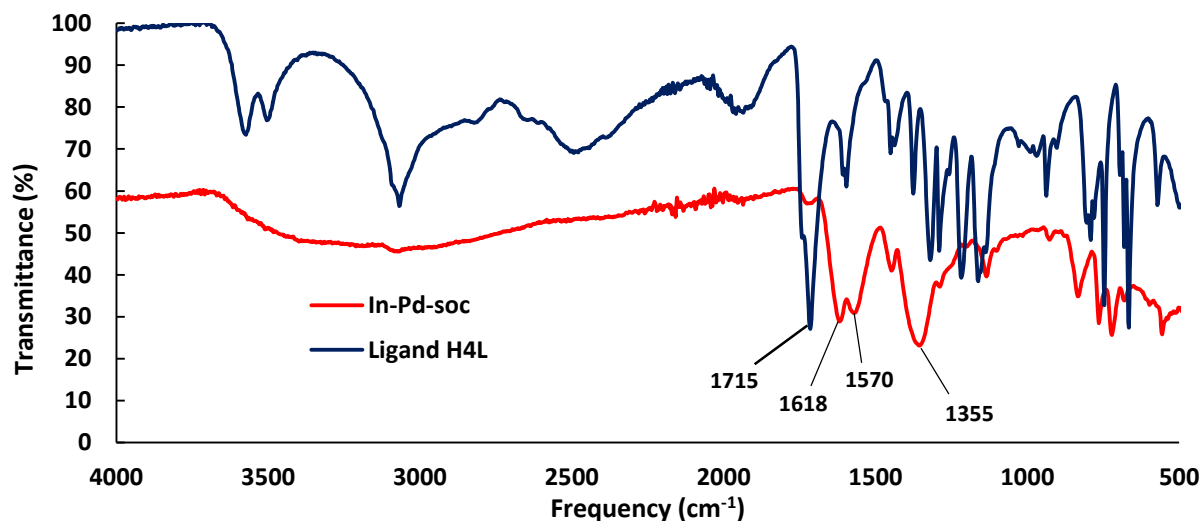


Figure 4.9: ATR-IR spectrum of as-made In-Pd-soc. For comparison, the corresponding spectrum of palladated ligand H₄L is also shown.

SCXRD study reveals that the structure comprises oxo-centered trimeric indium clusters linked by L⁴⁻ linkers, as shown in figure 4.10. The clusters contain three octahedrally coordinated In³⁺ cations sharing one central oxo-anion. In each octahedron, the In³⁺ is coordinated by four different carboxylate groups and one $\mu_3\text{-O}$ atom, while the apical site is occupied by 2/3 of a terminal water molecule and 1/3 of a chloride ion which counter balances the cationic framework. The trimeric clusters are bridged together by six different metalloligands L, resulting in an extended three-dimensional structure. Essentially, six metalloligands L, acting as 4-connected nodes with a rectangular planar geometry as can be seen in figure 4.10, connect the eight corners occupied by In₃O trimers, each of which can be considered as a 6-connected node with a trigonal prismatic geometry. This kind of assembly results in the construction of a connected structure in which the augmented soc net is assigned. This structure comprises of a periodic arrangement of cages with a diameter of 11.2 Å and two infinite intersecting channels with approximate diameter of 4.7 and 5.3 Å, both of which are decorated with PdCl₂ moieties. The cages are accessible only

through small trapezoidal-shaped windows (window dimensions are 7.9 X 4.8 Å). Using PLATON software, the total solvent accessible volume for In-Pd-soc is calculated to be 52%.⁹⁷

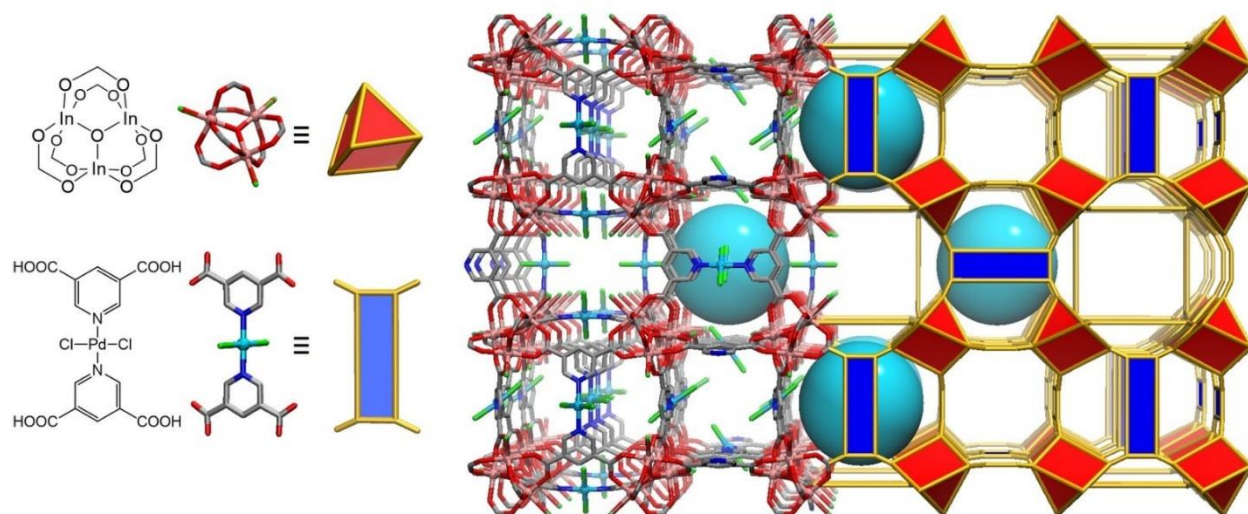


Figure 4.10: Visual representation of the oxo center In₃ cluster and the palladated organic linker H₄L (left) and X-ray structure of In-Pd-soc (right). [C = gray, N = blue, O = red, Pd = pale blue, Cl = green, In = pink; H's have been omitted for clarity].

The high phase purity of the sample was confirmed by the excellent agreement between the experimental PXRD pattern of In-Pd-soc and the calculated PXRD pattern derived from the single crystal structure analysis as can be seen in figure 4.11.

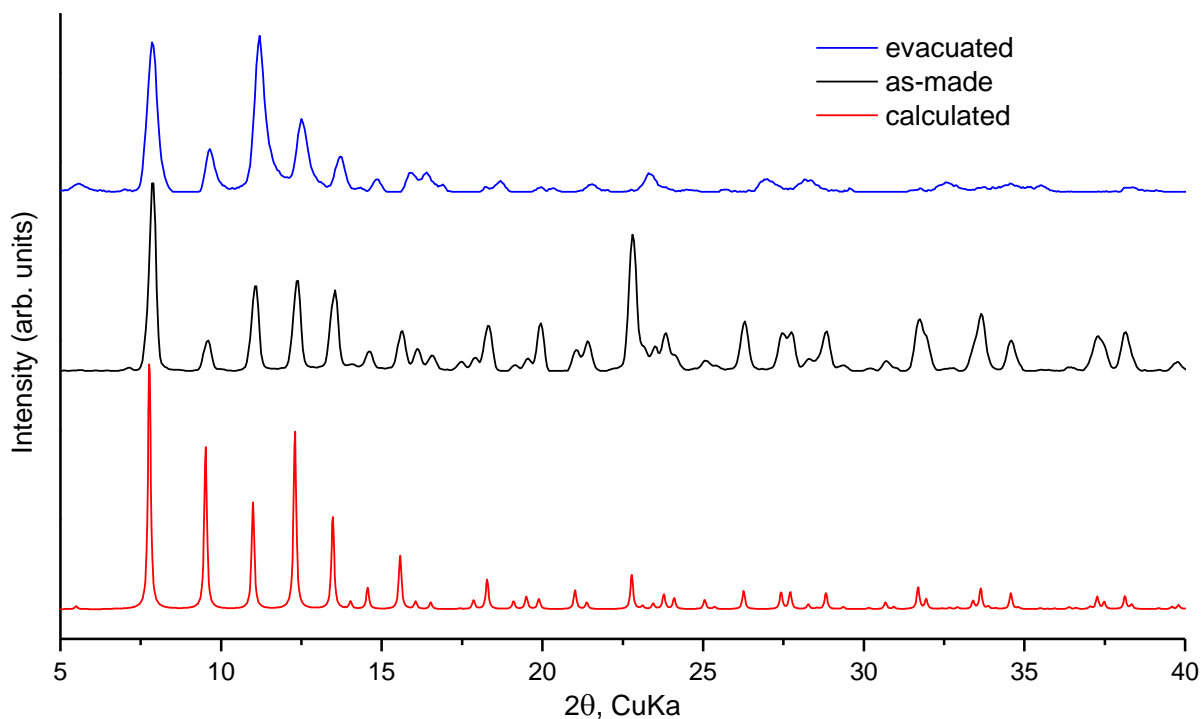


Figure 4.11: Experimental PXRD patterns of the as-made (black) and activated (blue) In-Pd-soc. For comparison, the PXRD pattern calculated from the single crystal structure (red) is also shown.

Moreover, it was verified that upon activation, the crystal structure of the material remains undamaged. Using equation 4.1 for the first 5 high intensity PXRD peaks of the activated In-Pd-soc, the average crystallite size was found to be 23.1 nm, slightly smaller than that of Cu-Pd-nbo.

Subsequently, the chemical stability of the material was investigated by immersing small amounts of crystals in various commonly used solvents. The corresponding XRD patterns are depicted in figure 4.12. In-Pd-soc appears to be stable in acetone, methanol and DMF. However, it seems to be completely destroyed in chloroform. Interestingly, when introduced to water the sample suffers a structural transformation although it maintains part of its crystallinity.

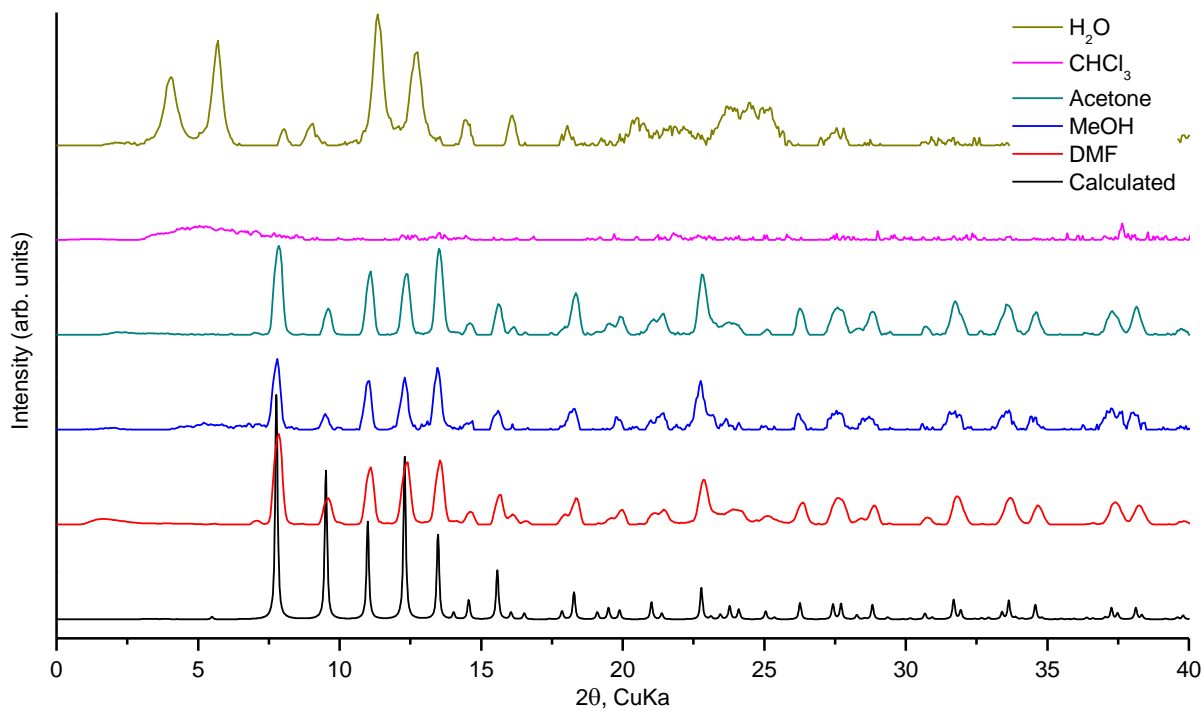


Figure 4.12: Experimental PXR patterns of In-Pd-soc in various solvents. For comparison, the PXR pattern calculated from the single crystal structure (black) is also shown.

4.4. Thermogravimetric analysis of Cu-Pd-nbo

In order to investigate the material's thermal stability, TGA/DSC experiments were performed up to 800 °C with a moderate heating rate of 5 °C/min under continuous argon flow of 20 ml/min.

Inside an argon MBraun glove box, approximately 8 mg of as made Cu-Pd-nbo were placed in a pre-weighed alumina crucible. Prior to the analysis, the furnace was purged with argon so that the exposure time of the sample in atmospheric air would be minimized. Along with the TGA/DSC curves, the 1st derivative gravimetric curve (DTG) was also produced; both are illustrated in figure 4.13. In order to determine the thermal stability limits T_{onset} and T'_{onset} values were calculated respectively and are presented in table 4.1. T'_{onset} values, result from the DTG curves and are considered to be a safer choice than the T_{onset} values which generally overestimate the thermal decomposition temperatures, since they are affected by the experimental parameters such as heating rate etc.^{113,114}

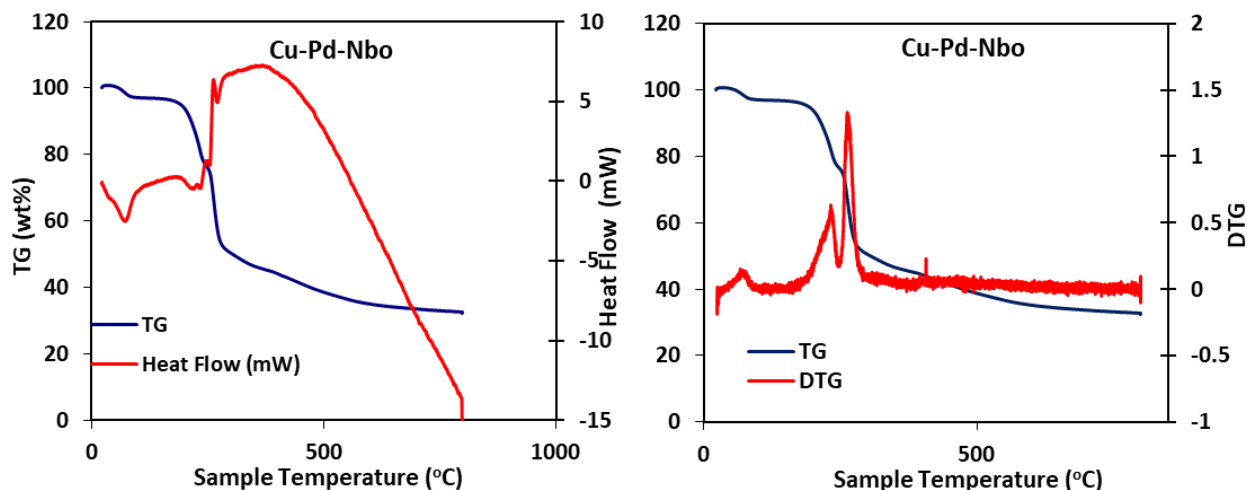


Figure. 4.13: TGA/DSC/DTG plots of as made Cu-Pd-nbo. (a) Change of weight percent with temperature and heat flow curves (b) change of derivative weight percent with temperature.

The sample exhibits thermal stability up to approximately 180 °C. Three weight loss steps, evident in the DTG curve, can be observed for as made Cu-Pd-nbo. Firstly, the solvent molecules

and other impurities occupying the porous structure of the MOF were removed up to 100 °C, as can be concluded by the characteristic endothermic DSC peak. After the solvent removal, a stable plateau was observed up to 180 °C. Further temperature increase results to the main two-step weight loss due to degradation of the organic linkers as can be seen by the broad exothermic DSC peaks, leading to the complete collapse of the porous framework. The remaining residue was metallic Cu and Pd powder.

Table 4.1: TGA/DTG Tonset and T'onset values for Cu-Pd-nbo

	T_{onset} (°C)	T'_{onset} (°C)
Cu-Pd-nbo	205	180

4.5. Thermogravimetric analysis of In-Pd-soc

TGA/DSC experiments were performed for In-Pd-soc according to the experimental procedure described above for Cu-Pd-nbo and the results are illustrated in figure 4.14. The first main weight loss that is complete before 210 °C, occurs due to evaporation of guest solvent molecules and other impurities from the porous structure of the material, evident for the broad endothermic peak on the heat flow curve. Almost immediately, a second main step is observed corresponding to structural breakdown as the palladated ligand decomposes. T_{onset} and T'_{onset} values were calculated to be 230 and 215 °C suggesting enhanced thermal stability compared to Cu-Pd-nbo. The remaining residue is considered to be metallic In and Pd powder.

Table 4.2: TGA/DTG T_{onset} and T'_{onset} values for In-Pd-soc

	T_{onset} (°C)	T'_{onset} (°C)
In-Pd-soc	230	215

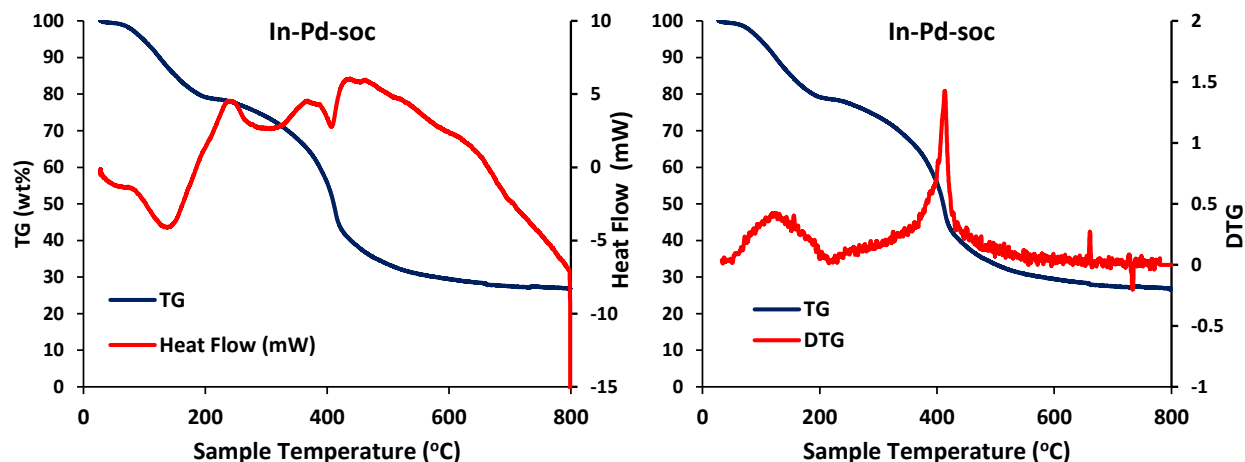


Figure. 4.14: TGA/DSC/DTG plots of as made In-Pd-soc. (a) Change of weight % as a function of temperature and heat flow curves (b) change of derivative weight % as a function of temperature.

4.6. Nitrogen/Argon adsorption isotherms for Cu-Pd-nbo

Argon and nitrogen isotherms were performed at 87 and 77K respectively, in order to evaluate the porous properties of the sample. Successful activation of Cu-Pd-nbo was easily achieved in two straightforward steps. Firstly, MeOH was used to exchange the DMF molecules occupying the porous framework during the synthetic procedure. The sample was soaked in methanol over a period of 4 days, replenishing the methanol 4 times a day. Subsequently, methanol was removed by drying under dynamic vacuum ($< 10^{-6}$ mbar) for 12 hours and heating at 50 °C. The successful activation of the sample can also be visually confirmed by a characteristic color change from green (as-synthesized) to deep blue-violet (activated), as can be clearly seen in figure 4.15.

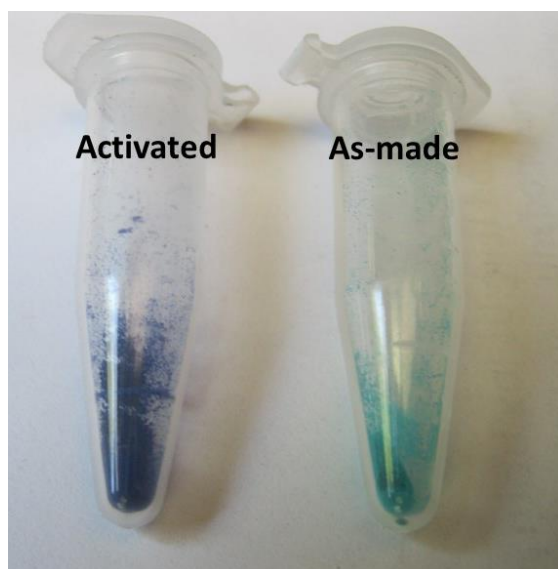


Figure 4.15: Color change before and after activation at 50°C under vacuum for Cu-Pd-nbo

Argon and nitrogen adsorption isotherms confirmed the permanent porosity of Cu-Pd-nbo by showing a fully reversible type-I isotherm, characteristic for predominantly microporous materials, as can be seen in figure 4.16. The BET area for nitrogen and argon, calculated with respect to the BET consistency criteria as described in section 3.1.4.3, was found to be $1473 \text{ m}^2 \text{ g}^{-1}$ and $1415 \text{ m}^2 \text{ g}^{-1}$, respectively (figure 4.17). The subtle difference between the values is attributed to nitrogen's quadrupole moment which results in enhanced electrostatic interactions with highly polar surfaces, such as Cu-Pd-nbo. This is evident by the sharp rise on nitrogen uptake at very low relative pressure ($< 1 \times 10^{-6}$) compared to argon. On the other hand, argon's lack of quadrupole

moment makes it the preferable adsorbate for more accurate calculations especially in the case of microporous materials with increased surface electron density. The total pore volume, calculated from the Ar adsorption isotherm at $0.995 P/P^0$ is $0.53 \text{ cm}^3/\text{g}$, very close to the crystallographic value of $0.65 \text{ cm}^3/\text{g}$, confirming that the structure remains intact after activation.

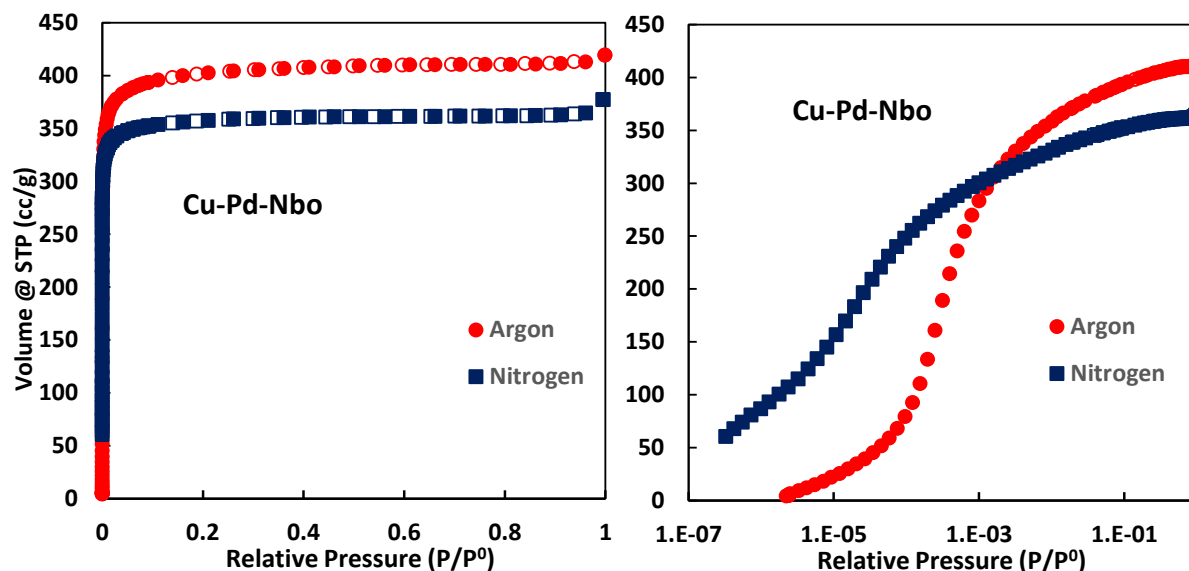


Figure 4.16: Argon and nitrogen adsorption isotherms at 87 and 77K, respectively for Cu-Pd-nbo. The measurements are plotted on logarithmic scale (right) in order to reveal the material's low-pressure behavior

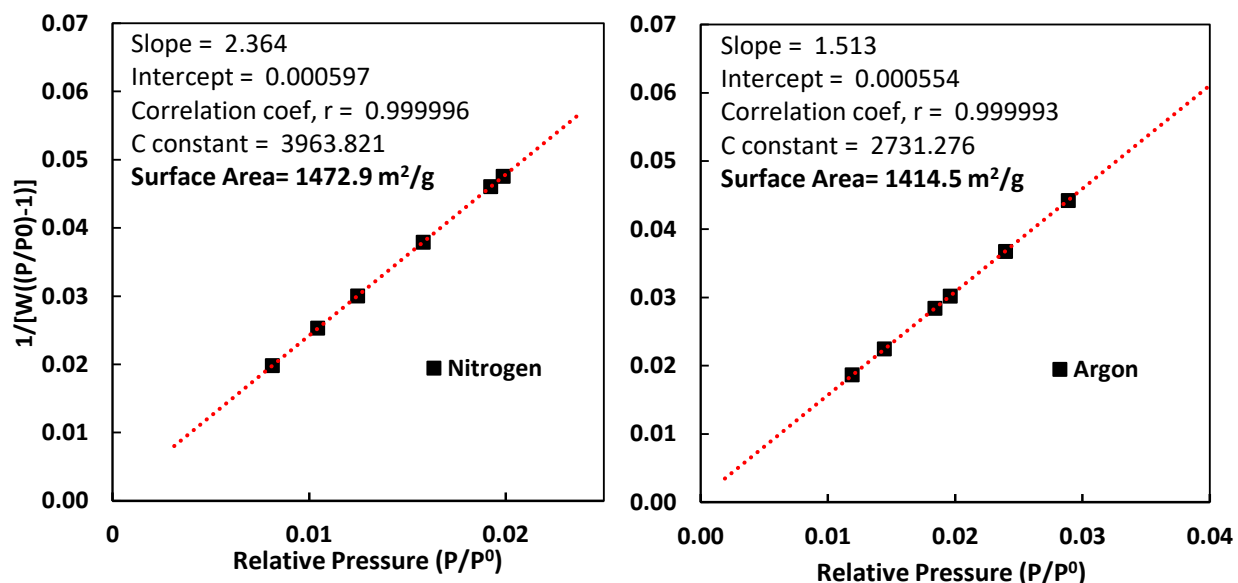


Figure 4.17: BET plot for Cu-Pd-nbo calculated from the nitrogen isotherm (left) at 77K and argon (right) at 87K

The pore size distribution was obtained using Non-Local Density Functional Theory (NLDFT) by applying an argon equilibrium NLDFT kernel at 87K for spherical/cylindrical pores. As can be seen in figure 4.18, the calculation results on a major peak centered at 9.5 Å, in full agreement with the crystallographic analysis. The validity of the calculation is confirmed by the successful fitting of the measured argon adsorption isotherm.

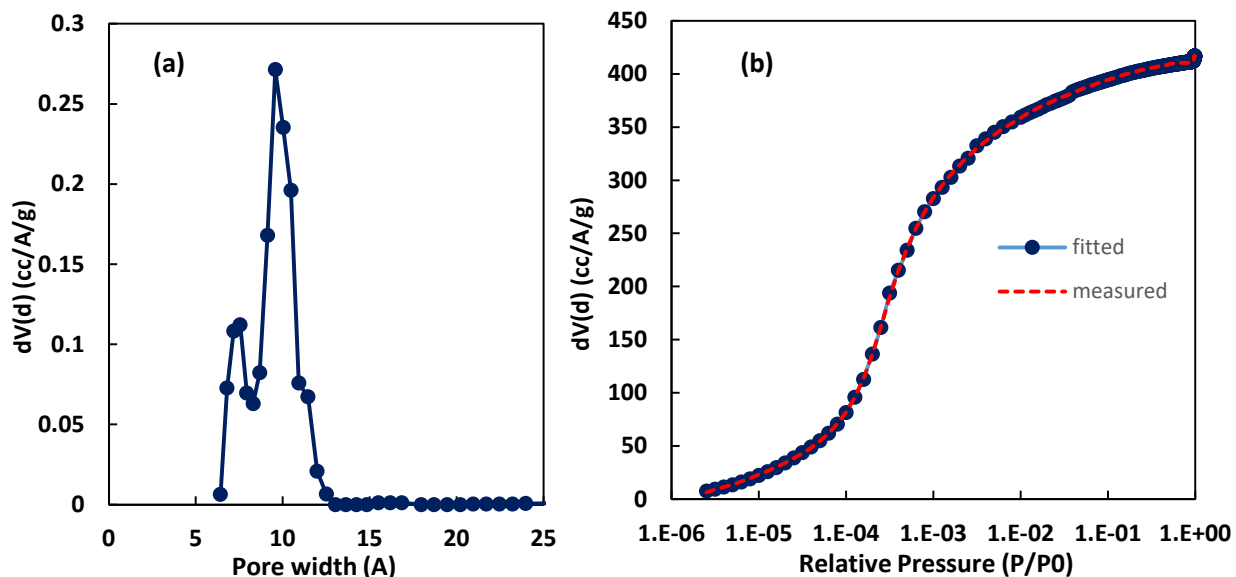


Figure 4.18: Pore size distribution (a) derived from the argon adsorption isotherm at 87K for Cu-Pd-nbo and the corresponding NLDFT fitting (b).

4.7. Low pressure single component isotherms for Cu-Pd-nbo

Following the structural characterization, the adsorption properties of the material were evaluated. The relatively large gravimetric surface area, due to the sample's microporosity, in combination with the presence of unsaturated Cu^{2+} sites and the square planar Pd^{2+} cations, constitute Cu-Pd-nbo a very promising material for selective CO_2 capture from various gas mixtures. As already mentioned, this dissertation focuses on the challenging separation of CO_2 from N_2 and/or CH_4 mixtures, as well as CH_4 storage, which are key topics in environmental/energy research. In a process like that, one of the main parameters that determine

the material's performance is the adsorbed amount that can be retained in specific pressure / temperature conditions. This property is determined through the adsorption isotherm. Accordingly, using the volumetric method, CO₂, N₂ and CH₄ sorption measurements were performed at different temperatures up to 1 bar, from which important properties including uptake, isosteric heats of adsorption (Q_{st}) and Ideal Adsorption Solution Theories (IAST) selectivities, were extracted. Low pressure, compared to high pressure isotherms, provide better resolution through many equilibrium points that are measured at sub-atmospheric pressure. Therefore, useful insight on the adsorbent-adsorbate interaction at very low loadings can be obtained.

Initially, CO₂ adsorption properties were evaluated for Cu-Pd-nbo by performing a series of isotherms from 195 to 293 K and pressure up to 1 bar, as illustrated in figure 4.19.

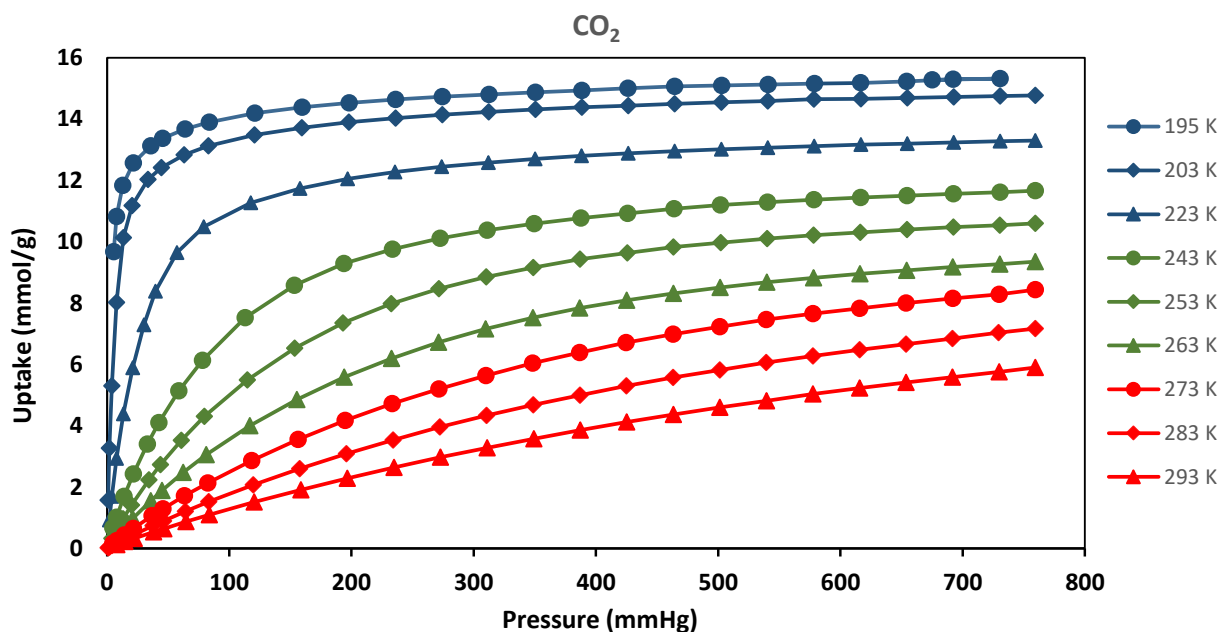


Figure 4.19: Excess CO₂ adsorption isotherms for Cu-Pd-nbo up to 1 bar at various temperatures

Cu-Pd-nbo performed exceptionally in terms of CO₂ uptake since it adsorbs 8.5 mmol/g (190.1 cm³/g, 373.5 mg/g) at 1 bar and 273K, a value which ranks it among the highest in the entire family of MOFs. In terms of volumetric uptake, which was calculated using the material's crystallographic density, Cu-Pd-nbo showed the highest value reported for the entire Cu-based nbo family of MOFs (186.2 cm³ STP/cm³). This can be attributed to the high density of relatively

strong CO₂ interacting sites (Cu²⁺ and Pd²⁺) within the microporous structure in combination with the material's high crystallographic density (0.98 g/cm³). At 293K, the material exhibits an almost linear increase in uptake as pressure rises suggesting that the strong adsorption sites are not yet saturated at these pressure/temperature conditions. As the temperature of the experiment is decreased the isotherm's shape gradually changes to a Langmuir type, displaying a sharp uptake rise at low pressure. At the same time, the adsorbed CO₂ quantity is increased as expected. At 195K, a clear saturation plateau is observed at 15.0 mmol/g. All the isotherms are completely reversible highlighting that sorption is purely physical and further indicating the absence of steric or kinetic hindrance even at low temperature.

In order to further assess the CO₂-surface interaction the isosteric heat of adsorption Q_{st} was calculated as a function of surface coverage. CO₂ adsorption isotherms at 0, 10 and 20 °C were fitted using the virial equation as described in section 3.2.4 and the results are depicted in figure 4.20.

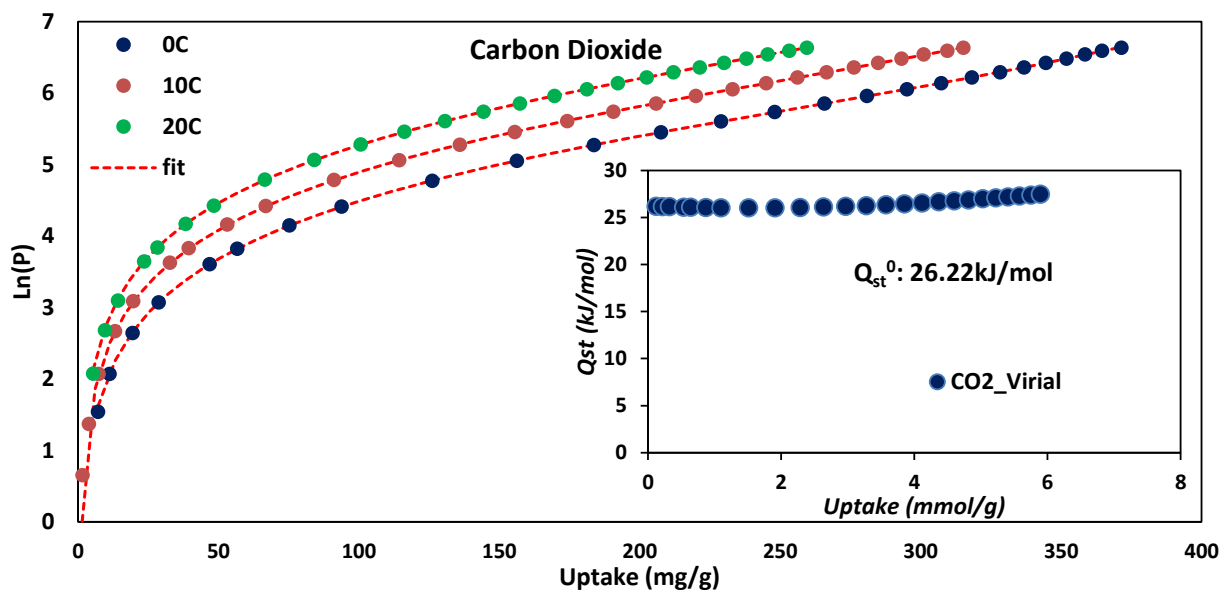


Figure 4.20: Virial type fitting of CO₂ adsorption isotherms for Cu-Pd-nbo at 0, 10 and 20 °C and the corresponding isosteric heat of adsorption as a function of CO₂ uptake (inset)

Zero coverage isosteric heat of adsorption Q_{st0} was calculated to be 26.2 kJ/mol which is lower than that of other high performance nbo-type MOFs whose values fluctuate around 30 kJ/mol. Considering the shape of the isotherms at the aforementioned temperatures which exhibit a slow but steady increase on CO_2 uptake, a synergistic effect of the open metal sites – adsorbate interactions and confinement in the material’s microporous network is suggested. Q_{st} slightly increases as the pressure reaches 1 bar, indicative of inhomogeneity of the adsorbed phase, probably due to adsorbate intermolecular forces as the active adsorption sites become gradually populated by CO_2 molecules. These results are consistent with quantum chemistry calculations which were executed and revealed a relatively strong Lewis base Pd^{2+} - CO_2 interaction, calculated to be 24.3 kJ/mol in addition to the expected Lewis acid Cu^{2+} - CO_2 interaction (30.3 kJ/mol).⁹⁸

Subsequently, CH_4 and N_2 adsorption isotherms were performed following the same experimental procedure. CH_4 adsorption isotherms up to 1 bar were measured for Cu-Pd-nbo at temperatures varying from 112 to 273 K as depicted in figure 4.21.

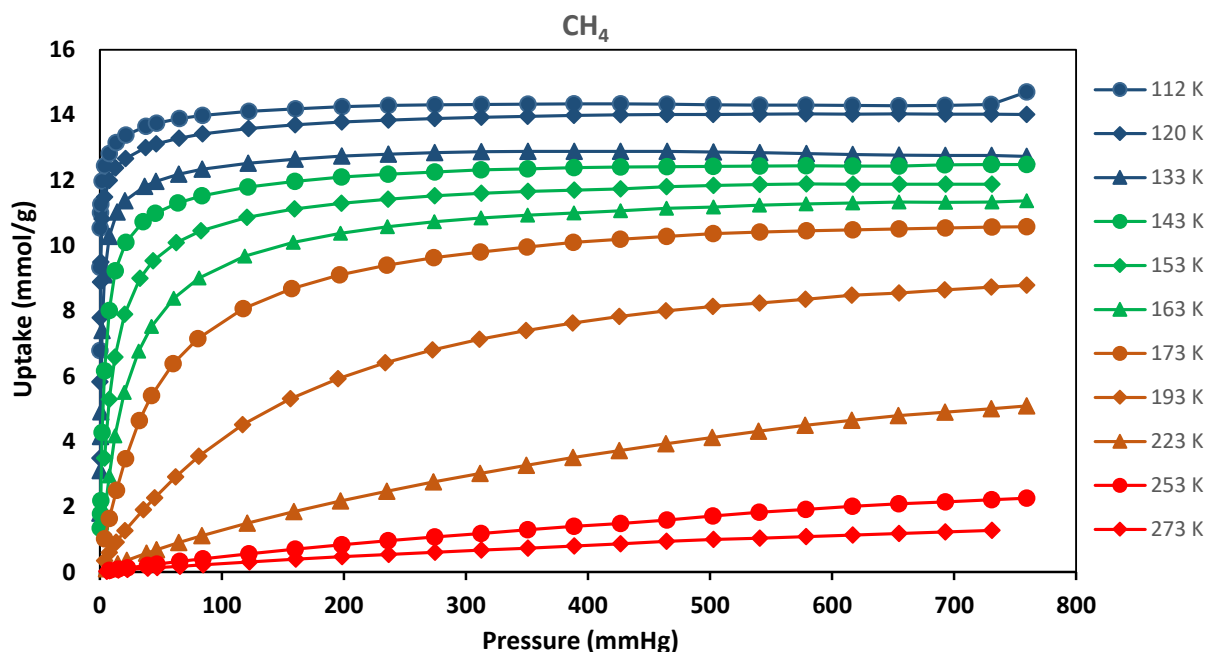


Figure 4.21: CH_4 adsorption isotherms for Cu-Pd-nbo up to 1 bar at various temperatures

The shape of the CH_4 adsorption isotherms follow the trend observed for CO_2 . However, the CH_4 – surface interactions are weaker compared to CO_2 since Cu-Pd-nbo adsorbs 1.3 mmol/g

(28.4 cm³/g, 20.3 mg/g, 27.3 cm³STP/ cm³) at 1 bar and 273K. The CH₄ adsorption isotherm recorded at its boiling point (112K), showed a fully reversible type-I isotherm with a saturation plateau at 14.32 mmol/g (320.7 cm³/g). Using CH₄ as the probe molecule, the material's total pore volume was calculated to be 0.54 cm³/g at P/P^0 : 0.96, which is in excellent agreement with the value calculated from the Ar adsorption isotherm. This verifies that the porous network is fully accessible to the methane molecules. Accordingly, the isosteric heat of adsorption was calculated and the results are illustrated in figure 4.22. Due to the low quantity adsorbed at low pressure and ambient temperature, isotherms at 273, 253 and 223K were selected for the calculation using the same procedure described above.

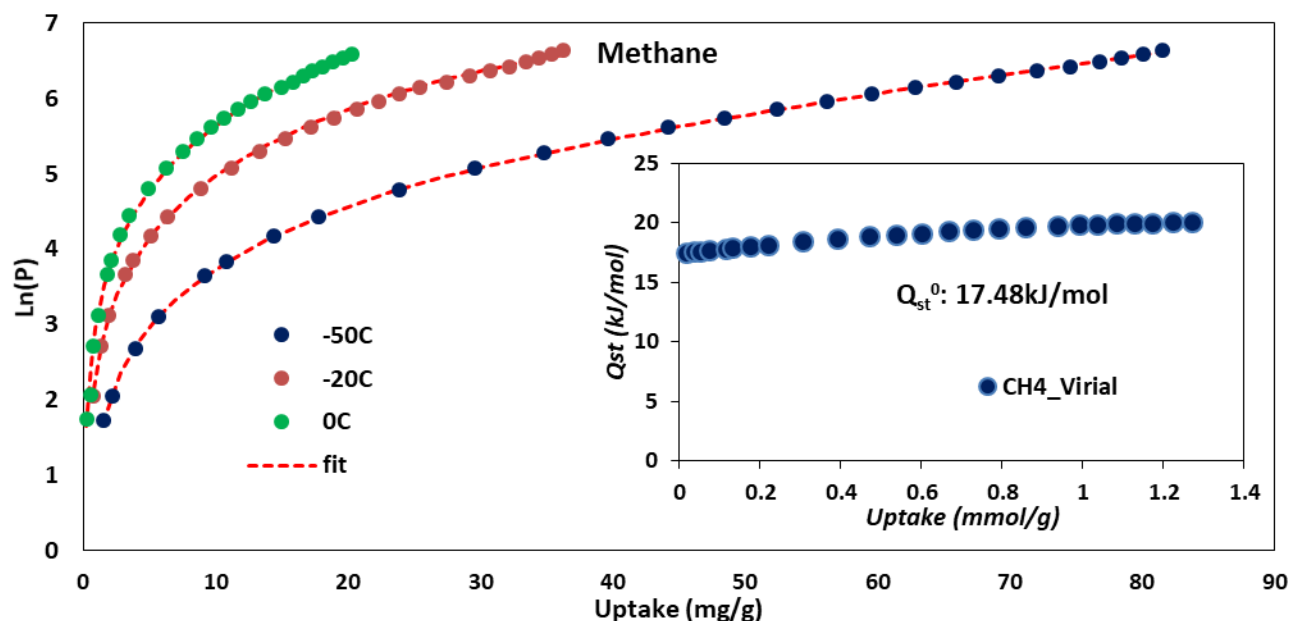


Figure 4.22: Virial type fitting of CH₄ adsorption isotherms for Cu-Pd-nbo at 0, -20 and -50 °C and the corresponding isosteric heat of adsorption as a function of CH₄ uptake (inset)

As expected, the CH₄ isosteric heat of adsorption for zero coverage yielded 17.48 kJ/mol compared to 26.22 kJ/mol for CO₂. The difference on the affinity for the material's surface between them can be explained by the reduced polarizability that the CH₄ molecule exhibits. Q_{st} slightly increases as a function of the adsorbed quantity but never exceeds 20 kJ/mol, a rather modest value compared to the ones reported in literature for methane storage⁵⁵. Based on the

difference in affinity for the surface between CO₂ and CH₄, Cu-Pd-nbo poses as a potentially successful candidate for CO₂/CH₄ separation applications through selective physical adsorption.

Furthermore, in order to investigate the material's ability on another important application, CO₂/N₂ separation, nitrogen adsorption isotherms were measured and the results are depicted in figure 4.23.

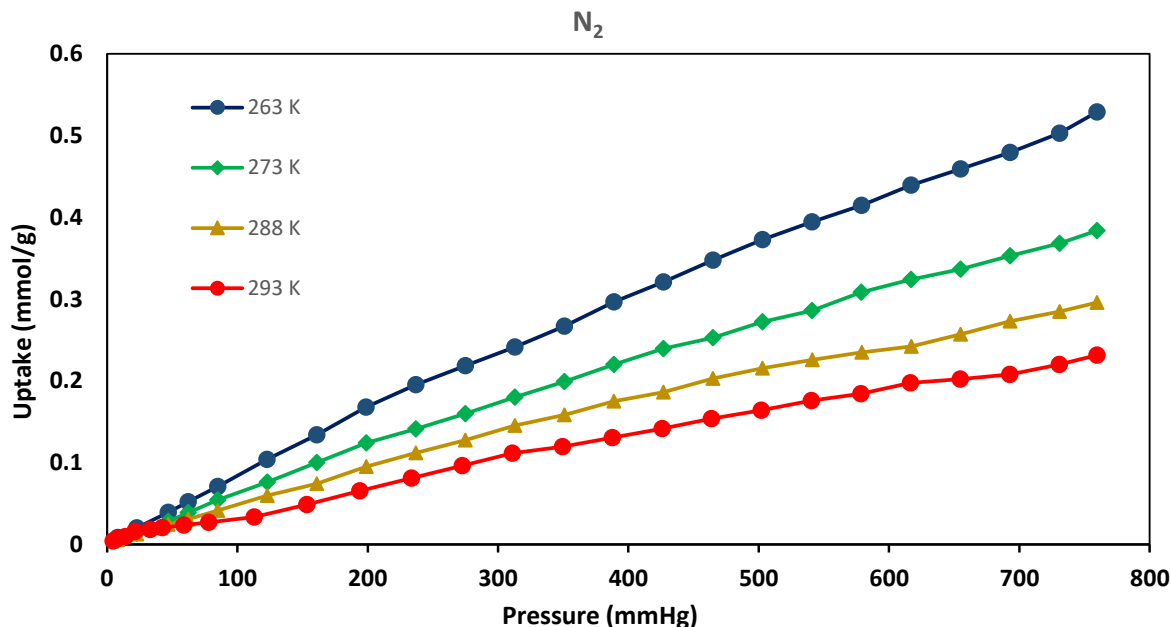


Figure 4.23: N₂ adsorption isotherms for Cu-Pd-nbo up to 1 bar at various temperatures

Nitrogen exhibits even lower affinity for the material's surface. Cu-Pd-nbo adsorbs 0.4 mmol/g (8.6 cm³/g, 5.4 mg/g, 8.3 cm³STP/cm³) at 1 bar and 0 °C. Accordingly, Q_{st0} was calculated to be 12.12 kJ/mol. Nitrogen isosteric heat of adsorption increases as the surface coverage is increased due to interactions between the adsorbed molecules but does not exceed 20 kJ/mol at 1 bar

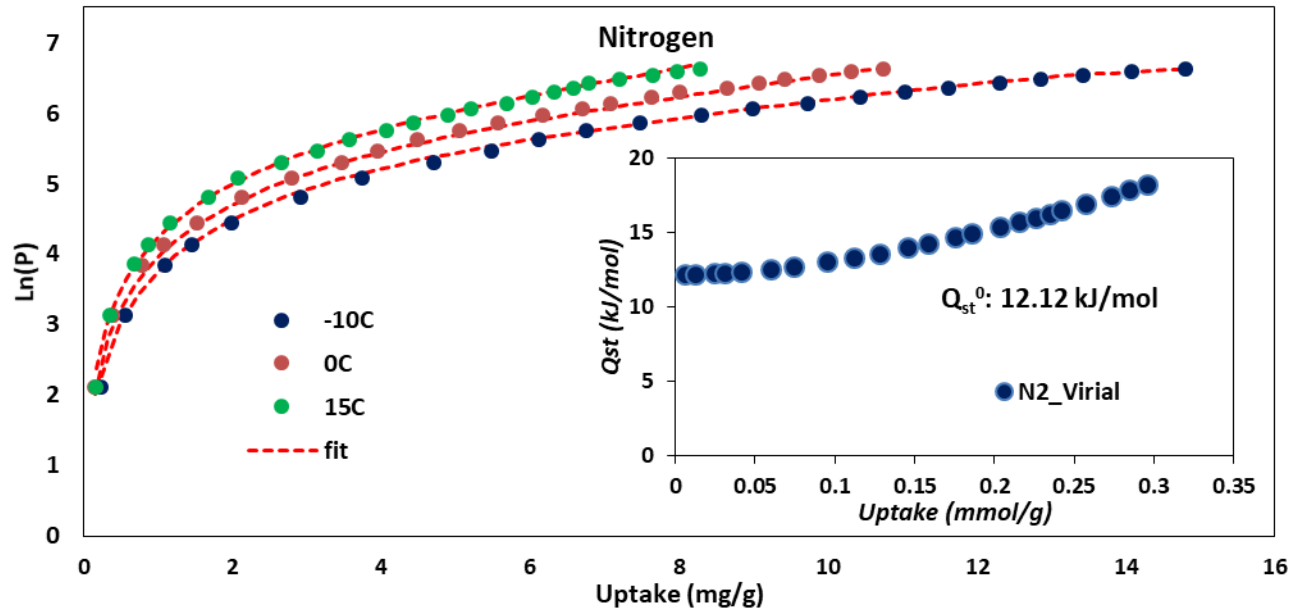


Figure 4.24: Virial type fitting of N_2 adsorption isotherms for Cu-Pd-nbo at -10 , 0 and 15°C and the corresponding isosteric heat of adsorption as a function of N_2 uptake (inset)

The values derived for the virial coefficients by successful fitting of the isotherms for the three gases as already described, are listed in table below.

Table 4.3: Virial coefficient values for CO_2 , CH_4 and N_2 .

	Virial equation					
	CO_2	error	CH_4	error	N_2	error
a₀	-3153.76203	66.01668	-2102.93687	48.88889	-1457.60821	152.6165
a₁	0.72469	1.1309	-25.99942	7.15937	-10.04834	76.45992
a₂	-0.00523	0.00384	0.48842	0.22287	-12.86891	8.78845
a₃	-1.84E-06	5.64E-06	1.46E-03	1.46E-03	5.64E-01	2.83E-01
a₄	9.90E-09	7.89E-09	-6.67E-06	8.80E-06	-1.81E-02	9.61E-03
b₀	11.19426	0.23305	10.65952	0.18804	9.21948	0.55139
b₁	-0.00008	0.00401	0.14101	0.02622	0.13342	0.27015
b₂	0.00002	0.00001	-0.00268	0.0007	0.02697	0.02818

In order to gain a first estimation on the gas separation properties of the material the Ideal Adsorption Solution Theory (IAST) was applied to the CO₂, CH₄ and N₂ adsorption isotherms. IAST was developed by Myers and Prausnitz¹¹⁵ in 1965 with the aim to provide gas mixture equilibrium data derived from individual single component isotherms. Considering the gas phase as an ideal gas mixture and the adsorbed phase as an ideal solution whose components exhibit activity coefficients equal to unity, IAST has been a powerful tool for researchers for obtaining mixture isotherm adsorption properties on a relatively accurate and less time-consuming way than performing actual gas mixture experiments. Although the ideality assumptions have been proved to lead to inaccurate results occasionally, careful choice of an appropriate adsorption model and successful fitting to the experimental adsorption data can produce qualitatively reliable results which can be used as a fingerprint for the material's properties. However, the solution of a system of non-linear equations is required in order to obtain the final results which can be a tedious process. For this reason, the IAST⁺⁺ GUI software¹¹⁶ was used and the final results are depicted below.

Initially, the CO₂/CH₄ separation ability of the material was investigated at 0 °C and low loadings. The respective single component isotherms can be seen on the left of figure 4.25. The red dotted lines correspond to the fitted data according to the selected adsorption model. For both isotherms the best fit was achieved when the Dual-Site Langmuir-Freundlich (DSLFF) model was adopted.

$$m(P) = q_1 \frac{(k_1 P)^{n_1}}{1+(k_1 P)^{n_1}} + q_2 \frac{(k_2 P)^{n_2}}{1+(k_2 P)^{n_2}} \quad (4.2)$$

where $m(P)$ is the experimentally determined amount adsorbed as a function of pressure P , q_1 and q_2 are the adsorbed amounts at saturation for the two different adsorption sites 1 and 2, k_1 , k_2 are the adsorption constants and n_1 , n_2 the coefficients accounting for heterogeneity for the respective sites.

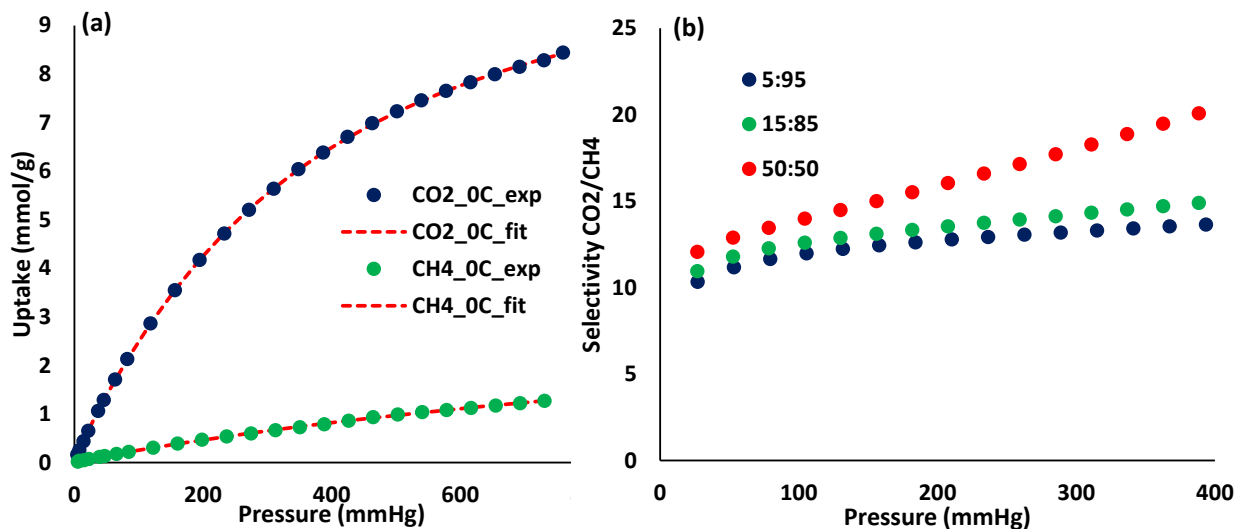


Figure 4.25: Cu-Pd-nbo excess adsorption isotherms for CO₂ and CH₄ at 0 °C and the corresponding DSLF fitted curves(a), IAST selectivities for three different CO₂:CH₄ mixture ratios (b)

For CO₂, which is evidently the most strongly adsorbed species of the mixture, the relation with the two sites of DSLF reflects the interaction of the adsorbate with the unsaturated Cu²⁺ centers found in the paddlewheel cluster and the π -orbitals of the planar Pd coordinated on the organic linkers, in agreement with the theoretical studies performed.⁹⁸ For CH₄ however, there is no solid evidence that two distinct interaction sites occur. Indeed, it can be seen from the fitted parameters (Table 4.4.) that the second component of the dual model is rather insignificant since q_2 is practically negligible (around 0.25% of q_1).

Subsequently, the binary adsorption isotherms were determined by IAST++ for three different mixture CO₂:CH₄ ratios at 0 °C and the corresponding selectivity S , as a function of pressure was calculated according to equation expressed below.

$$S_{1,2} = \frac{x_1/y_1}{x_2/y_2} \quad (4.3)$$

where x is the molar fraction of each of the components in the adsorbed phase and y the molar fraction of each component in the gas phase.

As can be seen in figure 4.25b, the material is predicted to exhibit significant selectivity for all the mixtures studied. However, a clear enhancement is observed at 50:50 ratio which

becomes more pronounced as the pressure rises. This behavior is probably attributed to the gradual saturation of CO₂ strong adsorbing sites with increasing loading. Essentially IAST confirms the picture that was already revealed by the shape (lack of steepness) of the isotherms and the moderate Q_{st0} value obtained for CO₂ in contrast to the exceptionally high uptake obtained at 1 bar.

Subsequently, the same procedure described above was employed for CO₂/N₂ mixtures at 0 °C and pressure up to 1 bar. The best fit to the N₂ experimental adsorption isotherm was achieved using the Langmuir model as follows:

$$m(P) = q \frac{kP}{1+kP} \quad (4.4)$$

Accordingly, the CO₂ over N₂ selectivity obtained at 0 °C as a function of pressure reveals an identical behavior to the CO₂/CH₄ mixtures. As can be seen in figure 4.26a, the difference in uptake is even larger since N₂ exhibits very low affinity for the material's surface. This results to higher values of selectivity for the material which for the 50:50 ratio exceeds 1000 at 1 bar. These high values need to be treated with caution since the presumed ideality of the adsorbed phase has been found to produce over-optimistic values for gasses with large Q_{st} differences.

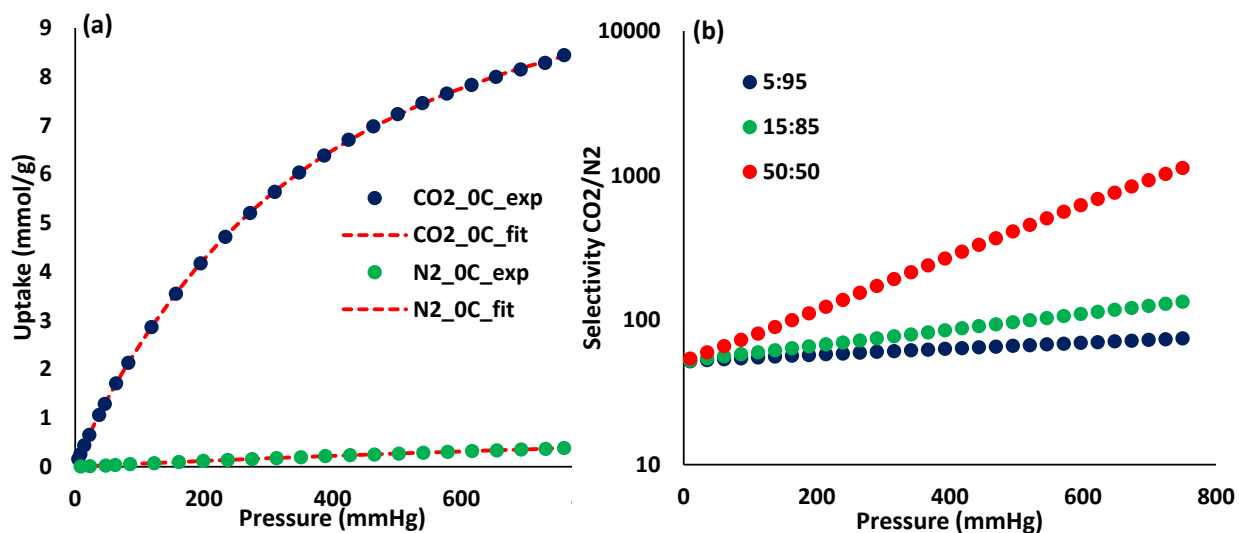


Figure 4.26: Cu-Pd-nbo excess adsorption isotherms for CO₂ and N₂ at 0 °C and the corresponding DSLF and Langmuir fits respectively (a), IAST selectivities for three different CO₂:N₂ mixture ratios (b)

All the parameters obtained from the fitting of the experimental isotherms, as described above, are listed in table.

Table 4.4: Values obtained from fitting the experimental isotherms

Dual Site Langmuir Freudlich			Langmuir	
	CO ₂	CH ₄		N ₂
q₁[*]	0.99	4.18	q[*]	1.65
n₂	1.24	1.00	k[*]	4x10 ⁻⁴
k₁^{**}	0.02	6x10 ⁻⁴		
k₂^{**}	3x10 ⁻³	0.17		
n₁	0.96	0.98		
q₂[*]	10.37	0.01		

[*mmol/g, **mmol/(g mmHg)]

The calculated IAST selectivities are comparable to some of the top-performing MOFs that appear in literature and are listed in table 4.5

Table 4.5: IAST CO₂/N₂ and CO₂/CH₄ selectivities for various adsorbents and Cu-Pd-nbo at 1 bar.

Materials	CO ₂ /N ₂ (15/85)	CO ₂ /CH ₄ (50/50)	Reference
Cu-Pd-nbo	25.8 (298K)	8.8 (298K)	This work
	134.2 (273K)	15.4 (273K)	This work
MOF-5	10.1 (298K)	2.3 (RT)	[117, 118]
Cu-BTC	34.4 (293K)	6.5 (RT)	[119, 118]
MIL-101	11.4 (298K)		[120]
MIL-101(Cr)		5.0 (RT)	[118]
PCN-88	29.8 (296K)		[9]
MOF-505	27.8 (298K)	7.6 (298K)	[121]
NJU-Bai21		7.8 (298K)	[96]
Cu-TDPAT		20 (298K)	[122]

The low-pressure adsorption isotherms revealed a promising behavior for the potential use of Cu-Pd-nbo in CO₂ capture processes by its selective adsorption from mixtures containing CH₄ and/or N₂. Cu-Pd-nbo performed exceptionally in terms of CO₂ uptake at 1 bar achieving values for gravimetric and volumetric capacity which rank it among the highest ever reported for the nbo family in general.⁹⁸ It needs to be noted that this was accomplished while the shape of the CO₂ adsorption isotherm does not exhibit a steep step in uptake at low pressure, indicative of enhanced

gas-solid interactions, but it presents a gradual but consecutive increase in adsorbed amount. This translates to a moderate value of Q_{st0} which is increased as the surface coverage proceeds. Thus, it is implied that the material will be able to be regenerated and reused under mild conditions, reducing substantially the cost and energy penalty usually associated with this stage of a potential future application. Furthermore, IAST calculations predict that the material will be an interesting candidate for CO₂ separation processes where the corresponding concentration is relatively high such as biogas upgrading or syngas processing.

4.8 Thermal Desorption Spectroscopy (TDS) experiments for Cu-Pd-nbo

In order to gain further insight on the CO₂-substrate interactions and the consequent impressive adsorption uptake the sample demonstrated, TDS experiments were performed on the AS-1 volumetric device. More specifically, by using the cryocooler and acquiring control of the instrument via the “manual mode” option, the following experimental procedure was followed. The activated sample was charged with different amounts of CO₂ at 300K and isolated until equilibrium was achieved by means of monitoring the pressure change. Subsequently, the sample was cooled down with a 4 K/min rate to 50 K and remained there for 15 minutes. Then, the sample was evacuated and consequently heated under dynamic vacuum back to 300 K using a ramp rate of 0.5 K/min while the pressure change was recorded, ultimately producing the thermal desorption spectrum that is depicted in figure 4.27.

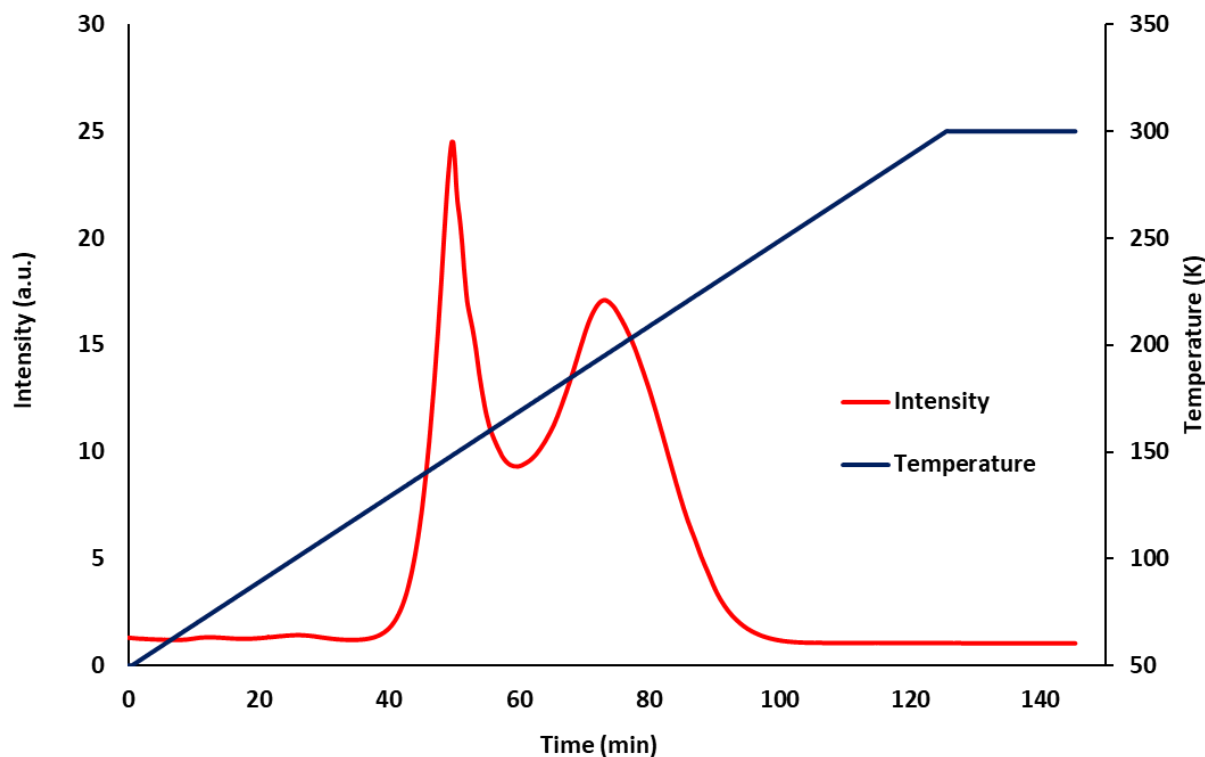


Figure 4.27: Low-temperature CO₂ TDS experiment for Cu-Pd-nbo

Initially, a series of TDS experiments were performed on an empty sample holder with various CO₂ loadings. Subsequently, 20 mg of (in situ) activated Cu-Pd-nbo were placed in the same sample holder and the same experimental procedure was followed for 8 different CO₂ loadings. During cooling, the sample adsorbs CO₂ to an extent which obviously depends on the amount that was initially introduced to the system at 300 K. At 50 K, which is below carbon dioxide's triple point, the gas even under vacuum remains either "trapped" inside the microporous network or, in case there is a surplus, solidified around the sample. In all cases, subsequent heating (the part of the experiment that is depicted in figure 4.27), was performed by using the same rate (0.5 K/min).

Evidently, two main peaks can be easily identified. The first, which can be seen for the initial loadings of 760, 600 and 475 mmHg and begins at approximately 120 K and is attributed to sublimation of bulk solid CO₂ which solidified "outside" the material (figure 4.28). The assumption made at this point is that the sample's porous network is completely filled with adsorbate and this hypothesis is validated by the fact that the three corresponding lines (black, orange and purple) coincide at approximately 160 K to form the second distinct peak centered at around 190 K. This peak is assigned to the desorption of the adsorbed phase in the sample micropores-. The adsorbed molecules need greater energy in order to be desorbed due to the enhanced interactions with the framework (including the metal centers). The area between the two peaks is attributed to CO₂ molecules that are adsorbed on the material's external surface area (or pores formed between the primary particles) and demand intermediate energy in order to be desorbed compared to the bulk gas and the adsorbed phase in the micropores.

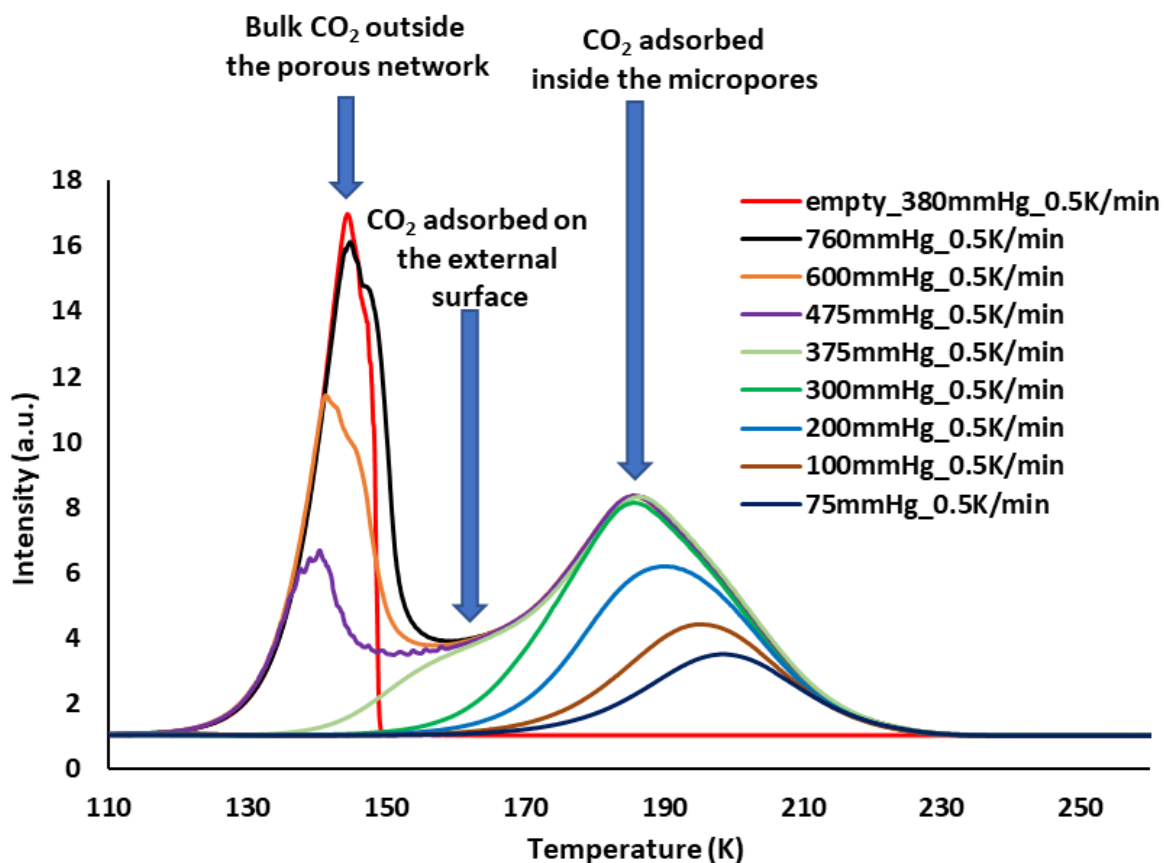


Figure 4.28: TDS experiments for CO₂ on an empty sample holder (red line) and on Cu-Pd-nbo (in the same sample holder) for various loadings

Although two distinct energy adsorption sites have been identified by quantum chemistry calculations, their presence could not be resolved or verified by these TDS experiments since only one peak is observed for the adsorbed species. However, a very “subtle” shoulder can be detected at high temperatures and this may be related to a second set of sites with slightly increased interaction with CO₂ (compared to the main peak at 190K). For this reason, the thermal desorption process was further investigated by applying lower CO₂ loadings which resulted in partial filling of the material’s microporous structure. Interestingly, the suggested energetic inhomogeneity of the structure is strongly suggested. As the amount of the adsorbed phase is decreased, the corresponding peak clearly shifts to higher temperatures (by more than 10 °C) indicating the existence of a second family of adsorption sites with increased CO₂ – surface interactions.

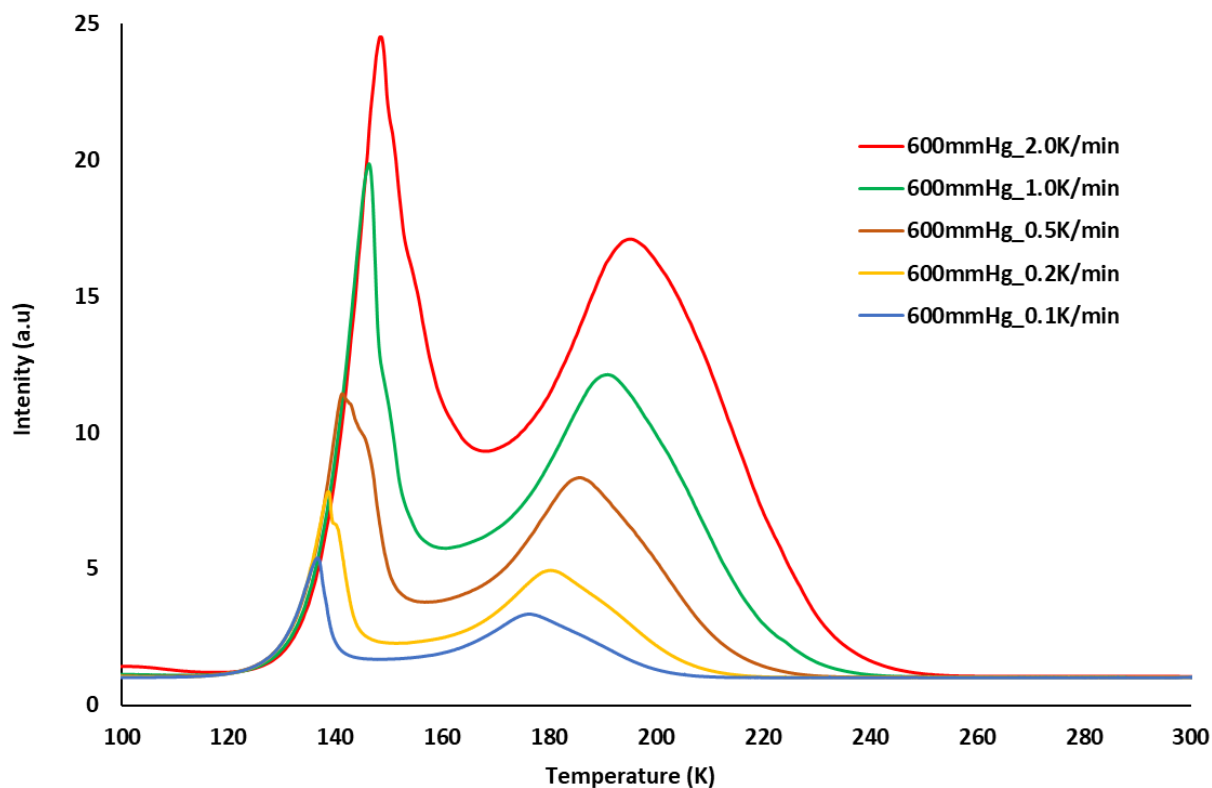


Figure 4.29: TDS experiments for the same CO_2 loading (600 mmHg) on Cu-Pd-nbo with various heating ramp rates

Subsequently, a series of TDS experiments were performed in order to pursue additional confirmation for the material's surface energetic inhomogeneity using the same CO_2 loading and different heating ramp rates ranging from 0.1 to 2.0 K/min (figure 4.29). Evidently, for the highest heating rate (2.0 K/min), the peak assigned to the adsorbed species in the sample's micropores presents a rather symmetrical shape indicating a homogeneous energetic landscape. This can be explained since the two distinct interactions have been theoretically calculated to be quite close to each other (30.3 and 24.3 kJ/mol) thus more difficult to be experimentally distinguished. However, as the heating ramp rate is decreased and the system is given more time to desorb the adsorbate, the peak gradually presents an asymmetry which indicates the existence of a second family of adsorption sites for which the CO_2 molecules exhibit higher affinity. Ideally a system that could achieve even lower heating rates than 0.1K/min would be able to distinguish the different

adsorption sites by complete peak splitting although this would translate to tedious experiment times.

4.9. High pressure single component isotherms for Cu-Pd-nbo

In order to gain a more complete picture of the material's behavior, CO₂, CH₄ and N₂ adsorption isotherms were measured over a broader pressure range using the gravimetric method. More specifically, gas adsorption isotherms were performed on the IGA-1 at different (near ambient) temperatures and pressure up to 20 bar.

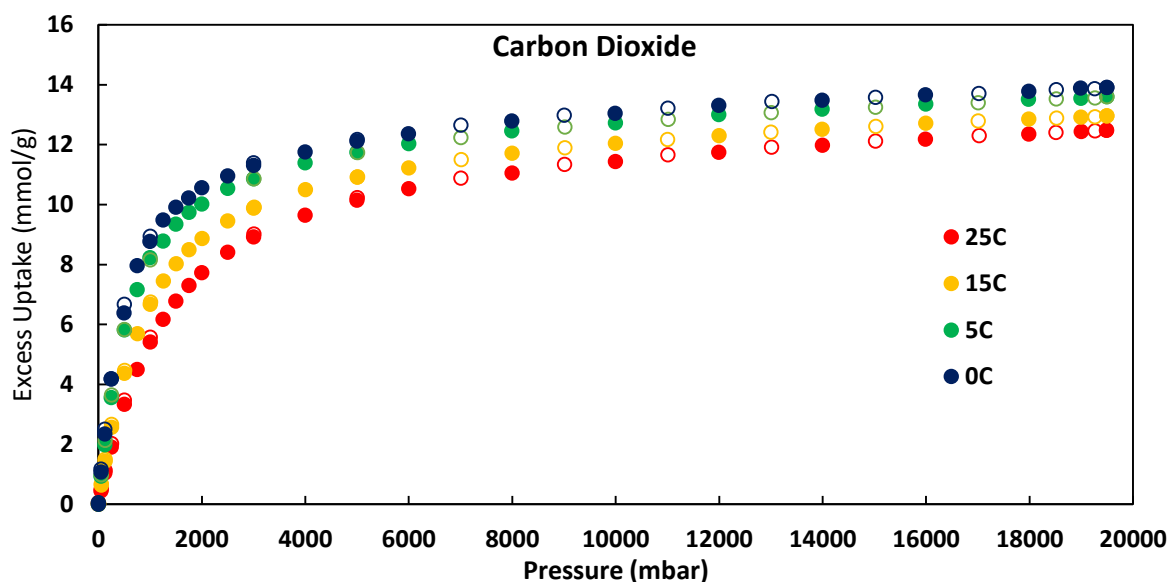


Figure 4.30: CO₂ excess adsorption isotherms for Cu-Pd-nbo at 0, 5, 15 and 25 °C and pressure up to 20 bar.

The CO₂ excess adsorption isotherms at different temperatures that are illustrated in figure 4.30 exhibit a gradual uptake increase up to 2 bar which upon further pressure increase reaches a quasi-saturation plateau of 12.48 mmol/g (549.2 mg/g, 279.6 cm³ STP/g, 274.0 cm³STP/cm³) at 19.5 bar and 25 °C. For comparison reasons, total uptake was also calculated according to the

equation described in section 2.4.1.3 and was found to be 12.95 mmol/g at 25 °C (570.0 mg/g, 290.1 cm³STP/g, 284.3 cm³STP/cm³) and pressure 19.5 bar. Isothermic heat of adsorption was also calculated (figure 4.31) as a function of surface coverage and revealed the same trend observed for low pressure isotherms.

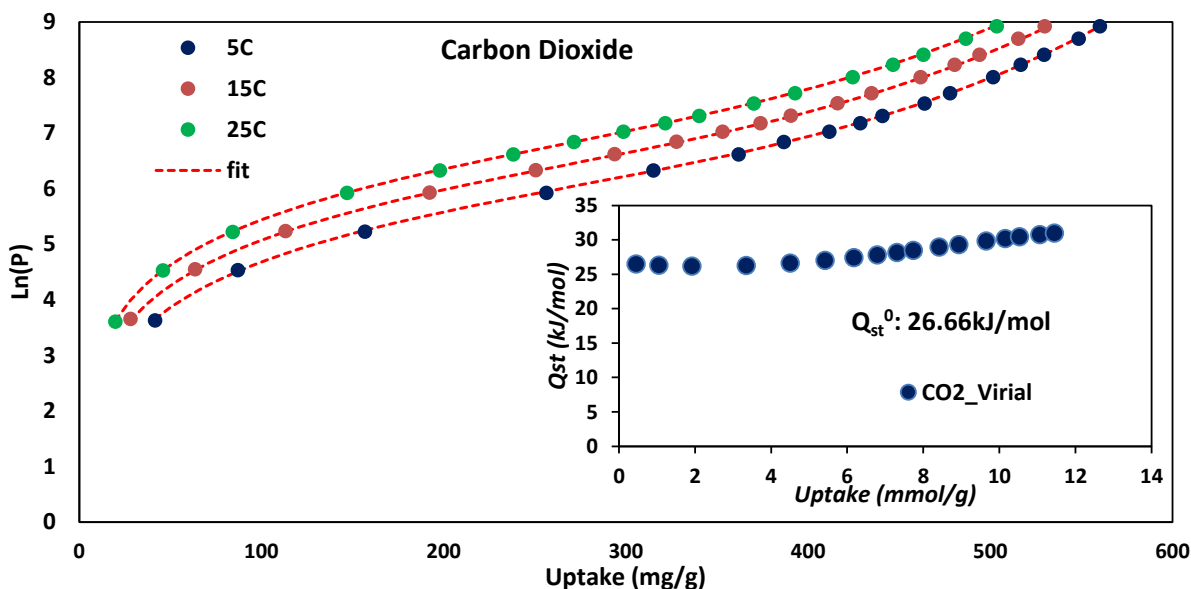


Figure 4.31: Virial type fitting of CO₂ adsorption isotherms for Cu-Pd-nbo at 5, 15 and 25 °C and the corresponding isosteric heat of adsorption as a function of CO₂ uptake (inset)

The Q_{st0} value calculated is very close to the one estimated from low pressure isotherms. As already shown from the low-pressure data, Q_{st} slightly increases for the whole uptake range suggesting favorable adsorbate-adsorbate interactions along the populated low energy sites of the unsaturated metal sites as well as the metal centers of the organic linker. The high-pressure isotherms appear to be completely reversible suggesting mild conditions required for the sample's regeneration even at high loadings.

Subsequently, methane excess adsorption isotherms were measured at identical experimental conditions as described for CO₂ above.

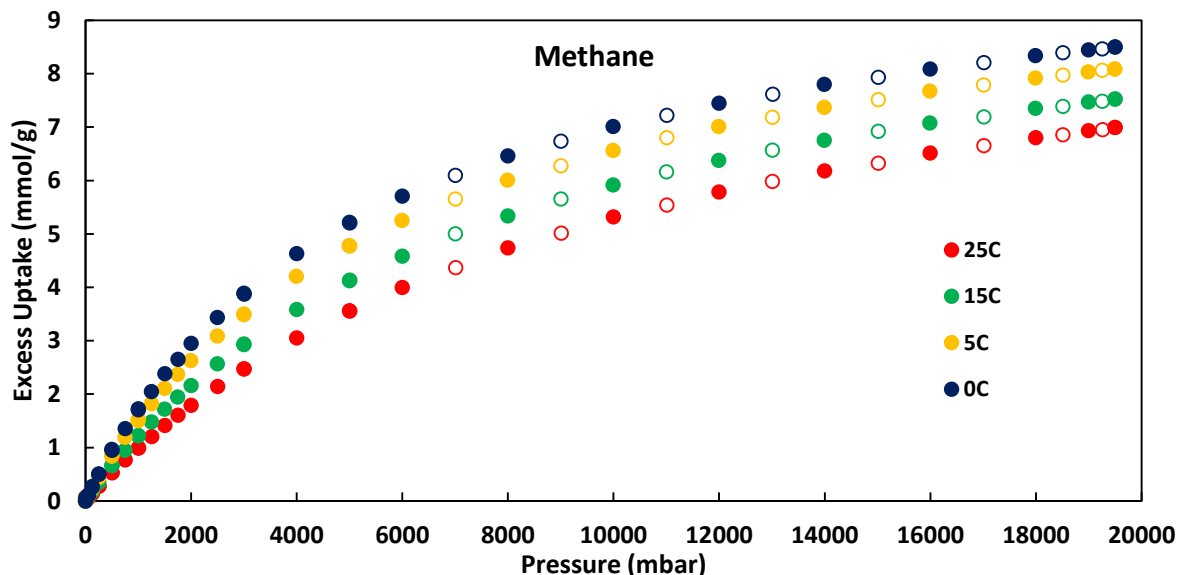


Figure 4.32: CH_4 excess adsorption isotherms for Cu-Pd-nbo at 0, 5, 15 and 25 °C and pressure up to 20 bar.

The measurements revealed completely reversible isotherms that exhibit a continuous increase in uptake as the pressure rises. Cu-Pd-nbo adsorbs (excess) 7.0 mmol/g (112.3 mg/g, 156.8 cm³ STP/g, 153.7 cm³ STP/ cm³) at 25 °C and 19.5 bar. Isostatic heat of adsorption is in complete agreement with the values obtained from low pressure isotherms. Interestingly, Q_{st} remains constant as the surface coverage increases with pressure up to 20 bar, suggesting (unlike CO₂) a homogeneous distribution of the adsorbed methane molecules within the microporous structure of the material. This can be explained taking into account that methane is a non-polar molecule with zero quadrupole moment. This way, methane would not “feel” the interaction with the active sites of the structure as strongly as the CO₂.

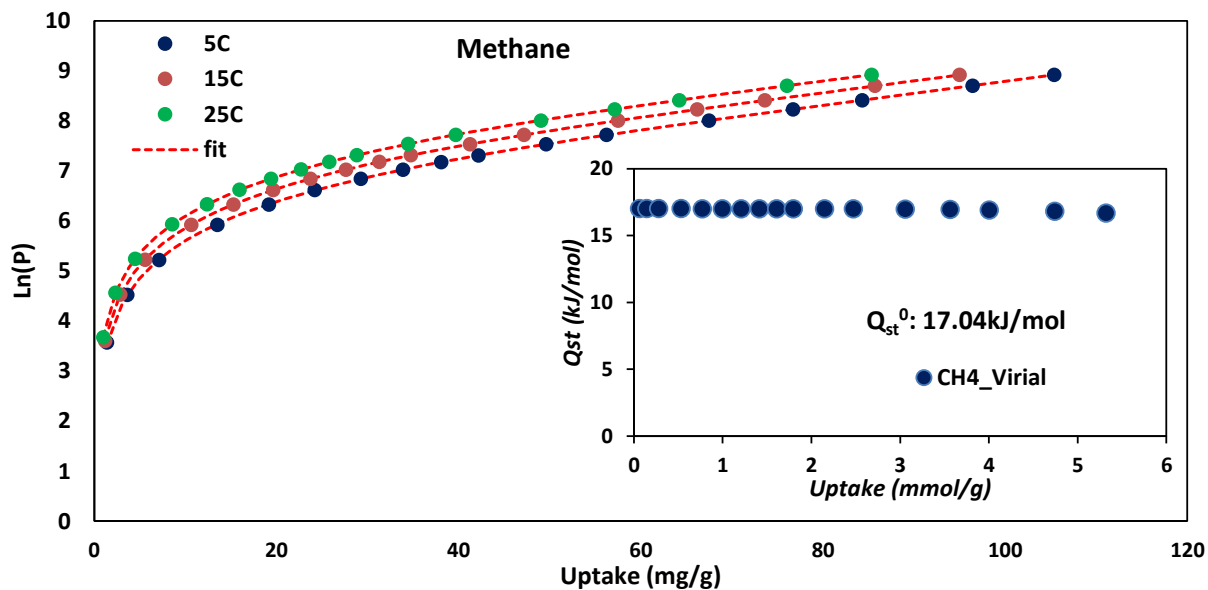


Figure 4.33: Virial type fitting of CH_4 adsorption isotherms for Cu-Pd-nbo at 5, 15 and 25 °C and the corresponding isosteric heat of adsorption as a function of CH_4 uptake (inset)

The shape of the isotherms, which continuously increase without reaching a plateau, suggest that the material could also serve as an adsorbent for ANG applications. In order to investigate its working capacity, adsorption isotherms were measured up to 100 bar at near ambient temperatures using the volumetric method and the results are illustrated in figure 4.34.

CH_4 excess adsorption isotherms for Cu-Pd-nbo exhibit the common isotherm shape for adsorption of supercritical fluids. CH_4 uptake at 25 °C is gradually increased and reaches a plateau at approximately 60 bar. Further pressure rise results to a slight decline as can be seen in figure 4.34. As the temperature decreases, the plateau is shifted to lower pressure and the subsequent uptake decline becomes more visible. This is an ordinary behavior for methane excess adsorption at higher pressures and near ambient temperatures. At a certain pressure the density of adsorbed phase in the pores reaches a maximum value and further densification is not possible. On the contrary, the bulk gas density is continuously increasing with pressure leading thus to a decreasing excess amount.

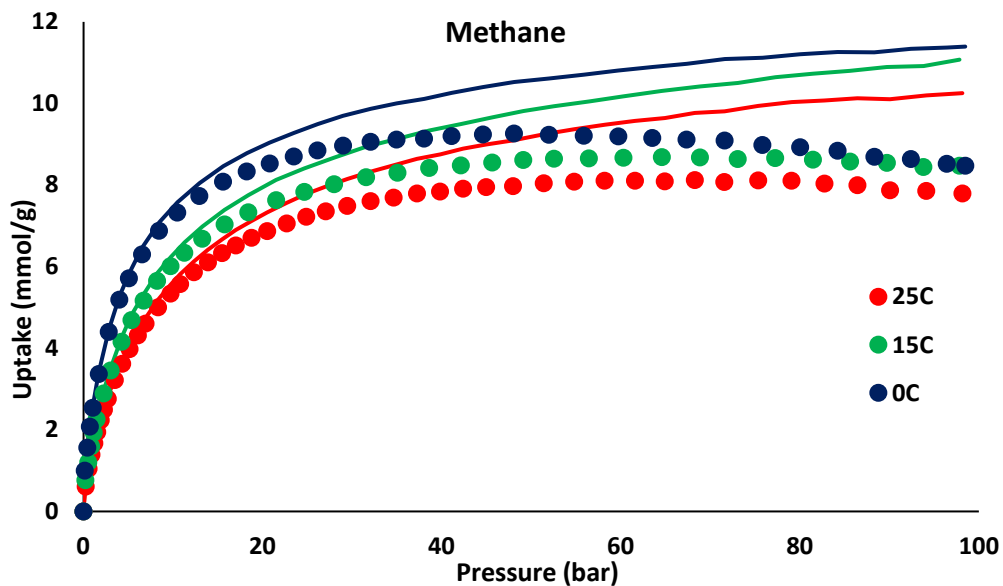


Figure 4.34: High pressure CH_4 excess (dots) and total (lines) adsorption isotherms for Cu-Pd-nbo at 0, 15 and 25 °C up to 100 bar.

For this reason, curves for total CH_4 uptake, which give a more realistic description of the system, were derived as described in chapter 2.1.4.3. Cu-Pd-nbo exhibits at 100 bar, total CH_4 uptake of 10.25 mmol/g (164.4 mg/g, 229.6 $\text{cm}^3\text{STP/g}$, 225.0 $\text{cm}^3\text{STP/cm}^3$) and 11.38 mmol/g (182.5 mg/g, 254.9 cc/g, 249.8 cc/cc) at 25 and 0 °C respectively.

This highlights a limitation of the strategic use of purely microporous adsorbents, which usually exhibit rather modest total pore volumes, for high pressure CH_4 storage applications. Essentially, the shape of the excess isotherm reveals that at pressure higher than 60 bar the material's contribution to the increase of the energy density is negligible since there is no more space inside the pores for CH_4 to be adsorbed. The slight increase observed in the total uptake curves at high pressures is attributed to the compression of bulk CH_4 as a result of the pressure rise. In order to address that, a material that would exhibit a well-defined pore size distribution ranging from large micropores to narrow mesopores or at least high total pore volume could potentially offer more space for CH_4 to be adsorbed, taking advantage of the process' whole pressure range.

Cu-Pd-nbo performs poorly when compared with the gravimetric DOE targets for methane storage due to its relatively low total pore volume and moderate gravimetric specific surface area value. As already mentioned, a linear relation between gravimetric capacity and specific surface area (SSA) has been established. Specifically, total gravimetric uptake at 25 °C and 65 bar was estimated to be 154.6 mg/g (215.9 cm³ STP/g) when the target is 500 mg/g (700 cm³ STP/g).

However, the total volumetric capacity of the material can be compared with the top performing adsorbents within the whole family of MOFs. Due to its relatively high crystallographic density (0.98 g/ cm³) Cu-Pd-nbo has been found to adsorb 211.6 cm³ STP/ cm³ CH₄ at 65 bar and 25 °C, which accounts for 80% of the DOE's new target of 263 cm³ STP/ cm³. Total CH₄ volumetric working capacities were calculated and are listed in table 4.6, along with four MOFs that reportedly exhibit the highest CH₄ storage capacities in literature.

Table 4.6: Porous properties, CH₄ total and working capacities for Cu-Pd-nbo with respect to other published top performing MOFs

	SSA (m²/g)	TPV (cm³/g)	CH₄ total uptake at 298K (cm³ STP/cm³)	CH₄ working capacity (cm³ STP/cm³)
NU-111 ⁵⁶	4930	2.09	123 (35 bar)	177 (65-5 bar)
Al-soc ⁵⁵	5585	2.30	205 (65 bar)	201 (80-5 bar)
MOF-519 ⁷²	2400	0.94	200 (35 bar) 279 (80 bar)	151 (35-5 bar) 230 (80-5 bar)
UTSA-20 ⁵⁸	1156	0.62	195 (35 bar)	
Cu-Pd-nbo ⁹⁸	1473	0.53	187 (35 bar) 212 (65 bar) 220 (80 bar)	101 (35-5 bar) 125 (65-5 bar) 134 (80-5 bar)

Cu-Pd-nbo demonstrates similar total CH₄ volumetric capacities with some high-performance MOFs, although it exhibits rather moderate structural characteristics (SSA, TPV), thus highlighting the cooperative effect of confinement in micropores and the presence of strong adsorbing sites. However, in terms of working capacity it delivers the lowest CH₄ amount in every

pressure range due to its Q_{st} which results from relatively enhanced adsorbate-adsorbent interactions at low pressure. Thus, a significant amount of adsorbed CH_4 is “trapped” and cannot be released by solely reducing the pressure at 5 bar.

Finally, the nitrogen adsorption properties of Cu-Pd-nbo were evaluated for pressure up to 20 bar and the results are depicted in figure 4.35.

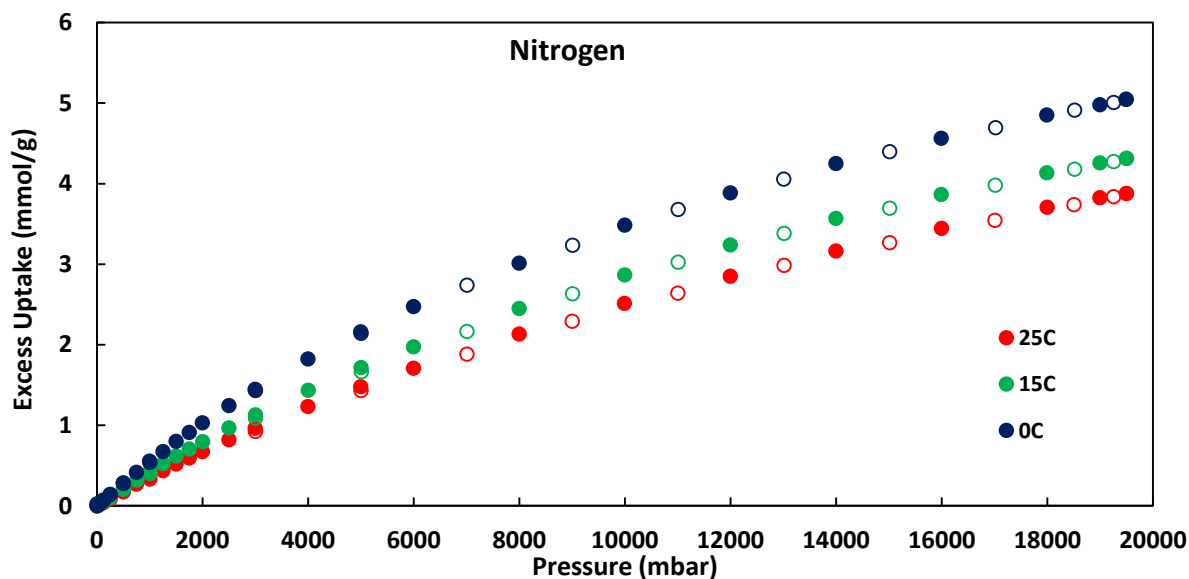


Figure 4.35: N_2 excess adsorption isotherms for Cu-Pd-nbo at 0, 15 and 25 °C and pressure up to 20 bar.

Cu-Pd-nbo demonstrates completely reversible nitrogen excess adsorption isotherms with an almost linear increase in adsorbed amount as the pressure is raised to 20 bar. However, the weak adsorbate-surface interactions result to uptake values of 3.88 and 5.07 mmol/g at 25 and 0 °C, respectively, at the pressure of 19.5 bar. Isostatic heat of adsorption was calculated to be 11.97 kJ/mol in full agreement with the value extracted from low pressure isotherms (12.12 kJ/mol) and remains practically constant as the surface coverage increases.

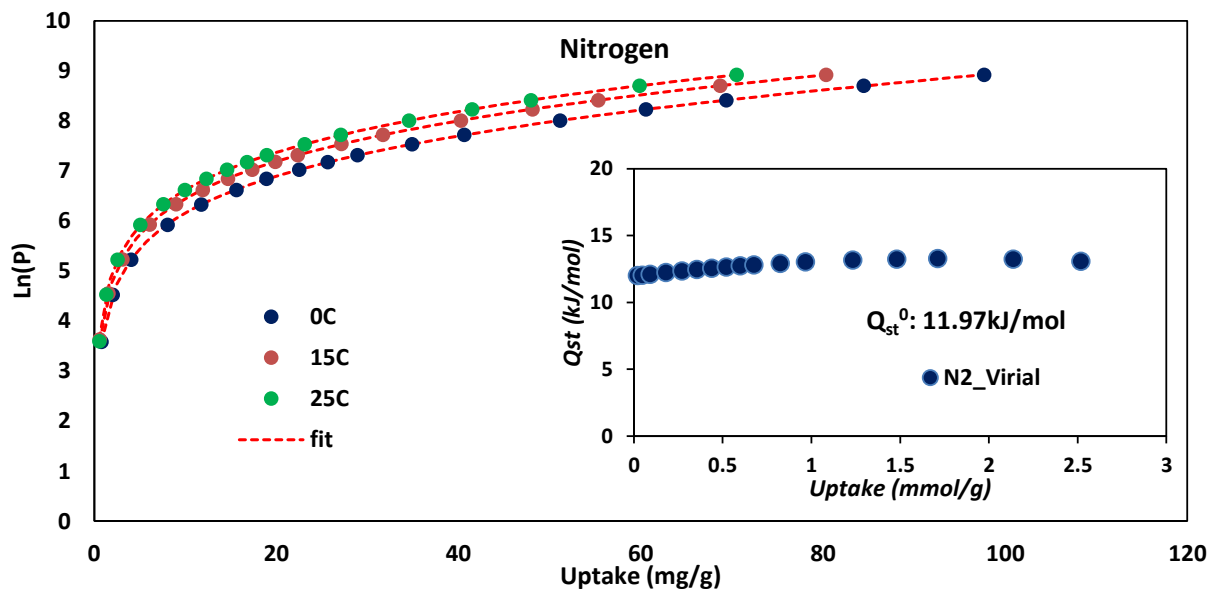


Figure 4.36: Virial type fitting of N_2 adsorption isotherms for Cu-Pd-nbo at 5, 15 and 25 °C and the corresponding isosteric heat of adsorption as a function of N_2 uptake (inset)

The values for the virial coefficients that were extracted from the CO_2 , CH_4 and N_2 adsorption isotherms fitting, as already described, are listed in table 4.7

Table 4.7: Values for virial coefficients as obtained from fitting of the experimental isotherms

	Virial equation					
	CO_2	error	CH_4	error	N_2	error
a0	-3206.65342	94.97523	-2049.73456	29.79078	-1440.28031	29.59981
a1	1.2256	0.7723	0.52169	1.70292	-6.83458	2.16552
a2	-0.00625	0.00148	-0.02027	0.01971	0.08941	0.0305
a3	-2.3232E-07	2.10E-06	0.00029	0.00012	-4.00E-04	2.10E-04
a4	7.4222E-09	1.80E-09	-6.70E-07	6.21E-07	1.78E-06	1.17E-06
b0	11.34271	0.3256	10.5725	0.10328	9.10551	0.10319
b1	-0.00131	0.00263	0.00894	0.00592	0.0267	0.00758
b2	0.00002	4.58E-06	-0.00002	0.00007	-0.00021	0.0001

An overview of the high-pressure results is provided in figure 4.35, where the adsorption isotherms of the three aforementioned gases at 25 °C and pressure up to 20 bar are plotted.

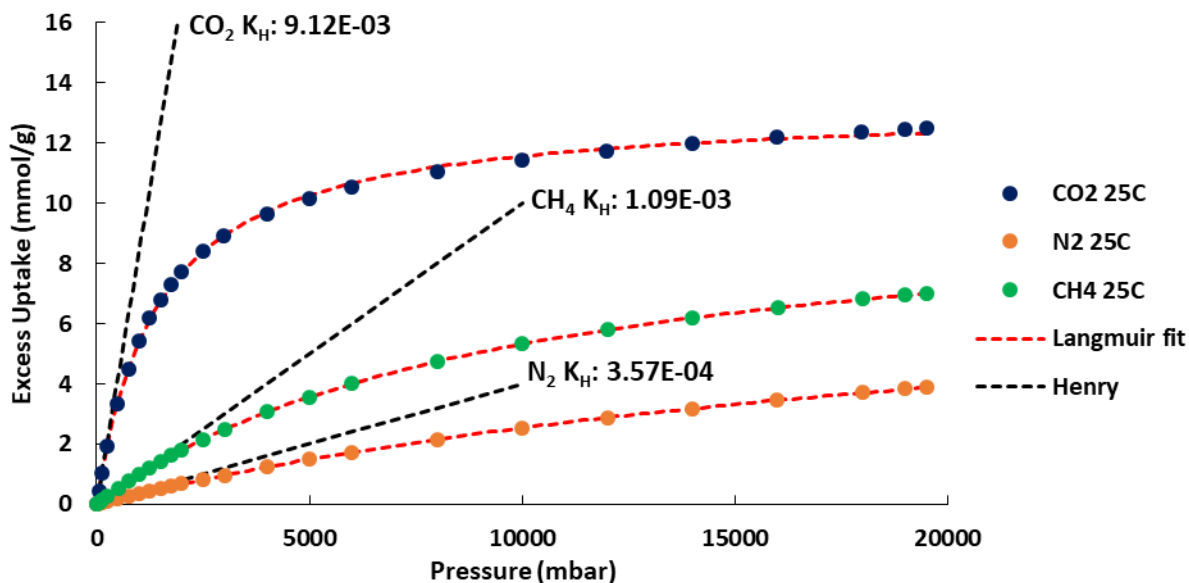


Figure 4.37: CO₂, CH₄ and N₂ excess adsorption isotherms for Cu-Pd-nbo at 25 °C and pressure up to 20 bar. The red dotted lines represent the corresponding Langmuir fit and the black dotted lines highlight the Henry region of the isotherms.

Evidently, CO₂ adsorption is thermodynamically favored over CH₄ and N₂, due to enhanced electrostatic interactions with the metals on the material's surface resulting from its inherent increased quadrupole moment values compared to N₂ and CH₄ which exhibit reduced polarity. The difference in uptake is even more pronounced at pressure up to 2 bar. Furthermore, CO₂ possesses the smallest kinetic diameter of the three (3.4 Å) which makes it easier and faster to enter the micropores (found to be 9.5 Å) that constitute the crystalline porous network. It should nevertheless be mentioned that while CH₄ and N₂ are supercritical fluids at ambient temperature, CO₂ is still “condensable” at ambient temperature; its adsorption is thus favored in any case, regardless the material. All the isotherms were successfully fitted using the Langmuir thermodynamic model according to the expression previously described and the parameters obtained are listed in table 4.8. Furthermore, the Henry constants (K_H), for each isotherm were calculated and are also listed in the same table. K_H essentially represents the slope of the linear part of the isotherm at low pressure, known as the Henry region. K_H ratios often have been used in

literature as a quick, though questionable way of estimating thermodynamic selectivities of CO₂ over other gases.

In order to highlight the importance of the isotherm's shape when it comes to gas storage applications, excess working capacities were calculated for all three gases at the pressure range of 2-20 bar. Interestingly, although CO₂ is much more strongly adsorbed than CH₄, does not possess the highest value for the aforementioned pressure range since it adsorbs most of the amount at pressure lower than 2 bar.

Table 4.8: Values obtained from fitting the experimental isotherms and indicative excess working capacities

	Langmuir		Working Capacity (2-20bar)*	Henry constant (K _H)**
	q	K		
CO ₂	13.24	6.89E-04	4.75	9.12E-03
CH ₄	10.45	1.04E-04	5.2	1.09E-03
N ₂	8.69	4.11E-05	3.2	3.57E-04

[*mmol/g], [**mmol/(g mbar)]

Subsequently, the kinetics of the adsorption process were studied for CO₂, CH₄ and N₂. By using the gravimetric method, a step change in gas pressure is applied and the material's mass relaxation is observed as a function of time under isothermal conditions and under constant adsorbate boundary concentration. Assuming the appropriate gas diffusion resistances, the diffusivity coefficients can be calculated and valuable information on the kinetic behaviour of the adsorbed gases on the material's surface can be derived. In this case, taking into account that Cu-Pd-nbo is predominantly microporous, it was assumed that the major resistance controlling the flux of the gas molecules in the porous network is micropore diffusion.

The shape of the particles was assumed to be spherical, however diffusivity coefficients could not be calculated since the radius of the material's particles, r_c , is unknown. Instead, the diffusion time constant D/r_c^2 , was calculated by fitting to the experimental kinetic data, a

theoretical curve which constitutes the solution of Fick's second law for a step change in pressure (equation 3.16)

In figure 4.38, selected kinetic data are depicted at 0 and 25 °C, for pressure step changes 125-250 mbar for CO₂ and 1500-2000 mbar for CH₄ and N₂. Interestingly, equilibrium is achieved within 15 minutes for all gases, pressure changes and temperatures, illustrated by the observed plateau of the kinetic curves. This finding indicates that the material's porous network does not present significant diffusion resistances to the adsorbate molecules. This satisfies another major prerequisite in gas separation applications since fast equilibrium is desired for Pressure/Vacuum/Temperature Swing Adsorption (PSA, VSA or TSA) cycles in order to achieve high productivity.

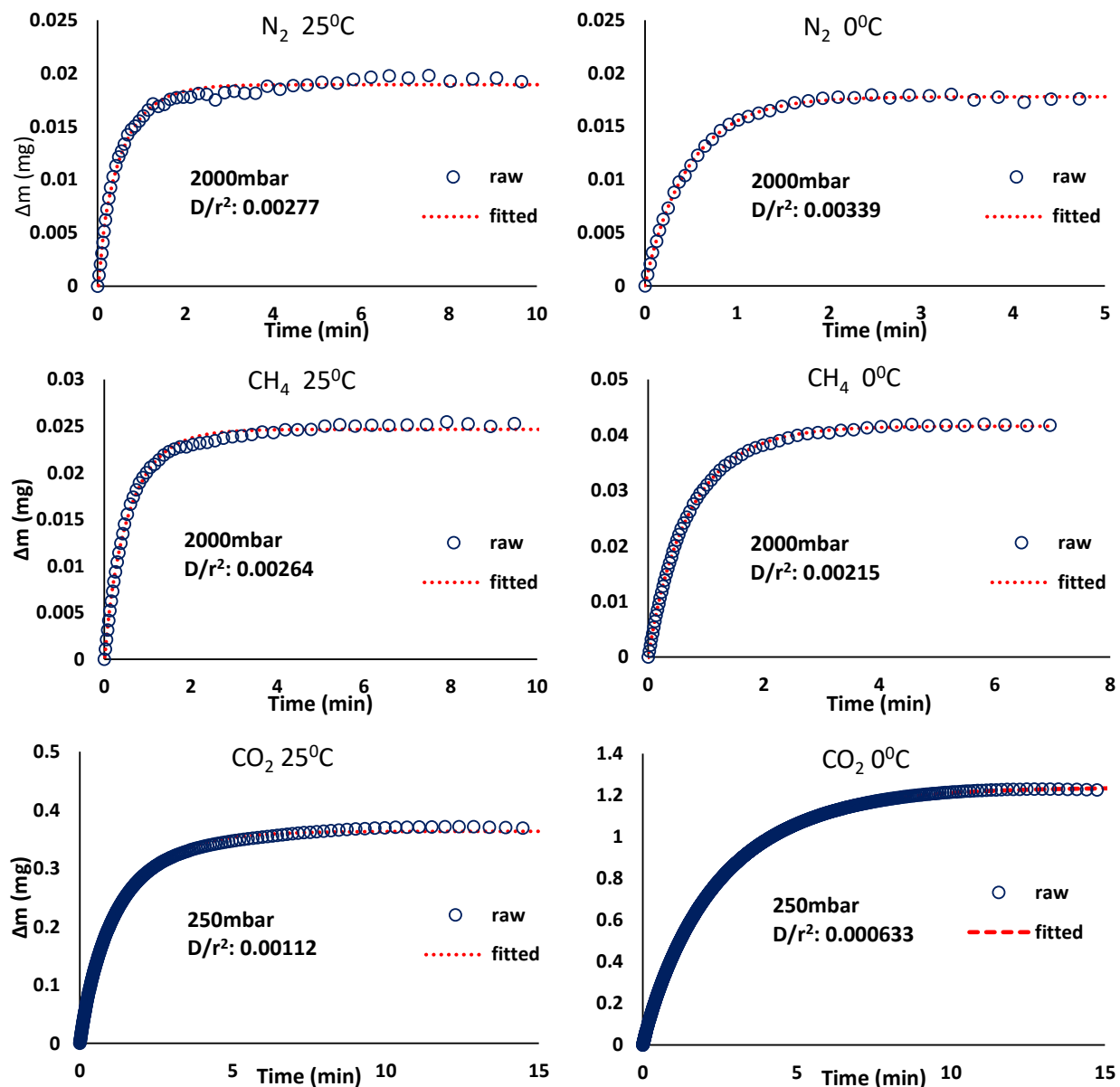


Figure 4.38: Selected kinetic data at 0 and 25 °C, for pressure step changes 125-250 mbar for CO₂ and 1500-2000 mbar for CH₄ and N₂. (D/r^2 are given in units min^{-1})

In order to successfully implement the equation to the experimental data, diffusivity coefficients must remain constant during the time required for equilibrium to be reached. This is achieved by applying the smallest possible pressure step changes needed for the corresponding mass change to be measurable. As can be seen in figure 4.38 the equation perfectly describes the adsorption process for all three gasses suggesting that micropore diffusion is indeed the controlling

mechanism of the gas adsorption in all cases. Taking into account the first 10 terms of the equation, diffusivity time constant values were derived and are listed in table 4.9.

Table 4.9: CO₂, CH₄ and N₂ diffusion time constant values as obtained from fitting of the experimental adsorption kinetic curves

Diffusion time constant (D/r²) (min⁻¹)						
Pressure (mbar)	CO ₂ 25 °C	CO ₂ 0 °C	CH ₄ 25 °C	CH ₄ 0 °C	N ₂ 25 °C	N ₂ 0 °C
125	1.48E-03					
250	1.12E-03	6.33E-04				
500	1.07E-03	7.20E-04				
750	8.53E-04	4.60E-04				
1000	7.84E-04	8.50E-04	2.71E-03		1.45E-03	3.11E-03
1500	7.75E-04	1.01E-03				
2000	7.32E-04	7.32E-04	2.64E-03	2.15E-03	2.77E-03	3.39E-03
3000			2.06E-03	2.45E-03		
5000			1.56E-03	2.70E-03		

For CO₂ which is strongly adsorbed in the material's micropores, the calculated D/r² values showed small variance ranging from 1.5 e⁻⁰³ to 7.3 e⁻⁰⁴ at 25 °C and 1.0e⁻⁰³ to 4.6 e⁻⁰⁴ at 0 °C from pressure 125 to 2000 mbar suggesting practically insignificant dependence on pressure. For CH₄ and N₂ that exhibit reduced affinity for the material's surface the D/r² values remain essentially constant for all pressure and temperature ranges that were investigated and displaying values comparable to the ones obtained for CO₂ ranging from 1.6 – 2.7 e⁻⁰³ and 1.5 – 3.4 e⁻⁰³ respectively. This suggests that there are not serious kinetic barriers for any of the gasses suggesting that the difference in adsorbed amount, hence the potential separation properties of Cu-Pd-nbo are predominantly thermodynamic.

4.10. Nitrogen/Argon porosimetry for In-Pd-soc

Nitrogen and argon adsorption isotherms were measured at 77 and 87K, respectively, in order to evaluate the material's porous properties and are depicted in figure 4.37. Prior to analysis, In-Pd-soc was attempted to be activated by outgassing at elevated temperatures up to 150 °C but the measured adsorption isotherms produced results deviating substantially from the crystallographic data. For this reason, activation via supercritical CO₂ drying on a custom-made experimental device was employed. The material was placed in a sample holder soaked in methanol. Subsequently, it was mounted on the device and was put under steady flow (1.5ml/min) of liquid CO₂ for 1.5 hours, so that the methanol would be completely exchanged. Then the device's temperature was raised at 50 °C and pressure at 120 bar by means of a back pressure regulator under the same flow for 1.5 hours. Eventually, the flow was stopped and the system was very slowly decompressed in a control manner. The sample holder was then moved to an argon glove box where the material was transferred to the porosimeter's sample cell. Finally, In-Pd-soc was outgassed at room temperature under high vacuum ($< 1 \times 10^{-6}$) for 3 hours before the nitrogen and argon adsorption isotherms were performed.

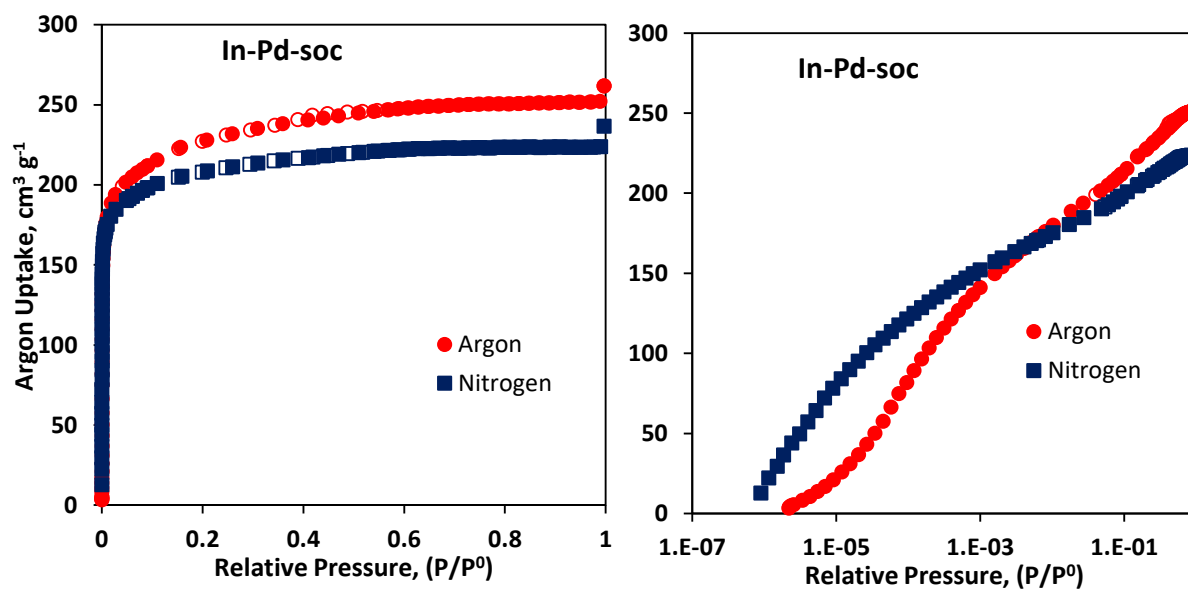


Figure 4.39: Argon and nitrogen adsorption isotherms at 87 and 77K, respectively for In-Pd-soc. The data are plotted on logarithmic scale (right) in order to reveal the material's low-pressure behavior

As expected, fully reversible type-I isotherms, characteristic of microporous materials were produced. The BET areas were calculated following the BET consistency criteria and were found to be 795 and 747 m²/g from nitrogen and argon isotherms, respectively, as illustrated in figure 4.40.

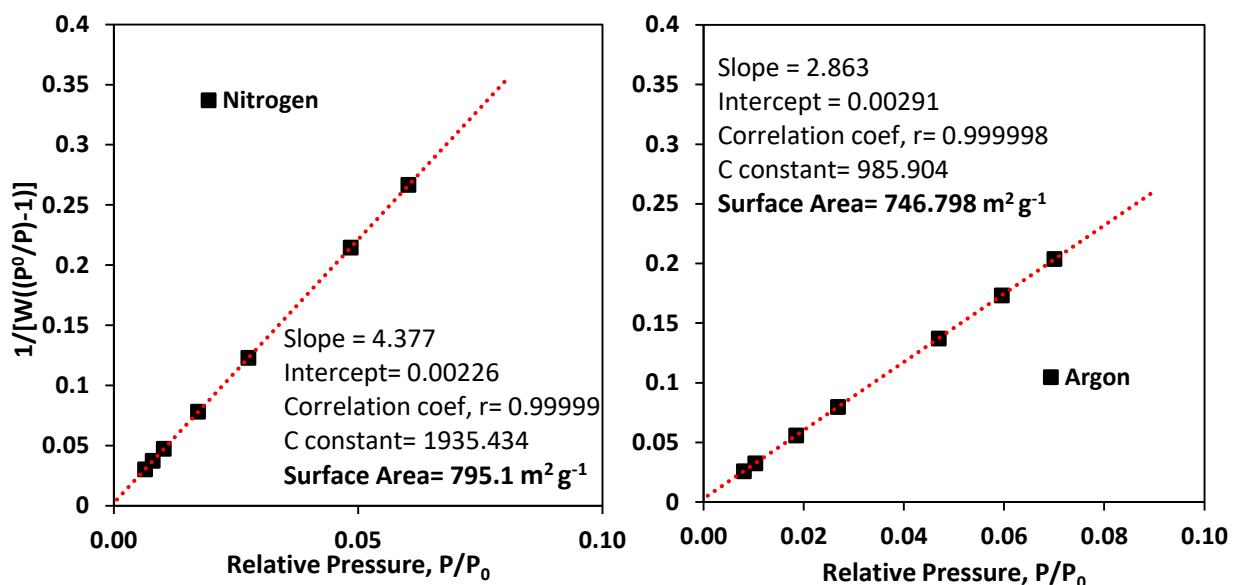


Figure 4.40: BET plots for In-Pd-soc calculated from the nitrogen (77K, left) and argon (87K, right) adsorption isotherms

Additionally, the total pore volume at 0.99 P/P^0 was determined from the nitrogen isotherm to be 0.35 cm³/g. The corresponding theoretical value obtained from the crystallographic data was 0.40 cm³/g, essentially verifying the successful activation of the material. By applying a NLDFT kernel on the argon adsorption branch for the isotherm at 87 K and assuming that the pores of the material are cylindrical, the pore size distribution plot for In-Pd-soc was obtained. As expected, the plot displays just one major peak centered at 5.8 Å, in full agreement with the pore size estimated by the single crystal structure analysis. The suitability of the aforementioned kernel was verified by successful fitting of the experimental data as can be seen in figure 4.41. A limited volume of pores with sizes in the low mesopore area (2-3 nm) can also be observed; the size of these pores is

compatible with crystal defects (either missing ligands or clusters); however, their volume is practically negligible.

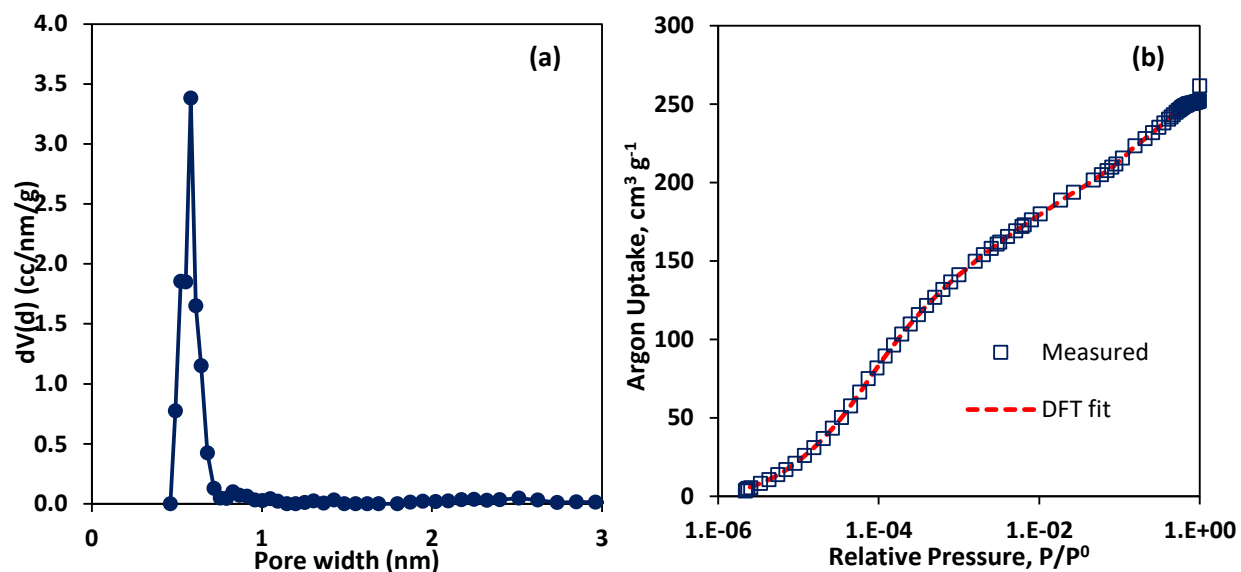


Figure 4.41: Pore size distribution (a) derived from the argon adsorption isotherm at 87K for In-Pd-soc and the corresponding NLDFT fitting (b).

Compared to the Cu-Pd-nbo which is constructed using the same palladated organic ligand, In-Pd-soc presents substantially lower BET area and total pore volume. This is explained if one takes into account that the latter bears a trinuclear cluster with indium which is much heavier than the paddlewheel cluster with 2 copper atoms. Considering the monomer's molecular weight being 1193.23 g/mol (for $[\text{In}_3\text{O}(\text{PdCl}_2(\text{PDC})_2)_{1.5}\text{Cl}(\text{H}_2\text{O})_2]$) compared to 670.65 g/mol (for $[\text{Cu}_2(\text{PdCl}_2(\text{PDC})_2)(\text{H}_2\text{O})_2]$), the gravimetric properties of In-Pd-soc are indeed expected to be significantly lower. However, the presence of the unsaturated indium sites (after the water molecules removal through the activation procedure) in combination with the ultramicropores of the crystal structure decorated with PdCl_2 moieties, point to an interesting adsorbent for further investigation of its sorption properties.

4.11. Low pressure single component isotherms for In-Pd-soc

Low pressure isotherms (up to 1 bar) were measured using the volumetric method at various temperatures for CO₂, CH₄ and N₂, in order to extract valuable initial information regarding the adsorbate – adsorbent interactions for different systems.

CO₂ excess adsorption isotherms for In-Pd-soc were measured at 0, 10 and 20 °C and are illustrated in figure 4.42. Completely reversible isotherms were produced showing a gradual increase and no indication of a plateau in uptake at this pressure range.

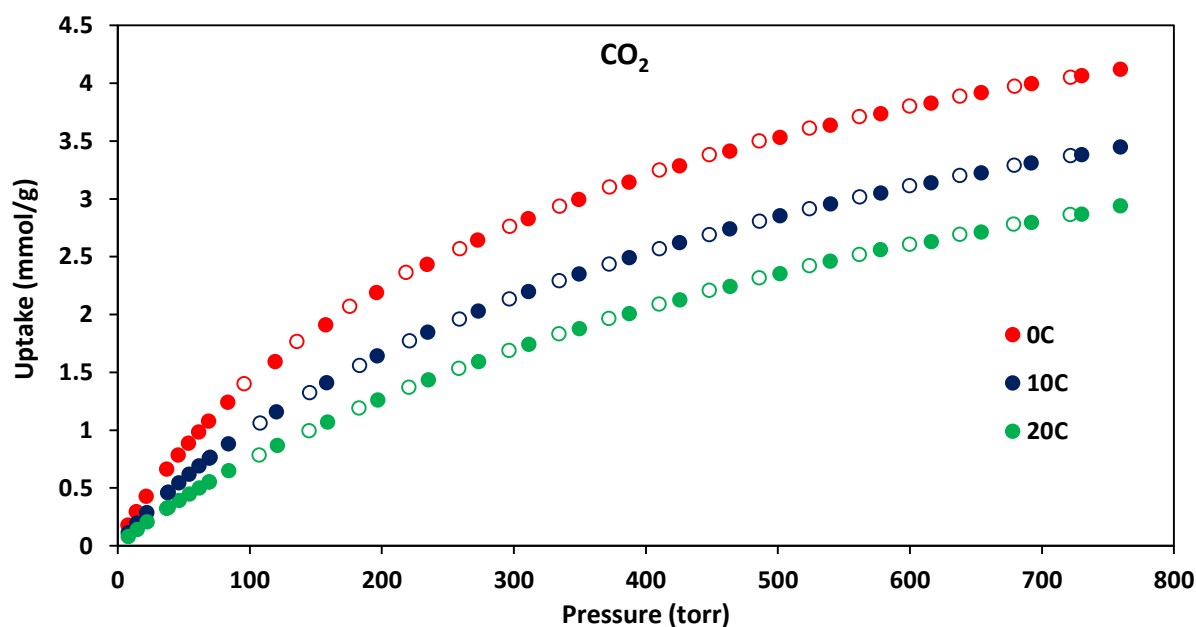


Figure 4.42: CO₂ adsorption isotherms for In-Pd-soc up to 1 bar at 0, 10 and 20 °C

In-Pd-soc adsorbed 4.1 (180.4 mg/g, 91.8 cm³ STP/g, 124.2 cm³ STP/cm³) and 2.9 mmol/g (127.6 mg/g, 64.96 cm³ STP/g, 87.8 cm³ STP cm³) at 0 and 20 °C, respectively. These values are comparable with other MOFs exhibiting similar porous properties. Compared to Cu-Pd-nbo, the expected lower gravimetric capacity is attributed to the lower BET surface area and total pore volume. However, the calculated volumetric capacity which is another important metric for gas storage applications was found to be 124.2 cm³ STP/cm³ at 273 K and 1 bar which rank it among

the highest performing soc MOFs⁹⁷. This is attributed to its high crystal density, highlighting once again the existing tradeoff between volumetric and gravimetric capacities.

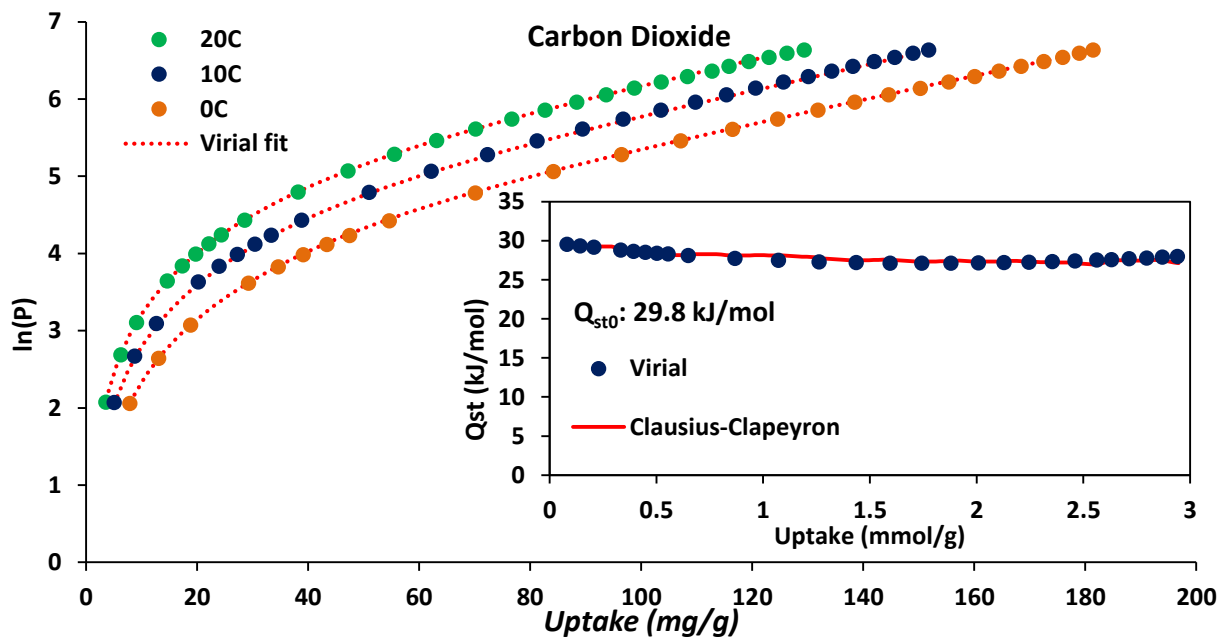


Figure 4.43: Virial type fitting of CO_2 adsorption isotherms for In-Pd-soc at 0, 10 and 20 °C and the corresponding isosteric heat of adsorption as a function of CO_2 uptake (inset)

By successful fitting of the CO_2 isotherms, using the virial equation as already described, the isosteric heat of adsorption for zero coverage was found to be 29.8 kJ/mol, which slightly decreases to approximately 25 kJ/mol. Interestingly, this value is higher than the one obtained for Cu-Pd-nbo (23.5 kJ/mol), probably because of the smaller pore size, thus increased adsorbate interaction with the pore walls, combined with the trinuclear Indium cluster. However, this value is lower than the ones that other high performance MOFs exhibit, suggesting mild regeneration conditions.

Accordingly, CH_4 adsorption isotherms were measured at temperatures ranging from -20 to 20 °C and 1 bar and are depicted in figure 4.44. Fully reversible isotherms are produced which exhibit increasing uptake as the temperature is lowered as expected. In-Pd-soc performs poorly in CH_4 uptake since it adsorbs less than 1 mmol/g at 0 °C and 1 bar

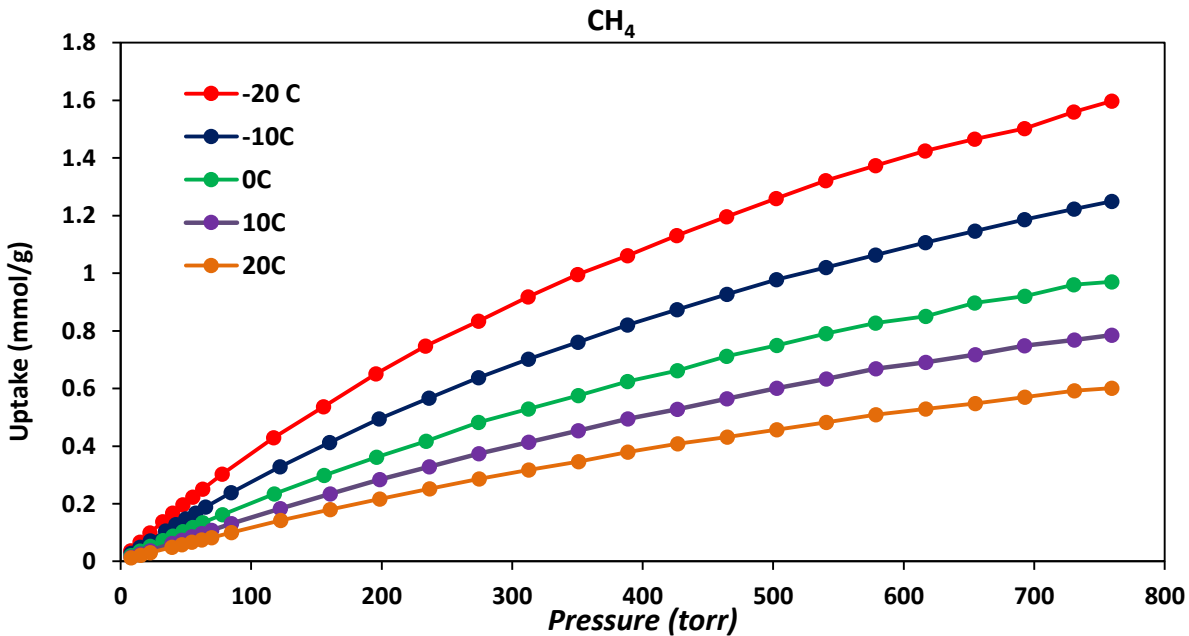


Figure 4.44: CH_4 adsorption isotherms for In-Pd-soc up to 1 bar at -20, -10, 0, 10 and 20 °C

The derived Q_{st0} was calculated at 19.6 kJ/mol and presents a slight increase as surface coverage proceeds to occur. This value is also slightly higher than the one obtained for Cu-Pd-nbo (17.5 kJ/mol). Considering the higher Q_{st} values calculated for In-Pd-soc for both the adsorbates, enhanced gas-surface interactions are suggested compared to Cu-Pd-nbo. This can be attributed to increased confinement effects due to the presence of ultra-micropores (calculated to be 5.8 compared to 9.5 Å for Cu-Pd-nbo) in combination with the increased electron density provided by the trinuclear SBU. However, its substantially lower gravimetric properties are expected to be a disadvantage for efficient use in gas storage and separation applications.

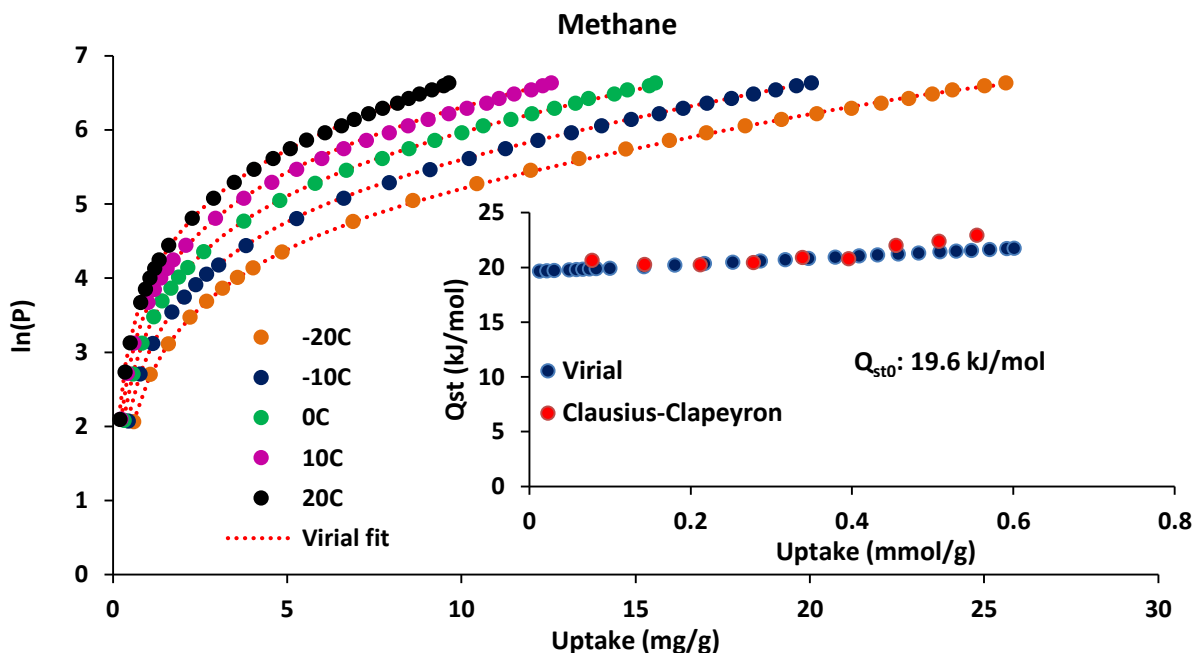


Figure 4.45: Virial type fitting of CH_4 adsorption isotherms for *In-Pd-soc* at -20, -10, 0, 10 and 20 °C and the corresponding isosteric heat of adsorption as a function of CH_4 uptake (inset)

N_2 adsorption isotherms were also performed at pressures up to 1 bar and a wide range of temperatures. In figure 4.46, the fully reversible isotherms from -90 to -50 °C which produced well defined experimental curves with measurable uptake are illustrated. Evidently, N_2 exhibits even lower affinity for the material's surface adsorbing 0.9 mmol/g at -50 °C. Because of that, measurements performed at higher temperatures resulted to adsorption isotherms exhibiting insignificant uptake at 1 bar thus were omitted from figure 4.44. High pressure experiments were performed and are analyzed in chapter 4.12 in order to gain insight on the material's nitrogen adsorption performance at ambient temperatures.

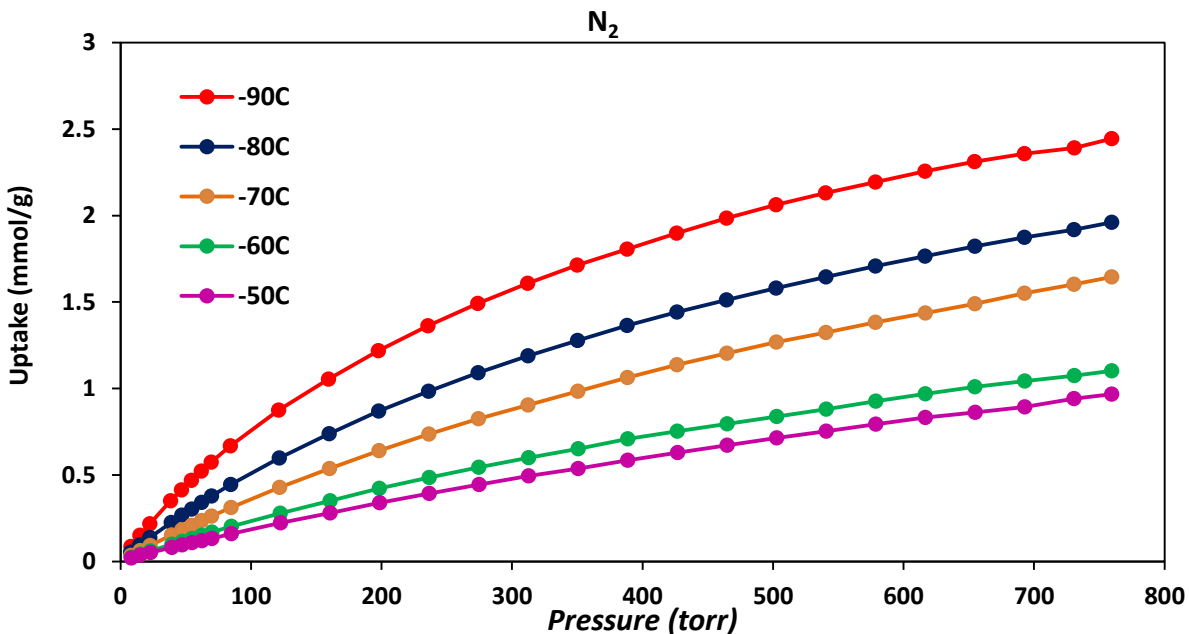


Figure 4.46: N_2 adsorption isotherms for In-Pd-soc up to 1 bar at -90, -80, -70, -60 and -50 °C

Accordingly, the derived value of Q_{st0} using the virial method was 15.3 kJ/mol which is slightly decreased as surface coverage is increased with pressure reaching 1 bar. Following the trend observed for CO_2 and CH_4 this value is higher compared to Cu-Pd-nbo. The material's CO_2 / N_2 separation ability is further investigated by IAST calculations in the following section. The values for the virial coefficients extracted from fitting the experimental isotherms for all the aforementioned gases are listed in table 4.10.

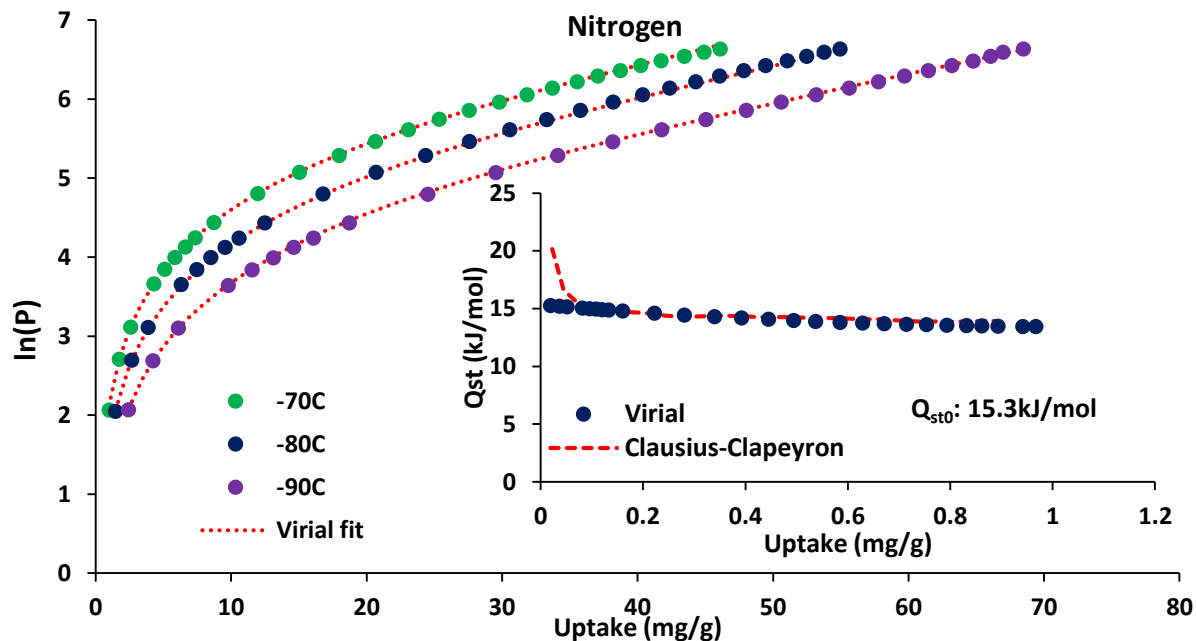


Figure 4.47: Virial type fitting of N_2 adsorption isotherms for In-Pd-soc at -70, -80 and -90 °C and the corresponding isosteric heat of adsorption as a function of N_2 uptake (inset)

Table 4.10: Values for virial coefficients as obtained from fitting of the experimental adsorption isotherms

	Virial equation					
	CO ₂	error	CH ₄	error	N ₂	error
a0	-3585.897	59.45401	-2361.18	31.80515	-1844.99	30.21861
a1	9.26566	1.96596	-22.1169	10.41563	15.93534	2.84916
a2	-0.08135	0.01339	-1.11143	0.75755	-0.32131	0.05795
a3	2.40E-04	4.00E-05	0.08247	0.01725	1.79E-03	5.70E-04
a4	-4.98E-07	1.11E-07	-1.49E-03	3.40E-04	-9.35E-06	4.24E-06
b0	13.03462	0.20772	11.88576	0.11359	11.20957	0.15364
b1	-0.01878	0.00689	0.15363	0.03588	-0.05745	0.0144
b2	0.00016	5.00E-05	-0.00141	0.00228	0.00116	0.00027

Following the same IAST analysis procedure previously described, an initial estimation of the material's selective CO₂ adsorption over CH₄ and N₂ at 0 °C and mixture pressures up to 1 bar was attempted.

Initially, the CO₂ / CH₄ separation ability of In-Pd-soc was studied. In figure 4.46a, CO₂ and CH₄ adsorption isotherms at 0 °C and 1 bar are plotted. Evidently, CO₂ adsorption is thermodynamically favored over CH₄ for the whole pressure range. Various theoretical adsorption models were used in order to fit the experimental adsorption data. For both gases, the best fit was achieved by Langmuir-Freudlich (LF) model expressed as:

$$m(P) = q \frac{(kP)^n}{1+(kP)^n} \quad (4.5)$$

where m is the amount adsorbed as a function of pressure P , q is the adsorbed amount at saturation, k is the Langmuir-Freundlich constant and n is a coefficient accounting for system heterogeneity. If $n=1$, the equation reduces to Langmuir isotherm which also produced an adequate fitting; in fact, n was calculated to be 0.97 for CH₄ indicating a very low degree of heterogeneity while for CO₂ was found to be 0.89 which can be attributed to the different Lewis acid / base interactions with the unsaturated indium sites and the palladium exposed orbitals. The corresponding IAST selectivities produced for three different mixture compositions at 0 °C, are depicted in figure 4.48b.

As it was suggested by the shape of the single component isotherms as well as the difference in adsorbed amount between the two gases and the corresponding variance of their isosteric heat of adsorption, In-Pd-soc is predicted to be a promising candidate for CO₂ / CH₄ separation applications, achieving selectivity values greater than 10 for all the investigated mixture compositions. Moreover, it is expected to perform better for mixtures containing CO₂ in high concentrations since for CO₂:CH₄ ratio of 50:50, the selectivity value reached 20 at 1 bar.

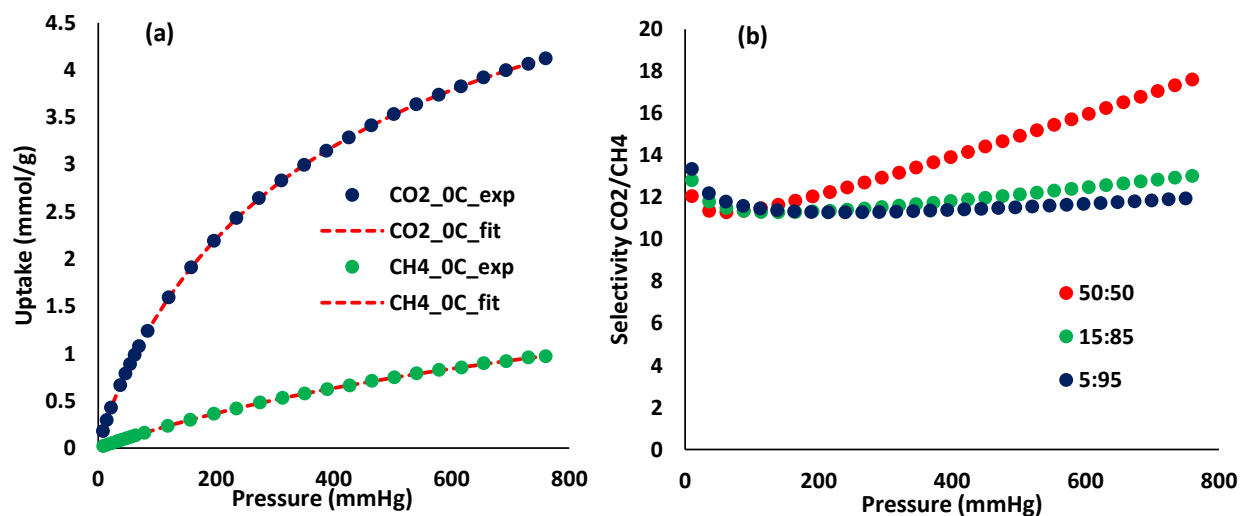


Figure 4.48: *In-Pd-soc* excess adsorption isotherms for CO_2 and CH_4 at 0°C and the corresponding Langmuir-Freundlich fits (a), IAST selectivities for three different CO_2 : CH_4 mixture ratios

Accordingly, the same analysis was performed for *In-Pd-soc* and its CO_2/N_2 separation properties as can be seen in figure 4.49. Likewise, the N_2 adsorption isotherm at 0°C and 1 bar was successfully fitted with Langmuir-Freundlich equation.

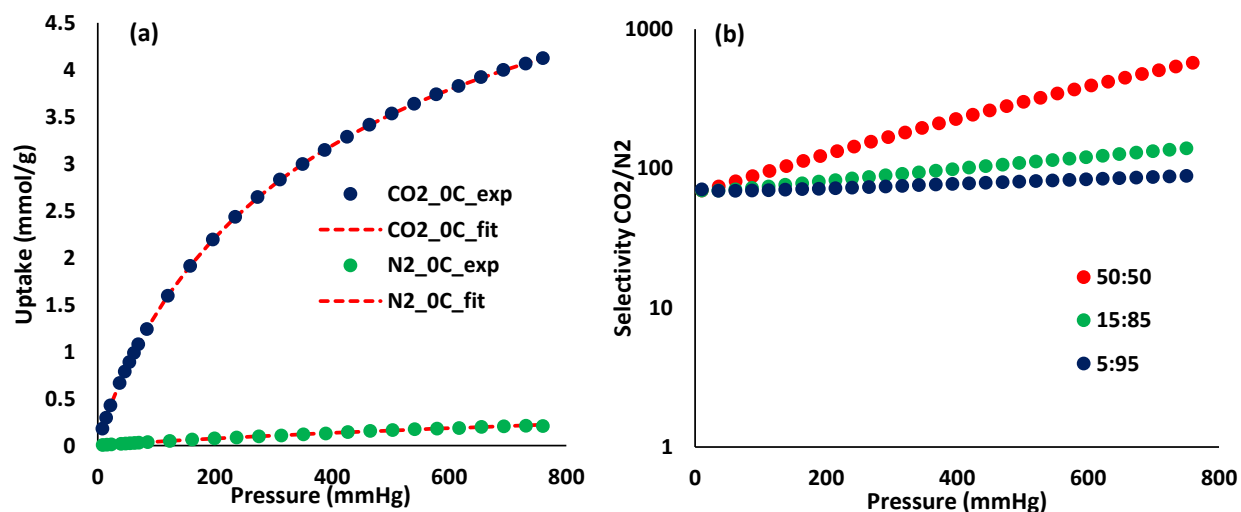


Figure 4.49: *In-Pd-soc* excess adsorption isotherms for CO_2 and N_2 at 0°C and the corresponding Langmuir-Freundlich fits (a), IAST selectivities for three different CO_2 : N_2 mixture ratios

Comparing figure 4.48a and figure 4.49a, as well as their corresponding Q_{st} values, it is obvious that N_2 exhibits even lower affinity for the material's surface than CH_4 does. This evidently translates to the extracted IAST selectivity values for three different CO_2/N_2 mixture compositions that are depicted in figure 4.49b. Similarly to the previously mentioned results, In-Pd-soc is expected to perform exceptionally in separation from mixtures containing high concentration of CO_2 by selectively adsorbing it over N_2 . All the parameters obtained from LF fitting to the experimental adsorption data are listed in table 4.11.

Table 4.11: Values of Langmuir-Freundlich parameters as obtained from fitting the experimental adsorption isotherms

Langmuir-Freundlich			
	CO₂	CH₄	N₂
q	6.59	2.59	1.14
n	0.89	0.97	0.92
k	2×10^{-3}	8×10^{-4}	3×10^{-4}

4.12. High pressure single component isotherms for In-Pd-soc

Further investigation of the adsorption properties of In-Pd-soc was attempted by means of the gravimetric method on an Intelligent Gravimetric Analyzer as described in chapter 3.2. High pressure (up to 20 bar) CO₂, CH₄ and N₂ excess adsorption isotherms were measured at various near ambient temperatures in order to evaluate the materials adsorption capacity up to 20 bar. Furthermore, the kinetic behavior of the adsorbates was studied in order to gain further insight on the gas-surface interactions under specific temperature – pressure conditions related to potential gas storage / separation applications.

Initially, CO₂ excess adsorption isotherms were measured at 0, 5, 15 and 25 °C and the results are illustrated in figure 4.50.

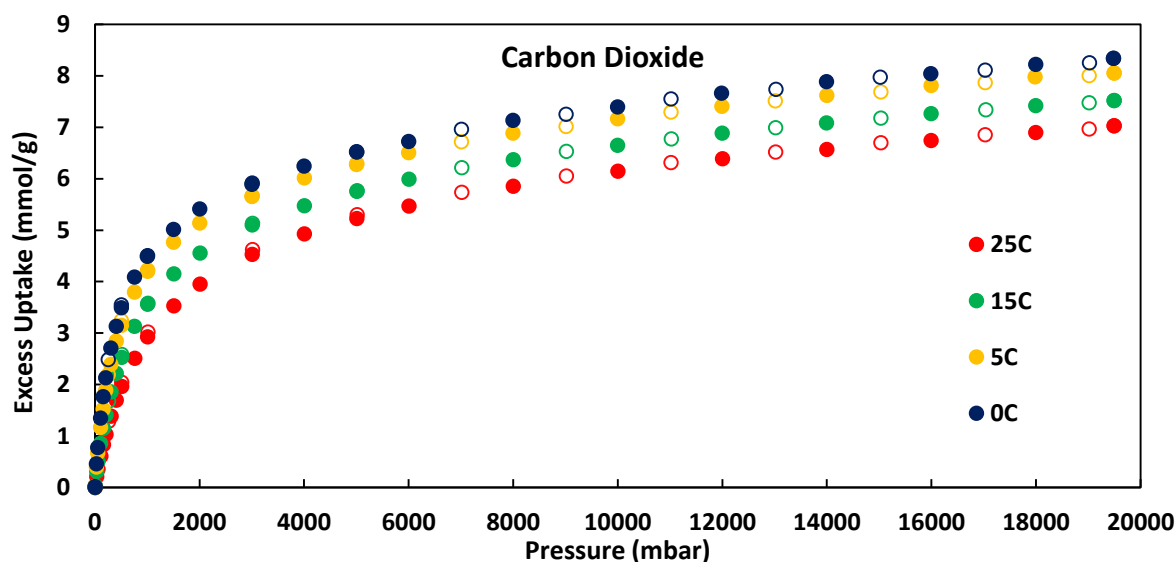


Figure 4.50: CO₂ excess adsorption isotherms for In-Pd-soc at 0, 5, 15 and 25 °C and pressure up to 20 bar.

Fully reversible isotherms were produced exhibiting the same shape and increasing uptake as temperature is decreased, as expected. The isotherm shape resembles the Langmuir isotherm though saturation is not observed at 20 bar. Uptake is increased up to 2 bar and then the isotherm's slope is gradually decreased as pressure raises. In-Pd-soc adsorbed 7.0 (308.1 mg/g, 156.8 cm³ STP/g, 212.0 cm³ STP /cm³) and 8.3 mmol/g (365.3 mg/g, cm³ STP/g, 251.4 cm³ STP /cm³) CO₂ at 25 and 0 °C, respectively. Successful fitting of the 5, 15 and 25 °C isotherms using the virial

coefficients method resulted to zero coverage isosteric heat of adsorption $Q_{st0}=29.2$ kJ/mol, in full agreement with the value calculated (29.8 kJ/mol) from low pressure CO_2 isotherms. Q_{st} remains practically constant as surface coverage increases as depicted in figure 4.51.

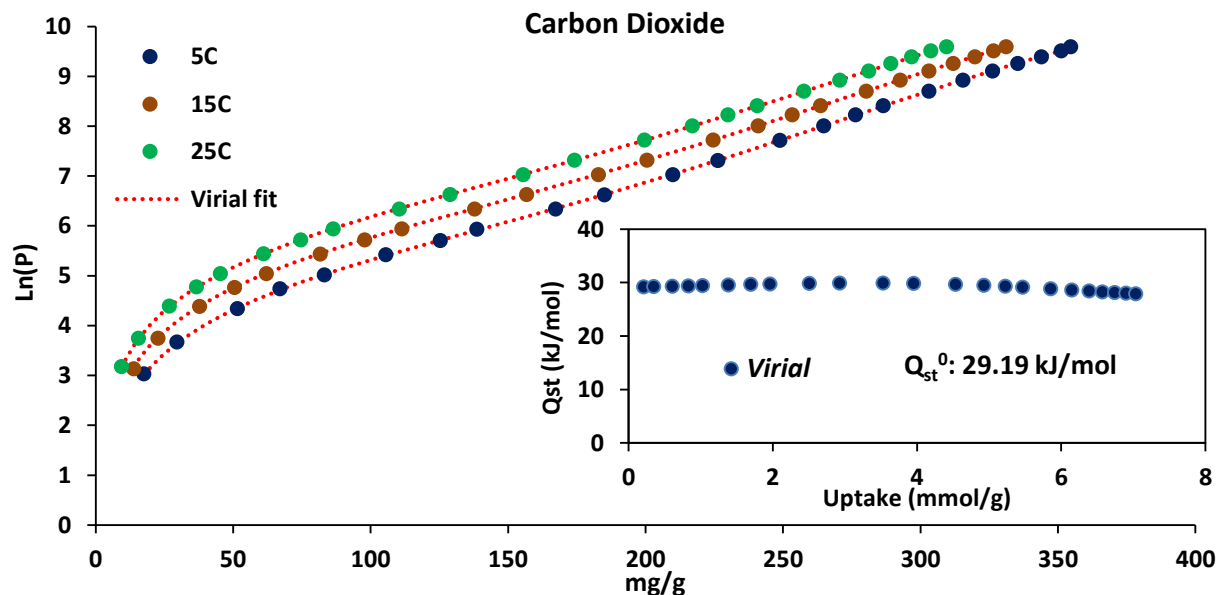


Figure 4.51: Virial type fitting of CO_2 adsorption isotherms for In-Pd-soc at 5, 15 and 25 °C and the corresponding isosteric heat of adsorption as a function of CO_2 uptake (inset)

Subsequently, CH_4 adsorption isotherms were measured for In-Pd-soc at the same pressure / temperature conditions as for CO_2 so that a direct comparison in adsorption properties is achieved.

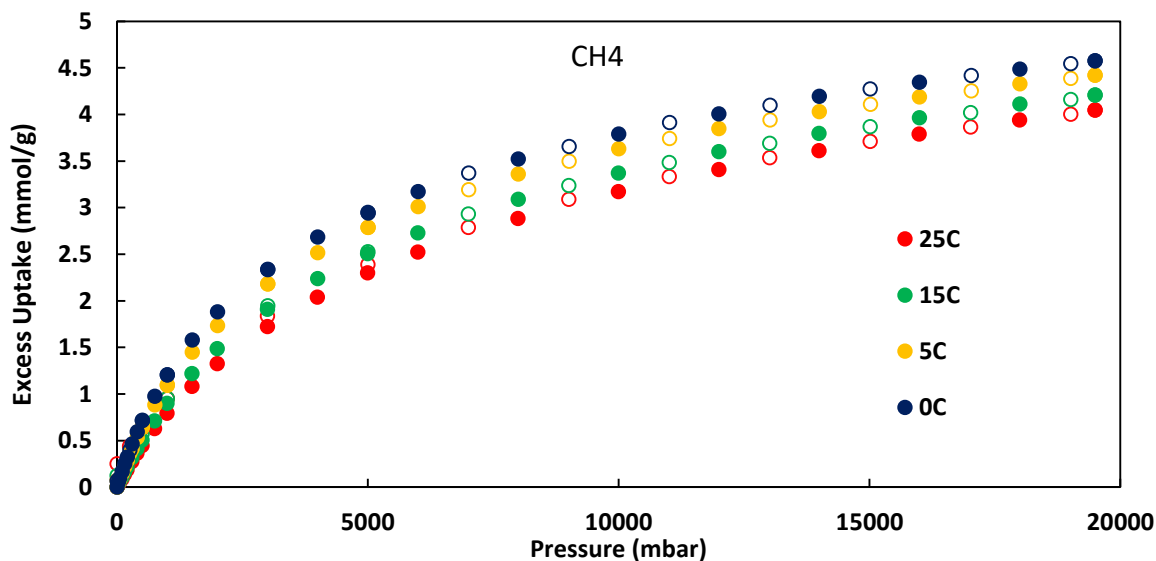


Figure 4.52: CH_4 excess adsorption isotherms for In-Pd-soc at 0, 5, 15 and 25 °C and pressure up to 20 bar.

Fully reversible excess adsorption isotherms were produced. CH_4 uptake is continuously increased reaching 4.1 (65.6 mg/g, 91.8 cm^3 STP/g, 124.2 cm^3 STP / cm^3) and 4.6 mmol/g (73.6 mg/g, 103.0 cm^3 STP/g, 139.3 cm^3 STP/ cm^3) at 25 and 0 °C, respectively and pressure of 19.5 bar. The isotherm's slopes were decreased compared to CO_2 , which is indicative of weaker gas - surface interactions. Consequently, Q_{st0} was found to be 16.19 kJ/mol, while it decreases slightly at higher coverage. This value is significantly lower than the one obtained from the low pressure CH_4 adsorption isotherms (19.6 kJ/mol). This discrepancy can be ascribed to the limited amount of equilibrium isotherm points at sub-atmospheric pressures compared to the low-pressure isotherm. Acknowledging the slight but continuous decrease in Q_{st} values evident in figure 4.53, a composition of the low- and high-pressure experiments should be considered regarding the optimal use of CH_4 isosteric heat of adsorption. The Q_{st0} value (19.6 kJ/mol) obtained from the low-pressure isotherms should be adopted but as surface coverage increases the plot in figure 4.53 describes the adsorption phenomenon accurately.

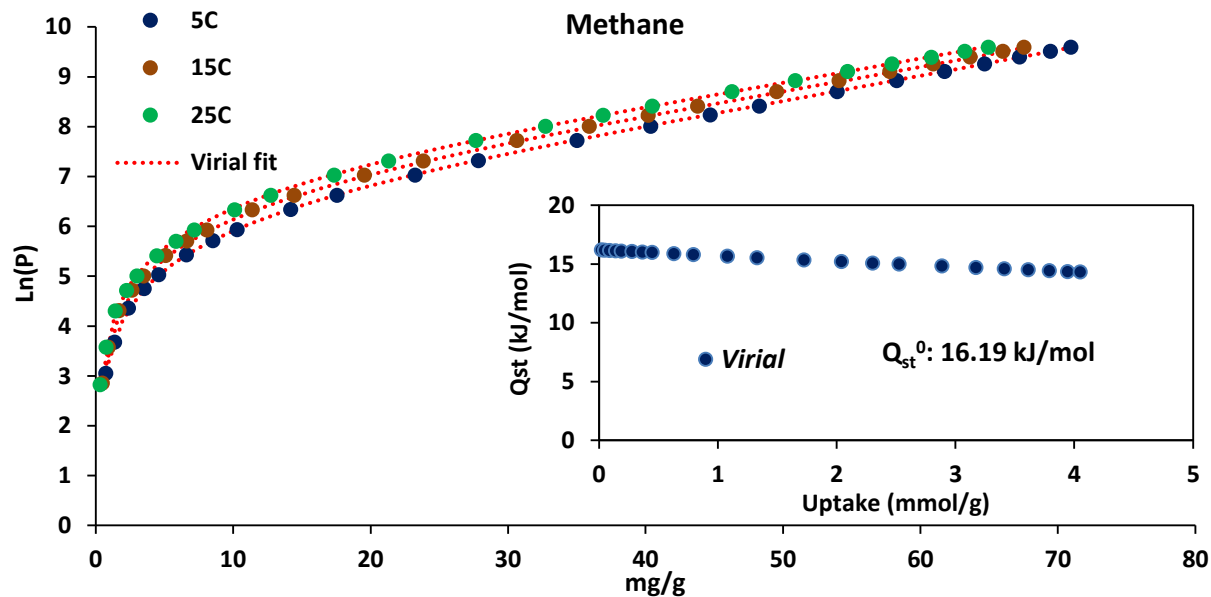


Figure 4.53: Virial type fitting of CH_4 adsorption isotherms for In-Pd-soc at 5, 15 and 25 °C and the corresponding isosteric heat of adsorption as a function of CH_4 uptake (inset)

Finally, N_2 adsorption properties for In-Pd-soc were evaluated as well by measuring isotherms under the same conditions described above and the results are illustrated in figure 4.54.

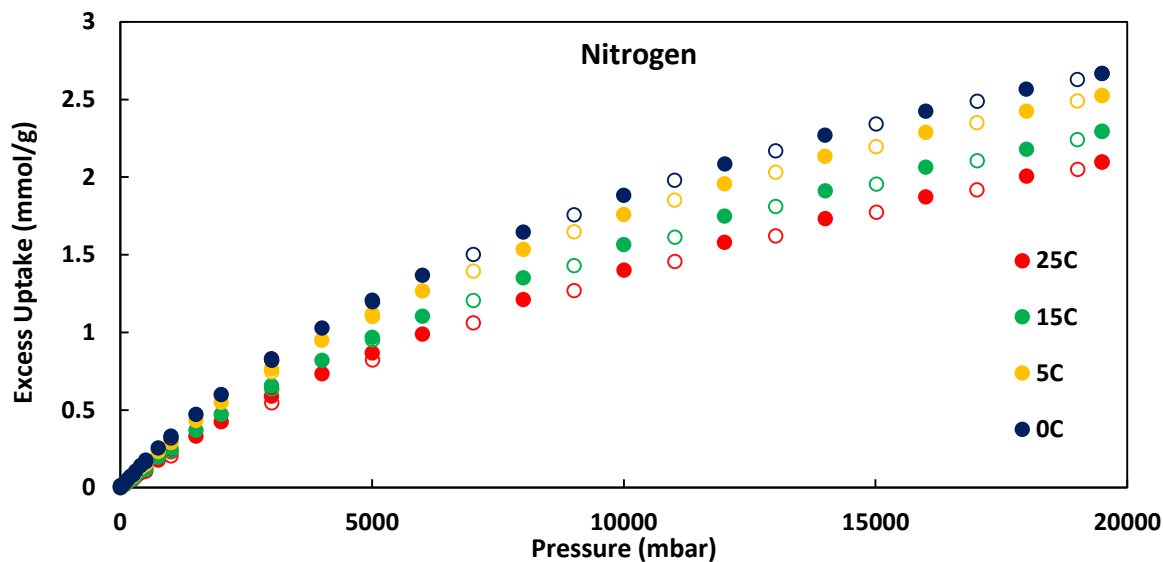


Figure 4.54: N_2 excess adsorption isotherms for In-Pd-soc at 0, 5, 15 and 25 °C and pressure up to 20 bar.

The experiments revealed fully reversible N₂ excess adsorption isotherms which exhibit almost linear uptake increase with pressure. However, due to nitrogen's weak interactions with the material's surface, In-Pd-soc adsorbed 2.1 mmol/g (128.8 mg/g, 103.0 cm³ STP/g, 139.3 cm³ STP/cm³) at 25 °C, and pressure of 19.5 bar. Virial fitting of the isotherms resulted at $Q_{st}^0=9.01$ kJ/mol which substantially deviates from the value obtained at low pressure isotherms, most probably due to limited amount of equilibrium pressure points below 1 bar, as already mentioned for CH₄ in combination with the low uptake demonstrated by the sample. However, isosteric heat of adsorption as a function of surface coverage increases to 15 kJ/mol, in agreement with the aforementioned results, as can be seen in the inset of figure 4.55.

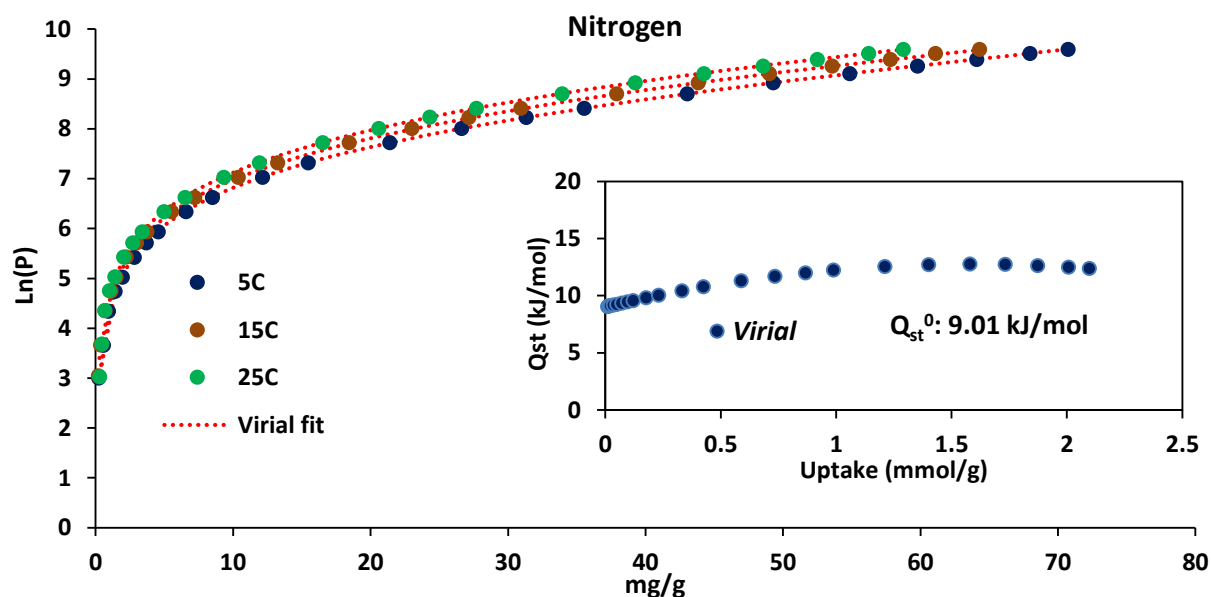


Figure 4.55: Virial type fitting of CH₄ adsorption isotherms for In-Pd-soc at 5, 15 and 25 °C and the corresponding isosteric heat of adsorption as a function of N₂ uptake (inset)

The values for the virial coefficients that were extracted from the CO₂, CH₄ and N₂ experimental adsorption data are listed in table 4.12.

Table 4.12: Virial coefficients values for In-Pd-soc as obtained from fitting the experimental adsorption isotherms

	Virial equation					
	CO ₂	error	CH ₄	error	N ₂	error
a0	-3510.36188	48.13204	-1947.91	77.33071	-1083.94	158.6612
a1	-0.19422	0.68567	10.48626	6.80744	-20.7758	17.06838
a2	-0.01332	0.0021	-0.04326	0.10911	0.25648	0.30244
a3	9.00E-05	4.53E-06	0.0002	0.00121	-5.70E-04	2.98E-03
a4	-1.28E-07	6.30E-09	1.39E-07	8.86E-06	3.89E-06	2.00E-05
b0	12.62557	0.16559	10.4143	0.26774	8.30532	0.55071
b1	0.01104	0.00236	-0.01857	0.02364	0.08457	0.05954
b2	-0.00001	6.80E-06	0.00021	0.00036	-0.0008	0.00104

The kinetic experimental data acquired using the gravimetric method, from the CO₂, CH₄ and N₂ adsorption isotherms were studied according to the procedure described earlier. Plots of mass relaxation as a function of time following a pressure step change at 0 and 25 °C for the three adsorbates are illustrated in figure 4.56. The indicated pressure step changes are 500 – 1000 mbar for N₂, 1500 – 2000 mbar for CH₄ and 250 – 500 mbar for CO₂. Similarly to Cu-Pd-nbo, equilibrium is achieved within 15 minutes in every case suggesting the absence of kinetic hindrance even though In-Pd-soc exhibits smaller pore size (5.8 compared to 9.8 Å). In order to calculate the diffusion time constants, equation 3.16 was used to fit the experimental kinetic data, assuming micropore diffusion as the main mass transfer resistance controlling the adsorption process. As can be seen in figure 4.56, the selected model adequately fits the experimental data suggesting the latter hypothesis to be accurate.

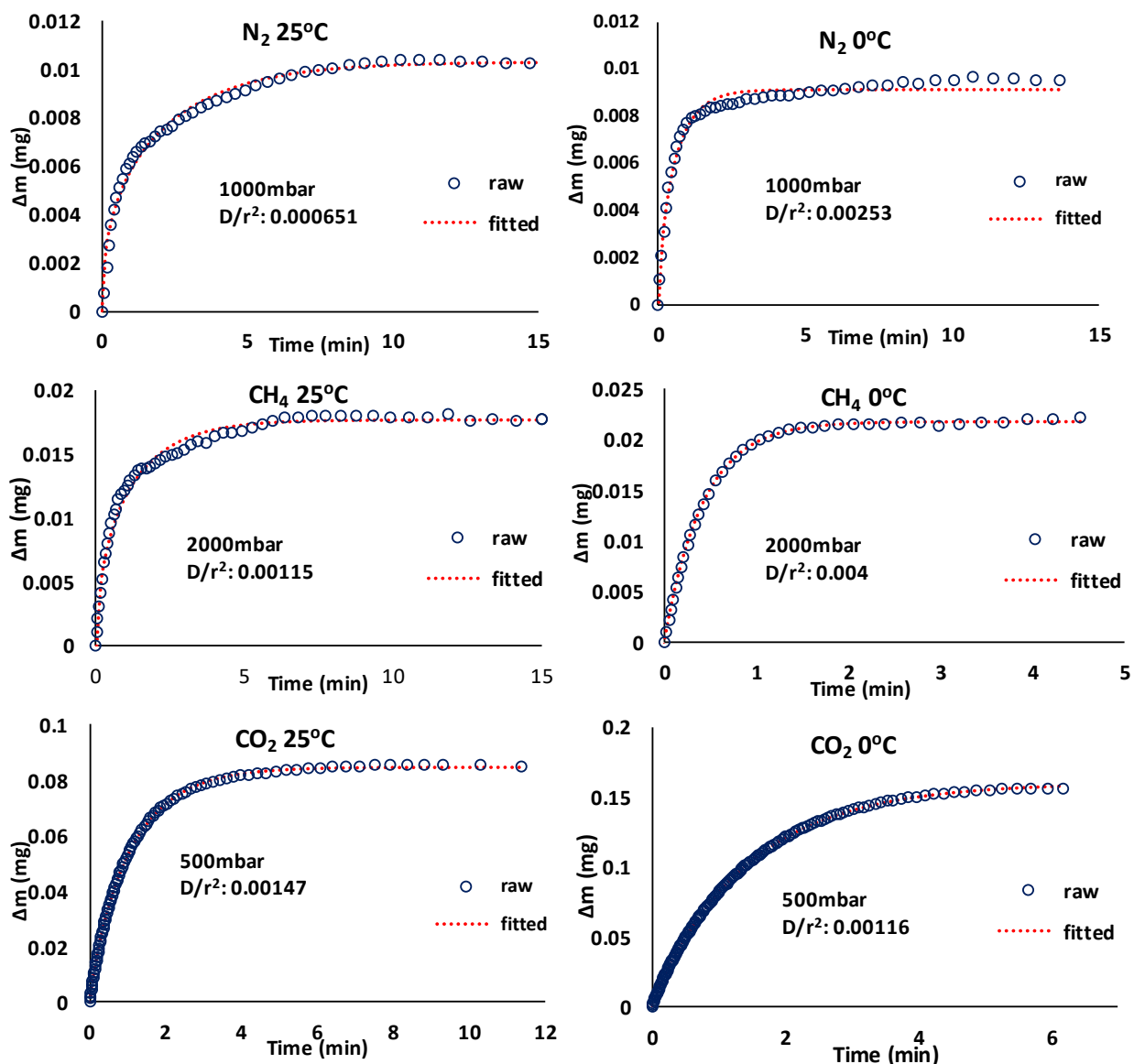


Figure 4.56: Selected kinetic data at 0 and 25 °C, for pressure step changes 250-500 mbar for CO₂ 500-1000 mbar for N₂ and 1500-2000 mbar for CH₄. (D/r^2 values are given in min^{-1} units)

Accordingly, the diffusion time constants (D/r_c^2) were calculated for CO₂, CH₄ and N₂ at different pressure step changes at 0 and 25 °C and are listed in table 4.13. For the most strongly adsorbed CO₂ D/r_c^2 values were found to be practically constant for the studied pressure ranges varying from 1.2 to 2.1×10^{-3} at 25 °C and from 6.9×10^{-4} to 1.6×10^{-3} at 0 °C, suggesting independence from pressure change and confirming the assumption of micropore diffusion as the

controlling mechanism of the adsorption process. The same stands for CH₄ and N₂. The diffusion time constants for CH₄ range from 1 to 2.1 x10⁻³ at 25 °C and 3.1 to 4 x10⁻³ at 0 °C while for N₂ fluctuate from 6.5 x10⁻⁴ to 2.7 x10⁻³ at 25 °C and 2.5 to 5.1 x10⁻³ at 0 °C.

Table 4.13: CO₂, CH₄ and N₂ diffusion time constant values as obtained from the experimental adsorption kinetic curves

Diffusion time constant (D/r²) (min⁻¹)						
Pressure (mbar)	CO₂ 25°C	CO₂ 0°C	CH₄ 25°C	CH₄ 0°C	N₂ 25°C	N₂ 0°C
125	2.12x10 ⁻³	1.60x10 ⁻³				
200	2.04x10 ⁻³	7.66x10 ⁻⁴				
500	1.47x10 ⁻³	1.16x10 ⁻³				
750	1.40x10 ⁻³	1.08x10 ⁻³		3.67 x10 ⁻³		
1000	1.27x10 ⁻³	1.46x10 ⁻³	1.04x10 ⁻³	3.72 x10 ⁻³	6.5110 ⁻⁴	2.53x10 ⁻³
1500	1.32x10 ⁻³	1.37x10 ⁻³				
2000	1.22x10 ⁻³	6.94x10 ⁻⁴	1.15x10 ⁻³	4.00 x10 ⁻³	1.60 x10 ⁻³	4.23x10 ⁻³
4000			2.07x10 ⁻³	3.09 x10 ⁻³	2.73 x10 ⁻³	5.11x10 ⁻³
6000			1.44x10 ⁻³	3.49 x10 ⁻³	1.90 x10 ⁻³	3.10x10 ⁻³

To sum up, CO₂, CH₄ and N₂ excess adsorption isotherms at 25 °C and pressure up to 20 bar are plotted together in figure 4.55. Evidently, CO₂ adsorption is favored over CH₄ and N₂ for the whole pressure range. The difference in uptake is larger for pressures up to 2 bar and subsequently the slopes of the three isotherms seem to become equal. Considering the information extracted from the experimental kinetic data the variance in uptake between the three adsorbates occurs predominantly for thermodynamic reasons.

Compared to Cu-Pd-nbo, In-Pd-soc is expected to perform better in CO₂ / CH₄ separation applications at relatively high pressure taking into account that it exhibits higher *Q_{st}* value for CO₂ and similar for CH₄. However, its substantially lower gravimetric adsorption properties cannot be overlooked in terms of efficient capacity in a real gas separation system.

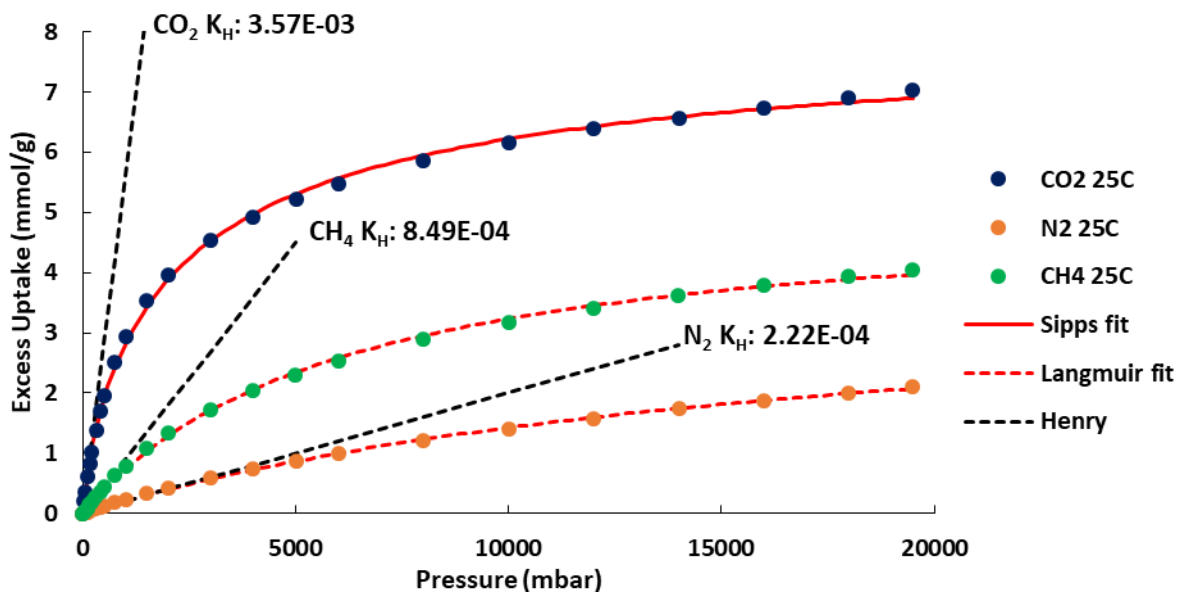


Figure 4.57: CO_2 , CH_4 and N_2 excess adsorption isotherms for In-Pd-soc at 25 °C and pressure up to 20 bar. The red dotted lines represent the corresponding Langmuir fit, the red continuous line the Langmuir-Freundlich fit (also known as Sips) and the black dotted lines the expansion of the Henry region of the isotherms.

CH_4 and N_2 adsorption isotherms were thermodynamically described using the Langmuir isotherm model as can be seen by the successful fitting of the experimental data in figure 4.57. However, Langmuir-Freundlich (also known as Sips) equation had to be used in order to fit the CO_2 adsorption isotherm, suggesting the inhomogeneity of the CO_2 adsorption sites due to the different electrostatic interactions induced by the presence of the unsaturated indium sites and the exposed palladium orbitals. All the parameters obtained as well as the corresponding Henry constants are listed in table 4.14.

Table 4.14: Values for the parameters obtained by fitting the In-Pd-soc experimental adsorption isotherms as well as calculated values for Henry constants, in mmol/(g mbar)

	Langmuir			Sipps	Henry	
	N_2	CH_4		CO_2	CO_2	K_H
q	3.97239	5.21452	q	8.19213	CO_2	3.57E-03
k	5.60E-05	1.63E-04	k	4.36E-04	CH_4	8.49E-04
			n	1.28249	N_2	2.22E-04

4.13. Dynamic Column Breakthrough (DCB) experiments

So far, the materials' adsorption properties have been determined through single component isotherms and selectivities between two adsorbates have been predicted using the Ideal Adsorption Solution Theory. Additionally, Dynamic Column Breakthrough (DCB) experiments have been performed in order to evaluate a material's gas mixture separating performance under conditions that approximate the ones of an actual separation process. The competitive adsorption of CO₂ and CH₄ or N₂ was studied through DCB experiments at room temperature and pressure ranging from 1 to 5 bar, according to the experimental procedure described in chapter 3.4.3.

The limited availability of the two materials which are synthesized in the scale of milligrams presents a challenging situation regarding the design of the experiment. For this reason, a custom-made sample holder (column) of 77 mm length and 3 mm internal diameter for small sample quantities was built. Moreover, low volumetric flow rates were used in order to extend the experiment duration and avoid significant pressure drop in the column, so that accurate and well-defined breakthrough responses (figure 4.58) can be produced.

Breakthrough curves contain valuable mixture equilibrium and kinetic information. Adsorbates' loadings can be determined for different temperature pressure conditions by using a simple dynamic molar balance of the form:

$$n_{acc} = n_{in} - n_{out} \quad (4.6)$$

where n_{acc} are the moles accumulated by the column, n_{in} are the moles entering the column related to the predetermined volumetric flows and n_{out} are the moles leaving the column, a fraction of which is analyzed by the mass spectrometer. The accumulated moles are the adsorbed moles on the material's structure plus the moles that are found in the gas phase, meaning in the dead volume before, after and inside the column. Considering the size of the particular sample holder, filled with a predominantly microporous material, it is assumed that its dead volume is negligible for this system. However, this is not the case for the volume outside the column. For this reason, as already mentioned in chapter 3.4.3, helium (the adsorption of which is considered negligible at room temperature) breakthrough curves were obtained under identical experimental conditions to the mixture measurements in order to account for the time needed by the gas to fill the void volume.

The mean retention time, t_t , of a breakthrough curve (time required for reaching the column's total capacity) is calculated by numerically integrating the expression:

$$t_t = \int_0^{\infty} \left(1 - \frac{C_t}{C_0}\right) dt \quad (4.7)$$

where C_t is the adsorptive's concentration at time t and C_0 is the feed concentration. Considering the shape of a typical DCB experiment with two components illustrated in figure 4.58, the integral of equation for component 2 reflects the area between the red line, the blue dotted line and the two axes. Component 1 exhibits normalized concentration values that exceed unity. This phenomenon, known as roll-up effect, is indicative for competitive adsorption on microporous materials presenting type-I isotherms. In this case, t_t corresponds to area A minus area B. The roll-up is observed on the breakthrough curve of the component which exhibits the weaker interactions with the surface, therefore moves faster within the column. As the strongly adsorbed gas (component 2 in figure 4.58) is transferred in the column, it displaces the already adsorbed first component, causing desorption of component 1 and thus a temporary increase in its concentration. The larger the difference of gas-surface interaction between the two components, (e.g. difference in Q_{st}), the more intense is the observed roll-up.

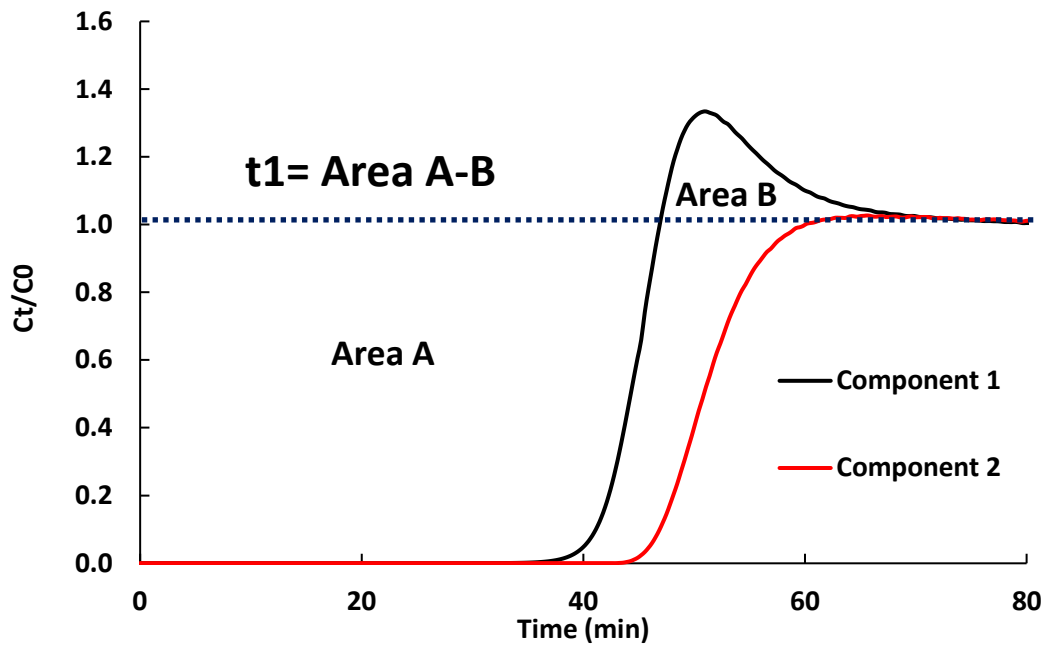


Figure 4.58: A typical DCB experiment with two components successfully separated at the exit of the column.

The calculation of t_i for each component allows the determination of the adsorbed quantities by using the following equation.

$$q_1 = \frac{y_f Q_f t_i P_s}{RT_s m_s} \quad (4.8)$$

where q_1 is the component 1 loading, y_f is component's feed molar fraction, Q_f the volumetric feed flow rate at STP, P_s the standard pressure, T_s the standard temperature and m_s is the mass of the activated sample. It needs to be noted that in equation 4.8, t_i is the "corrected" retention time after subtraction of helium mean retention time determined by the blank experiment.

Cu-Pd-nbo, which showed superior structural and adsorption properties was selected for further investigation and further tested for its separation potential in CO₂/CH₄ and CO₂/N₂ mixtures at 25 °C. Binary adsorption experiments were performed for the two mixtures at two different compositions: 10:90 and 50:50 at 0.97 bar. For CH₄ containing mixtures the experiments were additionally performed at 5 bar in order to further approximate processes that are relevant with natural gas applications. Initially, the CO₂/CH₄ breakthrough curves at 0.97 bar are considered and the results are illustrated in figure 4.59.

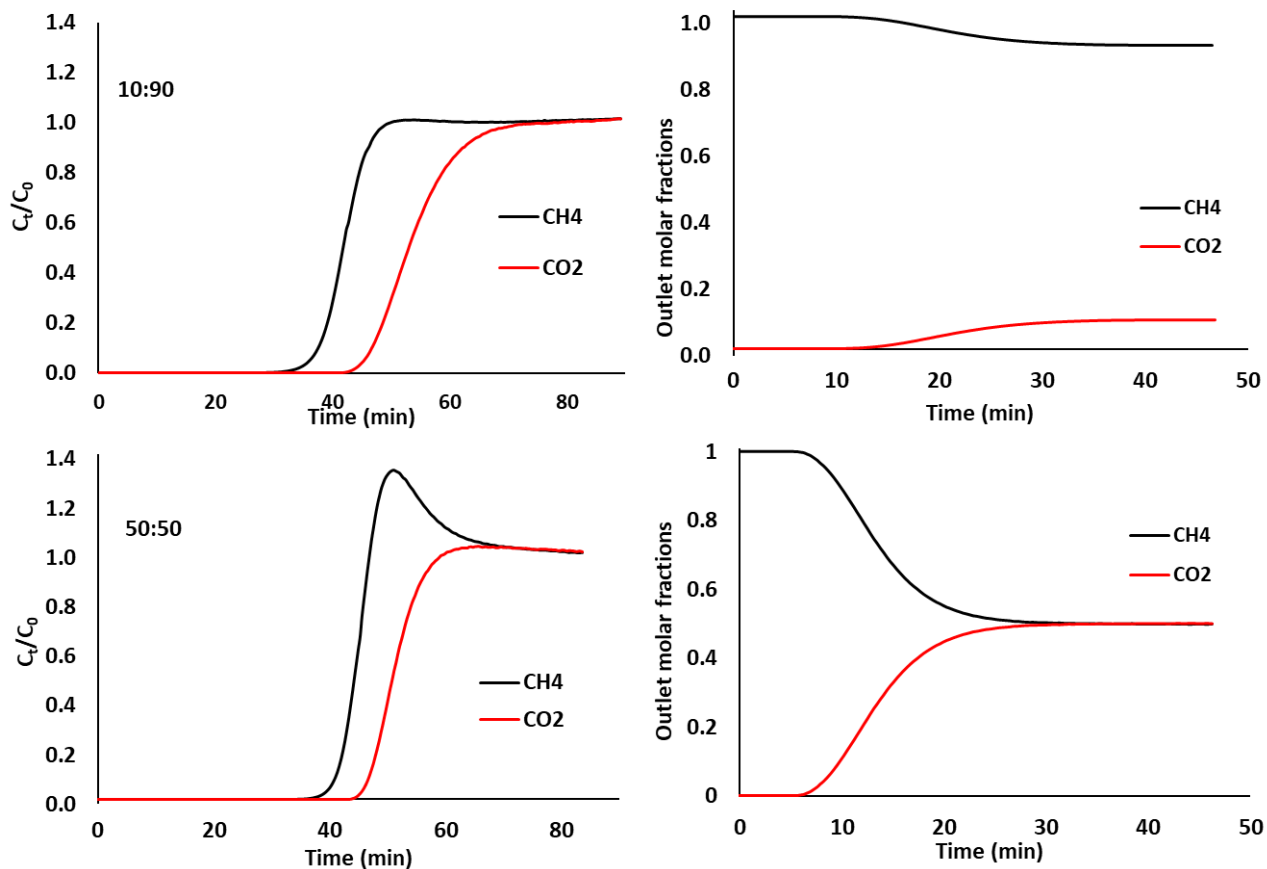


Figure 4.59: CO_2/CH_4 breakthrough profiles for compositions 10:90 and 50:50 at 0.97 bar and 25 °C (left), and the corresponding molar fractions of the effluents at the exit of the column after the first component breaks through (right).

These experiments were performed with a total flow of 1.5 ml/min in order to avoid significant pressure drop along the column. As can be seen from the breakthrough curves, Cu-Pd-nbo achieved complete separation of the mixtures even for the composition with the higher concentration on CO_2 as already predicted from the IAS theory. In both cases, CH_4 is eluted first and CO_2 follows after 8 and 12 minutes for the 50:50 and 10:90 mixtures respectively. The roll-up effect is observed for the 50:50 mixture as expected. Interestingly, in the case for the 10:90 composition, it is much less pronounced. This probably occurs due to the slower mass transfer of CO_2 in the column resulting to a “milder” displacement of the adsorbed CH_4 molecules. CH_4

breakthrough times are increased with decreasing concentration as anticipated. However, the same behavior is not clearly observed for CO₂, which is indicative of the enhanced interactions with the surface of the material. The sample exhibits similar CO₂ breakthrough times for the two compositions. However, for the 50:50 mixture the slope of the curve is clearly sharper, suggesting faster mass transfer in the column, as expected for the higher concentration mixture. The competitive loadings of CO₂ and CH₄ as well as the corresponding CO₂/CH₄ selectivities were calculated after the helium blank corrections. A summary of the results for all the breakthrough experiments can be found in table 4.14. The experimental results correlate excellent with the predicted IAST competitive loadings at 298K for the 50:50 composition resulting to almost identical selectivities (8.8 predicted by IAST vs 7.0 calculated by the experiment). However, a slight deviation is observed for the 10:90 mixture where the experimental selectivity was calculated 17.2 while the predicted IAST was 8.6. The limitations of IAST estimations have been addressed in literature. Especially for cage-like materials bearing unsaturated metals, CO₂ molecules tend to congregate around these sites resulting to an inhomogeneous adsorbate distribution in direct contrast to the assumption of homogeneity introduced by IAST.¹²³ The concept of energetic inhomogeneity on the material's porous network, was already suggested by the trend of the slight but continuous increase in CO₂ Q_{st} as a function of surface coverage, observed in both high and low pressure single component measurements as well as from the thermal desorption spectroscopy (TDS) experiments.

Subsequently, Cu-Pd-nbo was evaluated for its separation ability on CO₂/CH₄ mixtures at pressure of 5 bar and the results are illustrated in figure 4.60. The high-pressure binary adsorption experiments showed similar qualitative characteristics to the ones obtained from the 0.97 bar breakthrough curves. In both cases, complete separation of the mixture is achieved. CH₄ is eluted first and is the only component detected by the mass spectrometer before CO₂ breaks through the column. The CH₄ breakthrough curve obtained for the 50:50 mixture exhibits a pronounced roll-up effect, which is not present at the 10:90 experiment, precisely like the 0.97 bar experiments as described above. The competitive loadings of CO₂ and CH₄ were calculated after the helium blank corrections and are listed in table. The corresponding calculated selectivities exhibit the same trend observed from the experiments at 0.97 bar. More specifically, they were calculated to be 18.3 (vs 9.1 calculated from IAST) and 9.3 (vs 9.9 calculated from IAST) for the 10:90 and 50:50 mixture

compositions respectively. The unusual pattern of the increased selectivity with increasing pressure predicted by IAST was verified by the experimental data.

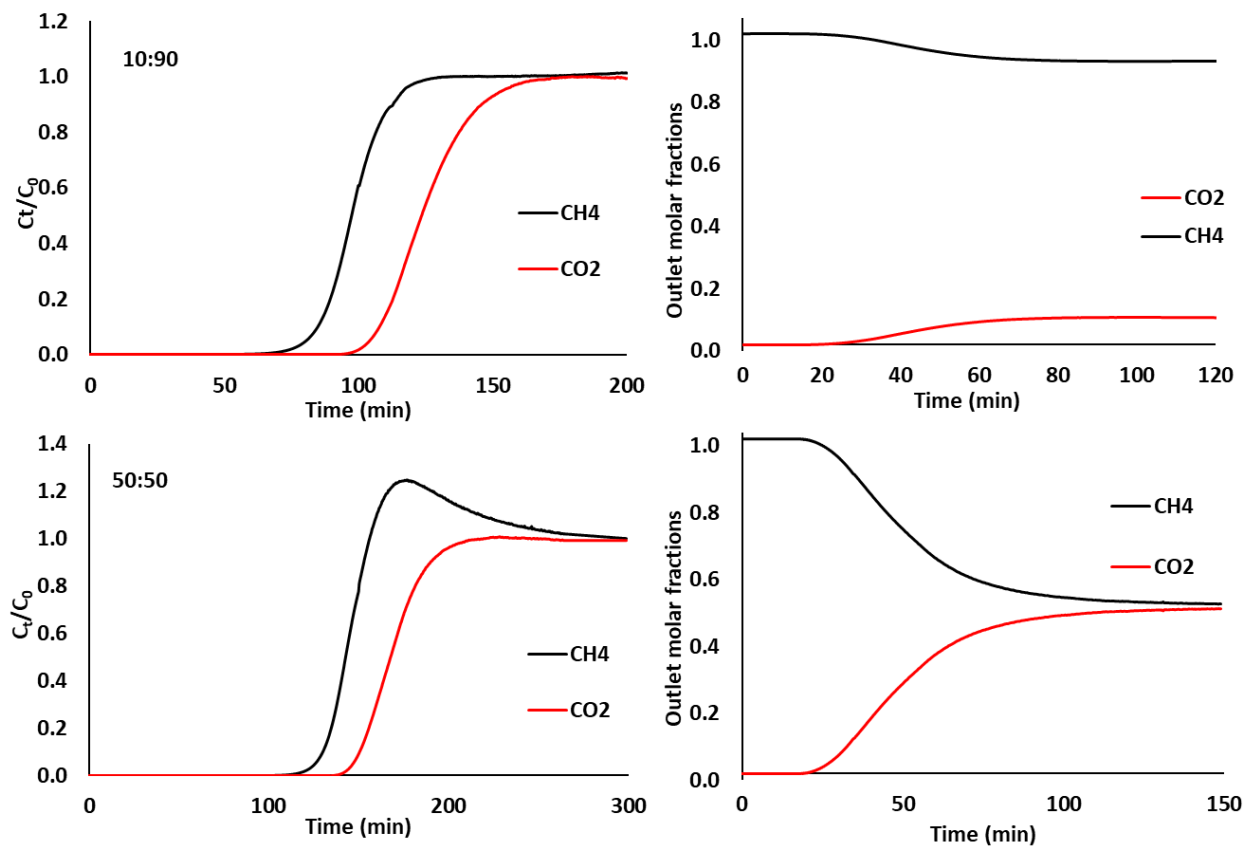


Figure 4.60: CO₂/CH₄ breakthrough profiles for compositions 10:90 (total flow: 2.25ml/min) and 50:50 (total flow: 1.5 ml/min) at 5.0 bar and 25 °C (left), and the corresponding molar fractions of the effluents at the exit of the column after the first component breaks through.

Then the material was tested at room temperature and pressure of 0.97 bar in mixtures containing CO₂ and N₂, a process linked with CO₂ separation from flue gas applications. Likewise, two different compositions were tested, containing 50% and 10% CO₂ molar fractions. The total flow was 1.5ml/min and the void volume correction was performed with helium at identical experimental conditions. As can be seen in figure 4.61, Cu-Pd-nbo achieved complete separation of the mixture in both cases.

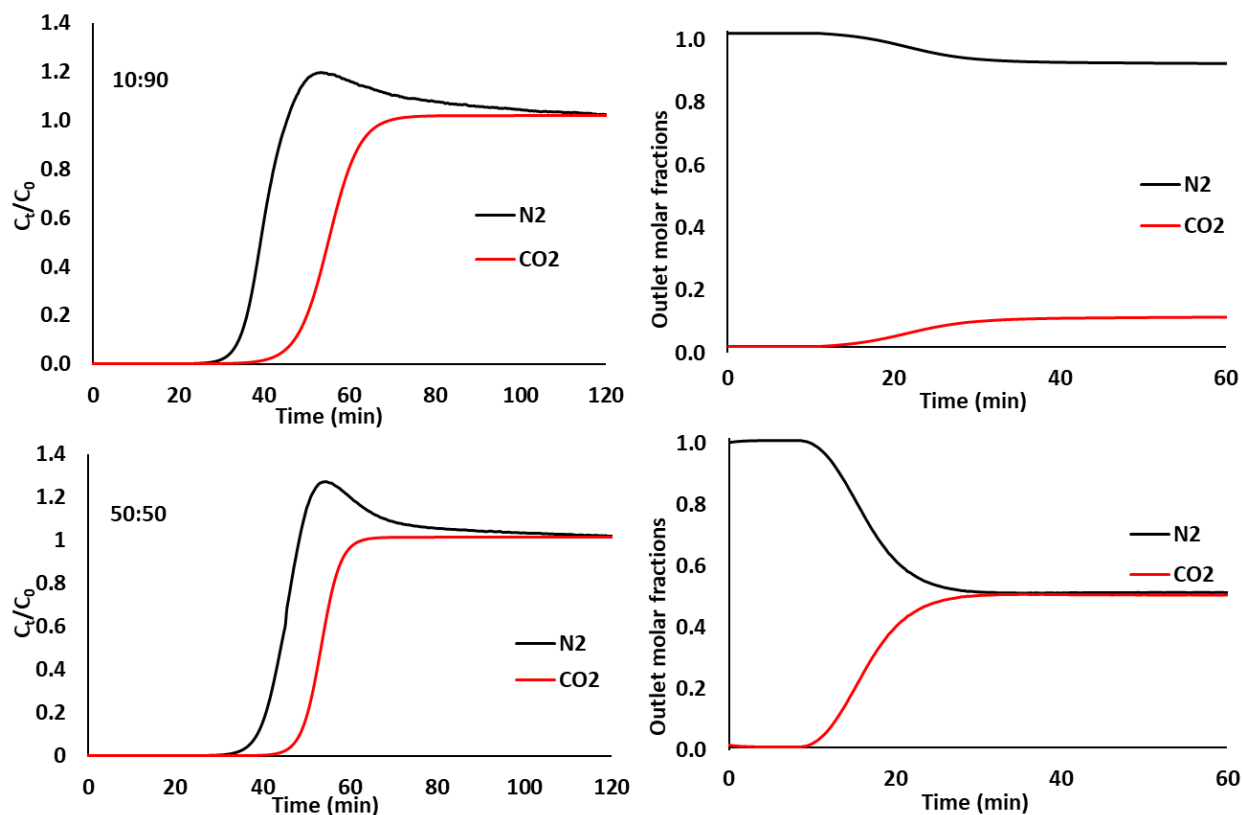


Figure 4.61: CO_2/N_2 breakthrough profiles for compositions 10:90 and 50:50 (left), and the corresponding molar fractions of the effluents at the exit of the column after the first component breaks through.

Evidently, N_2 breaks through first and the outlet composition reaches 100 mol% N_2 and after approximately 15 and 20 minutes later, CO_2 is eluted for the 50:50 and 10:90 mixture compositions, respectively. The roll up effect is observed in both cases although it is clearly more pronounced for the 50:50 mixture as expected. This probably occurs due to the low N_2 – surface affinity suggested by the low calculated Q_{st} values. Therefore, N_2 molecules are desorbed in a more pronounced way (compared to CH_4) as the strongly adsorbed CO_2 is transferred through the column. Competitive CO_2 loadings were calculated and are illustrated in table 4.15. N_2 loading was calculated to be 0.07 mmol/g for the 10:90 composition and the corresponding selectivity 79.8. However, for the 50:50 composition, N_2 loading calculations resulted to physically impossible negative values. In order to assess this, the dynamic column breakthrough experiments

were repeated so as to be checked for reproducibility. However, it was observed that although the curves were successfully repeated, the error persisted. It appears that an inherent unreliability for mixtures containing species with great difference in Q_{st} values between them, hence greater adsorption competition among them, is observed. The light component is eluted very fast and its quantitative determination through numerical integration of the breakthrough curve is associated with a certain degree of uncertainty related to the mass flow controllers' sensitivity. Similar results of negative or insignificant amounts of competitive adsorbed N_2 on zeolites have been reported in literature before.^{100,102} This highlights another concern for reporting selectivities based on single component isotherms only, especially for CO_2/N_2 mixtures where values exceeding 1000 are often calculated and is really difficult to be experimentally verified.

Table 4.15: Summary of the conducted DCB experiments and the calculated competitive adsorption loadings.

Gas	Q_{in} <i>(ml/min)</i>	P (bar)	y_{CO_2}	y_{CH_4}	y_{N_2}	q_{CO_2} <i>(mmol/g)</i>	q_{CH_4} <i>(mmol/g)</i>	q_{N_2} <i>(mmol/g)</i>
CO₂/CH₄	1.5	0.97	0.5	0.5	-	1.76	0.24	-
CO₂/CH₄	1.5	0.97	0.1	0.9	-	0.51	0.31	-
CO₂/CH₄	2.25	5.0	0.1	0.9	-	2.22	1.24	-
CO₂/CH₄	1.5	5.0	0.5	0.5	-	6.04	0.64	-
CO₂/N₂	1.5	0.97	0.5	-	0.5	2.43	-	[0]
CO₂/N₂	1.5	0.97	0.1	-	0.9	0.67	-	0.07

5. Conclusions

The synthetic procedure of two new heterobimetallic MOFs was briefly described. The novelty of this procedure lies within the idea for incorporation of additional strong adsorption sites in the structure by using a metallated organic linker. More specifically, a palladated planar linker was used in order to coordinate two different SBUs, the binuclear Cu-paddlewheel and the trinuclear In- μ^3 -oxo bridge, resulting to the formation of the corresponding novel structures, Cu-Pd-nbo and In-Pd-soc, respectively. The structures were fully resolved by synchrotron SC-XRD analysis.

PXRD, IR and SEM were used and confirmed the formation, phase purity and chemical stability of the newly synthesized crystalline materials. Although the materials appear to be stable in most organic solvents, they seem to be unstable in water. This can be a disadvantage for their application in processes like post-combustion CO₂ capture or natural gas/biogas upgrading where humidity is always present. However, this can be easily resolved with the use of an extra column containing a desiccant.

TGA analysis was performed and revealed satisfying thermal stability of the samples. More specifically it was found that Cu-Pd-nbo remained structurally intact up to 180 °C, while In-Pd-soc up to 215 °C.

Cu-Pd-nbo was easily activated by heating at 50 °C under high vacuum for 12 h. Ar/N₂ porosimetry at 87/77 K, respectively, revealed fully reversible type-I isotherms verifying the extensive microporous structure of the sample, already seen by the SC-XRD analysis. The corresponding BET specific surface areas were calculated 1415 and 1473 m²/g and the total pore volume 0.53 cm³/g. Moreover, application of an NLDFT kernel in the Ar isotherm produced a well-defined pore size distribution showing a major peak at 9.5 Å. These values are in agreement with the crystallographic data confirming the successful activation and the material's permanent porosity.

Subsequently, CO₂, CH₄ and N₂ excess adsorption isotherms were performed at a wide range of temperatures and pressures up to 20 bar. Cu-Pd-nbo presented exceptional CO₂ adsorption capacity which was calculated to be 8.5 mmol/g (190.1 cm³ STP/g, 373.5mg/g) at

0 °C and 1 bar. These values rank it among the highest reported for the entire nbo-family and it is a strong indication of enhanced gas-surface interactions, essentially verifying the novel synthetic idea. Moreover, due to its relatively high crystallographic density (0.98 g/cc) volumetric capacity of 186.2 cm³ STP/cm³ was calculated which is one of the highest values ever reported for the entire family of MOFs. The unusually high crystallographic density is attributed to the presence of Pd on the organic linker and constitutes an interesting choice to increase the adsorbent's volumetric capacity which is also a crucial parameter for efficient applications. The corresponding CO₂ isosteric heat of adsorption, Q_{st} , was calculated equal to 26.2 kJ/mol at zero coverage, while it increases continuously with increasing loading. This suggests inhomogeneous distribution of the adsorbed species within the porous network of the material which was already suggested by quantum chemistry calculations that revealed two distinct, relatively high interactions of the CO₂ molecules with the unsaturated Cu centers as well as the exposed Pd orbitals found on the planar rectangular linker. TDS experiments for CO₂ that were performed verified this finding. Although the two distinct adsorption sites did not appear as two well resolved spectroscopic peaks, a clear shift of the peak assigned to the adsorbed species to higher temperature as the loading was decreased was observed. Interestingly, this Q_{st} value is rather modest compared to other high performing MOFs. This attribute is evident by the lack of steepness on the low-pressure adsorption isotherm and implies that mild conditions are required for the regeneration of the adsorbent.

CH₄ and N₂ excess adsorption isotherms revealed comparatively reduced affinity of the gas molecules with the surface and the corresponding Q_{st} values were found to be 17.5 and 12.1 kJ/mol respectively. The total pore volume calculated after performing CH₄ adsorption measurements at 111.5 K (CH₄ boiling point) was identical to the one obtained by Ar (87 K) confirming that the microporous structure is fully accessible to CH₄. Moreover, CH₄ adsorption isotherms were performed at near ambient temperatures. Although the gravimetric capacity was rather modest, it was found that Cu-Pd-nbo adsorbed 211.6 cm³ STP/cm³ at 65 bar which reaches the 80% of the DOE volumetric target, highlighting once more the cooperative effect of unsaturated metal sites and confinement in micropores in combination with the influence of a relatively high crystallographic density. However, it is evident that achieving simultaneously high gravimetric and volumetric capacities constitutes an elaborate task. The material's excess CH₄ high pressure isotherm revealed a plateau at approximately 60 bar suggesting that the

microporous structure was already filled with condensed adsorbate thus further pressure increase has negligible effect on the adsorbed phase. Therefore, there is a strong indication that the solution to the development of efficient adsorbents for gas storage applications will not be found through an optimal pore size but via a rather optimum combination of pore sizes ranging from wide micropores to narrow mesopores.

Taking into account all of the above, IAST calculations were performed for various compositions of CO₂/CH₄ and CO₂/N₂ mixtures. The corresponding selectivities ranged from 10 to 20 and 80 to 1000, respectively, with a trend to increase with increasing pressure and the best estimations being for mixtures containing CO₂ in high concentration.

Subsequently, the same experimental sequence was attempted for In-Pd-soc. Traditional activation methods proved unsuccessful for the material. For this reason, a sc-CO₂ drying routine on a custom-made experimental device was applied. Ar/N₂ porosimetry at 87/77 K, respectively revealed fully reversible type-I isotherms verifying the successful activation and revealing the extensive microporous structure of the sample, in agreement with the SC-XRD analysis. The corresponding BET SSA (747 and 795 m²/g, respectively) and TPV (0.35 cm³/g) confirmed the successful activation of the sample. Moreover, the PSD derived from the argon isotherm revealed a major peak at 5.8 Å, in full agreement with the crystallographic data. In-Pd-soc exhibits substantially lower gravimetric capacities due to the larger mass of its In-trinuclear SBU and its corresponding higher crystallographic density. This highlights a limitation that needs to be taken into consideration when synthetically targeting new MOF structures.

Accordingly, low- and high-pressure CO₂, CH₄ and N₂ adsorption isotherms were performed. As expected, the gravimetric uptakes determined for In-Pd-soc were substantially lower, i.e., 4.1 mmol/g for CO₂ and 1.0 mmol/g for CH₄ at 0 °C and 1 bar. However, the sample revealed appealing CO₂ volumetric capacity (124.2 cc/cc) due to its high crystallographic density. Interestingly, higher Q_{st} values were determined for all gases compared to Cu-Pd-nbo. The corresponding Q_{st0} values were found to be 29.8, 19.6 and 15.3 kJ/mol, for CO₂, CH₄ and N₂ respectively. This can be attributed to the smaller micropores (5.8 Å) that constitute the crystalline framework as well as the increased number of UMS per SBU. IAST calculations

revealed similar behavior to Cu-Pd-nbo and the corresponding selectivity estimations were found to range between 10 to 18 for CO₂/CH₄ and 90 to 1000 for the CO₂/N₂ mixtures.

Cu-Pd-nbo, due to its superior sorption properties, was selected to be further studied for its gas separation activity by performing dynamic column breakthrough experiments on a custom-made experimental rig specially designed for analyzing small quantities of sample. The material was tested for different compositions of CO₂/CH₄ mixtures, namely 10:90 and 50:50, at 25 °C and pressure 0.97 and 5 bar. Cu-Pd-nbo achieved complete separation of all the mixtures by selectively adsorbing CO₂ over CH₄. Competitive adsorption loadings for both components were calculated from the corresponding breakthrough curves and were found to be in good agreement with IAST predictions. Slight deviations can be explained taking into account the energetic inhomogeneity of the surface which is suggested by the CO₂ sorption studies. Moreover, the unusual behavior of increasing selectivity with increasing pressure was experimentally confirmed.

Subsequently, the material was tested in CO₂/N₂ mixtures at 0.97 bar, 25 °C and two different compositions, 10:90 and 50:50. As expected, successful separation was achieved in both cases. CO₂ competitive adsorption loadings were calculated accurately. However, this is not the case for N₂ due to extended degree of competition with CO₂ which leads to very low retention times for the first effluent, leading to increased uncertainty in the calculations.

Future plans derived from this dissertation can be categorized in two main directions; one as purely scientific and one application-oriented. Taking advantage of the experimental expertise in combination with the instrumentation plurality of the research group, an open dialogue between advanced synthetic strategies, theoretical studies, elaborate characterization techniques and extensive evaluation of sorption properties at a wide range of pressures and temperatures, can lead to in depth understanding of the optimum characteristics which will intensify adsorption phenomena in an efficient way.

More specifically, research on new bi-metallic MOF structures that would exhibit an ensemble of pore sizes and correlation of the pore size distribution with the high-pressure adsorption uptakes for CH₄ storage. Special attention needs to be put on the choice of metals and the samples' corresponding crystallographic densities in order to simultaneously achieve high gravimetric and volumetric working capacities, as well as low-cost and sustainable

syntheses. The same strategy can be further implemented for cryogenic hydrogen storage using nanoporous materials, which is a research field that is expected to blossom the following years.

On the other hand, the experimental rig that was built especially for performing dynamic column breakthrough experiments for small amounts of sample can be further modified so that analysis of mixtures containing more gases can be achieved. Moreover, integration of a humidity chamber in order to evaluate in situ the adsorbent performance in the presence of H₂O vapors. The long-term goal derived from this work lies on the construction of a fully automated, lab-scale, temperature-, vacuum-, pressure swing adsorption system (TSA, VSA, PSA) where small amounts of adsorbents will be analyzed under conditions that will approximate the ones of the actual separation process, while the experimental data derived from sorption studies will be used for the construction of an accurate theoretical model which will describe the process in detail.

6. References

1. Sholl, D. S. & Lively, R. P. Seven chemical separations to change the world. *Nature* **532**, 435–437 (2016).
2. Li, H. *et al.* Recent advances in gas storage and separation using metal–organic frameworks. *Mater. Today* **21**, 108–121 (2018).
3. Yu, J. *et al.* CO₂ Capture and Separations Using MOFs: Computational and Experimental Studies. *Chem. Rev.* **117**, 9674–9754 (2017).
4. Nugent, P. *et al.* Porous materials with optimal adsorption thermodynamics and kinetics for CO₂ separation. *Nature* **495**, 80–84 (2013).
5. Chaemchuen, S., Kabir, N. A., Zhou, K. & Verpoort, F. Metal-organic frameworks for upgrading biogas via CO₂ adsorption to biogas green energy. *Chem. Soc. Rev.* **42**, 9304–9332 (2013).
6. Lin, Y., Kong, C., Zhang, Q. & Chen, L. Metal-Organic Frameworks for Carbon Dioxide Capture and Methane Storage. *Adv. Energy Mater.* **7**, (2017).
7. Broom, D. P. *et al.* Outlook and challenges for hydrogen storage in nanoporous materials. *Appl. Phys. A Mater. Sci. Process.* **122**, 1–21 (2016).
8. Broom, D. P. *et al.* Concepts for improving hydrogen storage in nanoporous materials. *Int. J. Hydrogen Energy* **44**, 7768–7779 (2019).
9. Li, J. R. *et al.* Porous materials with pre-designed single-molecule traps for CO₂ selective adsorption. *Nat. Commun.* **4**, 1–8 (2013).
10. Ren, J., Langmi, H. W., North, B. C. & Mathe, M. Review on processing of metal-organic framework (MOF) materials towards system integration for hydrogen storage. *Int. J. Energy Res.* n/a-n/a (2014) doi:10.1002/er.3255.
11. Kayser, H. *Wied. Ann.* **451**, 450–468 (1881).
12. Sing, K. S. W. & Gregg, S. J. *Sing_Adsorption - Surface Area and Porosity_2nd_edition.* (1982).
13. Zsigmondy, A. Z. Uber die Struktur des Gels der Kieselsaure. Theorie der Entwässerung. *Anorg. Chem.* **71**, 356 (1898).
14. Langmuir, I. The constitution and fundamental properties of solids and liquids. II. Liquids. *J. Am. Chem. Soc.* **39**, 1848–1906 (1917).

15. Brunauer, S., Emmett, P. H. & Teller, E. Adsorption of Gases in Multimolecular Layers. *J. Am. Chem. Soc.* **60**, 309–319 (1938).
16. Everett, D. H. INTERNATIONAL UNION OF PURE AND APPLIED CHEMISTRY, MANUAL OF SYMBOLS AND TERMINOLOGY FOR PHYSICOCHEMICAL QUANTITIES AND UNITS. *Pure Appl. Chem.* **31**, 579–638 (1972).
17. Sing, K. S. W. & Everett, D. H. INTERNATIONAL UNION OF PURE COMMISSION ON COLLOID AND SURFACE CHEMISTRY INCLUDING CATALYSIS * REPORTING PHYSISORPTION DATA FOR GAS / SOLID SYSTEMS with Special Reference to the Determination of Surface Area and Porosity. *Int. UNION PURE Comm. COLLOID Surf. Chem.* **57**, 603–619 (1985).
18. Lowell, S., Shields, J. E. & Morral, J. E. *Powder Surface Area and Porosity, 2nd Edition. Journal of Engineering Materials and Technology* vol. 107 (1985).
19. Keller, J. U., Staudt, R. & Tomalla, M. Volume-Gravimetric Measurements of Binary Gas Adsorption Equilibria. *Berichte der Bunsengesellschaft für Phys. Chemie* **96**, 28–32 (1992).
20. Thommes, M. *et al.* Physisorption of gases, with special reference to the evaluation of surface area and pore size distribution (IUPAC Technical Report). *Pure Appl. Chem.* **87**, 1051–1069 (2015).
21. Thommes, M. & Cychosz, K. A. Physical adsorption characterization of nanoporous materials: Progress and challenges. *Adsorption* **20**, 233–250 (2014).
22. Sethia, G., Somani, R. S. & Chand Bajaj, H. Adsorption of carbon monoxide, methane and nitrogen on alkaline earth metal ion exchanged zeolite-X: Structure, cation position and adsorption relationship. *RSC Adv.* **5**, 12773–12781 (2015).
23. Lowell, S., Shields, J.E., Thomas, M.A., Thommes, M. *Characterization of porous solids and powders: Surface area, pore size and density. Kluwer Academic Publishers* vol. 4 (SPRINGER SCIENCE+BUSINESS MEDIA, LLC, 2004).
24. Young, D.M., Crowell, A. D. *Physical Adsorption of Gases.* (Butterworths, London, 1962).
25. Lennard-Jones, J. E. No Title. *Phys.* **4**, 941 (1937).
26. Cunningham, R.E., Williams, R. J. J. Diffusion in Gases and Porous Media. *Plenum Press. New York* 27 (1980).

27. Karger, J., Ruthven, D. M. & Theodorou, D. N. *Diffusion in Nanoporous Materials*. (Wiley-VCH Verlag & Co. KGaA, Boschstr. 12, 69469 Weinheim, Germany, 2012).
28. Crank, J. *The Mathematics of Diffusion*. *Oxford Univ. Press* (1975).
29. Karger, J., Ruthven, D. *Diffusion in Zeolites and other Microporous Materials*. *John Wiley sons inc.* (1991).
30. Present, R. D. *Kinetic Theory of Gases*. *McGraw-Hill, New York* **222**, (1958).
31. Liu, J. & Wei, J. Knudsen diffusion in channels and networks. *Chem. Eng. Sci.* **111**, 1–14 (2014).
32. Rodríguez-Reinoso, F. Characterization of porous solids VI: Preface. *Stud. Surf. Sci. Catal.* **144**, (2002).
33. Polarz, S. & Smarsly, B. Nanoporous Materials. *J. Nanosci. Nanotechnol.* **2**, 581–612 (2002).
34. Powl, J. C., Everett., D. H. Adsorption in slit-like and cylindrical micropores in the Henry's law region. *J. Chem. Soc., Faraday Trans 1* **72**, (1976).
35. Ockwig, N. W., Delgado-Friedrichs, O., O'Keeffe, M. & Yaghi, O. M. Reticular chemistry: Occurrence and taxonomy of nets and grammar for the design of frameworks. *Acc. Chem. Res.* **38**, 176–182 (2005).
36. Cordova, K. E. & Yaghi, O. M. The 'folklore' and reality of reticular chemistry. *Mater. Chem. Front.* **1**, 1304–1309 (2017).
37. Furukawa, H., Cordova, K. E., O'Keeffe, M. & Yaghi, O. M. The chemistry and applications of metal-organic frameworks. *Science (80-)*. **341**, (2013).
38. Yaghi, O. M. *et al.* Reticular synthesis and the design of new materials. *Nature* **423**, 705–714 (2003).
39. Bai, Y. *et al.* Zr-based metal-organic frameworks: Design, synthesis, structure, and applications. *Chem. Soc. Rev.* **45**, 2327–2367 (2016).
40. Yaghi, O. M. Reticular Chemistry - Construction, Properties, and Precision Reactions of Frameworks. *J. Am. Chem. Soc.* **138**, 15507–15509 (2016).
41. Keffe, M. O., Peskov, M. a, Ramsden, S. J. & Yaghi, O. M. (RCSR) Database of , and Symbols for , Crystal. *Acc. Chem. Res.* **41**, 1782–1789 (2008).
42. Celzard, A. & Fierro, V. Preparing a suitable material designed for methane storage: A comprehensive report. *Energy and Fuels* **19**, 573–583 (2005).

43. Mason, J. A., Veenstra, M. & Long, J. R. Evaluating metal-organic frameworks for natural gas storage. *Chem. Sci.* **5**, 32–51 (2014).
44. Alternative Fuels Data Center – Fuel Properties Comparison. http://www.afdc.energy.gov/fuels/fuel_comparison_%0Achart.pdf. (2013).
45. Yildirim, T. Methane Storage in Metal – Organic Frameworks: Current Records, Surprise Findings, and Challenges. *J. Am. Chem. Soc.* **135**, 11887–11894 (2013).
46. Lozano-Castelló, D., Alcañiz-Monge, J., De La Casa-Lillo, M. A., Cazorla-Amorós, D. & Linares-Solano, A. Advances in the study of methane storage in porous carbonaceous materials. *Fuel* **81**, 1777–1803 (2002).
47. Saha, D., Grappe, H. A., Chakraborty, A. & Orkoulas, G. Postextraction Separation, On-Board Storage, and Catalytic Conversion of Methane in Natural Gas: A Review. *Chem. Rev.* **116**, 11436–11499 (2016).
48. Menon, V. C. & Komarmani, S. Porous Adsorbents for Vehicular Natural Gas Storage: A Review. *J. Porous Mater.* **75**, 43–58 (1998).
49. Casco, M. E., Martínez-Escandell, M., Kaneko, K., Silvestre-Albero, J. & Rodríguez-Reinoso, F. Very high methane uptake on activated carbons prepared from mesophase pitch: A compromise between microporosity and bulk density. *Carbon N. Y.* **93**, 11–21 (2015).
50. U.S. Department of Energy. ARPA-E funding Opportunity Announcements–DE-FOA-0000672: Methane Opportunities of Vehicular Energy (MOVE). ARPA-E. <https://arpa-e-foa.energy.gov/%0ADefault.aspx?Search=DE-FOA-0000672>.
51. Wang, X., French, J., Kandadai, S., & Chua, H. T. Adsorption Measurements of Methane on Activated Carbon in the Temperature Range (281 to 343) K and Pressures to 1.2 MPa. *J. Chem. Eng. Data* **8**, 2700–2706 (2010).
52. Casco, M. E. *et al.* High-pressure methane storage in porous materials: Are carbon materials in the pole position? *Chem. Mater.* **27**, 959–964 (2015).
53. Policicchio, A., Filosa, R., Abate, S., Desiderio, G. & Colavita, E. Activated carbon and metal organic framework as adsorbent for low-pressure methane storage applications: an overview. *J. Porous Mater.* **24**, 905–922 (2017).
54. Matranga, K. R., Stella, A., Myers, A. L. & Glandt, E. D. Molecular Simulation of Adsorbed Natural Gas. *Sep. Sci. Technol.* **27**, 1825–1836 (1992).

55. Alezi, D. *et al.* MOF Crystal Chemistry Paving the Way to Gas Storage Needs: Aluminum-Based MOF for CH_4 , O_2 , and CO_2 Storage. *J. Am. Chem. Soc.* **137**, 13308–13318 (2015).
56. Peng, Y. *et al.* Simultaneously high gravimetric and volumetric methane uptake characteristics of the metal-organic framework NU-111. *Chem. Commun.* **49**, 2992–2994 (2013).
57. Furukawa, H., Ko, N., Go, Y. B., Aratani, N., Choi, S. B., Choi, E., ... Yaghi, O. M. Ultrahigh Porosity in Metal-Organic Frameworks. *Science*, 329(5990), 424–428. doi:10.1126/science.1192160. *Science* (80-.). 424–428 (2010).
58. Guo, Z. *et al.* A metal-organic framework with optimized open metal sites and pore spaces for high methane storage at room temperature. *Angew. Chemie - Int. Ed.* **50**, 3178–3181 (2011).
59. Wu, H. *et al.* Metal-organic frameworks with exceptionally high methane uptake: Where and how is methane stored? *Chem. - A Eur. J.* **16**, 5205–5214 (2010).
60. Wu, H., Zhou, W. & Yildirim, T. High-capacity methane storage in metal-organic frameworks M2(dhtp): The important role of open metal sites. *J. Am. Chem. Soc.* **131**, 4995–5000 (2009).
61. Wilmer, C. E. *et al.* Large-scale screening of hypothetical metal-organic frameworks. *Nat. Chem.* **4**, 83–89 (2012).
62. Sircar, S. Measurement of Gibbsian Surface Excess. *AIChE J.* **47**, 1169–1176 (2001).
63. Murata, K., El-Merraoui, M. & Kaneko, K. A new determination method of absolute adsorption isotherm of supercritical gases under high pressure with a special relevance to density-functional theory study. *J. Chem. Phys.* **114**, 4196–4205 (2001).
64. Myers, A. L. & Monson, P. A. Adsorption in porous materials at high pressure: Theory and experiment. *Langmuir* **18**, 10261–10273 (2002).
65. Gumma, S. & Talu, O. Net adsorption: A thermodynamic framework for supercritical gas adsorption and storage in porous solids. *Langmuir* **26**, 17013–17023 (2010).
66. Dinča, M. *et al.* Hydrogen storage in a microporous metal-organic framework with exposed Mn^{2+} coordination sites. *J. Am. Chem. Soc.* **128**, 16876–16883 (2006).
67. Chen, B. Methane storage in metal-organic frameworks. *Chem. Soc. Rev.* **00**, 1–23 (2013).
68. Senkovska, I. & Kaskel, S. High pressure methane adsorption in the metal-organic

- frameworks Cu₃(btc)₂, Zn₂(bdc)₂dabco, and Cr₃F(H₂O)₂O(bdc)₃. *Microporous Mesoporous Mater.* **112**, 108–115 (2008).
69. Li, B., Wen, H. M., Zhou, W., Xu, J. Q. & Chen, B. Porous Metal-Organic Frameworks: Promising Materials for Methane Storage. *Chem* **1**, 557–580 (2016).
 70. He, Y., Zhou, W., Yildirim, T. & Chen, B. A series of metal-organic frameworks with high methane uptake and an empirical equation for predicting methane storage capacity. *Energy Environ. Sci.* **6**, 2735–2744 (2013).
 71. Quinn, D F, MacDonald, J A, and Sosin, K. *Microporous carbons as adsorbents for methane storage. United States: N. p., 1994.*
 72. Gándara, F., Furukawa, H., Lee, S. & Yaghi, O. M. High methane storage capacity in aluminum metal-organic frameworks. *J. Am. Chem. Soc.* **136**, 5271–5274 (2014).
 73. Mason, J. A. *et al.* Methane storage in flexible metal-organic frameworks with intrinsic thermal management. *Nature* **527**, 357–361 (2015).
 74. Keith, D. W. Why capture CO₂ from the atmosphere? *Science (80-.)*. **325**, 1654–1655 (2009).
 75. Haines, M., Kemper, J., Davison, J., Gale, J., Singh, P., Santos, S. Assessment of emerging CO₂ capture technologies and their potential to reduce costs. *Int. Energy Agency Paris, Fr.* (2014).
 76. Iglesias, R. S. Carbon Capture and Storage: How Green Can Black Be? *Science (80-.)*. **325**, 1647–1652 (2009).
 77. <https://www.iea.org/data-and-statistics/charts/global-energy-related-co2-emissions-1990-2021>, IEA, Paris2-emissions-1990-2021. (2021).
 78. Rochelle, G. T. Amine Scrubbing for CO₂ Capture. *Science (80-.)*. **325**, 1652–1654 (2009).
 79. Wang, Q., Luo, J., Zhong, Z. & Borgna, A. CO₂ capture by solid adsorbents and their applications: Current status and new trends. *Energy Environ. Sci.* **4**, 42–55 (2011).
 80. D’Alessandro, D. M., Smit, B. & Long, J. R. Carbon dioxide capture: Prospects for new materials. *Angew. Chemie - Int. Ed.* **49**, 6058–6082 (2010).
 81. Rowsell, J. L. C. & Yaghi, O. M. Metal-organic frameworks: A new class of porous materials. *Microporous Mesoporous Mater.* **73**, 3–14 (2004).
 82. Lee, K.B., Sircar, S. Removal and Recovery of Compressed CO₂ from Flue Gas by a

- Novel Thermal Swing Chemisorption Process. *AIChE J.* **54**, 2293–2302 (2008).
83. Jansen, D., Gazzani, M., Manzolini, G., Dijk, E. Van & Carbo, M. Pre-combustion CO₂ capture. *Int. J. Greenh. Gas Control* **40**, 167–187 (2015).
 84. Bhatt, P. M. *et al.* A Fine-Tuned Fluorinated MOF Addresses the Needs for Trace CO₂ Removal and Air Capture Using Physisorption. *J. Am. Chem. Soc.* **138**, 9301–9307 (2016).
 85. Yang, L., Ge, X., Wan, C., Yu, F. & Li, Y. Progress and perspectives in converting biogas to transportation fuels. *Renew. Sustain. Energy Rev.* **40**, 1133–1152 (2014).
 86. Liu, Y. *et al.* Enhanced CO₂/CH₄ Separation Performance of a Mixed Matrix Membrane Based on Tailored MOF-Polymer Formulations. *Adv. Sci.* **5**, 2–6 (2018).
 87. Skarstrom, C. W. U.S. Patent 2,944,627 (Feb. 1958) to Esso Research and Engineering Company.
 88. Guerin de Montgareuil, P. & Domine, D. French Patent 1,223,261 (Dec. 1957) to Air Liquide.
 89. Wiheeb, A. D., Helwani, Z., Kim, J. & Othman, M. R. Pressure Swing Adsorption Technologies for Carbon Dioxide Capture. *Sep. Purif. Rev.* **45**, 108–121 (2016).
 90. Ruthven, D. M., Farooq, S., Knaebel, K. S. *Pressure Swing Adsorption*. (VCH Publishers, 1994).
 91. Shen, C., Yu, J., Li, P., Grande, C. A. & Rodrigues, A. E. Capture of CO₂ from flue gas by vacuum pressure swing adsorption using activated carbon beads. *Adsorption* **17**, 179–188 (2011).
 92. Cavalcante Jr., C. L. Industrial adsorption separation processes: Fundamentals, modeling and applications. *Lat. Am. Appl. Res.* **30**, 357–364 (2000).
 93. Huang, H. *et al.* Enhancing CO₂ adsorption and separation ability of Zr(IV)-based metal-organic frameworks through ligand functionalization under the guidance of the quantitative structure-property relationship model. *Chem. Eng. J.* **289**, 247–253 (2016).
 94. Belmabkhout, Y., Mouttaki, H., Eubank, J. F., Guillerm, V. & Eddaoudi, M. Effect of pendant isophthalic acid moieties on the adsorption properties of light hydrocarbons in HKUST-1-like tbo -MOFs: Application to methane purification and storage. *RSC Adv.* **4**, 63855–63859 (2014).
 95. Qiao, Z., Wang, N., Jiang, J. & Zhou, J. Design of amine-functionalized metal-organic

- frameworks for CO₂ separation: The more amine, the better? *Chem. Commun.* **52**, 974–977 (2016).
96. Lu, Z. *et al.* The Utilization of Amide Groups to Expand and Functionalize Metal-Organic Frameworks Simultaneously. *Chem. - A Eur. J.* **22**, 6277–6285 (2016).
 97. Bratsos, I. *et al.* Heterometallic In(III)-Pd(II) Porous Metal-Organic Framework with Square-Octahedron Topology Displaying High CO₂ Uptake and Selectivity toward CH₄ and N₂. *Inorg. Chem.* **57**, 7244–7251 (2018).
 98. Spanopoulos, I. *et al.* Exceptional gravimetric and volumetric CO₂ uptake in a palladated NbO-type MOF utilizing cooperative acidic and basic, metal-CO₂ interactions. *Chem. Commun.* **52**, 10559–10562 (2016).
 99. Rajagopalan, A. K. & Rajendran, A. The effect of nitrogen adsorption on vacuum swing adsorption based post-combustion CO₂ capture. *Int. J. Greenh. Gas Control* **78**, 437–447 (2018).
 100. Wilkins, N. S. & Rajendran, A. Measurement of competitive CO₂ and N₂ adsorption on Zeolite 13X for post-combustion CO₂ capture. *Adsorption* **25**, 115–133 (2019).
 101. Hefti, M., Marx, D., Joss, L. & Mazzotti, M. Adsorption equilibrium of binary mixtures of carbon dioxide and nitrogen on zeolites ZSM-5 and 13X. *Microporous Mesoporous Mater.* **215**, 215–228 (2015).
 102. Avijegon, G., Xiao, G., Li, G. & May, E. F. Binary and ternary adsorption equilibria for CO₂/CH₄/N₂ mixtures on Zeolite 13X beads from 273 to 333 K and pressures to 900 kPa. *Adsorption* **24**, 381–392 (2018).
 103. Wilkins, N. S., Rajendran, A. & Farooq, S. Dynamic column breakthrough experiments for measurement of adsorption equilibrium and kinetics. *Adsorption* **27**, 397–422 (2021).
 104. Kepert, C. J. & Rosseinsky, M. J. Zeolite-like crystal structure of an empty microporous molecular framework. *Chem. Commun.* **536**, 375–376 (1999).
 105. Reichenauer, G. & Scherer, G. W. Nitrogen sorption in aerogels. *J. Non. Cryst. Solids* **285**, 167–174 (2001).
 106. Düren, T., Millange, F., Férey, G., Walton, K. S. & Snurr, R. Q. Calculating geometric surface areas as a characterization tool for metal - Organic frameworks. *J. Phys. Chem. C* **111**, 15350–15356 (2007).
 107. Thommes, M. & Findenegg, G. H. Pore Condensation and Critical-Point Shift of a Fluid

- in Controlled-Pore Glass. *Langmuir* **10**, 4270–4277 (1994).
108. Thommes, M., Köhn, R. & Fröba, M. Sorption and pore condensation behavior of pure fluids in mesoporous MCM-48 silica, MCM-41 silica, SBA-15 silica and controlled-pore glass at temperatures above and below the bulk triple point. *Appl. Surf. Sci.* **196**, 239–249 (2002).
 109. Stefanopoulos, K. L. *et al.* Total neutron scattering study of supercooled CO₂ confined in an ordered mesoporous carbon. *Carbon N. Y.* **167**, 296–306 (2020).
 110. Tampaxis, C. *et al.* Enhanced Densification of CO₂ Confined in the Pores of a Carbon Material: an in Situ Total Neutron Scattering Study. *J. Surf. Investig.* **14**, S221–S224 (2020).
 111. Sircar, S. & Hufton, J. R. Why does the linear driving force model for adsorption kinetics work? *Adsorption* **6**, 137–147 (2000).
 112. Monshi, A., Foroughi, M. R. & Monshi, M. R. Modified Scherrer Equation to Estimate More Accurately Nano-Crystallite Size Using XRD. *World J. Nano Sci. Eng.* **02**, 154–160 (2012).
 113. Seeberger, A., Andresen, A. K. & Jess, A. Prediction of long-term stability of ionic liquids at elevated temperatures by means of non-isothermal thermogravimetric analysis. *Phys. Chem. Chem. Phys.* **11**, 9375–9381 (2009).
 114. Akçay, A., Babucci, M., Balci, V. & Uzun, A. A model to predict maximum tolerable temperatures of metal-oxide-supported 1-n-butyl-3-methylimidazolium based ionic liquids. *Chem. Eng. Sci.* **123**, 588–595 (2015).
 115. Myers, A. L., Prausnitz, J. M. Thermodynamics of Mixed-Gas Adsorption. *A.I.Ch.E. J.* **11**, 121–126 (1965).
 116. Lee, S., Lee, J. H. & Kim, J. User-friendly graphical user interface software for ideal adsorbed solution theory calculations. *Korean J. Chem. Eng.* **35**, 214–221 (2018).
 117. Zhang, Z., Yao, Z. Z., Xiang, S. & Chen, B. Perspective of microporous metal-organic frameworks for CO₂ capture and separation. *Energy Environ. Sci.* **7**, 2868–2899 (2014).
 118. Simmons, J. M., Wu, H., Zhou, W. & Yildirim, T. Carbon capture in metal-organic frameworks - A comparative study. *Energy Environ. Sci.* **4**, 2177–2185 (2011).
 119. Aprea, P., Caputo, D., Gargiulo, N., Iucolano, F. & Pepe, F. Modeling carbon dioxide adsorption on microporous substrates: Comparison between Cu-BTC metal-organic

- framework and 13X zeolitic molecular sieve. *J. Chem. Eng. Data* **55**, 3655–3661 (2010).
120. Lin, Y., Yan, Q., Kong, C. & Chen, L. Polyethyleneimine incorporated metal-organic frameworks adsorbent for highly selective CO₂ capture. *Sci. Rep.* **3**, 14–16 (2013).
 121. Chen, Y. *et al.* A new MOF-505@GO composite with high selectivity for CO₂/CH₄ and CO₂/N₂ separation. *Chem. Eng. J.* **308**, 1065–1072 (2017).
 122. Zhang, Z., Li, Z. & Li, J. Computational study of adsorption and separation of CO₂, CH₄, and N₂ by an rht-type metal-organic framework. *Langmuir* **28**, 12122–12133 (2012).
 123. Krishna, R. & Van Baten, J. M. How Reliable Is the Ideal Adsorbed Solution Theory for the Estimation of Mixture Separation Selectivities in Microporous Crystalline Adsorbents? *ACS Omega* **6**, 15499–15513 (2021).